

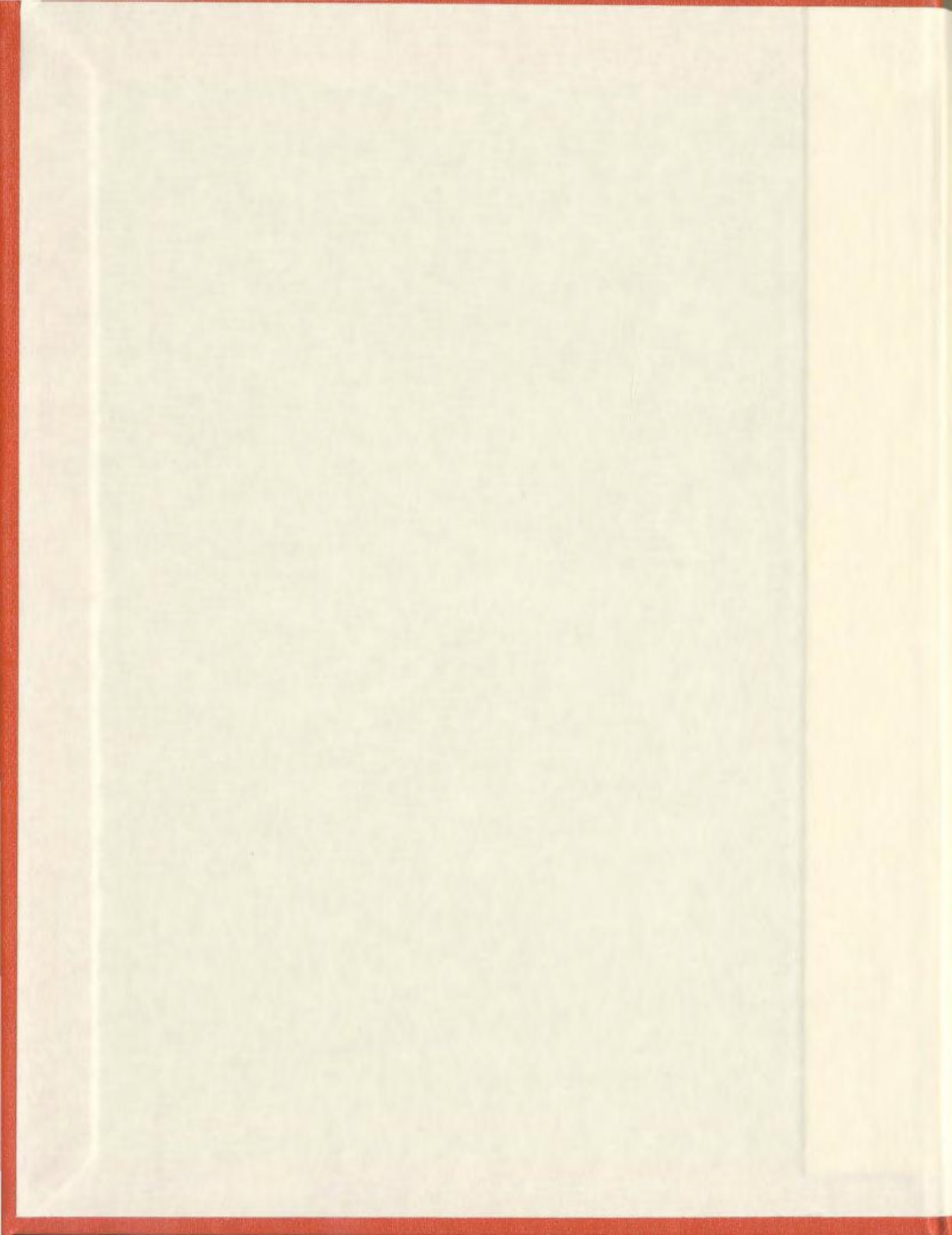
COMPARISON OF CONTROLLED RECTIFIER AND
CHOPPER POWER SUPPLIES FOR DC SMELTING
FURNACE APPLICATIONS

CENTRE FOR NEWFOUNDLAND STUDIES

**TOTAL OF 10 PAGES ONLY
MAY BE XEROXED**

(Without Author's Permission)

JASON KARL SPARKES



UNIVERSITY OF CALIFORNIA LIBRARY
1000 UNIVERSITY AVENUE, LOS ANGELES, CALIF. 90024

THE JAMES EARL RAY CASE

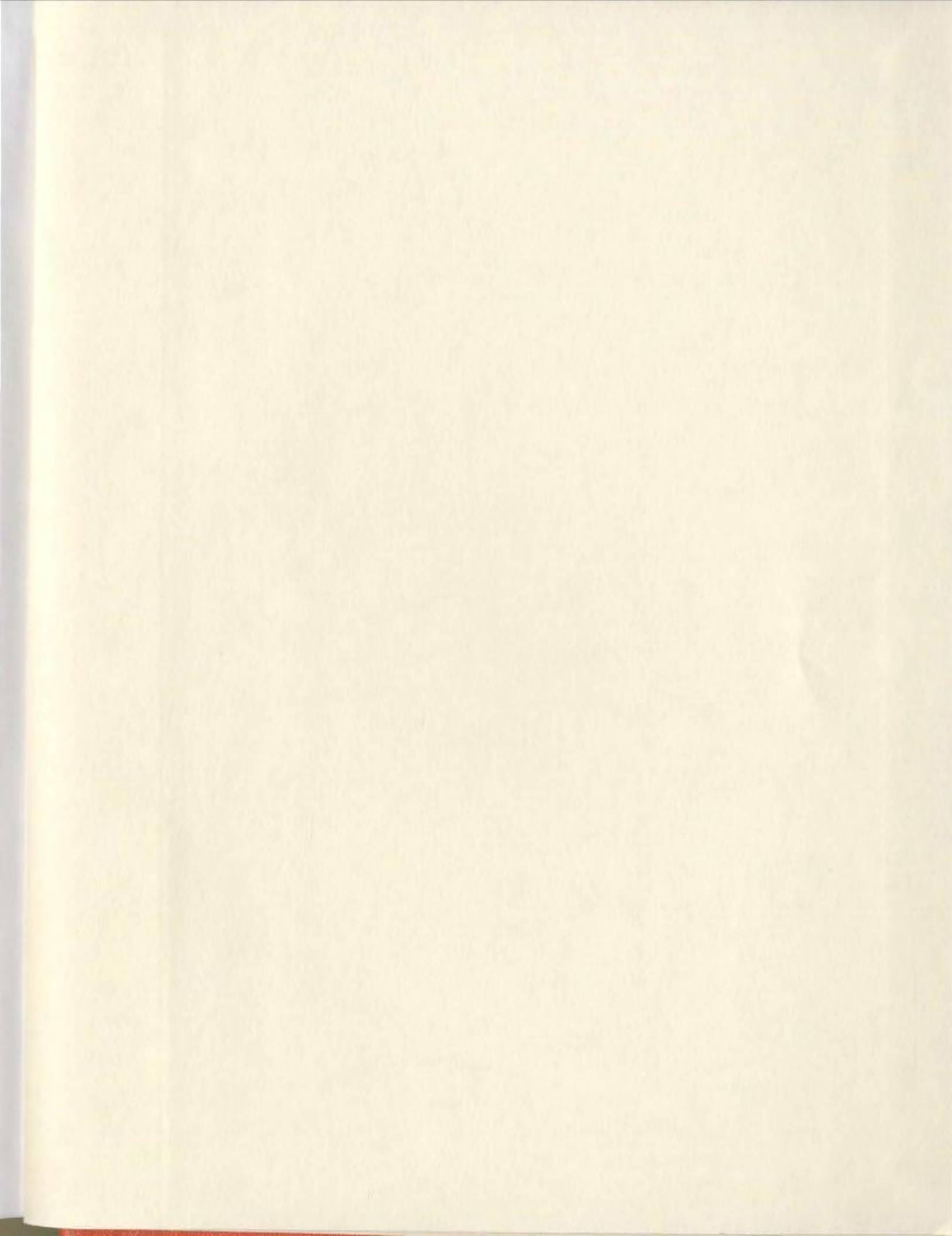
A FIVE VOLUME SET
EDITED BY JAMES EARL RAY
IN THE INTERESTS OF THE
PEOPLE OF THE UNITED STATES
OF AMERICA
AND THE PEOPLE OF THE WORLD

THE JAMES EARL RAY CASE
A FIVE VOLUME SET

1971

THE JAMES EARL RAY CASE







Library and
Archives Canada

Bibliothèque et
Archives Canada

Published Heritage
Branch

Direction du
Patrimoine de l'édition

395 Wellington Street
Ottawa ON K1A 0N4
Canada

395, rue Wellington
Ottawa ON K1A 0N4
Canada

0-612-99116-4

NOTICE:

The author has granted a non-exclusive license allowing Library and Archives Canada to reproduce, publish, archive, preserve, conserve, communicate to the public by telecommunication or on the Internet, loan, distribute and sell theses worldwide, for commercial or non-commercial purposes, in microform, paper, electronic and/or any other formats.

The author retains copyright ownership and moral rights in this thesis. Neither the thesis nor substantial extracts from it may be printed or otherwise reproduced without the author's permission.

AVIS:

L'auteur a accordé une licence non exclusive permettant à la Bibliothèque et Archives Canada de reproduire, publier, archiver, sauvegarder, conserver, transmettre au public par télécommunication ou par l'Internet, prêter, distribuer et vendre des thèses partout dans le monde, à des fins commerciales ou autres, sur support microforme, papier, électronique et/ou autres formats.

L'auteur conserve la propriété du droit d'auteur et des droits moraux qui protège cette thèse. Ni la thèse ni des extraits substantiels de celle-ci ne doivent être imprimés ou autrement reproduits sans son autorisation.

In compliance with the Canadian Privacy Act some supporting forms may have been removed from this thesis.

Conformément à la loi canadienne sur la protection de la vie privée, quelques formulaires secondaires ont été enlevés de cette thèse.

While these forms may be included in the document page count, their removal does not represent any loss of content from the thesis.

Bien que ces formulaires aient inclus dans la pagination, il n'y aura aucun contenu manquant.


Canada

COMPARISON OF CONTROLLED RECTIFIER AND CHOPPER POWER
SUPPLIES FOR DC SMELTING FURNACE APPLICATIONS

by

© Jason Karl Sparkes, B.Eng.

A Thesis submitted to the
School of Graduate Studies
in partial fulfillment of the
requirements for the degree of
Master of Engineering



Faculty of Engineering and Applied Science
Memorial University of Newfoundland

May 2004

St. John's, Newfoundland, Canada

To My Parents...

Abstract

High power electric arc furnaces are used in the metals industry for smelting various ore types and melting scrap steel. To a power system an arc furnace represents an erratic load, which is a leading cause of voltage flicker, harmonic distortion, and low power factor. In an attempt to reduce the impact on the power system and to reduce production cost new electric arc furnaces have been constructed with DC power supplies. DC electric arc furnaces have been proven to be superior to AC furnaces with regard to reducing voltage flicker and lowering production cost.

Traditionally DC furnaces have been supplied from thyristor-controlled rectifiers. However, as transistor ratings increase alternative configurations become available. Namely active rectifiers, and uncontrolled rectifier chopper combinations. To date only the uncontrolled rectifier chopper power supply has been used as an alternative to the controlled rectifier power supply. The purpose of this thesis is to describe each configuration in detail and investigate their suitability to DC smelting furnace applications. The comparison will investigate the line side power quality, rectifier performance, and reliability.

Acknowledgements

This thesis work began in May 2001 with an industrial internship at Hatch Associates Limited. Since that time periods of academic research at Memorial University of Newfoundland have been combined with periods of industrial work at Hatch. Funding for this project has been provided by the National Science and Engineering Research Council of Canada (NSERC), Hatch Associates Limited, and Memorial University of Newfoundland.

First and foremost I would to thank Dr. John Quaicoe for his guidance and supervision over the past three years. I would also like to thank Ms. Moya Crocker from the Office of the Associate Dean of Graduate Studies for ensuring that things proceeded smoothly throughout my time at the University.

At Hatch I would like to thank Mr. Dave MacIntyre for giving me a job and supporting my decision to undertake the Masters of Engineering Degree. The idea for the project came from Dr. Tom Ma at Hatch and I would like to thank him for answering questions and providing me with contacts to obtain practical information relating to DC smelting furnaces. Industrial data has been provided to me by Hatch, and I would like to thank Dr. Laszlo Kadar and Mr. Dawid Theron for sending me the controlled rectifier industrial data. I would also like to thank Mr. James Wikston, Dr. Brian Perkins, and Dr. Mohammad Sedighy for answering questions on a variety of topics relating to this study. Also with Hatch I would like to thank Mr. David Hogarth and Mr. Nils Voermann for ensuring that the funding for this project was made available.

In addition to the University and Hatch I would also like to thank several individuals from industry in helping me obtain information to complete the thesis. These include Mr. Vince Scaini, Mr. Patrick McGinn, and Mr. Bill Holmes from Satcon Power Systems for providing information on the uncontrolled rectifier chopper power supply. Mr. John Metric from Gulf Chemical and Metallurgical Corporation for providing me with the opportunity to obtain the industrial measurements from the only commercial DC EAF uncontrolled rectifier chopper power supply. Dr. Wolfgang Hoeger from Siemens for providing information on the controlled rectifier power supply, and Mr. Morgan Ming from Praxair Canada for providing the transport properties of electric arc furnace plasma.

Table of Contents

Abstract	i
Acknowledgements	ii
Table of Contents	iii
List of Figures	vi
List of Tables	ix
Nomenclature	x
1 Introduction	1
1.1 Thesis Objectives	4
1.2 Thesis Organization	5
1.3 Literature Review	6
2 Controlled Rectifier Power Supply	11
2.1 Major Components	12
2.1.1 Rectifier Transformers	12
2.1.2 Controlled Rectifiers	14
2.1.3 DC Reactors	17
2.2 Rectifier Operation	17
2.2.1 Constant Current Load Without Supply Reactance	19
2.2.2 Constant Current Load With Supply Reactance	27
2.2.3 Normal Operation	35
2.3 Converter Control	37
2.3.1 Constant Current Control	38
2.3.2 Constant Power Control	39
2.3.3 Constant Power Control With Current Limit	43
2.4 Summary	45

3	Uncontrolled Rectifier Chopper Power Supply	47
3.1	Major Components	48
3.1.1	Rectifier Transformers	49
3.1.2	Uncontrolled Rectifiers	50
3.1.3	DC Link Capacitors	52
3.1.4	Chopper Sections	52
3.1.5	Output Reactors	56
3.2	Rectifier Operation	57
3.2.1	Constant Voltage Load Discontinuous Conduction	58
3.2.2	Constant Voltage Load Continuous Conduction	67
3.3	Chopper Operation	75
3.3.1	Constant Current Load With Output Reactance	77
3.3.2	Normal Operation	82
3.4	Converter Control	83
3.4.1	Constant Current Control	84
3.4.2	Constant Power Control	85
3.4.3	Constant Power Control With Current Limit	89
3.5	Summary	91
4	DC Electric Arc Furnace Model	93
4.1	Electric Arc Properties	94
4.2	Channel Arc Model	96
4.2.1	Electrical Energy Input	98
4.2.2	Conduction Heat Transfer	100
4.2.3	Convection Heat Transfer	103
4.2.4	Radiation Heat Transfer	106
4.2.5	Model Validation	108
4.3	Electric Arc Furnace Model	115
4.3.1	Slag Resistance	118
4.3.2	Voltage and Current Fluctuation	118
4.3.3	Model Validation	120
4.4	Summary	124
5	Power Supply Comparison	125
5.1	Case Study	126
5.1.1	Controlled Rectifier	126
5.1.2	Uncontrolled Rectifier Chopper	132
5.2	Power Quality	138
5.2.1	Harmonic and Interharmonic Distortion	139
5.2.2	Unbalanced Voltage	142
5.2.3	Voltage Flicker	144
5.2.4	Power and Power Factor	146

5.3	Rectifier Performance	150
5.3.1	Efficiency	150
5.3.2	Rectification Ratio	152
5.3.3	Ripple Factor	152
5.3.4	Form Factor	153
5.3.5	Transformer Utilization Factor	154
5.4	Reliability	155
5.4.1	Controlled Rectifier	156
5.4.2	Uncontrolled Rectifier Chopper	157
5.5	Summary	158
6	Conclusion	159
6.1	Orginal Contributions	160
6.2	Future Analysis	161
	References	163
A	EUPEC Device Data Sheets	175
B	PSCAD Screenshots	188
C	Matlab Programs	191
D	PSCAD Flickermeter Test Results	194

List of Figures

1.1	Power Fluctuations for AC Arc Smelting and DC Arc Smelting	2
2.1	Simplified 12-Pulse Controlled Rectifier Power Supply	13
2.2	Three-Phase Bridge Layout	15
2.3	Controlled Rectifier Protection Circuit	16
2.4	Controlled Rectifier Output Voltage Waveforms (Without Supply Reactance)	22
2.5	Voltage and Current Waveforms at Secondary of Δ/Δ Transformer (Without Supply Reactance)	23
2.6	Voltage and Current Waveforms at Secondary of Y/ Δ Transformer (Without Supply Reactance)	24
2.7	Controlled Rectifier Input Voltage and Current Waveforms (Without Supply Reactance)	25
2.8	Controlled Rectifier Output Voltage Waveforms (With Supply Reactance)	30
2.9	Voltage and Current Waveforms at Secondary of Δ/Δ Transformer (With Supply Reactance)	31
2.10	Voltage and Current Waveforms at Secondary of Y/ Δ Transformer (With Supply Reactance)	32
2.11	Controlled Rectifier Input Voltage and Current Waveforms (With Supply Reactance)	33
2.12	Controlled Rectifier Current Control Block Diagram	38
2.13	Controlled Rectifier Current Control (Step Response)	40
2.14	Controlled Rectifier Power Control Block Diagram	41
2.15	Controlled Rectifier Power Control (Step Response)	42
2.16	Controlled Rectifier Power Control with Current Limit Block Diagram	43
2.17	Controlled Rectifier Current Limited Power Control (Setpoint Tracking)	44
3.1	Simplified 12-Pulse Uncontrolled Rectifier Chopper Power Supply . .	49
3.2	Uncontrolled Rectifier Chopper Protection Circuit	52
3.3	Basic Chopper Module	53
3.4	Parallel Chopper Connection	55
3.5	Chopper Protection Circuit	56

3.6	Voltage and Current Waveforms at Secondary of Δ/Δ Transformer (Discontinuous Conduction)	63
3.7	Voltage and Current Waveforms at Secondary of Δ/Y Transformer (Discontinuous Conduction)	64
3.8	Uncontrolled Rectifier Input Voltage and Current Waveforms (Discontinuous Conduction)	65
3.9	Voltage and Current Waveforms at Secondary of Δ/Δ Transformer (Continuous Conduction)	71
3.10	Voltage and Current Waveforms at Secondary of Δ/Y Transformer (Continuous Conduction)	72
3.11	Uncontrolled Rectifier Input Voltage and Current Waveforms (Continuous Conduction)	73
3.12	Chopper Output Voltages	79
3.13	Chopper Unit 1 Currents	80
3.14	Chopper Unit 2 Currents	81
3.15	Chopper Current Control Block Diagram	84
3.16	Chopper Current Control (Step Response)	86
3.17	Chopper Power Control Block Diagram	87
3.18	Chopper Power Control (Step Response)	88
3.19	Chopper Power Control with Current Limit Block Diagram	89
3.20	Chopper Current Limited Power Control (Setpoint Tracking)	90
4.1	Simplified Schematic Diagram of Arc Profile	95
4.2	Channel Arc Model	97
4.3	EAF Plasma Electrical Conductivity	99
4.4	EAF Plasma Thermal Conductivity	100
4.5	EAF Plasma Density	104
4.6	EAF Plasma Enthalpy	105
4.7	EAF Plasma Radiation Density	107
4.8	Arc Parameters as A Function of Arc Current (With Fe Ions)	109
4.9	Arc Parameters as A Function of Arc Length (With Fe Ions)	110
4.10	Energy Balance (With Fe Ions)	111
4.11	Arc Parameters as A Function of Arc Current (Without Fe Ions)	112
4.12	Arc Parameters as A Function of Arc Length (Without Fe Ions)	113
4.13	Energy Balance (Without Fe Ions)	114
4.14	Load Resistance Versus Electrode Tip Position	117
4.15	Measured and Simulated Uncontrolled Rectifier Chopper Output Voltage Waveform	121
4.16	Measured Uncontrolled Rectifier Chopper Input Voltage and Current Waveforms	122
4.17	Simulated Uncontrolled Rectifier Chopper Input Voltage and Current Waveforms	123

5.1	Simulated Controlled Rectifier Process Parameters	128
5.2	Simulated Controlled Rectifier Input Characteristics	129
5.3	Simulated Controlled Rectifier Output Characteristics	130
5.4	Simulated Controlled Rectifier Harmonic Content	131
5.5	Simulated Uncontrolled Rectifier Chopper Process Parameters	134
5.6	Simulated Uncontrolled Rectifier Chopper Input Characteristics . . .	135
5.7	Simulated Uncontrolled Rectifier Chopper Output Characteristics . .	136
5.8	Simulated Uncontrolled Rectifier Chopper Harmonic Content	137
5.9	Measured DC Smelting Furnace Harmonic Distortion	142
5.10	Measured DC Smelting Furnace Voltage Flicker	146
5.11	Measured DC Smelting Furnace Power	147
5.12	Measured DC Smelting Furnace Power Factor	149

List of Tables

4.1	Electrical Conductivity Coefficients (1000 K - 25000 K)	99
4.2	Thermal Conductivity Coefficients (1000 K - 3000 K)	101
4.3	Thermal Conductivity Coefficients (3000 K - 6000 K)	101
4.4	Thermal Conductivity Coefficients (6000 K - 15000 K)	102
4.5	Thermal Conductivity Coefficients (15000 K - 25000 K)	102
4.6	Density Coefficients (1000 K - 25000 K)	104
4.7	Enthalpy Coefficients (1000 K - 25000 K)	105
4.8	Radiation Density Coefficients (1000 K - 25000 K)	107
5.1	Simulated Controlled Rectifier Harmonic Distortion	141
5.2	Simulated Uncontrolled Rectifier Chopper Harmonic Distortion . . .	141
5.3	Simulated Controlled Rectifier Voltage Unbalance	143
5.4	Simulated Uncontrolled Rectifier Chopper Voltage Unbalance	143
5.5	Simulated Controlled Rectifier Instantaneous Voltage Flicker	145
5.6	Simulated Uncontrolled Rectifier Chopper Instantaneous Voltage Flicker	145
5.7	Simulated Controlled Rectifier Power Factor	148
5.8	Simulated Uncontrolled Rectifier Chopper Power Factor	148
5.9	Simulated Controlled Rectifier Efficiency	151
5.10	Simulated Uncontrolled Rectifier Chopper Efficiency	151
5.11	Simulated Controlled Rectifier Rectification Ratio	152
5.12	Simulated Uncontrolled Rectifier Chopper Rectification Ratio	152
5.13	Simulated Controlled Rectifier Ripple Factor	153
5.14	Simulated Uncontrolled Rectifier Chopper Ripple Factor	153
5.15	Simulated Controlled Rectifier Form Factor	154
5.16	Simulated Uncontrolled Rectifier Chopper Form Factor	154
5.17	Simulated Controlled Rectifier Transformer Utilization Factor	155
5.18	Simulated Uncontrolled Rectifier Transformer Utilization Factor . . .	155
5.19	Controlled Rectifier Parts Count	156
5.20	Uncontrolled Rectifier Chopper Parts Count	157

Nomenclature

Abbreviations

<i>AC</i>	: Alternating Current
<i>DC</i>	: Direct Current
<i>EAF</i>	: Electric Arc Furnace
<i>IPT</i>	: Interphase Transformer
<i>SVC</i>	: Static Var Compensator
<i>HVDC</i>	: High Voltage Direct Current
<i>SCR</i>	: Silicon Controlled Rectifier
<i>IGBT</i>	: Insulated Gate Bipolar Transistor
<i>ONAN</i>	: Oil Natural Air Natural Cooling
<i>ONAF</i>	: Oil Natural Air Forced Cooling
<i>OFAF</i>	: Oil Forced Air Forced Cooling
<i>OFWF</i>	: Oil Forced Water Forced Cooling
<i>AFWF</i>	: Air Forced Water Forced Cooling
<i>WFAN</i>	: Water Forced Air Natural Cooling
<i>WFWF</i>	: Water Forced Water Forced Cooling
di/dt	: Current Rate of Change
dv/dt	: Voltage Rate of Change
<i>MFD</i>	: Magneto Fluid Dynamic Arc Model
<i>CAM</i>	: Channel Arc Model
<i>RMS</i>	: Root Mean Square
<i>RSS</i>	: Root Sum Square
<i>PI</i>	: Proportional Integral Controller
<i>PF</i>	: Power Factor
<i>DPF</i>	: Displacement Power Factor
<i>TDHD</i>	: Total Discrete Harmonic Distortion
<i>TIHD</i>	: Total Interharmonic Distortion
<i>THD</i>	: Total Harmonic Distortion
<i>TDDD</i>	: Total Discrete Demand Distortion
<i>TIDD</i>	: Total Inter Demand Distortion
<i>TDD</i>	: Total Demand Distortion

<i>RF</i>	: Ripple Factor
<i>FF</i>	: Form Factor
<i>TUF</i>	: Transformer Utilization Factor
<i>MTBF</i>	: Mean Time Between Failure
<i>MTTR</i>	: Mean Time To Repair

Symbols

<i>V</i>	: Average or RMS Voltage
<i>v</i>	: Instantaneous Voltage
<i>I</i>	: Average or RMS Current
<i>i</i>	: Instantaneous Current
<i>Z</i>	: Impedance
<i>R</i>	: Resistance
<i>X</i>	: Reactance
<i>L</i>	: Inductance
<i>C</i>	: Capacitance
<i>f</i>	: Frequency
ω	: Radian Frequency
α	: Firing Angle
μ	: Interphase Commutation Overlap Angle
ζ	: Interbridge Commutation Overlap Angle
β	: Conduction Angle
γ	: Extinction Angle
ϕ	: Phase Shift Angle

Subscripts

<i>a</i>	: Phase A
<i>b</i>	: Phase B
<i>c</i>	: Phase C
<i>L</i>	: Line
<i>N</i>	: Neutral
<i>p</i>	: Positive
<i>n</i>	: Negative
<i>d</i>	: DC Side

Superscripts

<i>p</i>	: Transformer Primary
<i>s</i>	: Transformer Secondary
<i>c</i>	: Commutating Interval
<i>n</i>	: Non-Commutating Interval

Chapter 1

Introduction

High power electric arc furnaces (EAF) are used in the metals industry for smelting various ore types and melting scrap steel. Electric furnaces offer high throughput capacity and productivity. However their present day use is burdened by the escalating cost of electric power and stricter power quality constraints. To a power system an arc furnace represents an erratic load, which is a leading cause of voltage flicker, harmonic distortion, and low power factor. The arc furnace, with its related problems, represents a significant load on the power system because of its high energy consumption.

Initially all smelting furnaces were operated at an AC mains frequency with power being regulated through positioning of the electrodes and adjusting the transformer tap position. The transformer tap is used to get in the vicinity of the operating point while fine control is obtained by positioning the electrodes to get the desired setpoint impedance. This mechanical movement of electrodes is slow and cannot compensate for fluctuations caused by arc instabilities.

As an alternative the DC furnace uses fast acting power electronic control and is able to partially compensate for arc fluctuations. This coupled with the fact that a DC arc is inherently more stable than an AC arc results in significant reductions in power fluctuations [1]. Measurements showing fluctuations from an AC smelting

furnace and a DC smelting furnace are provided in Figure 1.1. Both data sets were trended at a 200 ms rate and were recorded at the primary of the furnace transformers. In each case the data shows furnace operation at approximately the 40 MW level.

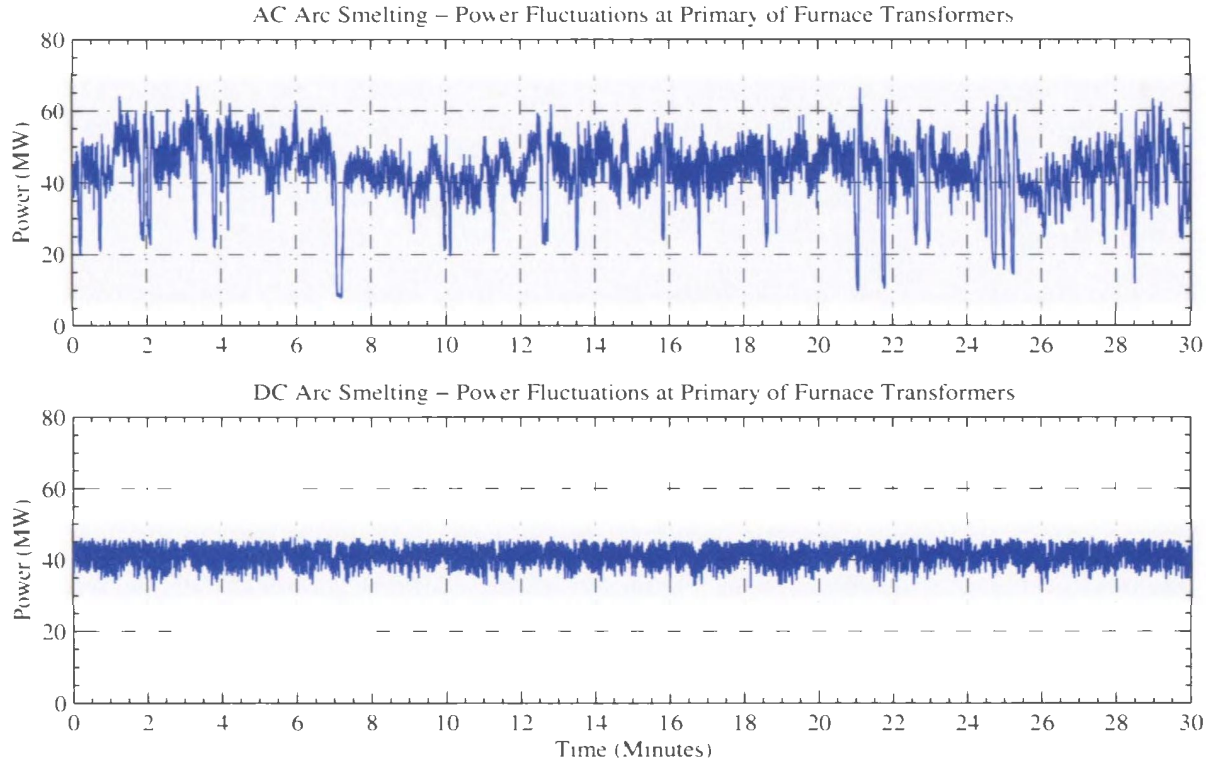


Figure 1.1: Power Fluctuations for AC Arc Smelting and DC Arc Smelting

The measurements clearly show a reduction in power fluctuations when using the DC smelting furnace. The large down swings in power observed in the AC smelting case are caused by a loss of arc in one or more of the three phases. There are no loss of arc conditions recorded in the DC smelting case, which suggest improved arc stability. This improved arc stability and reduction in power fluctuations will result in improved power quality, including voltage fluctuations and unbalance, on the AC power system [2,3].

The improved power quality performance often dictates that DC melting furnaces be used on weak utility systems to minimize the impact on nearby customers [4].

Since a number of smelting facilities are located in remote areas with inexcusably captive generation, a DC furnace would conceivably allow a reduction in the generator requirements. DC furnaces also provide considerable process benefits including reduced electrode consumption [5] and improved stirring in the bath [6]. The more stable DC arc has also found application in smelting fine ore types, which would otherwise need to be pelletized before smelting in an AC furnace to prevent excessive loss in the off gas column [1].

The DC furnace power supply is required to convert the plant distribution electrical energy to a form applicable to process requirements. Normally the plant medium voltage bus is between 12 to 45 kV and is supplied at an AC mains frequency of 50 or 60 Hz. In contrast, the DC furnace will operate with a direct current between 50 to 130 kA and a voltage between 600 to 1150 V. Since the process is continually changing the power supply must be capable of converting high voltage AC to controlled low voltage DC.

In addition the power supply should operate in a manner that minimizes disturbances on the AC system while delivering process energy with maximum reliability. In order to minimize harmonic currents in the AC supply and to reduce ripple content in the DC output the furnace power supply normally includes a 12-pulse rectifier at the front end. Furthermore, the output of each individual bridge circuit is connected in parallel to effectively double the current supplied to the load.

Traditionally DC furnaces have been supplied from controlled rectifier power supplies using thyristors to control the level of current or power delivered to the load. With the emergence of high power transistors other configurations for the power circuit have been developed including active rectifiers and uncontrolled rectifier chopper combinations [7]. To date only the controlled rectifier and uncontrolled rectifier chopper combinations have been successfully employed in industrial applications and as such only these two configurations will be investigated.

The controlled rectifier power supply is a proven technology used extensively in

the steel industry for DC arc furnace applications. The power supply consists of rectifier transformers, thyristor rectifiers, and output reactors. Passive filters are normally installed on the AC system to improve the power factor and reduce the effects of harmonics. However, since filters are not part of the power supply they will not be included in this study. The controlled rectifier directly converts power from low voltage AC to controlled low voltage DC at the output.

Commercial application of chopper power supplies have been traditionally limited to small scale plasma torch applications, however, one low power DC arc furnace has been operated with a chopper supply. The power supply consist of rectifier transformers, diode rectifiers, DC link capacitors, and output reactors. The diode rectifier converts power from low voltage AC to uncontrolled low voltage DC. From here the DC chopper converts the uncontrolled DC voltage to controlled low voltage DC at the output.

1.1 Thesis Objectives

Throughout the thesis both power supply configurations will be analyzed in detail to obtain the open-loop and the closed-loop characteristics. The analysis will focus on both the line side and load side characteristics and also compare the suitability of each configuration to smelting furnace applications. The objective is to give an unbiased opinion as to which power is more suitable for improved power quality, performance, and reliability.

The power quality parameters investigated will be those of most concern when using an EAF and include, harmonic and interharmonic distortion, voltage flicker, unbalanced voltage, and power factor. To determine the rectifier performance several indices will be compared including the efficiency, rectification ratio, and the transformer utilization factor. In addition, the output waveforms will be analyzed and compared on the basis of the ripple factor of the output voltage, and the form factor

of the output current. The reliability analysis will be simplified using the parts count method.

Previous comparisons have been completed by equipment manufactures recommending the controlled rectifier power supply [7] and the uncontrolled rectifier chopper power supply [8]. Measurements at low power are available comparing both configurations [9,10], however, the results do not reflect typical smelting furnace operation.

1.2 Thesis Organization

The report is organized into six chapters for easy reading and access to information pertaining to each specific topic. A description of the controlled rectifier power supply is given in Chapter 2, while the uncontrolled rectifier chopper power supply is described in Chapter 3. The power supply chapters contain information relating to the equipment and configuration, open-loop characteristics under ideal conditions, and closed-loop characteristics to show the various control modes. A static DC arc model, which is shown to give results similar to those recorded at several operating DC electric arc furnaces is presented in Chapter 4. The static model is modified by adding fluctuation to represent a DC smelting furnace.

In Chapter 5 a case study example and the results from the simulations of both power supply configurations are presented. As well the results of some industrial measurements to verify that the smelting furnace model presented in Chapter 4 is accurate. Chapters 1 and 6 provide the report introduction and conclusion, respectively, whereas additional information is contained in the appendices.

The thesis was prepared as part of the requirements for the completion of a Master of Engineering Degree from Memorial University of Newfoundland. The text was prepared using L^AT_EX Version 2e whereas the analysis and design was carried out using Matlab Revision 12 and PSCAD/EMTDC Version 4.0.1. All drawings were prepared using Microsoft Visio 2000.

1.3 Literature Review

The various sections of the thesis were prepared after an extensive literature review of previous work in all relevant areas. There are several papers that highlight the benefits of choosing a DC furnace as opposed to an AC furnace [1–6]. These references compare the operation of a typical three-electrode AC furnace with a traditional single-electrode DC furnace using a thyristor-controlled rectifier power supply. The controlled rectifier power supply is used for the majority of industrial furnaces, and to the authors knowledge only one low power smelting furnace has been commercially operated with an alternative arrangement.

An alternative is desirable to improve the power factor and reduce the harmonic distortion caused by the controlled rectifier power supply. Reference [7] shows two possible alternative arrangements including an active rectifier and an uncontrolled rectifier chopper power supply. The paper [7] concludes by recommending the controlled rectifier power supply because of its proven reliability. The benefits of using the uncontrolled rectifier chopper power supply are provided in reference [8]. While references [9,10] show measured data from both power supply configurations. However, the results in [9] are at very low power and do not represent normal operation, and the results in [10] compare a controlled rectifier with a 6-pulse front end against a chopper with a 12-pulse front end.

The operation and structure of the controlled rectifier power supply is described in several books [11–15]. Schaefer [11] provides the most comprehensive source on rectifier circuits covering various configurations operating with different load types, including the ideal cases of constant current output and constant voltage output. More information on operation is presented by both Pelly [12] and Kimbark [13], while reference [14] provides a detailed description of power system harmonics, including harmonics produced by large rectifiers and arc furnaces.

A more detailed description of the controlled rectifier structure used in the DC EAF power supply is provided in [16]. References [17,18] provide information on

the design of EAF transformers. Reference [19] describes the structure of the bridge circuit used in high current rectifiers to ensure current sharing between devices connected in parallel. References [15,20] describe the configuration and sizing of snubbers commonly used in bridge circuits, while [21] provides information on fusing in DC semiconductor circuits. References [11, 22] describe the operation and sizing of the interphase transformer (IPT).

The modes of operation of a 12-pulse rectifier with and without an IPT are compared in [23], while [24] provides additional information on rectifier operation without an IPT. Other sources showing the modes of operation from DC drives are provided in references [25,26]. Tzeng [27] extends on the work presented in [23] to compare the harmonics of a 12-pulse rectifier with and without an IPT. A description of rectifier harmonic calculations provided by Rice [28], shows the effect of using calculations for an ideal constant current load for a non-ideal load. References [13,14,29] also provide information on non-ideal operation.

Many of the same sources of information used to describe the controlled rectifier power supply [11, 13–15, 20, 21, 28] are also applicable to the uncontrolled rectifier. Additional books [30,31] containing information on both rectifiers and choppers are available. While references [32,33] present information on the structure of an uncontrolled rectifier chopper applicable for use in a DC EAF power supply. Reference [34] provides information on rerating old rectifiers with chopper outputs, which improves the transformer utilization factor. More information on converter transformer design is presented by Linden [35]. Rashid [36] presents information on DC link filter design for multiphase choppers, while references [31,37] discuss snubber design for transistor switching circuits. Although it will not be used in this study Dawson [38], presents a design for an IPT applicable for used in a multiphase chopper circuit.

The modes of operation of an uncontrolled rectifier supplying a constant voltage load are provided by Hancock [39] for a 6-pulse converter. This work is expanded upon in references [40,41] for an inductive supply, reference [40] also provides the boundaries

between the various modes in terms of voltage regulation. Reference [42] shows the shape of the line-to-neutral voltage at the load side of the supply reactance for the case when three diodes in the bridge circuit are conducting. Additional information on calculating current harmonics from an uncontrolled rectifier with a DC filter is presented in [43].

Multiphase chopper operation is described by Barton [44,45]. Reference [44] provides a symmetrical component analysis, while reference [45] provides an analytic solution. Other sources of information showing the modes of operation from DC drives are provided in references [46–48].

In order to represent the DC smelting furnace load in simulation the DC arc is first modeled then fluctuation added to represent an operating furnace. An introductory level description of the arc physics is provided by Hoyaux [51], which describes arc characteristics and modelling. The available arc models are generally of two types which include the Magneto Fluid Dynamic Model (MFD) [52–61], and the Channel Arc Model (CAM) [62–67]. The MFD model is complicated and uses fixed boundary conditions to solve for the spatial distribution of arc parameters, as such is not well suited for an electromagnetic simulation.

Simplifications made in the CAM model make it more appropriate for this study and it has been proven to represent the arc in a steel melting furnace. The CAM model is described by Sakulin [62,63], by presenting the energy balance equations taking into account the heat loss mechanisms from convection, conduction, and radiation. The results were modified in reference [64] to represent an EAF arc, and were determined to be accurate in [65]. To be accurate the model uses the thermodynamic and transport properties from a typical arc furnace plasma [67,68]. References [57,69,71] provide additional information on industrial electric arc characteristics.

Process parameters dictate that the smelting furnace has a different characteristic than a steel melting furnace. Smelting processes are described by Robiette [72], which presents information on both reduction smelting and matte smelting. Infor-

mation on power system design for various smelting types is provided in [73], while reference [74] describe the control system for the electrode movement and furnace feed system. Other aspects of furnace design and smelting types are presented in [75], while reference [76] describes the furnace structure.

Methods of analyzing electric arc furnace electrical data is presented in references [77,78]. Reference [79] presents the load characteristics from both AC and DC furnaces, while reference [80] presents the load characteristics and harmonic analysis from DC furnaces. Harmonic measurements and power factor correction from a steel melting facility is described in [81]. References [82–87] present information on flicker generated from EAF operation. While references [88,89] present information on interharmonics generated by DC furnaces and their contribution to flicker problems. In particular, reference [88] presents an actual case in which 187 Hz distortion caused voltage flicker problems at a steel melting facility.

Electric arc furnace models have been developed to assess their impact on power quality. Since power quality is part of the comparison in this study some aspects of the existing models will be incorporated into the fluctuation part of CAM model. The majority of electric arc furnace models have been developed to assess flicker from AC furnace [90–96], while others are more general and include more power quality disturbances [97–103]. Very little information is available on DC EAF models. However, tools including electromagnetic transient type programs have been used for DC furnace power supply design [104]. Additional DC arc furnace models are provided in references [105,106], while reference [107] also includes the influence of the controller on voltage fluctuations.

The comparison is done on the basis of power quality, rectifier performance, and converter reliability. In order to define indices to compare both power supply configurations various sources of information were consulted including books, international standards, and papers. The bulk of published information was on power quality including several books devoted to the topic [108–110], international standards pro-

viding measurement techniques and limits [111–119], and papers presenting the latest information on the topic [120–142]. The information on rectifier performance indices were taken from [143], while the information on reliability is presented in [144, 145].

Chapter 2

Controlled Rectifier Power Supply

The controlled rectifier power supply uses thyristors to directly convert the low voltage AC at the transformer secondary into controlled low voltage DC at the output. The power supply consists of rectifier transformers, thyristor bridge rectifiers, and output reactors. The controlled rectifier is a proven technology used extensively in the steel industry and at the majority of smelting facilities for electric arc furnace applications. Thyristors are also commonly used in other high power converters including HVDC converters, SVC converters, and large motor drives.

In the following sections the basic concepts and equations required to analyze the traditional controlled rectifier power supply are developed. Equations are developed for the ideal case of constant current output with and without supply reactance, and are provided for parameters at the input and output of the power supply. Input parameters include the RMS line current and harmonic magnitudes, power, and power factor, while output parameters include the average voltage and harmonic magnitudes. Waveforms depicting various operating conditions are also provided throughout the chapter to illustrate converter operation.

Although the assumptions made in the development of equations are appropriate to approximate the steady-state behavior of the converter they do not illustrate the dynamic performance of the converter. In order to show the dynamic performance of the converter closed-loop simulations were performed for constant current output.

constant power output, and constant power output with current limit. In each case plots are provided depicting the converter response to a step change in setpoint, as well as setpoint tracking performance. Simplified block diagrams showing the control structure are also provided for completeness.

Since the 12-pulse controlled rectifier configuration is used in the majority of DC smelting furnaces, it will be the focus of this chapter. The analysis assumes that all devices are ideal and perfectly matched with synchronized control signals. Since this is not the case in practice a section providing additional sources of information pertaining to non-ideal operation is also included. The chapter concludes by listing the benefits and problems associated with the controlled rectifier technology and provides several methods to improve the power supply performance.

2.1 Major Components

The controlled rectifier power supply uses two forms of energy conversion and one form of energy storage to convert the AC mains frequency, at the plant medium voltage bus, into controlled low voltage DC at the output. The power supply consists of rectifier transformers (energy conversion), thyristor-controlled converters (energy conversion), and output reactors (energy storage). A typical 12-pulse thyristor-controlled rectifier intended for use as an electric arc furnace power supply is provided for reference in Figure 2.1.

2.1.1 Rectifier Transformers

The converter transformers are similar to standard three-phase arc furnace transformers. However, additional windings are normally used and arranged to increase the converter pulse number [18]. For instance in Figure 2.1 a combination of a Δ/Δ transformer and a Y/Δ transformer is used to obtain 12-pulse operation. The 12-pulse characteristic is achieved by phase shifting one 6-pulse bridge circuit by 30° with

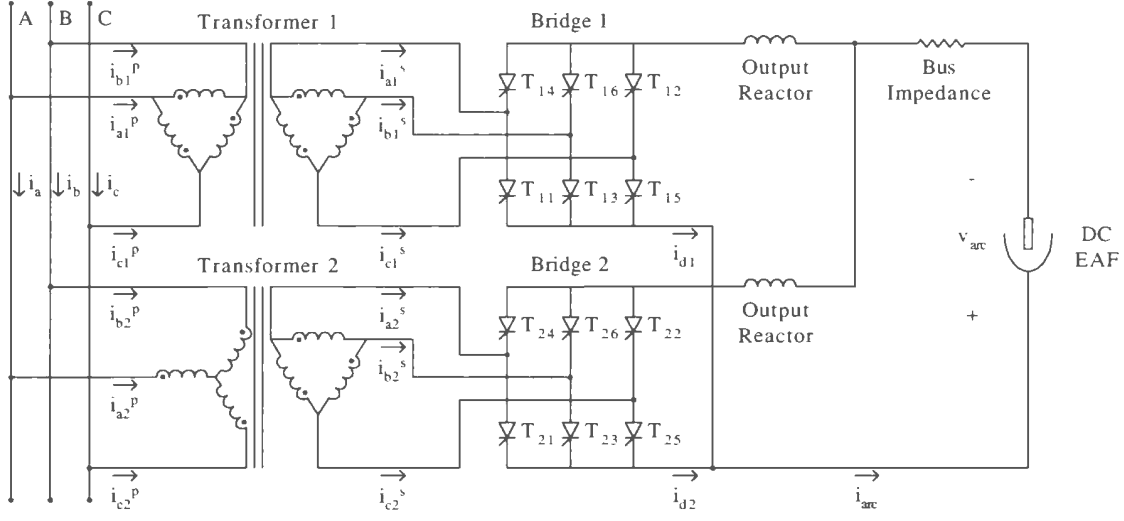


Figure 2.1: Simplified 12-Pulse Controlled Rectifier Power Supply

respect to the other. A Δ connection is used in each case to minimize zero sequence harmonics from entering the AC system.

Higher order pulse numbers can be obtained by using special phase shifting transformers. However, the benefits of going from 6-pulse to 12-pulse are not matched when increasing beyond the 12-pulse level [11]. While it is possible to use phase shifting transformers in a 12-pulse scheme normally a combination of Δ and Y windings are preferred since they provide an economic and simple connection without increasing the equivalent transformer rating. However, one disadvantage in using a transformer with a Δ winding and a Y winding, in combination with a Δ/Δ transformer, is that the secondary voltages cannot be exactly matched since a $1 : \sqrt{3}$ turns ratio will be required [11].

Mechanically the transformers are designed for high current density and K factors up to 10 to withstand the current harmonics generated by the random arc behavior and converter switching characteristics. In most cases the transformer cooling is accomplished using oil [17], as part of an oil-forced air-forced (OFAF) or oil-forced

water-forced (OFWF) combination. In order to minimize losses from the transformers to the converters the connections are made as short as possible by mounting the transformer secondary bushings on the side of the transformer tank [16]. When using the controlled rectifier power supply the transformers are equipped with tap changers to optimize the furnace operating point and ensure that an adequate control range is provided while maintaining maximum power factor.

2.1.2 Controlled Rectifiers

The controlled rectifier power supply will utilize thyristors as the controlling element. Thyristors are power electronic devices that permit the control of device turn-on provided that there is a positive voltage across the device. Device turn-off is governed by the zero-crossing of the line current, hence the thyristor is classified as a line-commutated device. The point at which the thyristor is turned on is often referred to as the firing angle and is denoted as α . The firing angle is often measured in degrees or radians from the positive zero-crossing of the voltage.

Thyristors are generally used in high power applications because of their capability to conduct large currents and withstand large voltages. Devices are available with mean current ratings in excess of 5000 A and voltage ratings up to 8000 V. A typical phase controlled thyristor data sheet applicable for an EAF power supply is provided for reference in Appendix A.

Since the furnace will normally be operated with a high current the thyristors require external cooling and this is usually provided using deionized water. The deionized water is pumped through a closed circuit equipped with a heat exchanger that may be part of a water-forced air-natural (WFAN) or water-forced water-forced (WFWF) arrangement, depending on the cooling requirements.

Despite the high current capacity of the thyristor, devices will still need to be connected in parallel to provide the necessary amount of current to the process. When thyristors are connected in parallel it becomes necessary to ensure current sharing

between individual devices. The high currents required by the smelting process produce strong magnetic fields in series with the devices through conductors and fuses, and between individual devices. These magnetic fields are similar to adding a small inductance in series with each device and it has been shown that the bridge circuit can be constructed to have a positive effect on current sharing [19].

For the standard bridge circuit there are two construction possibilities, one with two continuous DC conductors the other with three continuous AC conductors. Both configurations are shown in Figure 2.2. Based on work presented in [19] it has been shown that the configuration with three continuous AC conductors is superior to the configuration with two continuous DC conductors for current sharing. It is for this reason that the DC furnace power supply is constructed with three continuous AC conductors.

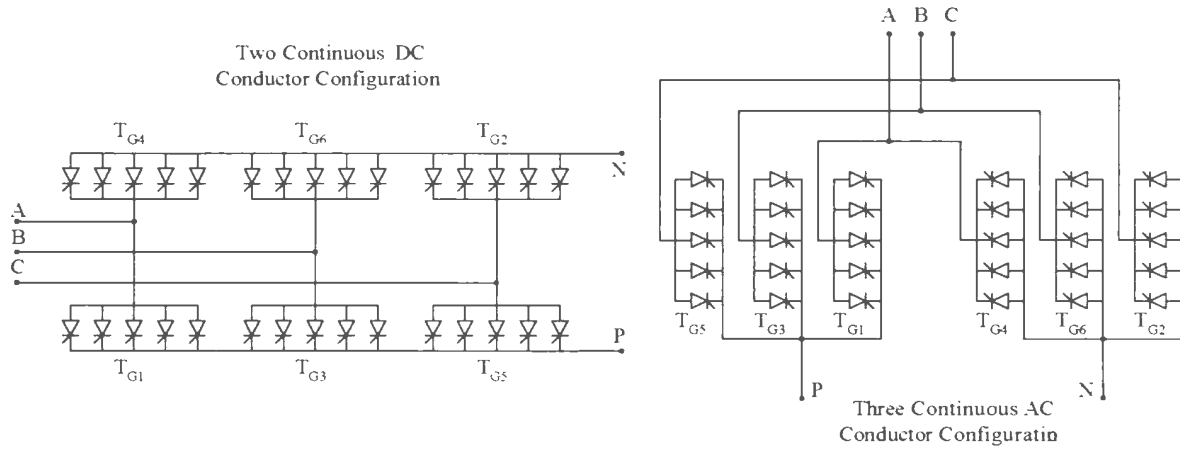


Figure 2.2: Three-Phase Bridge Layout

The power supply is partially protected using overcurrent relays to trip the main breaker. Additional protection is provided to the major components using temperature detectors, pressure sensors, flow meters, and level indicators to monitor the cooling system and to trip the main breaker in the event of a potential problem.

When deionized water is used in the cooling circuit a conductivity meter is also required. The power supply is protected from transient voltages using surge arrestors connected between the phases, between the phases and ground, and at the output of each bridge circuit. A damping circuit will be installed in parallel with the arrestors at the input as shown in Figure 2.3.

The thyristors themselves also require protection from excessive fault currents, as well as large rates of change in current (di/dt) through the device, and voltage (dv/dt) across the device. If the dv/dt is too large the device will begin to conduct without a gate signal present [15]. If the di/dt is too large localized heating will result from the high current density [15]. Generally the dv/dt snubber consists of an unpolarized capacitor in series with a resistor placed across the device while the di/dt snubber is an inductor placed in series with the device. Thyristor protection and snubber circuits are shown in Figure 2.3.

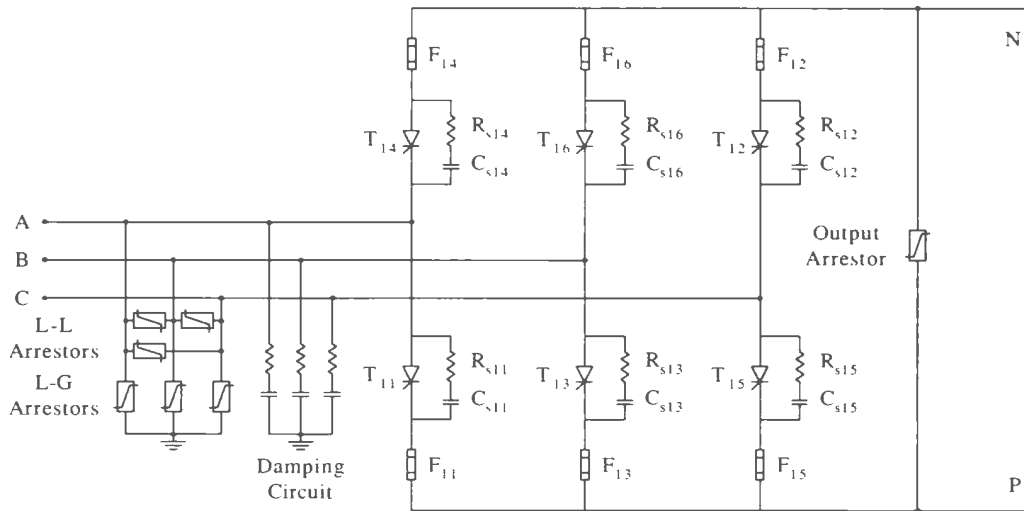


Figure 2.3: Controlled Rectifier Protection Circuit

For an electric arc furnace application the dv/dt snubber is used in conjunction with a current limiting fuse on each thyristor. The di/dt protection is provided to all thyristors through the transformer reactance at the input and the DC reactors

at the output. Snubbers for bridge circuits are discussed further in [15,20], while information on DC fusing in semiconductor circuits is provided in [21].

2.1.3 DC Reactors

Normally when two 6-pulse bridges are connected in parallel at the output an interphase transformer (IPT) is used to prevent interaction between both converters. The IPT is required to sustain the instantaneous voltage differences between both rectifier circuits caused by the phase displacement on the AC side [11,22]. Without an IPT a circulating current will develop between both converters. It is possible to construct a high-current power supply without an IPT. Modes of operation for such a system are discussed in detail in [23,24], while an harmonic analysis is provided in [27].

In an electric arc furnace power supply two air core DC reactors are used to perform the operation of an IPT. The DC reactors are constructed as part of the high-current secondary bus and consist of several turns of water-cooled aluminum. In order to properly function as an IPT the reactors are arranged such they are magnetically coupled as shown in [16]. In addition to ensuring that both bridge circuits share current equally the output reactors limit the short-circuit current at the converter to acceptable values and moderate the arc fluctuations to reduce the impact on the power system [16].

2.2 Rectifier Operation

Under ideal operation the load will be modeled as a constant current source. It is also assumed that the output reactors are sufficiently large enough to allow both bridge circuits to conduct simultaneously and share current equally. Two cases will be presented including a system without supply reactance followed by a more realistic case in which the supply reactance is included.

Without supply reactance two thyristors from each bridge circuit will conduct simultaneously and switching between thyristors occur instantly. When the supply reactance is included this switching is no longer instant and there will be a period of overlap, the length of which will depend on the amount of supply reactance. The turn-off of a thyristor is often referred to as commutation, and the overlap as the commutation overlap angle, denoted as μ . Since the output current is constant the commutation overlap angle can be determined from the amount of inductance in the supply using Equation 2.1.

$$\cos(\mu) = 1 - \frac{\omega L_s I_d}{\sqrt{2} V_{LL}} \quad (2.1)$$

When analyzing the 12-pulse bridge circuit another term is often introduced to represent the amount of overlap between both 6-pulse groups. For the purpose of this study, ζ , will be used to represent this value and will be referred to as the interbridge commutation overlap angle. Since both bridge circuits are phase shifted by 30° an expression for ζ can be written as

$$\zeta = \mu - \frac{\pi}{6} \quad (2.2)$$

This term is only applicable for $\mu > 30^\circ$. To distinguish between the two terms used to describe the same condition, μ will be referred to as the interphase commutation overlap angle.

At $\mu = 0^\circ$ there is no commutation interval and two devices in each bridge are always conducting for a total of four devices. This will be referred to as the 4-4 mode of operation and is often used in simplified analysis to approximate the converter operating characteristics. Practically this mode will never exist in the electric arc furnace power supply since it requires that the supply contain zero reactance.

In the interval $0^\circ < \mu < 30^\circ$ each bridge will alternate between two devices conducting in the conduction interval to three devices conducting in the commutation interval. Since there is no interbridge commutation overlap at this point the total converter will alternate between four devices conducting in the conduction interval

to five devices conducting in the interphase commutation interval. This is normally referred to as the 5-4 mode of operation and will be the mode most often encountered in the electric arc furnace power supply.

At $\mu = 30^\circ$ each individual bridge will operate as in the previous interval, however, at this point $\zeta = 0^\circ$, which signifies the onset of interbridge commutation overlap. This is a special case in which a total of five devices are always conducting and as such will be referred to as the 5-5 mode of operation.

In the interval $30^\circ < \mu < 60^\circ$ each individual bridge will operate as in the previous two intervals, however, the interbridge commutation overlap angle will be between $0^\circ < \zeta < 30^\circ$. This means that the total converter will alternate between six devices conducting in the interbridge commutation interval to five devices conducting in the interphase commutation interval. This will be referred to as the 6-5 mode of operation.

At $\mu = 60^\circ$ in each individual bridge when a commutation interval ends another begins hence there is no longer a conduction interval. At this time $\zeta = 30^\circ$ hence there is always interbridge commutation overlap and as such a total of six devices are always conducting. This will be referred to as the 6-6 mode of operation. Since it only occurs at one point it can be regarded as another special case that is not often encountered.

In general the power supply will only operate in the 5-4 mode and anything beyond this will only occur at elevated current levels. It is possible for more than six devices to conduct, however, this is abnormal and will only occur under fault conditions. Kimbark [13] provides a detailed analysis of the 6-pulse bridge under both normal and abnormal operation.

2.2.1 Constant Current Load Without Supply Reactance

The assumption of zero supply reactance is a limited case as the transformer will have an associated leakage reactance. However, the case is beneficial to describe the basic operation of the converter and will be presented in detail. Since the output

current is constant it does not require analysis. The line current on both sides of the transformer and the output voltage will be analyzed in detail.

First the voltage waveforms at the input and output of the rectifier will be analyzed. When describing the ideal case it is easier to use the line-to-line voltages as a reference point. Based on Figure 2.1 the line-to-line voltages of bridge 2 will lag those of bridge 1 by 30° , the following open-circuit voltages have been assumed on the secondary side of the transformers

$$v_{ab1}^s = \sqrt{2}V_{LL} \cos\left(\omega t - \frac{\pi}{6}\right) \quad (2.3)$$

$$v_{bc1}^s = \sqrt{2}V_{LL} \cos\left(\omega t - \frac{5\pi}{6}\right) \quad (2.4)$$

$$v_{ca1}^s = \sqrt{2}V_{LL} \cos\left(\omega t + \frac{\pi}{2}\right) \quad (2.5)$$

$$v_{ab2}^s = \sqrt{2}V_{LL} \cos\left(\omega t - \frac{\pi}{3}\right) \quad (2.6)$$

$$v_{bc2}^s = \sqrt{2}V_{LL} \cos(\omega t - \pi) \quad (2.7)$$

$$v_{ca2}^s = \sqrt{2}V_{LL} \cos\left(\omega t + \frac{\pi}{3}\right) \quad (2.8)$$

In order to transfer the line currents from the secondary of the furnace transformers to the primary, the Y/Δ currents need to be properly transformed and added to the currents from the Δ/Δ transformer. Assuming a 1:1 turns ratio in the transformers the primary currents can be expressed using the following equations:

$$i_a^p = i_{a1}^p + i_{a2}^p = i_{a1}^s + \frac{i_{a2}^s - i_{b2}^s}{\sqrt{3}} \quad (2.9)$$

$$i_b^p = i_{b1}^p + i_{b2}^p = i_{b1}^s + \frac{i_{b2}^s - i_{c2}^s}{\sqrt{3}} \quad (2.10)$$

$$i_c^p = i_{c1}^p + i_{c2}^p = i_{c1}^s + \frac{i_{c2}^s - i_{a2}^s}{\sqrt{3}} \quad (2.11)$$

To illustrate the operation of the controlled rectifier without supply reactance four cases are presented in Figures 2.4-2.7. The cases represent $\alpha = 0^\circ$, $\alpha = 15^\circ$, $\alpha = 30^\circ$, and $\alpha = 45^\circ$. Waveforms are included for the output voltage (Figure

2.4). line currents at the secondary of each transformer (Figures 2.5 and 2.6). as well as voltage and current at the input to the converter (Figure 2.7). The waveforms are plotted over a 20 ms period and are intended to represent one cycle at a power system frequency of 50 Hz. All resulting waveforms are normalized using $V_{LL} = 1pu$ and $I_d = 1pu$.

The output voltage is almost constant at $\alpha = 0^\circ$, which represents full conduction of the thyristor. As the delay angle is increased beyond this value the average DC voltage decreases while the magnitude of the voltage ripple increases. This can be observed by comparing the output voltage in Figure 2.4. Based on these waveforms the average DC voltage for the 12-pulse rectifier without supply reactance and an ideal interphase transformer can be written as

$$V_d = \frac{3\sqrt{2}}{\pi} V_{LL} \cos(\alpha) \quad (2.12)$$

Assuming that the system and bridge currents are balanced, harmonics in the DC voltage will occur at integer multiples of the pulse number, which in the present case results in harmonics at the following frequencies

$$h = 12k \quad (2.13)$$

where k is an integer. The magnitude of the harmonics will be inversely proportional to their harmonic number and will increase as α increases. An expression for the harmonic magnitudes of the output voltage as a function of α is given as [14]

$$V_h = \frac{V_{d0}}{\sqrt{2}(h^2 - 1)} \left[2h^2 + 2 - 2(h^2 - 1) \cos(2\alpha) \right]^{1/2} \quad (2.14)$$

where V_{d0} is the maximum average DC voltage at $\alpha = 0^\circ$ and h is a value obtained from Equation 2.13.

Without supply reactance the line currents have a staircase shape due to the constant DC load current assumption. The input line currents at $\alpha = 0^\circ$ in Figure 2.7 and are observed to be in phase with the corresponding line-to-neutral voltages. As α is increased the phase angle between the line-to-neutral voltages and the line

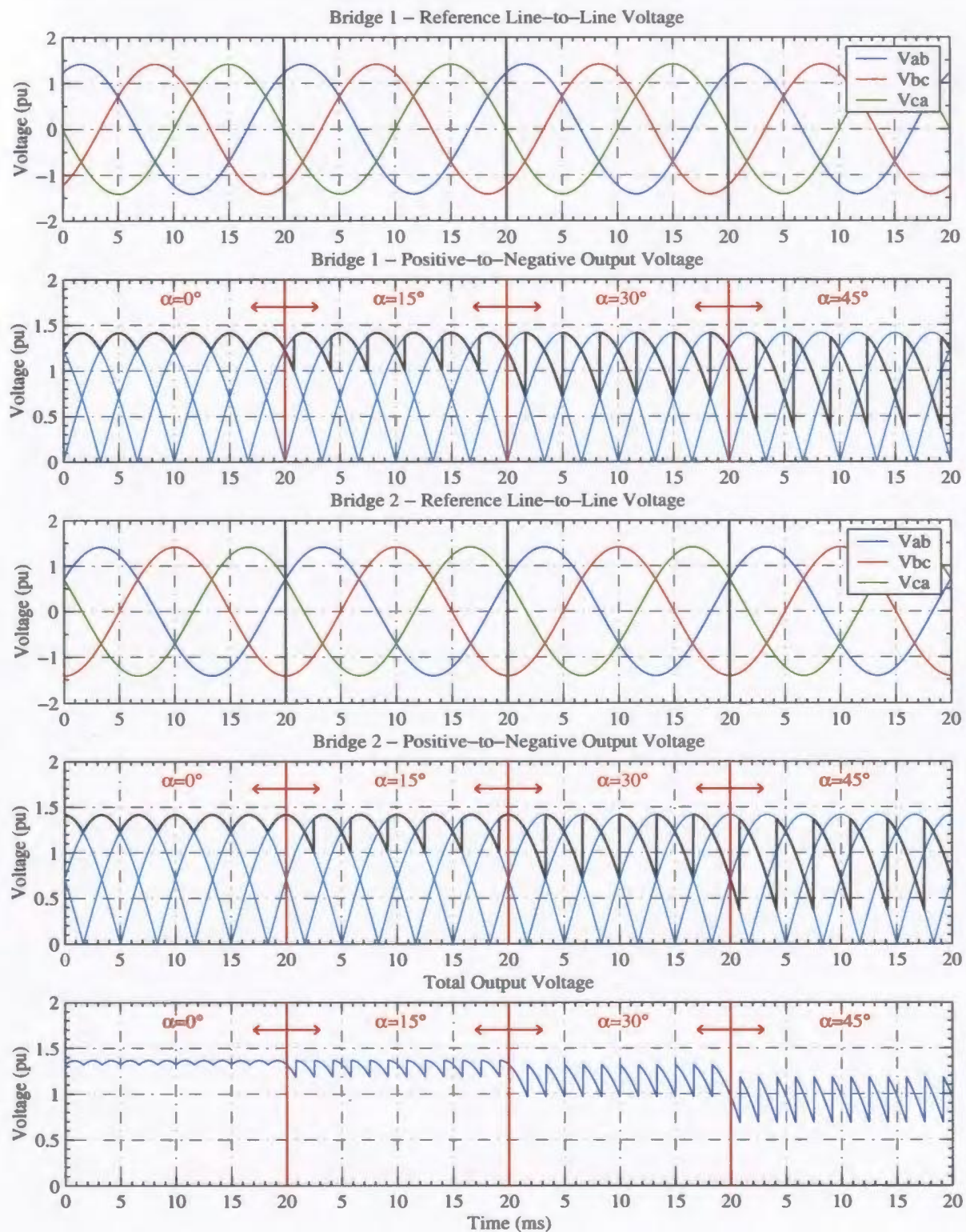


Figure 2.4: Controlled Rectifier Output Voltage Waveforms

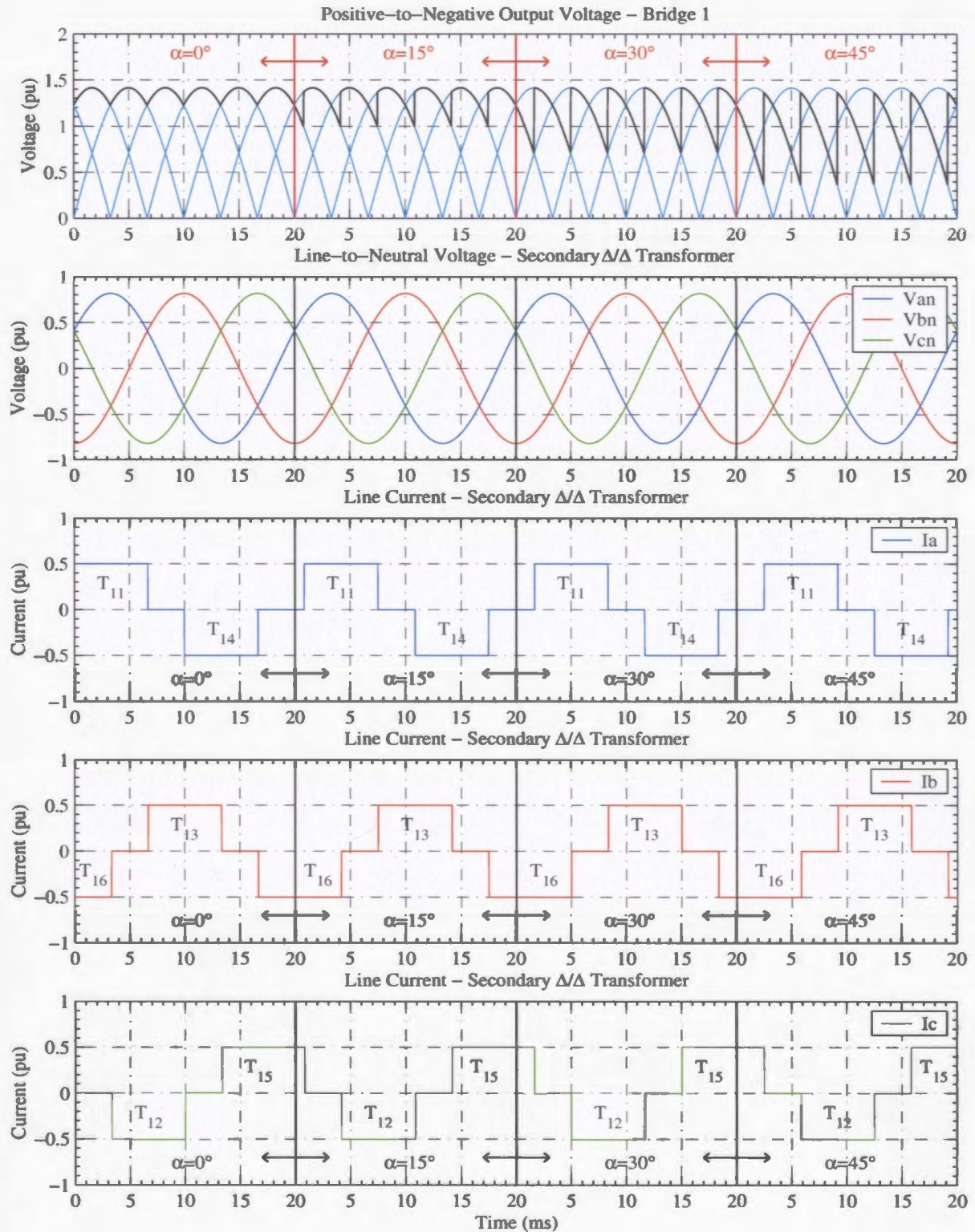


Figure 2.5: Voltage and Current Waveforms at Secondary of Δ/Δ Transformer

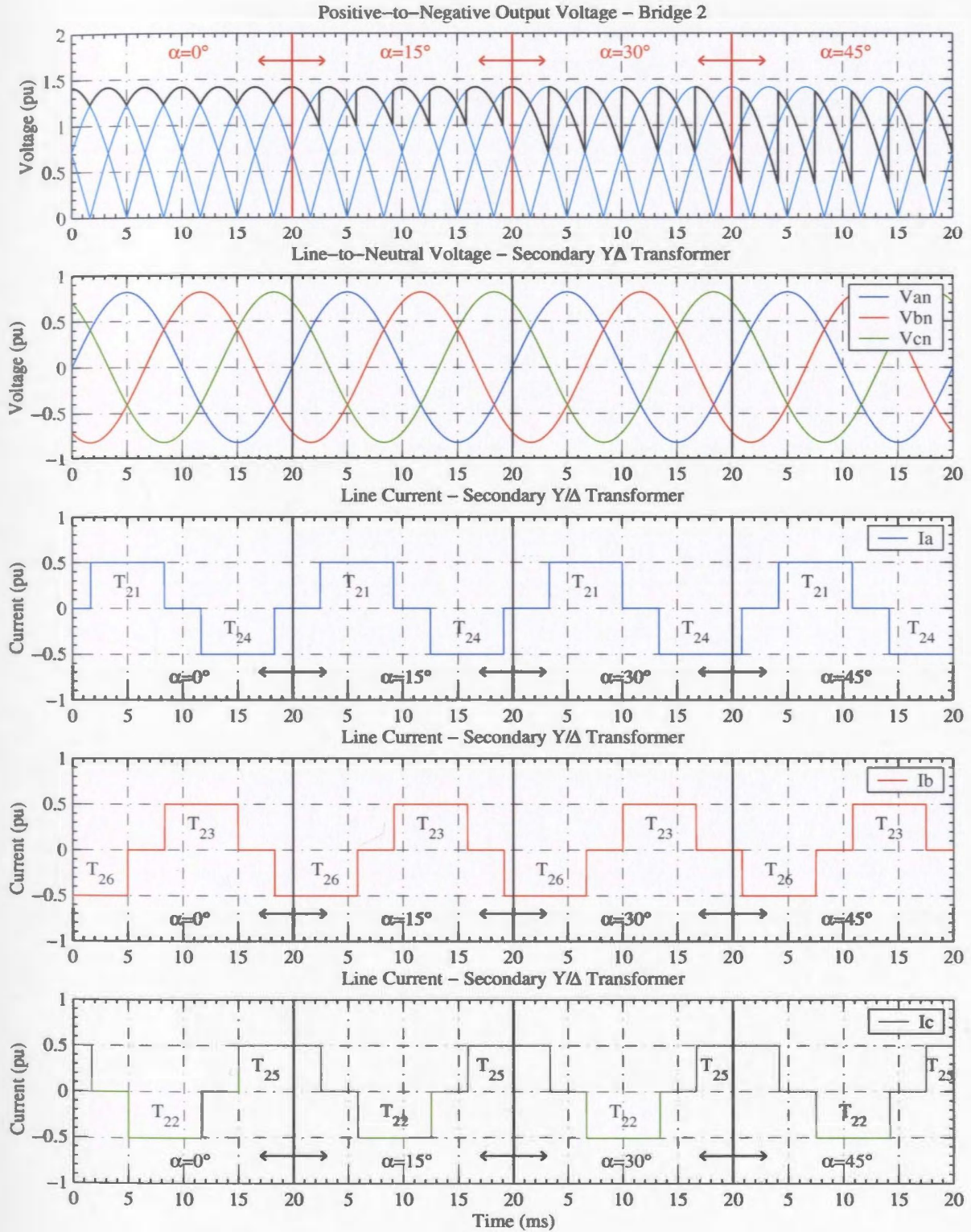


Figure 2.6: Voltage and Current Waveforms at Secondary of Y/Δ Transformer

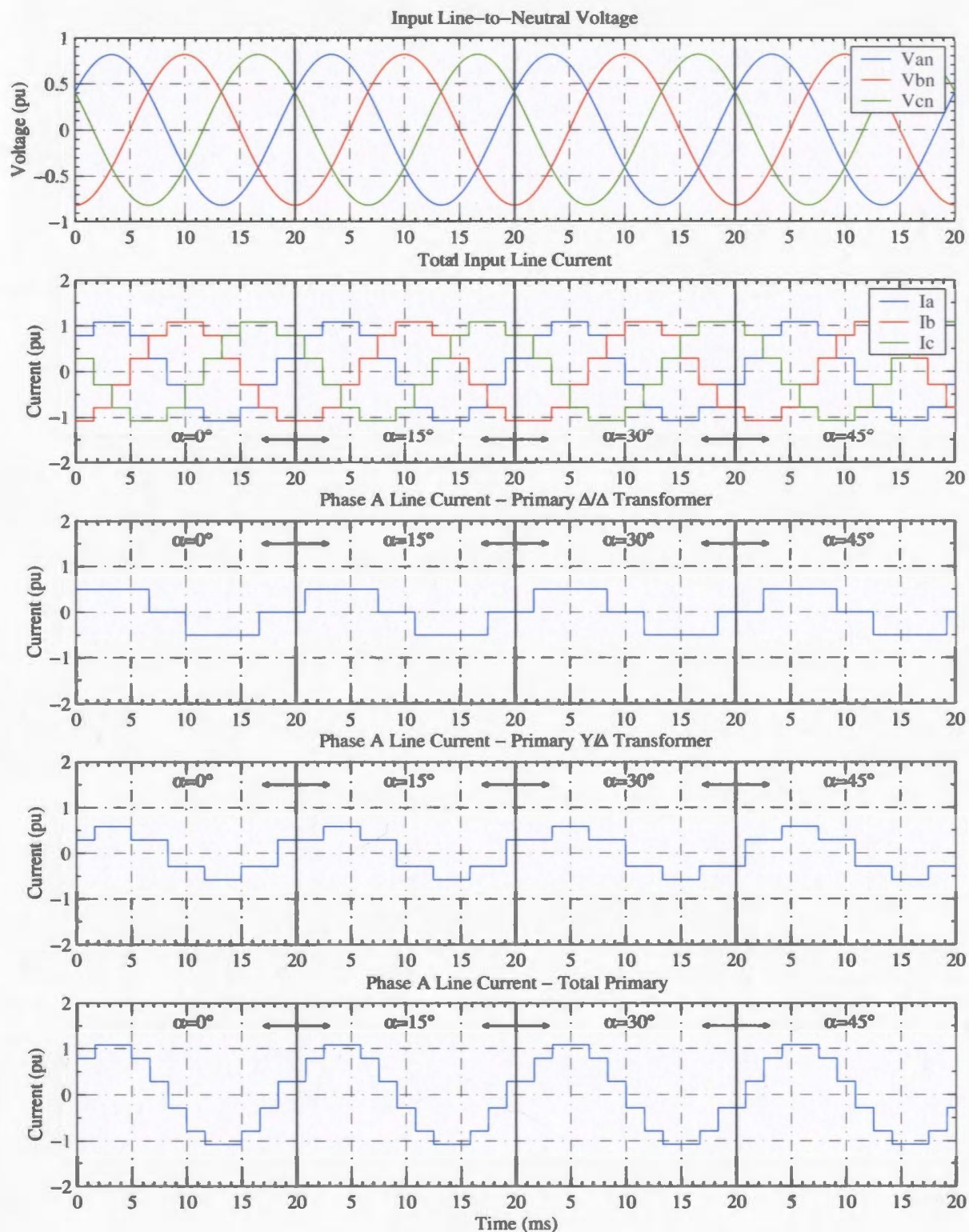


Figure 2.7: Controlled Rectifier Input Voltage and Current Waveforms

currents increase. However, since the load current is assumed constant the shape of the line current waveforms remain constant. This can be observed by comparing the cases presented in Figure 2.7. Based on these waveforms the total RMS line current including harmonics can be written as

$$I_L = \left(\frac{3 + \sqrt{3}}{6} \right) I_d \quad (2.15)$$

Assuming that the system and bridge currents are balanced harmonics in the line currents will occur at the following frequencies

$$h = 12k \pm 1 \quad (2.16)$$

where k is an integer. Unlike the DC voltage the line current harmonics, current magnitude, and RMS value, remain constant as α varies. An expression for the harmonic magnitudes of the line current is given as [14]

$$I_h = \frac{I_1}{h} \quad (2.17)$$

where I_1 is the magnitude of the fundamental component and h is a value obtained from Equation 2.16. The fundamental component of the line current can be determined from Fourier analysis as

$$I_1 = \frac{\sqrt{6}}{\pi} I_d \quad (2.18)$$

An expression for the power drawn by the converter is similar to that encountered in traditional power system analysis and can be written as

$$P = V_d I_d = \frac{3\sqrt{2}}{\pi} V_{LL} I_d \cos(\alpha) \quad (2.19)$$

The traditional power factor equation is based on the cosine of the phase angle between the line-to-neutral voltage and the line current. A similar term exists when harmonics are present and is called the displacement power factor (DPF). The displacement power factor for the controlled rectifier power supply without supply reactance and constant current load is defined as

$$DPF = \cos(\alpha) \quad (2.20)$$

This term alone is not sufficient to describe the power factor and will not give accurate results when harmonics are present. For instance, the line current and line-to-neutral voltage waveforms for $\alpha = 0^\circ$ are in phase, however, the power factor is not unity. The expression for power factor taking into account current harmonics can be written as

$$PF = \frac{I_1}{I_L} DPF \quad (2.21)$$

where I_L is the RMS value of the line current taking into account all significant harmonic components.

2.2.2 Constant Current Load With Supply Reactance

In this section the load is still represented as a constant current source. However, the supply now has some associated inductance. This inductance is mainly due to transformer leakage reactance and exists in practice. For the purpose of this section only it is assumed that all supply reactance is contained in the transformers and will be referred to the secondary side. These simplifications mean that the transformers are decoupled magnetically and that supply voltages at the primary of the transformers are ideal.

When describing the case with supply reactance it is easier to use line-to-neutral voltages as a reference point. The following open-circuit voltages have been assumed as reference and are equal to the line-to-neutral voltages on the secondary of the transformers in a case without supply reactance. The voltages have been calculated from the line-to-line voltages in the previous section and thus correspond to the same system over the same time interval.

$$v_{an1}^s = \frac{\sqrt{2}}{\sqrt{3}} V_{LL} \cos \left(\omega t - \frac{\pi}{3} \right) \quad (2.22)$$

$$v_{bn1}^s = \frac{\sqrt{2}}{\sqrt{3}} V_{LL} \cos (\omega t - \pi) \quad (2.23)$$

$$v_{cn1}^s = \frac{\sqrt{2}}{\sqrt{3}} V_{LL} \cos \left(\omega t + \frac{\pi}{3} \right) \quad (2.24)$$

$$v_{an2}^s = \frac{\sqrt{2}}{\sqrt{3}} V_{LL} \cos \left(\omega t - \frac{\pi}{2} \right) \quad (2.25)$$

$$v_{bn2}^s = \frac{\sqrt{2}}{\sqrt{3}} V_{LL} \cos \left(\omega t + \frac{5\pi}{6} \right) \quad (2.26)$$

$$v_{cn2}^s = \frac{\sqrt{2}}{\sqrt{3}} V_{LL} \cos \left(\omega t + \frac{\pi}{6} \right) \quad (2.27)$$

In the non-commutating intervals the line-to-line and line-to-neutral voltages at the secondary of the furnace transformer will be equal to those presented in Equations 2.3-2.8 and 2.22-2.27, respectively. During commutation the line-to-line voltage of the short-circuited phase is zero while the line-to-neutral voltages are equal to each other and to the average of the corresponding open-circuit voltages [13]. If it is assumed that the only supply reactance is contained in the transformer then the following pairs of equations can be used to describe the secondary voltages during the various commutation intervals

$$v_{ab}^s = 0 \quad v_{an}^s = v_{bn}^s = \frac{v_{an}^s + v_{bn}^s}{2} = -\frac{v_{cn}^s}{2} \quad (2.28)$$

$$v_{bc}^s = 0 \quad v_{bn}^s = v_{cn}^s = \frac{v_{bn}^s + v_{cn}^s}{2} = -\frac{v_{an}^s}{2} \quad (2.29)$$

$$v_{ca}^s = 0 \quad v_{cn}^s = v_{an}^s = \frac{v_{cn}^s + v_{an}^s}{2} = -\frac{v_{bn}^s}{2} \quad (2.30)$$

The line currents during commutation will consist of a DC component and a sinusoidal component, which will lag the corresponding commutating voltage by 90°. Simplified expressions for the line current during commutation have been provided in [11], for both an increasing current, and a decreasing current. The correct equations for the positive half-cycle are provided, and since the waveform is symmetric, the same equations are applicable to the negative half-cycle by changing the polarity and increasing the phase shift angle by 180°.

The phase shift angle is denoted by ϕ , and represents the position of the line-to-neutral voltage with respect to time zero. For instance, based on Equation 2.22, the phase shift angle for Phase A at the secondary of the Δ/Δ transformer will be 60°.

The current in the positive half cycle consists of four intervals. The first interval occurs between $\alpha < \omega t < \alpha + \mu$, and the current in this interval can be written as

$$i_{l1}^s = \frac{I_d}{2} \left[\frac{\cos(\alpha) - \cos(\omega t + \pi/3 - \phi)}{\cos(\alpha) - \cos(\alpha + \mu)} \right] \quad (2.31)$$

This represents a rising current during the commutation interval. The second interval occurs between $\alpha + \mu < \omega t < \alpha + 2\pi/3$, and the current in this interval can be written as

$$i_{l2}^s = I_d \quad (2.32)$$

This represents current in the non-commutating interval. The third interval occurs between $\alpha + 2\pi/3 < \omega t < \alpha + \mu + 2\pi/3$, and the current in this interval can be written as

$$i_{l3}^s = \frac{I_d}{2} \left[1 - \left(\frac{\cos(\alpha) - \cos(\omega t - \pi/3 - \phi)}{\cos(\alpha) - \cos(\alpha + \mu)} \right) \right] \quad (2.33)$$

This represents a falling current during the commutation interval. The fourth interval occurs between $\alpha + \mu + 2\pi/3 < \omega t < \alpha + \pi$, and the current in this interval can be written as

$$i_{l4}^s = 0 \quad (2.34)$$

This represents the period of no conduction between the positive half-cycle and negative half-cycle.

To illustrate the operation of the controlled rectifier power supply with supply reactance two cases are presented in Figures 2.8-2.11. The cases represent $\alpha = 0^\circ$ with $\mu = 30^\circ$, $\alpha = 15^\circ$ with $\mu = 30^\circ$, $\alpha = 30^\circ$ with $\mu = 15^\circ$, and $\alpha = 45^\circ$ with $\mu = 15^\circ$. The waveforms include the output voltage (Figure 2.8), voltage and current at the secondary of each transformer (Figures 2.9 and 2.10), as well as voltage and current at the input to the converter (Figure 2.11). All waveforms are plotted over a 20 ms period and are intended to represent one cycle at a power system frequency of 50 Hz. As in the previous section the waveforms are normalized using $V_{LL} = 1pu$ and $I_d = 1pu$.

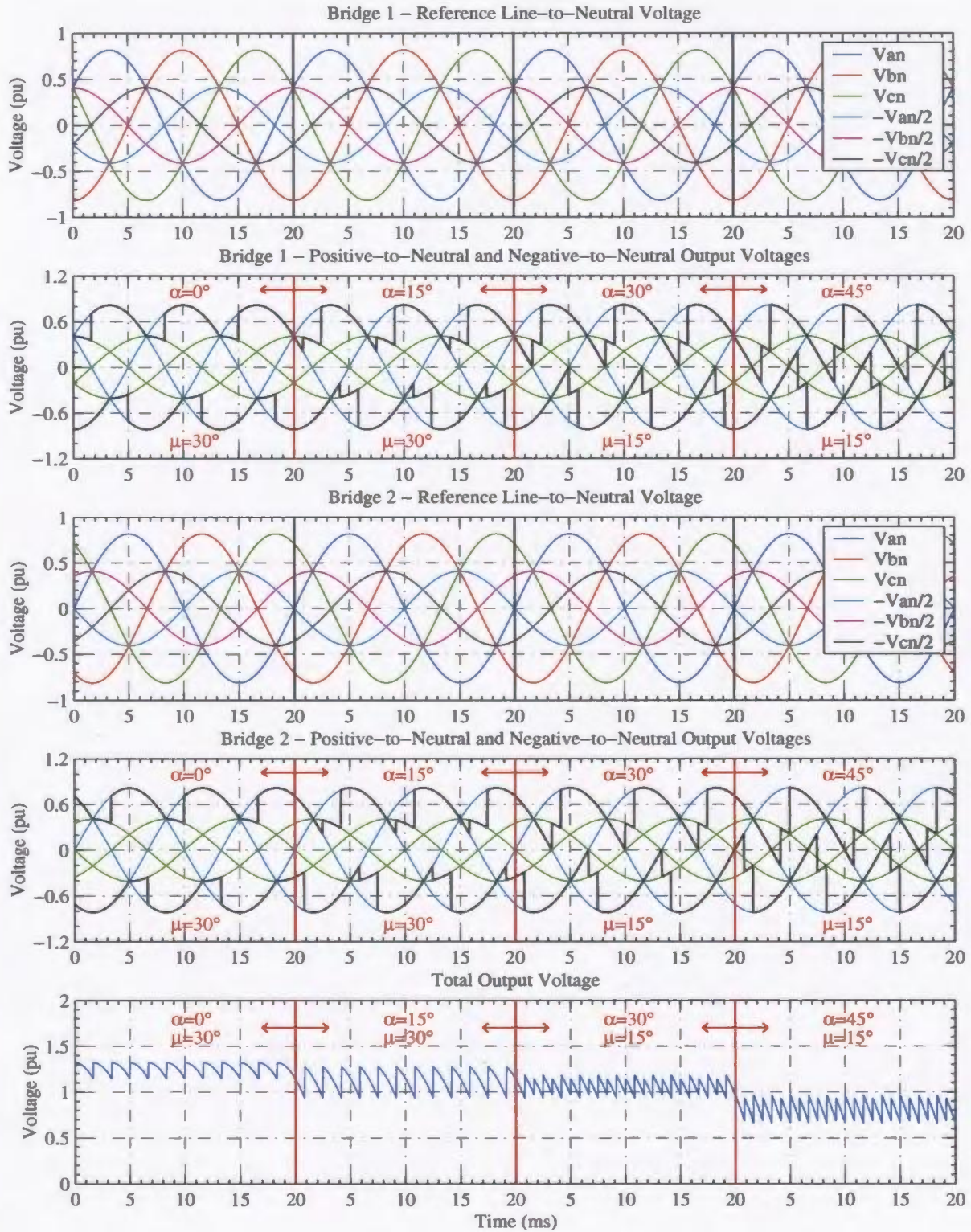


Figure 2.8: Controlled Rectifier Output Voltage Waveforms

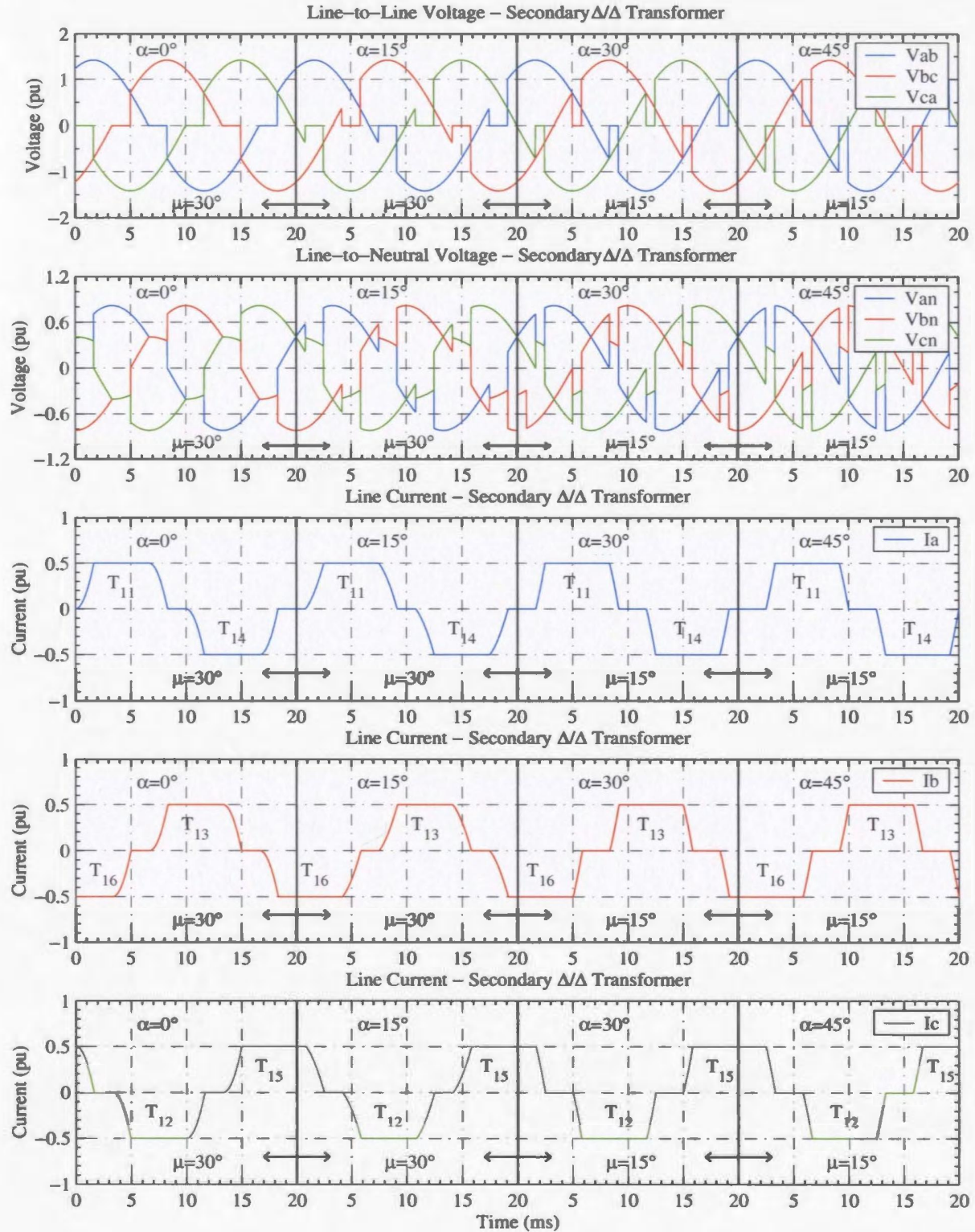


Figure 2.9: Voltage and Current Waveforms at Secondary of Δ/Δ Transformer

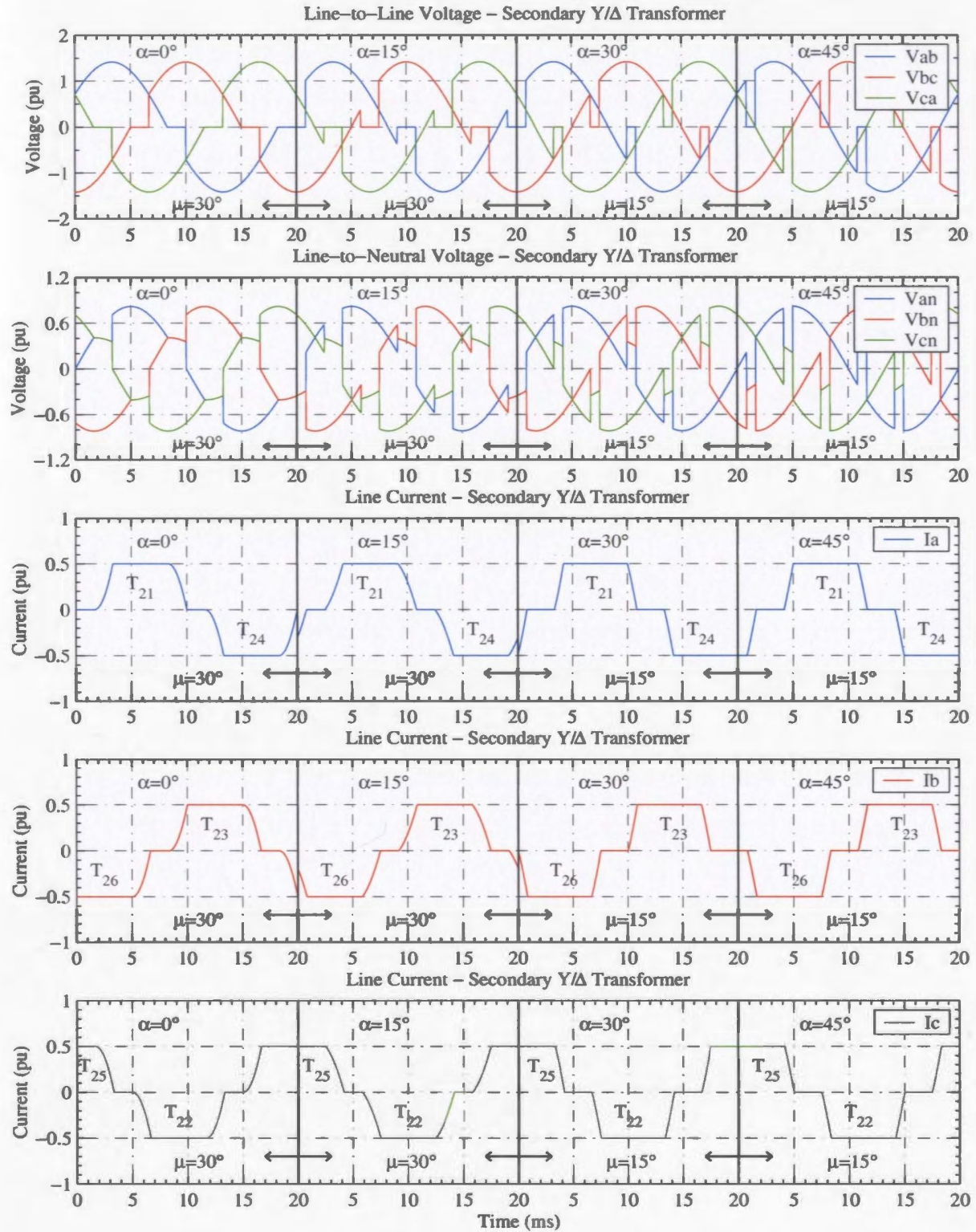


Figure 2.10: Voltage and Current Waveforms at Secondary of Y/Δ Transformer

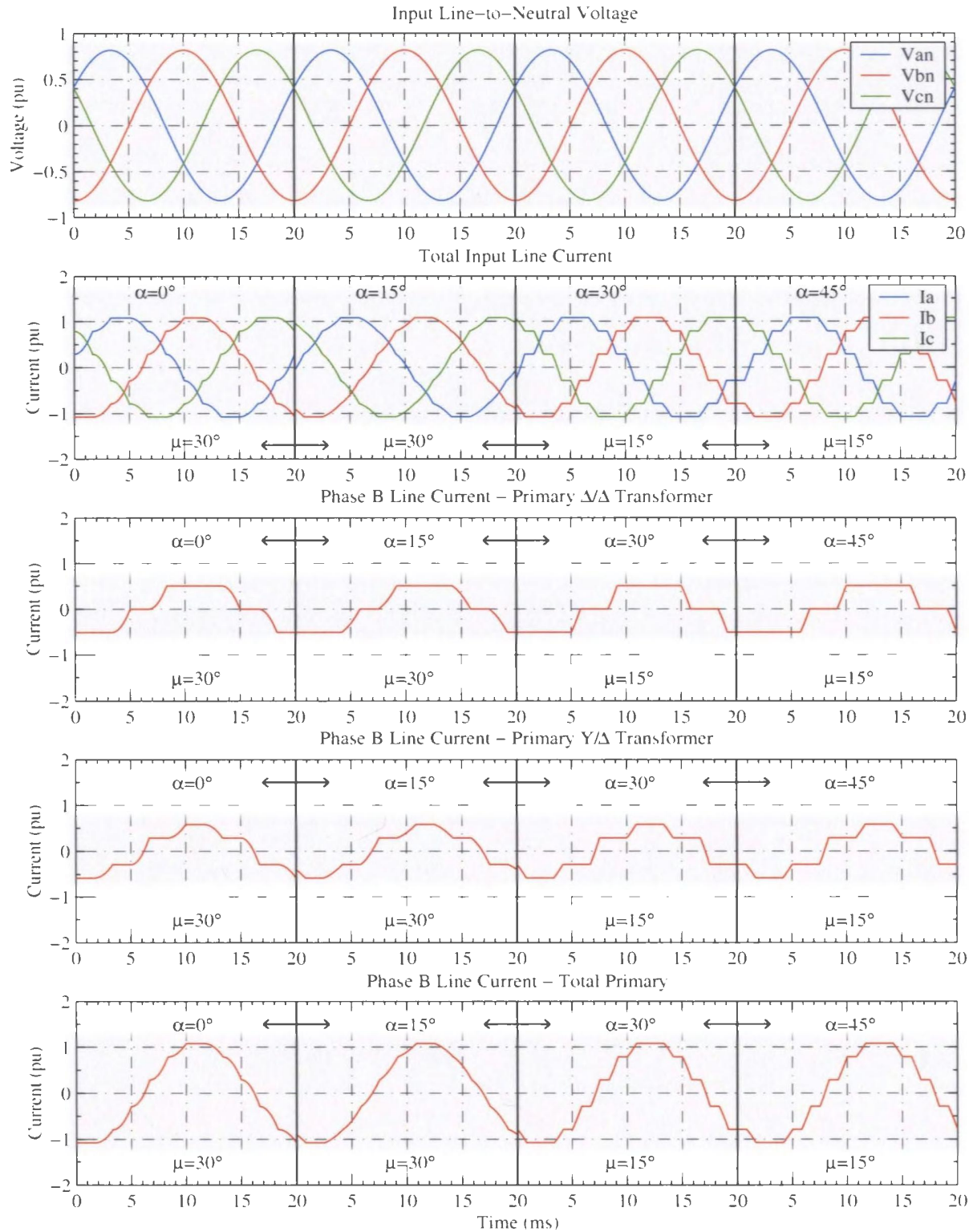


Figure 2.11: Controlled Rectifier Input Voltage and Current Waveforms

The output voltages for $\alpha = 0^\circ$ and $\alpha = 15^\circ$ with $\mu = 30^\circ$ contains more ripple than that presented in the previous section for $\alpha = 0^\circ$ and $\alpha = 15^\circ$ with $\mu = 0^\circ$. However, if the cases for $\alpha = 30^\circ$ and $\alpha = 45^\circ$ with $\mu = 0^\circ$ are compared with the case for $\alpha = 30^\circ$ and $\alpha = 45^\circ$ with $\mu = 15^\circ$ it is noticed that the commutation overlap has actually reduced the amount of ripple in the output voltage. This suggests a nonlinear relationship between α and μ , which is observed in the output voltage. Based on the waveforms the average DC voltage for the 12-pulse rectifier including supply reactance and an ideal interphase transformer can be written as

$$V_d = \frac{3\sqrt{2}}{2\pi} V_{LL} [\cos(\alpha) + \cos(\alpha + \mu)] \quad (2.35)$$

As in the previous section, harmonics in the DC output voltage will appear at integer multiples of the pulse number, provided that the system and bridge currents are balanced. The magnitude of the harmonics will depend on α and μ and can be expressed using the following equation [14]

$$V_h = \frac{V_{d0}}{(h^2 + 1)} \left\{ (h-1)^2 \cos^2 \left[(h+1) \frac{\mu}{2} \right] + (h+1)^2 \cos^2 \left[(h-1) \frac{\mu}{2} \right] - 2(h-1)(h+1) \cos \left[(h-1) \frac{\mu}{2} \right] \cos \left[(h+1) \frac{\mu}{2} \right] \cos(2\alpha + \mu) \right\}^{1/2} \quad (2.36)$$

where V_{d0} is the maximum average DC voltage at $\alpha = \mu = 0^\circ$ and h is a value obtained from Equation 2.13.

The staircase shape of the line currents observed in the previous section become rounded in the commutation intervals when the supply reactance is included in the analysis. As a result the line current is no longer independent of α and is actually dependent on both α and μ . Correction factors presented in [11] have been adjusted for the case under investigation to give an expression for the total RMS line current including harmonics as

$$I_L = \left(\frac{3 + \sqrt{3}}{6} \right) I_d - \left(\frac{6 + 2\sqrt{3}}{2 + \sqrt{3}} \right) \frac{I_d}{2\pi} \left\{ \frac{\sin(\mu) [2 + \cos(2\alpha + \mu)]}{[\cos(\alpha) - \cos(\alpha + \mu)]^2} - \frac{\mu [1 + 2\cos(\alpha)\cos(\alpha + \mu)]}{[\cos(\alpha) - \cos(\alpha + \mu)]^2} \right\} \quad (2.37)$$

The effect of commutation is a reduction in current harmonics. However, the reduction is nonlinear and also depends on α and μ . Current harmonics still occur at frequencies obtained in Equation 2.16 and can be expressed using the following equation [13]

$$I_h = \frac{I_1}{h [\cos(\alpha) - \cos(\alpha + \mu)]} \left\{ \left[\frac{\sin[(h-1)\mu/2]}{h-1} \right]^2 + \left[\frac{\sin[(h+1)\mu/2]}{h+1} \right]^2 - 2 \left[\frac{\sin[(h-1)\mu/2]}{h-1} \right] \left[\frac{\sin[(h+1)\mu/2]}{h+1} \right] \cos(2\alpha + \mu) \right\}^{1/2} \quad (2.38)$$

where I_1 is the magnitude of the fundamental component and h is a value obtained from Equation 2.16. The fundamental component of the line current neglecting commutation effects now requires a correction factor to be accurate for the case including supply reactance. An expression for the correction factor was obtained from [11] and is included below in Equation 2.39.

$$I_1 = \frac{\sqrt{6}}{\pi} I_d \left\{ \left[\frac{\cos(\alpha) + \cos(\alpha + \mu)}{2} \right]^2 + \left[\frac{2\mu + \sin(2\alpha) - \sin(2\alpha + 2\mu)}{4 [\cos(\alpha) - \cos(\alpha + \mu)]} \right]^2 \right\}^{1/2} \quad (2.39)$$

An expression for the power drawn by the converter is similar to that obtained in Equation 2.19 and can be written as

$$P = V_d I_d = \frac{3\sqrt{2}}{\pi} V_{LL} I_d [\cos(\alpha) + \cos(\alpha + \mu)] \quad (2.40)$$

The power factor can still be calculated using Equation 2.21, however the displacement power factor changes to

$$DPF = \frac{1}{2} [\cos(\alpha) + \cos(\alpha + \mu)] \quad (2.41)$$

As in the previous section increasing α will reduce the power factor. However, μ now also serves to reduce the power factor.

2.2.3 Normal Operation

Under normal operation the converter will not operate with a constant current load, the power system will not provide an ideal sinusoidal voltage waveform, balanced between the phases, nor will the components used in the power supply be

perfectly matched. Each of these system parameters will cause deviations from the ideal analysis presented in this chapter. In addition, controller imperfections will also cause further deviations from the ideal case.

The effects of non-ideal conditions on the controlled rectifier operation are most easily observed in the harmonics generated by the converter. Since the load is not a constant current source the line currents will not have a flat top and the characteristic harmonics will be different than those predicted for the ideal case [28]. Any modulation in the DC voltage will cause current harmonics on the AC system [14]. Since the arc will randomly change in length at various frequencies non-characteristic voltage harmonics will be produced at the load and cause distortion on the AC system. This distortion can be at any frequency and as such will cause interharmonic distortion, as well as, harmonic distortion.

Any unbalance in the supply voltages will cause firing angle asymmetries that lead to an increase in the levels of triplen harmonics, particularly those of the third order [13]. Impedance and firing angle imbalance between both 6-pulse groups will result in non-characteristic harmonics at orders $6k \pm 1$. This current imbalance can also cause problems with proper operation of the interphase transformer [29], used to parallel the outputs of both 6-pulse converters. If the thyristors in the positive and negative valve groups begin to conduct at slightly different offsets from the intended firing angle then even order harmonics will be produced on the AC system [13]. The magnitude of these even order harmonics will be decreased as the commutation overlap angle is increased.

These non-ideal conditions not only cause changes to the predicted harmonic spectrum but also increase power quality problems and decrease the system efficiency. The deviations also change the expected relationship between the firing angle and the output parameters. As such the control system must be robust enough to operate under the various conditions and still effectively maintain the desired setpoint at the output. This is generally achieved by using a controller with a feedback loop.

2.3 Converter Control

In order to maintain a constant setpoint the controlled rectifier power supply uses a feedback PI controller. The control variable is either the total current or power into the furnace. Additional modes for constant voltage and constant firing angle are sometimes included but not normally used. In the case of power control a current limit is included to protect the equipment from additional stress without tripping the protection relays. Since there are two bridge circuits connected in parallel a current balancing loop is also included in each control configuration to ensure that the total current is shared equally.

Typical control block diagrams for constant current control, constant power control, and constant power control with current limit are presented in this section. Controller response to a change in setpoint is also provided for a constant resistive load scaled to provide typical current and power levels associated with the operation of a 50 MW smelting furnace. For the purpose of this section the load is set to $14m\Omega$ and the transformer secondary voltages are set to 920 V.

Transient response for both current control and power control is investigated by applying a $\pm 10\%$ step change in setpoint and measuring the transient response parameters. Parameters are recorded for both increasing setpoints and decreasing setpoints to show controller linearity. The current limiting function within the power controller is shown to function properly by applying a slowly varying power setpoint which results in currents above the set limit. All tuning was performed using the stability limit method [49], while the controller response characteristics are those presented in [50].

Power control is most often used during normal operation since smelting is a continuous process which relies on a constant power to feed ratio [74]. Current control is used during cold startups since the load experiences many current peaks and loss of arc conditions in this interval.

2.3.1 Constant Current Control

Constant current control was implemented using the control configuration outlined in Figure 2.12. The process variables include the output current from each bridge rectifier, which are filtered using a first order low-pass filter with a gain of 1 and a time constant of 1 ms. The current regulator was tuned using the stability limit method and has a proportional gain of 0.02 and an integral time constant of 0.15 s. The balance regulator was set to have the same proportional gain as the current regulator and an integral time constant 10 times greater to avoid interaction between the two control loops.

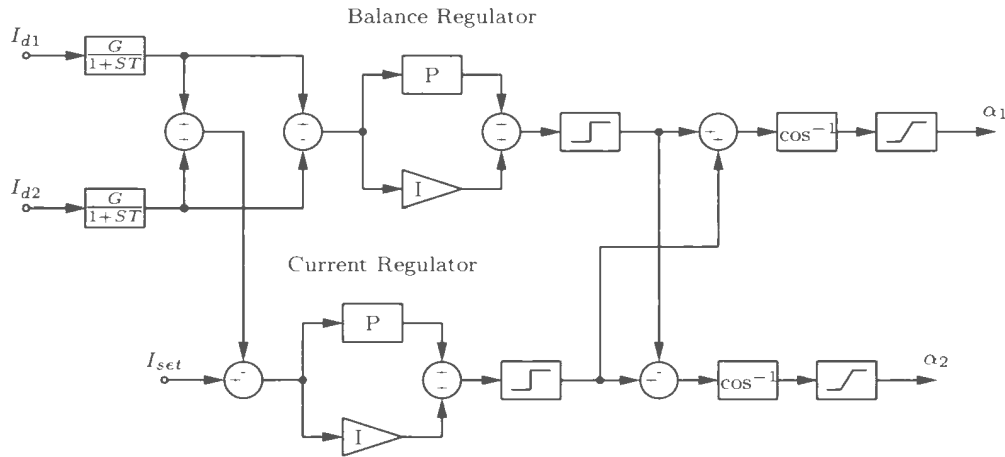


Figure 2.12: Controlled Rectifier Current Control Block Diagram

Although a slew rate limit is shown on both control signals it was determined through simulation that it was not required for the current controller. Instead only a hard limit of 0° to 90° was implemented at the output of the controller and represents the control range of the rectifier. Another hard limit of 0 to 1 was used at the output of each regulator and was required to ensure that the values into the inverse cosine

functions were valid. The inverse cosine functions were required to linearize the controller response.

The transient response for the current controller shown in Figure 2.12 is provided for reference in Figure 2.13. The nominal output current was chosen as 60 kA and the setpoints were switched between 54 kA to 66 kA then back again. For the positive step change the delay time and rise time were 2.525 ms and 4.725 ms, respectively. The maximum overshoot was 1.818 kA corresponding to 2.75% and occurred at a peak time of 6.95 ms. The settling time based on a 2% tolerance band was 8.6 ms.

For the negative step change the delay time and rise time were 2.425 ms and 4.725 ms, respectively. The maximum overshoot was 1.498 kA corresponding to 2.77% and occurred at a peak time of 6.9 ms. The settling time based on a 2% tolerance band was 8.575 ms. When compared with the values for the positive step change these are slightly different which indicate that the inverse cosine function is not a perfect linearization block. However, it comes very close and the difference in the maximum overshoot is less than 500 A.

2.3.2 Constant Power Control

Constant power control was implemented using the control configuration outlined in Figure 2.14. The process parameters include the output current from each bridge rectifier and the output voltage, which are filtered using a first order low-pass filter with a gain of 1 and a time constant of 1 ms. The power regulator was tuned using the stability limit method and has a proportional gain of 0.02 and an integral time constant of 0.2 s. The balance regulator was set as in the previous section.

A slew rate limit is shown on both control signals and is required to prevent sudden changes in the control variable. The slew rate limit functions to stabilize the controller during large disturbances and for the purpose of this study was chosen as $720^\circ/\text{cycle}$. A hard limit of 0° to 90° was also implemented at the output of the controller and represents the control range of the rectifier. Another hard limit of 0

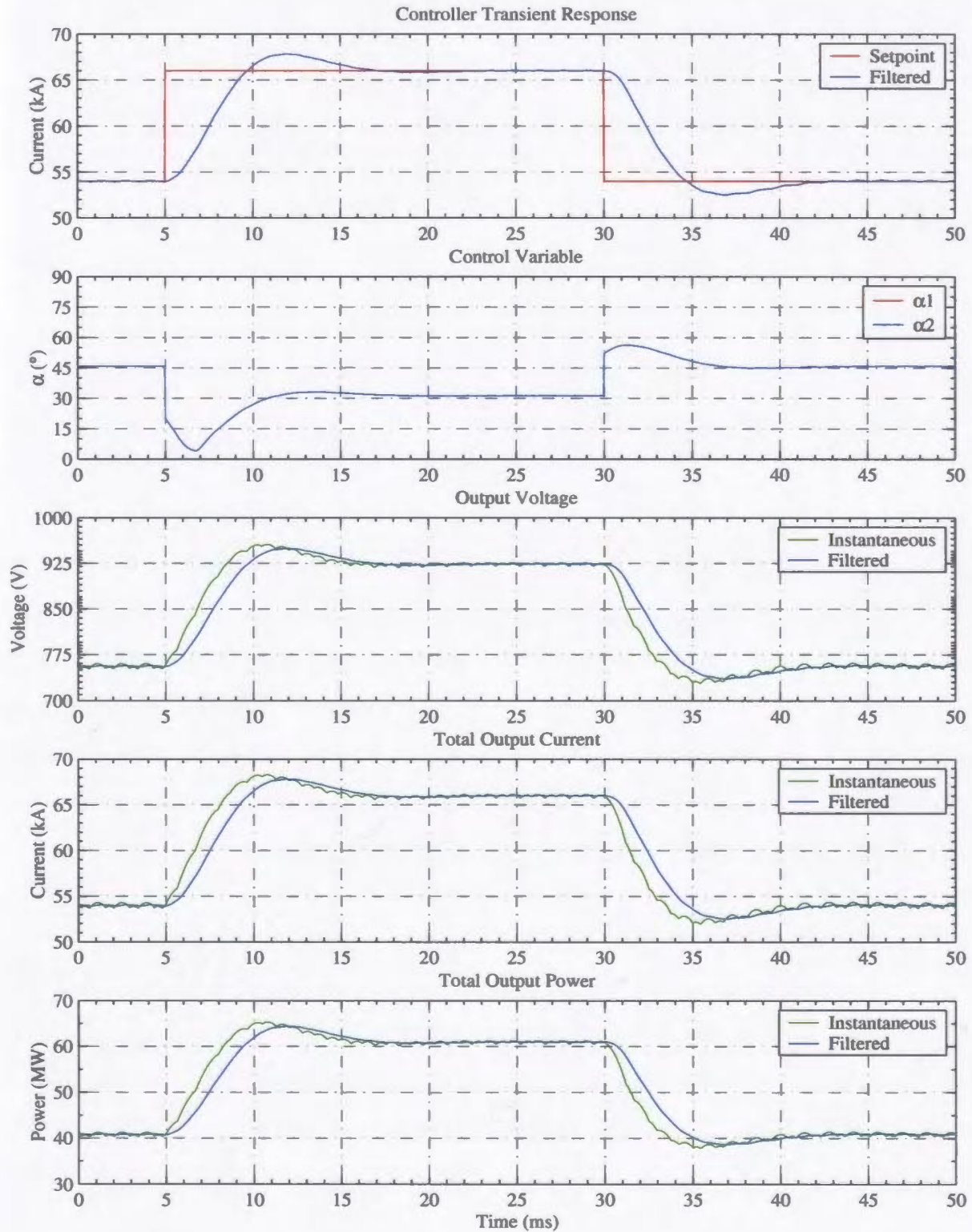


Figure 2.13: Controlled Rectifier Current Control (Step Response)

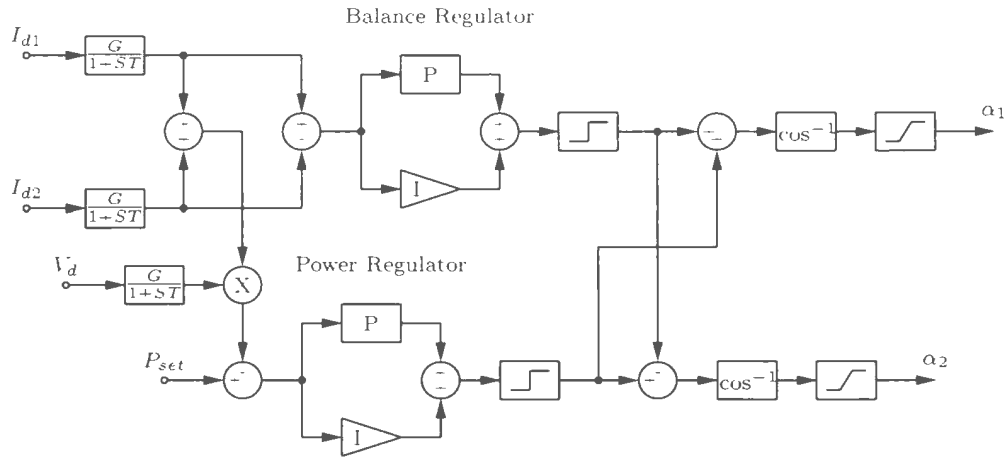


Figure 2.14: Controlled Rectifier Power Control Block Diagram

to 1 was used at the output of each regulator and, as for the current controller, was required to ensure that the values into the inverse cosine functions were valid. The inverse cosine functions were again used to linearize the controller response.

The transient response for the power controller shown in Figure 2.14 is provided for reference in Figure 2.15. The nominal output power was chosen as 50 MW and the setpoints were switched between 45 MW to 55 MW then back again. For the positive step change the delay time and rise time were 2.15 ms and 3.525 ms, respectively. The maximum overshoot was 2.322 MW corresponding to 4.22% and occurred at a peak time of 4.95 ms. The settling time based on a 2% tolerance band was 6.65 ms.

For the negative step change the delay time and rise time were 1.85 ms and 3.35 ms, respectively. The maximum overshoot was 1.402 MW corresponding to 3.12% and occurred at a peak time of 5.25 ms. The settling time based on a 2% tolerance band was 6.125 ms. When compared with the values for the positive step change these are slightly different which indicate that the inverse cosine function is not a perfect linearization block. Although the difference is greater than that observed in the current controller it comes very close and the difference in the maximum overshoot is less than 920 kW.

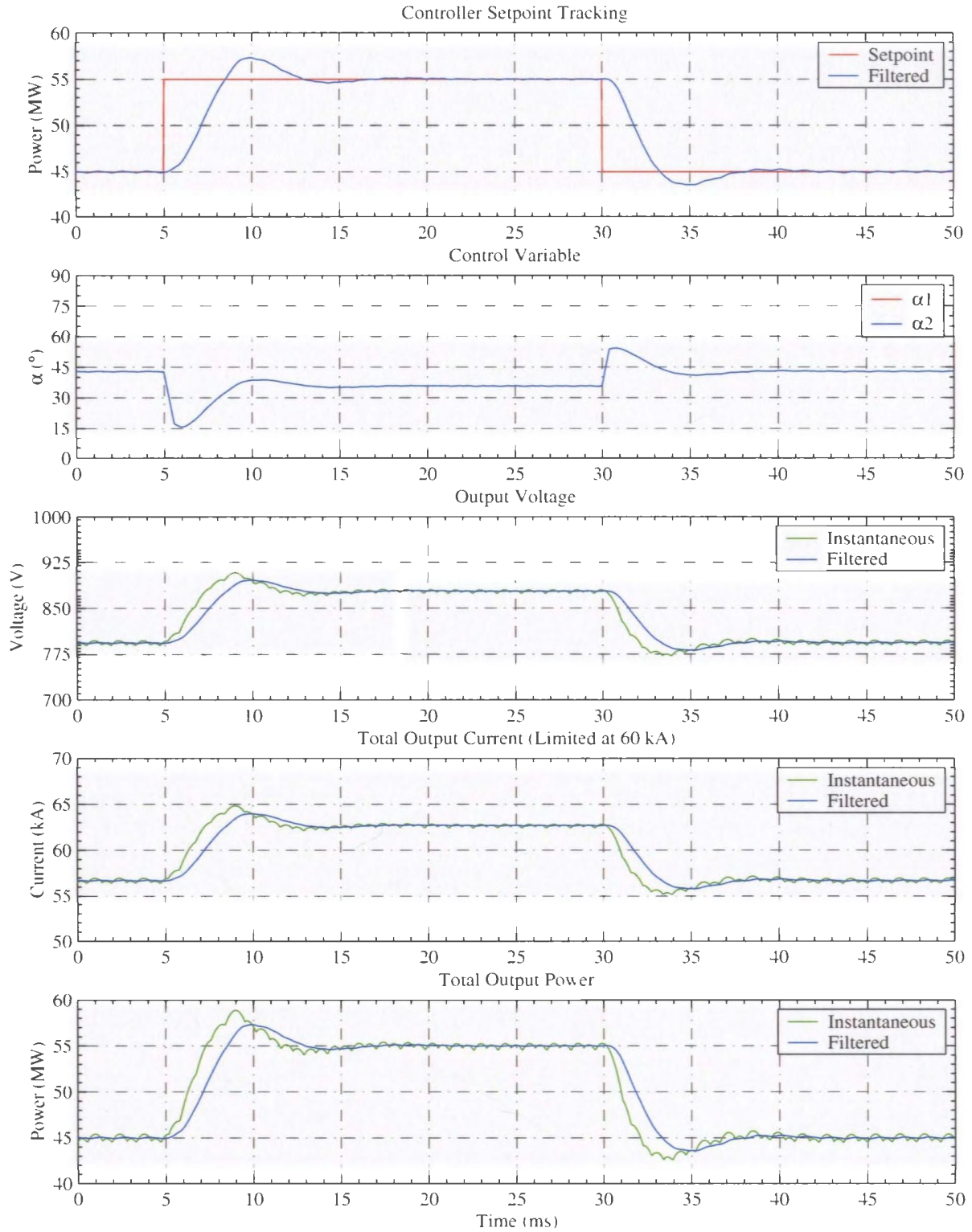


Figure 2.15: Controlled Rectifier Power Control (Step Response)

2.3.3 Constant Power Control With Current Limit

Normally when constant power control is used a current limit is also imposed to keep within the equipment ratings. The control configuration chosen for power control with current limit is provided for reference in Figure 2.16 and is a combination of the first two configurations. The proportional gains and integral time constants in the power regulator, current regulator, and balance regulator are the same as those previously specified. The slew rate limit was set as in the power controller.

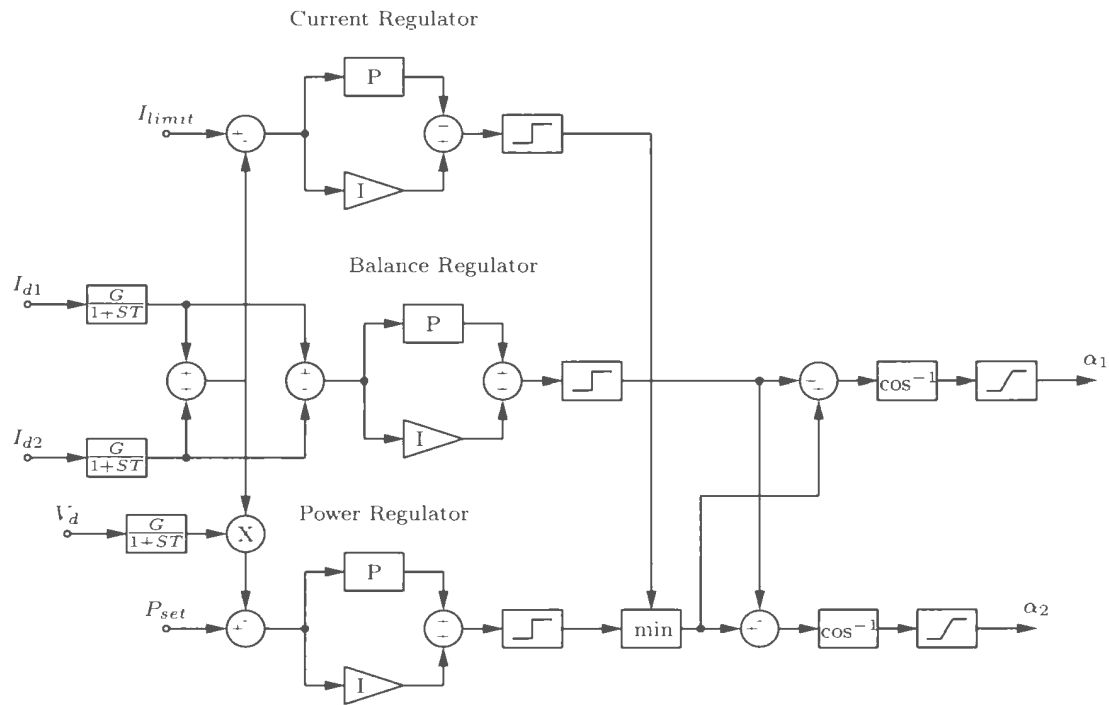


Figure 2.16: Controlled Rectifier Power Control with Current Limit Block Diagram

To verify that the current limit functions correctly the power setpoint was slowly varied between 45 MW and 55 MW with a current limit of 60 kA. The results are presented in Figure 2.17 and show the current being limited to 60 kA. It can also be observed that when in current limiting mode power control is lost.

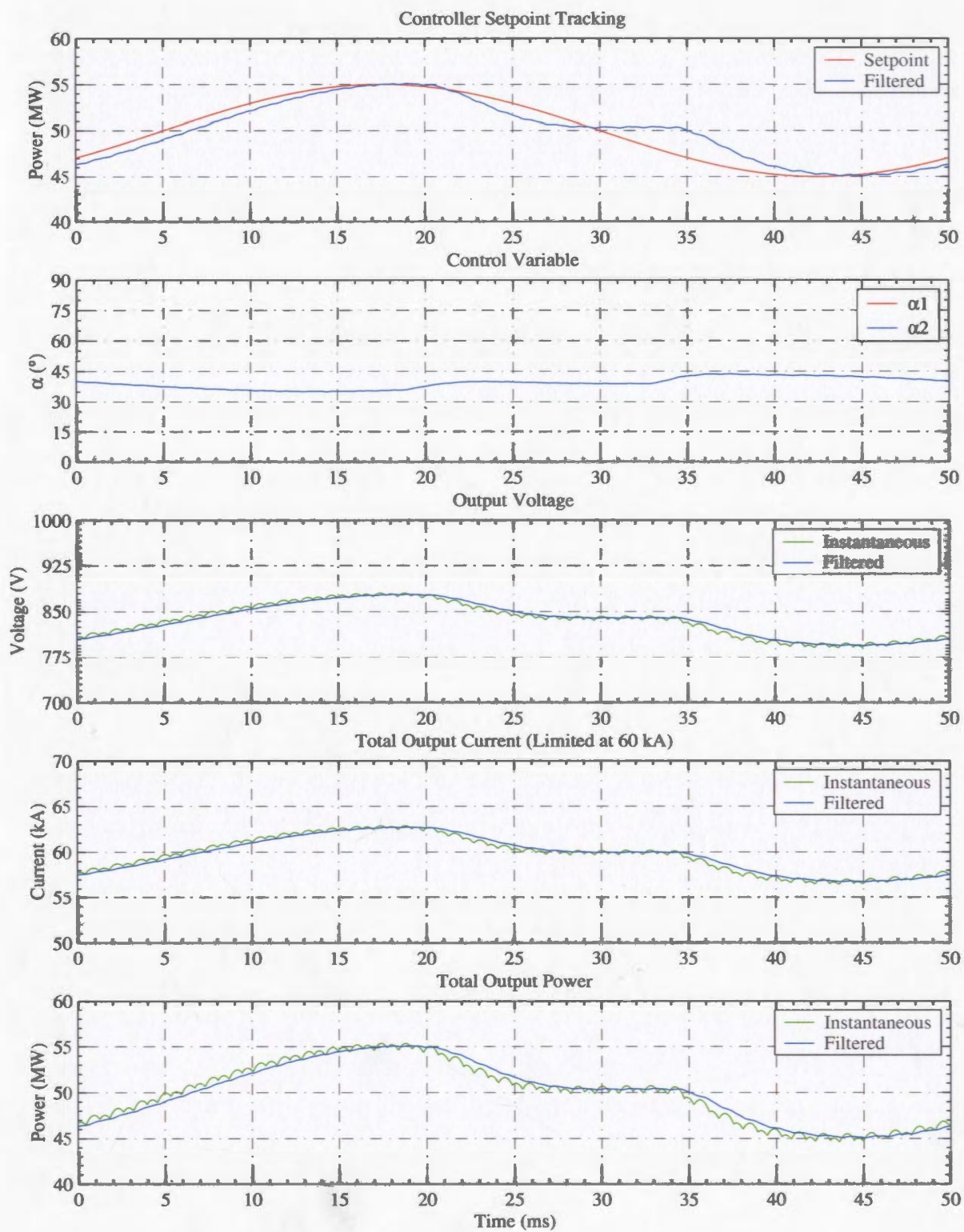


Figure 2.17: Controlled Rectifier Current Limited Power Control (Setpoint Tracking)

2.4 Summary

A description of the configuration and operation of the controlled rectifier power supply has been presented in this chapter. The converter is intended for high power operation and has been implemented in various applications including the majority of electric smelting furnace power supplies. Generally for high current operation the converter is arranged in the 12-pulse configuration with the outputs connected in parallel. This requires that the output reactors are arranged in such a way to promote current sharing between the bridge circuits. The thyristors are also arranged to improve current sharing and are connected in parallel to carry the required process current.

Under normal operation each bridge circuit will alternate between two thyristors conducting in the conduction interval to three thyristors conducting in the commutation interval. For the entire converter this results in the 5-4 mode of operation and will most often be encountered in electric smelting furnace power supplies. It is possible to have more thyristors conducting. However, this only occurs at elevated current levels which tend to increase the commutation overlap angle. Equations presented in this chapter are only valid for commutation overlap angles up to 60° .

Equations were provided for the ideal case of constant current output with and without supply reactance. The analysis focused on the line current magnitude and harmonics, power and power factor, and the output voltage and harmonics. The harmonics were shown to be dependent on converter number and amount of reactance in the supply. It was also shown that increasing the firing angle reduces the power factor at the input and the voltage at the output. The reduction in power factor represents a major drawback in using the controlled rectifier technology and dictates that the converter transformers be equipped with tap changers to partially compensate.

Equations for power and current were shown to include a cosine term and this was used in the control configurations to linearize the response. Converter control

for both constant current and constant power was described and shown to function properly during transient disturbances. The response to a positive step change and a negative step change in setpoint were slightly different indicating that a degree of nonlinearity still exist. However, the differences were small and acceptable for the required application. The power controller was also shown with a current limit, which represents the actual case and was shown to function correctly. A balance regulator was included in each configuration to ensure that both bridge circuits shared the output current equally.

The performance of the controlled rectifier presented in this chapter can be improved by increasing the pulse number or by adding filter capacity at the input. The pulse number can be increased by adding bridge circuits and using transformers that provide the required phase shift. This will effectively reduce the harmonics at the input and the ripple at the output, such high pulse number converters are not usually employed due to additional transformer requirements. If harmonics and power factor become a problem the solution is to provide a fixed filter bank at the input. The filter bank can be tuned to reduce the dominant harmonic components and provide a leading power factor to compensate for converter operation.

Chapter 3

Uncontrolled Rectifier Chopper Power Supply

The uncontrolled rectifier chopper power supply uses diodes to convert the low voltage AC at the transformer secondary into fixed low voltage DC at the rectifier output. The choppers then convert this fixed DC voltage into controlled low voltage DC at the converter output. The power supply consists of rectifier transformers, diode bridge rectifiers, DC link capacitors, IGBT chopper sections, and output reactors. To date the uncontrolled rectifier chopper technology has been installed on one low power smelting furnace and several plasma torch applications. Similar power supplies have traditionally been used in low power motor drives and for DC traction.

In the following sections the basic concepts and equations required to analyze the uncontrolled rectifier chopper power supply are presented. Rectifier equations are developed for the ideal case of constant voltage output under discontinuous and continuous current conduction. Chopper equations are developed assuming that the input voltage is constant and that the output current is constant. Rectifier input parameters of interest include the RMS line current and harmonic magnitudes, power, and power factor. Chopper output parameters include the average voltage and harmonic magnitudes. Waveforms depicting various operating conditions are also provided throughout the chapter to illustrate converter operation.

Although the assumptions made in the development of the equations are appropri-

ate to approximate the steady-state operation of the converter they do not illustrate the dynamic performance of the converter. In order to show the performance, closed-loop simulations were performed for constant current output, constant power output, and constant power output with current limit. In each case plots are provided depicting the converter response to a step change in setpoint, as well as setpoint tracking performance. Simplified block diagrams showing the control structure are also provided for completeness.

The converter investigated in this chapter was a 12-pulse diode bridge at the input. Each 6-pulse rectifier provides a fixed DC voltage, which is controlled using multiple chopper sections connected in parallel at the output. The analysis assumes that all devices are ideal and perfectly matched with synchronized control signals. Since this is not the case in practice a section providing additional sources of information pertaining to non-ideal operation is also included. The chapter concludes by listing the benefits and problems associated with the uncontrolled rectifier chopper technology, and several methods to improve the power supply performance are suggested.

3.1 Major Components

The uncontrolled rectifier chopper power supply uses three forms of energy conversion and two forms of energy storage to convert the AC mains frequency, at the plant medium voltage bus, into controlled low voltage DC at the output. The power supply consists of rectifier transformers (energy conversion), uncontrolled diode converters (energy conversion), DC link capacitors (energy storage), DC/DC choppers (energy conversion), and output reactors (energy storage). A 12-pulse rectifier 2-phase chopper intended for use in an electric arc furnace power supply is provided for reference in Figure 3.1.

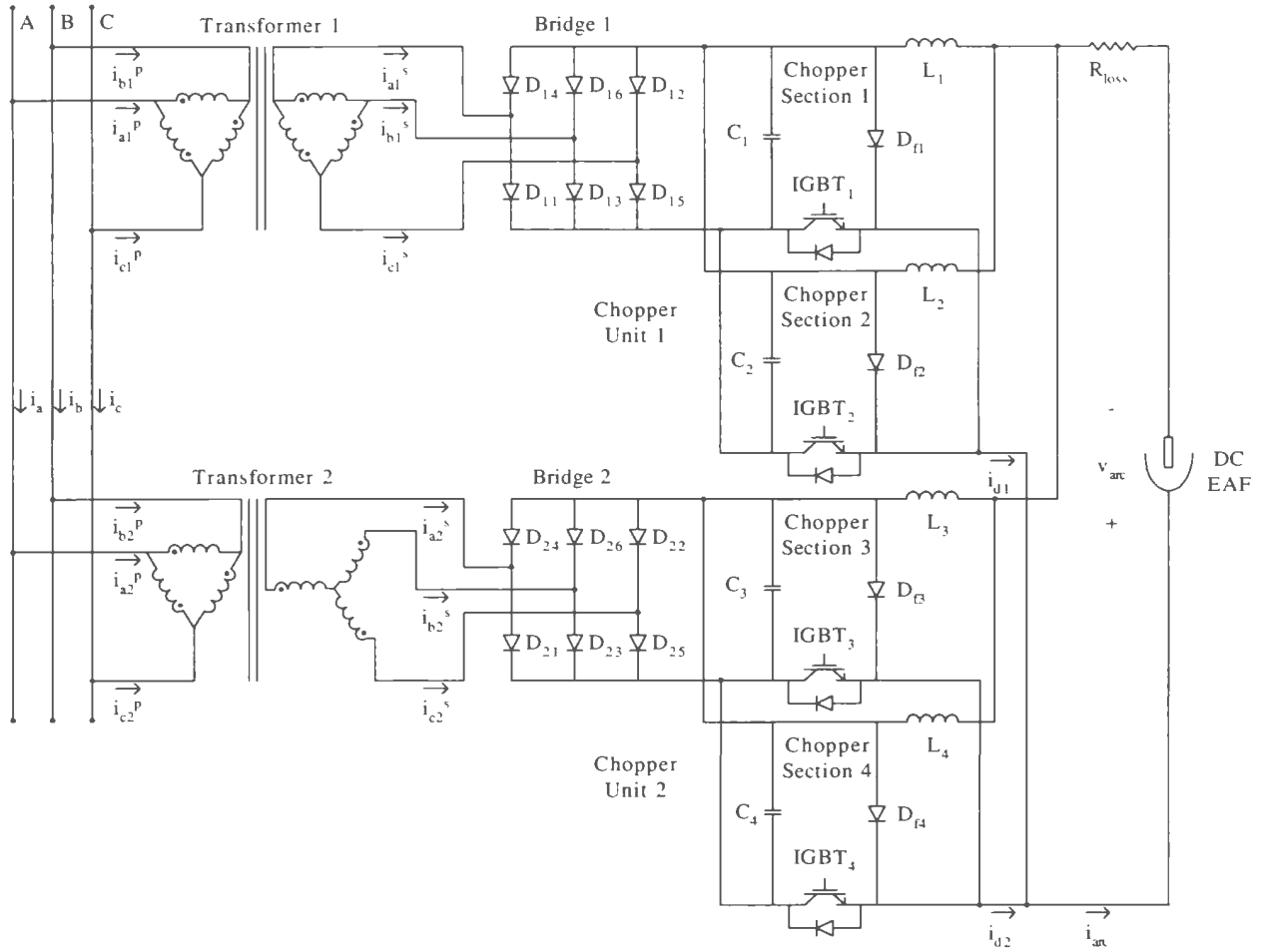


Figure 3.1: Simplified 12-Pulse Uncontrolled Rectifier Chopper Power Supply

3.1.1 Rectifier Transformers

The converter transformers are standard rectifier transformers and are not specially designed for electric arc furnace duty. This is possible since the harmonic loading and power factor seen at the transformer are those associated with operation of the diode bridge rectifier. The operation is essentially the same as that presented in Chapter 2 for the controlled rectifier power supply with $\alpha = 0^\circ$. Since phase control is not employed in the uncontrolled rectifier case the transformer size can be reduced by up to 25% [8].

As with the controlled rectifier power supply additional windings are used to increase the converter pulse number. For instance in Figure 3.1 the combination of a Δ/Δ transformer and a Δ/Y transformer are used to obtain 12-pulse operation. The configuration depicted in Figure 3.1 also shows that the output from each transformer is used to supply a separate uncontrolled DC voltage. Chopper sections are then used to independently control and balance the amount of current drawn from each transformer. This allows some voltage mismatch at the transformer secondary and it has been stated that the uncontrolled rectifier chopper power supply can tolerate as much as 4% unbalance [8] between both transformers.

Mechanically the transformers need to be designed to withstand large currents, however, the reduction in harmonics generally dictate that the K factors can be reduced to 2 or 3 [8]. Reduced harmonics also eliminate the need for heat exchangers and water requirements within the transformer cooling circuit. Transformer cooling is normally achieved using an ONAF combination, in situations where the cooling requirements are greater or less, an oil-natural air-forced (OFAF) or oil-natural air-natural (ONAN) combination may be used, respectively. Unlike the controlled rectifier power supply tap changers are not required when using the uncontrolled rectifier chopper power supply.

3.1.2 Uncontrolled Rectifiers

The uncontrolled rectifier utilizes power diodes in the bridge circuits to convert the AC voltage to DC voltage. Power diodes are similar to thyristors without gating control and are used in other high power applications including aluminum pot lines and other chemical refining processes which require a relatively fixed DC voltage. The diode will turn-on and begin to conduct once there is a positive voltage across the device. As with the thyristor device turn-off is governed by the zero-crossing of the line current. Power diodes are available with mean current ratings in excess of 5000 A and voltage ratings up to 10000 V. A typical rectifier diode data sheet applicable

for an EAF power supply is provided for reference in Appendix A.

Since the furnace will normally be operated at high current levels the diodes will need to be connected in parallel to provide the necessary amount of current to the process. Current sharing is accomplished by arranging the bridge circuits with three continuous AC conductors [19]. This is the same configuration used for the controlled rectifier power supply and relies on the magnetic fields between the devices to distribute the current equally. The benefit in using this approach is that current sharing is obtained without adding inductance in series with the individual diodes.

High currents within the bridge circuit also require that the diodes be cooled using deionized water. The deionized water is pumped through a closed circuit heat exchanger that may be part of an WFAN or WFWF arrangement, depending on the cooling requirements. A conductivity meter is also required in the cooling circuit for protection.

The power supply is partially protected using overcurrent relays to trip the main breaker. Additional protection is provided to the major components using temperature detectors, pressure sensors, flow meters, and level indicators to monitor the cooling system and to trip the main breaker in the event of a potential problem. The power supply is protected from transient voltages using surge arrestors will be connected between phases, and between phases to ground. A damping circuit will be installed in parallel with the arrestors at the input as shown in Figure 3.2

The diodes are protected from excessive fault currents, as well as the rate of change in voltage and current using a combination of fuses and snubber circuits. The protection and snubber circuits used in the uncontrolled rectifier power supply are shown in Figure 3.2.

The arrangement is similar to that used in the controlled rectifier power supply whereby a dv/dt snubber is used in conjunction with a current limiting fuse on each device. The di/dt protection is provided to all diodes through the transformer reactance at the input and the DC reactors at the output. Snubbers for bridge circuits

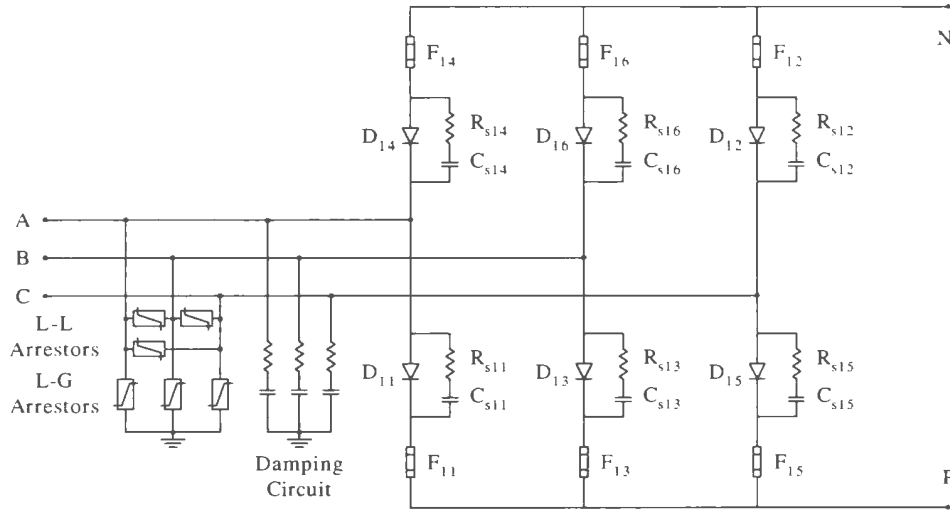


Figure 3.2: Uncontrolled Rectifier Chopper Protection Circuit

are discussed further in [15, 20], while information on DC fusing in semiconductor circuits is provided in [21].

3.1.3 DC Link Capacitors

The DC link capacitors are required to sustain any mismatch between the rectifier output current and the chopper input currents. The capacitors are also used to filter the ripple voltage from the diode bridge converter to provide a near constant DC voltage at the input to the chopper modules.

When used in this application the capacitors are required to sustain a constant ripple voltage from the bridge rectifier. In order to ensure maximum reliability film type self-healing capacitors are used. Unlike electrolytic capacitors, film type capacitors fail in the open-circuit condition and as such do not damage other components.

3.1.4 Chopper Sections

The chopper power supply uses insulated gate bipolar transistors (IGBT) as the controlling element. IGBTs are power electronic devices that permit the control of

both turn-on and turn-off. IGBTs are commonly used in low power motor drives. However, recent advancements in semiconductor technology have permitted devices to be constructed with ratings applicable for some high power applications. Devices are now commercially available with mean current ratings in excess of 1500 A and voltage ratings up to 6500 V. A typical IGBT data sheet applicable for an EAF power supply is provided for reference in Appendix A.

The chopper module used in the EAF power supply is of the single-quadrant step-down configuration. This is often referred to as a type A chopper and essentially means that current can only be conducted in one direction and that the output voltage must be lower than the input voltage [30]. The basic circuit configuration is depicted in Figure 3.3 and includes an input capacitor, a transistor switching element, and a freewheeling diode. For high current applications it is often necessary to connect multiple IGBTs and freewheeling diodes in parallel to increase the current rating of the individual modules.

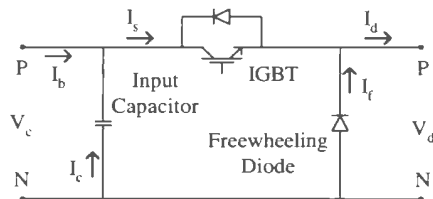


Figure 3.3: Basic Chopper Module

The DC link capacitor was described in the previous subsection and is intended to provide a constant voltage at the input to the chopper module. Since the load is assumed to have a reactive component the freewheeling diode is required to provide a path for the energy released by the load inductance when the switch is in the open position. Without the freewheeling diode this energy would be dissipated in the IGBT, possibly destroying the switch. As an additional protection measure a fast acting diode is also installed across the IGBT to allow some current conduction in the opposite direction. This is a common feature and most manufacturers include the IGBT and fast acting

diode in a common package.

The power supply shown in Figure 3.1 consists of two multiphase chopper units, which are supplied from two separate unregulated DC buses. Each chopper unit consists of two chopper sections, which contain a number of chopper modules connected in parallel to provide the necessary current rating for the load requirements. For an EAF power supply the chopper sections and chopper units will also be connected in parallel at the output to further increase the current rating.

The connections within the individual modules and between modules are described in [33] and are shown for a two section chopper unit in Figure 3.4. Each module consist of two IGBTs and two freewheeling diodes connected in parallel. Each section consist of four chopper modules connected in parallel. When paralleling individual modules it becomes necessary to include a small inductance at the input and output to ensure proper current sharing. When connecting chopper sections or chopper units in parallel more reactance is added at the output of each section. The current rating of the structure is easily increased by adding more modules to each section.

In addition to paralleling devices the high currents dictate that the IGBTs be water cooled. Unlike the thyristors and power diodes the IGBTs are available in isolated base plate modules that provide isolation between the heatsink and electrical circuit [32], hence deionized water is not required. The water is pumped through a heat exchanger that may be part of a WFAN or WFAF arrangement, depending on the cooling requirements.

As with the bridge rectifier the chopper modules need snubbers to function correctly and fuses for protection. Device protection and snubber circuits required for a chopper module are provided for reference in Figure 3.5. As in the bridge circuit the snubbers are required to limit the di/dt and dv/dt . However, for a controlled switch the snubbers are also required to keep within the device safe operating area and to limit the power dissipation that occurs during switching [31]. One snubber is generally used to control the turn-off transition and another to control the turn-on

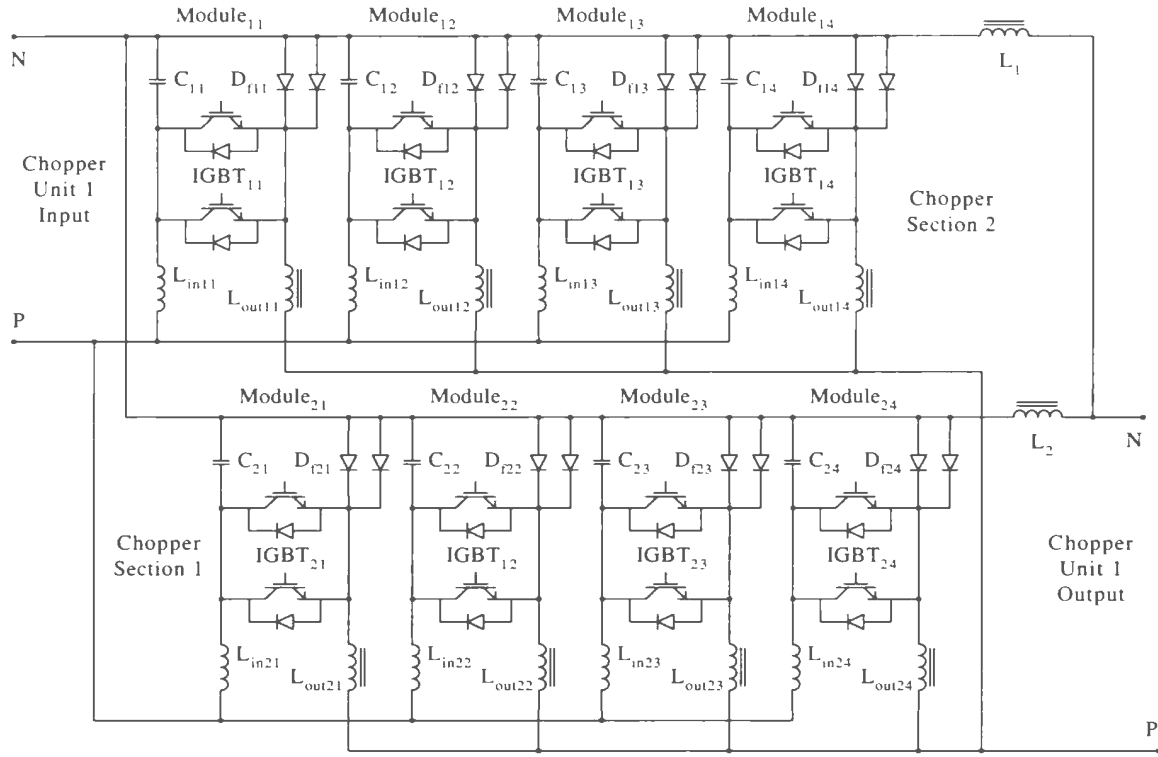


Figure 3.4: Parallel Chopper Connection

transition.

For the chopper module a combined snubber will be used to control both the turn-off transition and the turn-on transition. The snubber consist of a polarized capacitor, diode, resistor, and an inductor. Since switching the IGBT also changes the state of the freewheeling diode it will also require the same type of snubber. This snubber is required to make the transition slow enough to keep the forward recovery voltage and reverse recovery current of the freewheeling diode from excessively stressing the IGBT [31]. Snubbers for transistor switching circuits are discussed further in [31,37].

Other protection features in the chopper module include fuses, a resistor across the input capacitor, and a surge arrestor at the output. The fuses are required to protect the devices from overcurrent and are placed at the input to the module, and in series with both the IGBT and freewheeling diode. The resistor across the

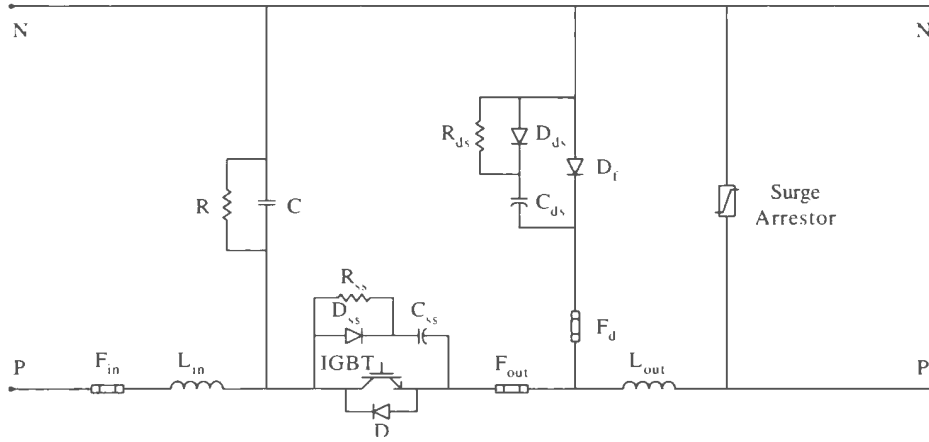


Figure 3.5: Chopper Protection Circuit

capacitor is required to provide a discharge path when the power is turned off and to ensure equal voltage sharing across capacitors connected in series. The surge arrester is required to protect the devices from voltage transients on the load side of the converter. Additional information on DC fusing in semiconductor circuits is provided in [21].

3.1.5 Output Reactors

The output reactors are required to ensure current sharing between the chopper sections and to sustain any difference between the chopper output voltage and process load voltage. Unlike the reactors used in the controlled rectifier power supply the chopper reactors are iron core choke reactors. Choke reactors are used to minimize losses when operating at low power.

The reactors are required to carry large currents and as such require water cooling. The reactors are connected between the chopper section outputs and the secondary buswork that connects the power supply to the furnace electrodes.

3.2 Rectifier Operation

In this section the rectifier is supplied from an inductive source and is assumed to drive a constant voltage load. Unlike the case for constant current loading presented in Chapter 2 analytical expressions for the constant voltage case are not readily available in the literature. Although Schaefer [11] does devote a chapter to these types of converters, analysis of the 6-pulse bridge is mainly focused on discontinuous conduction, noting that analysis for the continuous case becomes more complex.

Hancock [39] does analyze the 6-pulse bridge with a constant voltage load from open-circuit to short-circuit and defines the various modes of operation under different supply impedance configurations. The results are presented graphically and clearly show four modes of operation, two discontinuous modes referred to as the 2-0 mode and the 2-3-2-0 mode, and two continuous modes referred to as the 3-2 mode and the 3-3 mode. The paper goes on to explain that for a purely resistive supply only the 2-0 mode and 3-2 mode are present.

The work presented by Hancock [39] was analyzed further in [40] for an inductive supply and provides the boundaries between the various modes in terms of voltage regulation. For instance the 2-0 mode occurs for small regulation values between $0.958 < V_c/V_{LL} < 1$ in which the rectifier produces a discrete pulse every 60° . This is the simplest mode to analyze and will be used to introduce the operation of the converter in Section 3.2.1. The 3-2 mode occurs for higher regulation values between $0.746 < V_c/V_{LL} < 0.9496$. This will be the most common mode for the electric arc furnace power supply and will be analyzed in detail in Section 3.2.2.

The 2-3-2-0 mode occurs in a small regulation range between $0.9496 < V_c/V_{LL} < 0.958$. As with the 2-0 mode the 2-3-2-0 mode is not expected to occur during normal operation of the electric arc furnace power supply. The 3-3 mode occurs for regulation values between $0 < V_c/V_{LL} < 0.746$ in which case three diodes are always conducting. The phase currents become more sinusoidal, however, the amount of regulation is impractical for normally rated conditions. A simplified analysis of the 3-3 mode is

provided in [42] and shows the shape of the line-to-neutral voltage at the load side of the supply reactance.

When both bridge circuits are included in the analysis, modes of operation similar to those presented in Chapter 2 will be obtained. For instance if both converters are independently operating in the 2-3 mode then it is possible for the combined converters to be in the 5-4 mode, the 5-5 mode, or the 6-5 mode. The combined mode will depend on the amount of voltage regulation, which has the effect of changing the commutation overlap angle. This concept will be further illustrated in the proceeding two subsections. As with the controlled rectifier power supply the uncontrolled rectifier will generally operate in the 5-4 mode.

3.2.1 Constant Voltage Load Discontinuous Conduction

The assumption of discontinuous current is not practical since even a small amount of reactance in the supply will ensure that the currents are continuous. However, the case is useful in describing the basic operation of the converter and is presented in detail. For the purpose of this section the 2-0 mode will be analyzed since it represents the simplest discontinuous case.

Since each bridge circuit in the power supply feeds a separate chopper section the analysis focuses on one 6-pulse bridge with an inductive source. The line currents and power factor expected at the primary of the transformers are analyzed assuming that the load voltages from each 6-pulse rectifier are equal.

Furthermore, for this section and the next, it is assumed that all supply reactance is included in the transformers and is referred to the secondary side. These simplifications mean that the transformers are decoupled magnetically and that the supply voltages at the primary of the transformers are ideal. Based on the circuit configuration depicted in Figure 3.1 the line-to-neutral voltages of bridge 1 will lag those of bridge 2 by 30° . The following open-circuit voltages are assumed on the

secondary side of the rectifier transformers

$$v_{an1}^s = \frac{\sqrt{2}}{\sqrt{3}} V_{LL} \cos \left(\omega t - \frac{\pi}{3} \right) \quad (3.1)$$

$$v_{bn1}^s = \frac{\sqrt{2}}{\sqrt{3}} V_{LL} \cos (\omega t - \pi) \quad (3.2)$$

$$v_{cn1}^s = \frac{\sqrt{2}}{\sqrt{3}} V_{LL} \cos \left(\omega t + \frac{\pi}{3} \right) \quad (3.3)$$

$$v_{an2}^s = \frac{\sqrt{2}}{\sqrt{3}} V_{LL} \cos \left(\omega t - \frac{\pi}{6} \right) \quad (3.4)$$

$$v_{bn2}^s = \frac{\sqrt{2}}{\sqrt{3}} V_{LL} \cos \left(\omega t - \frac{5\pi}{6} \right) \quad (3.5)$$

$$v_{cn2}^s = \frac{\sqrt{2}}{\sqrt{3}} V_{LL} \cos \left(\omega t + \frac{\pi}{2} \right) \quad (3.6)$$

In order to transfer the line currents from the secondary of the furnace transformers to the primary, the Δ/Y currents need to be properly transformed and added to the currents from the Δ/Δ transformer. Assuming a 1:1 turns ratio in the transformers the primary currents can be expressed using the following equations:

$$i_a^p = i_{a1}^p + i_{a2}^p = i_{a1}^s + \frac{i_{a2}^s - i_{c2}^s}{\sqrt{3}} \quad (3.7)$$

$$i_b^p = i_{b1}^p + i_{b2}^p = i_{b1}^s + \frac{i_{b2}^s - i_{a2}^s}{\sqrt{3}} \quad (3.8)$$

$$i_c^p = i_{c1}^p + i_{c2}^p = i_{c1}^s + \frac{i_{c2}^s - i_{b2}^s}{\sqrt{3}} \quad (3.9)$$

Since the output voltage is constant it does not require analysis. However, a suitable value must be chosen to operate in the 2-0 mode. Assuming that the voltage regulation is 0.975 and line-to-line voltages are 1 pu then the required output voltage would be 1.3789 pu. In order to present values that are not dependent on circuit parameters the line currents are normalized using the per-phase short-circuit current from each 6-pulse bridge [15].

$$I_{d0} = \frac{V_{LL}}{\sqrt{3}\omega L} \quad (3.10)$$

To aid in the analysis two additional angles are defined and referred to as the delay angle, β , and the extinction angle, γ . The delay angle represents the point at which current begins to flow and if we assume a sine wave as the reference it can be determined from Equation 3.11 [11].

$$\sin(\beta) = \frac{V_c}{\sqrt{2}V_{LL}} \quad (3.11)$$

At β the line-to-line voltage exceeds the capacitor voltage and conduction through a pair of diodes begins. The current will continue to rise until $180^\circ - \beta$ at which time the line-to-line voltage decreases to a value below the capacitor voltage. The current will now start to decrease and the time required to go to zero can be determined. The point at which conduction stops is referred to as the extinction angle and can be determined by solving Equation 3.12 [11].

$$\cos(\beta) - \cos(\gamma) = (\gamma - \beta) \sin(\beta) \quad (3.12)$$

For the 2-0 mode each 60° interval consists of a period of no conduction followed by a period when two devices are conducting. For the period when two devices are conducting the line-to-neutral voltages can be determined using Equations 3.13 to 3.15.

$$v_{an} = v_{bn} = \frac{v_{an} + v_{bn} \pm V_c}{2} \quad (3.13)$$

$$v_{bn} = v_{cn} = \frac{v_{bn} + v_{cn} \pm V_c}{2} \quad (3.14)$$

$$v_{cn} = v_{an} = \frac{v_{cn} + v_{an} \pm V_c}{2} \quad (3.15)$$

To obtain the correct line-to-neutral voltages in the positive and negative half-cycles the capacitor voltage will need to have the matching polarity. For the period when no devices are conducting the line-to-neutral voltages will be equal to the open-circuit voltages presented in Equations 3.1 to 3.6.

Since the voltages at the primary and secondary of the rectifier transformers are now known the voltage drop in the supply reactance can be determined. This voltage

drop is used to obtain instantaneous currents in the conduction intervals. Simplified expressions for the line currents are provided in [40], and are rewritten for the case presented in this section. The correct equations for the positive half-cycle are provided. Since the waveform is symmetric, the same equations are applicable to the negative half-cycle by changing the polarity and increasing the phase shift angle, ϕ , by 180° .

The current in the positive half-cycle consists of four intervals. The first interval occurs between $\beta < \omega t < \gamma$, and the current in this interval can be written as

$$i_{l1}^s = \frac{\sqrt{2}V_{LL}}{2\omega L} \left[\cos(\beta) - \cos\left(\omega t + \frac{\pi}{3} - \phi\right) + \left(\beta - \omega t - \frac{\pi}{3} + \phi\right) \sin(\beta) \right] \quad (3.16)$$

This represents the first conduction interval. The second interval occurs between $\gamma < \omega t < \beta + \pi/3$, and the current in this interval can be written as

$$i_{l2}^s = 0 \quad (3.17)$$

This represents the non-conduction interval within the positive half-cycle. The third interval occurs between $\beta + \pi/3 < \omega t < \gamma + \pi/3$, and the current in this interval can be written as

$$i_{l3}^s = \frac{\sqrt{2}V_{LL}}{2\omega L} [\cos(\beta) - \cos(\omega t - \phi) + (\beta - \omega t + \phi) \sin(\beta)] \quad (3.18)$$

This represents the second conduction interval. The fourth interval occurs between $\gamma + \pi/3 < \omega t < \beta + \pi$, and the current in this interval can be written as

$$i_{l4}^s = 0 \quad (3.19)$$

This represents the non-conduction interval between the positive half-cycle and the negative half-cycle.

To illustrate the operation of the uncontrolled rectifier with a constant voltage load and discontinuous current conduction several plots for voltage regulation of 0.975, 0.968, 0.961, and 0.950 are presented in Figures 3.6 to 3.8. Figures 3.6 and 3.7 depict

the AC voltages and currents expected at the secondary of the Δ/Δ transformer and Δ/Y transformer, respectively. Figure 3.8 shows the same information combined at the primary of the rectifier transformers. The first three cases show each rectifier operating in the 2-0 mode, whereas the fourth case shows each rectifier operating in the 2-3-2-0 mode. All waveforms are plotted over a 20 ms period and are intended to represent one cycle at a power system frequency of 50 Hz.

Since the line currents at the secondary of both transformers consist of two distinct pulses per half-cycle it can be concluded that the output current from each bridge circuit is discontinuous. For the case showing operation with a voltage regulation of 0.975 both 6-pulse rectifiers independently operate in the 2-0 mode. However, the combined line currents at the primary of the transformers suggest that the 12-pulse rectifier is operating in the 4-2 mode. This is possible since the combined currents consist of one component from the Δ/Δ transformer plus the phase shifted component from the Δ/Y transformer.

The RMS line current will increase as the voltage regulation decreases. For the purpose of this section the total RMS line current is written in integral form to keep the equations as short as possible. Based on the four intervals described above the total RMS line current including harmonics can be written as

$$I_L = \left(\frac{\sqrt{2} + \sqrt{6}}{2} \right) \left\{ \frac{1}{\pi} \int_{\beta}^{\gamma} i_{l1}^s (\omega t)^2 d(\omega t) + \frac{1}{\pi} \int_{\beta+\pi/3}^{\gamma+\pi/3} i_{l3}^s (\omega t)^2 d(\omega t) \right\}^{1/2} \quad (3.20)$$

where i_{l1}^s and i_{l3}^s represent the instantaneous currents in intervals one and three, respectively. The integrals inside the square root represent one half-cycle of one 6-pulse bridge only, whereas the factor outside the square root provides the necessary correction to take into account the contribution from both rectifiers at the primary of the transformers. Since the waveform is symmetric one half-cycle is sufficient to give the correct result for the total RMS line current.

Assuming that the bridge currents and output voltages are balanced, harmonics

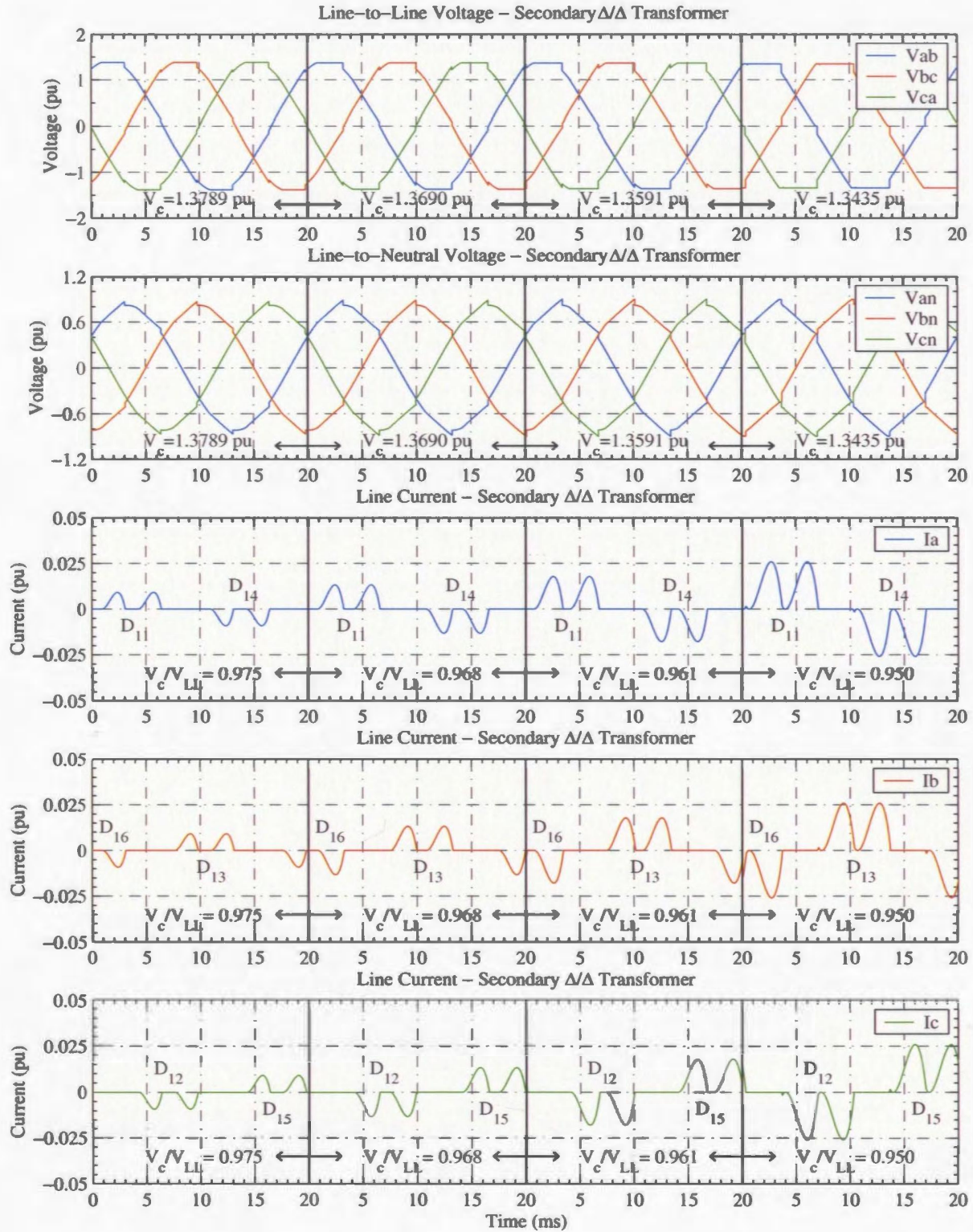


Figure 3.6: Voltage and Current Waveforms at Secondary of Δ/Δ Transformer (Discontinuous Conduction)

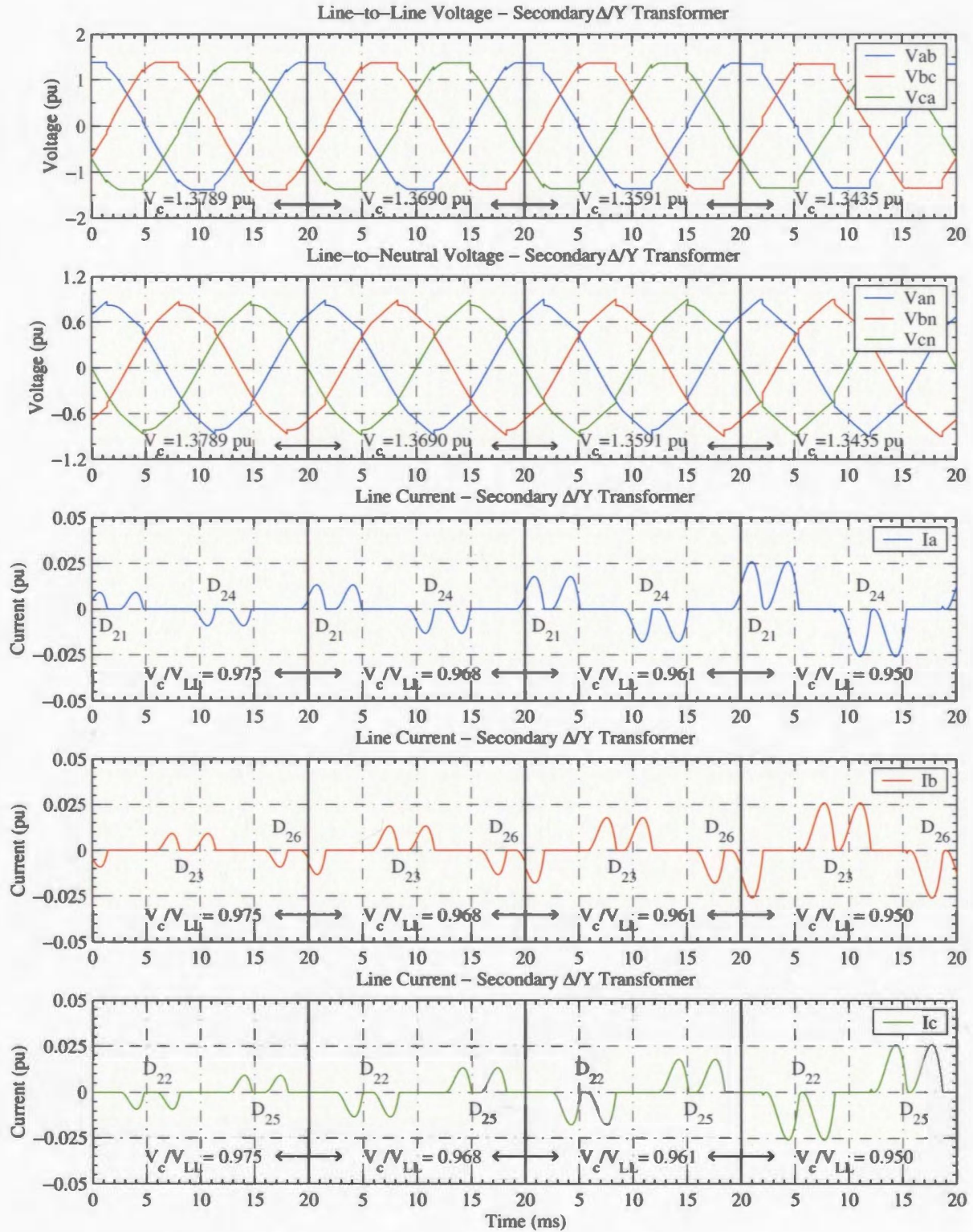


Figure 3.7: Voltage and Current Waveforms at Secondary Δ/Y Transformer (Discontinuous Conduction)

in the line currents occur at the following frequencies

$$h = 12k \pm 1 \quad (3.21)$$

where k is an integer. The harmonics will depend on the voltage regulation and can be determined from Fourier analysis of the line current waveform as

$$I_h = I_1 \sqrt{a_h^2 + b_h^2} \quad (3.22)$$

where I_1 is the magnitude of the fundamental component and a_h and b_h are coefficients determined from Equations 3.23 and 3.24, respectively [14].

$$a_h = \frac{2}{\pi} \int_3^\gamma i_{l1}^s(\omega t) \cos(h\omega t) d(\omega t) + \frac{2}{\pi} \int_{3+\pi/3}^{\gamma+\pi/3} i_{l3}^s(\omega t) \cos(h\omega t) d(\omega t) \quad (3.23)$$

$$b_h = \frac{2}{\pi} \int_3^\gamma i_{l1}^s(\omega t) \sin(h\omega t) d(\omega t) + \frac{2}{\pi} \int_{3+\pi/3}^{\gamma+\pi/3} i_{l3}^s(\omega t) \sin(h\omega t) d(\omega t) \quad (3.24)$$

The fundamental component of the line current can also be determined from Fourier analysis by setting h in Equations 3.23 and 3.24 to 1 and solving Equation 3.25.

$$I_1 = \sqrt{a_1^2 + b_1^2} \quad (3.25)$$

The displacement power factor can be determined by taking the cosine of the phase angle between the fundamental components of the line-to-neutral voltage and the line current. The displacement power factor for the uncontrolled rectifier with supply reactance and a constant voltage load can be determined as

$$DPF = \cos \left[\theta_1 - \tan^{-1} \left(\frac{b_1}{a_1} \right) \right] \quad (3.26)$$

where θ_1 is the phase angle of the fundamental component of the line-to-neutral voltage and a_1 and b_1 are determined from Equations 3.23 and 3.24 by setting h to 1.

This term alone is not sufficient to describe the power factor and will not give accurate results when harmonics are present. The correct equation for power factor taking into account harmonic distortion can be written as

$$PF = \frac{I_1}{I_L} DPF \quad (3.27)$$

where I_L is the RMS value of the line current taking into account all significant harmonic components.

3.2.2 Constant Voltage Load Continuous Conduction

For this case the rectifier is still supplied from an inductive source and feeds a constant voltage load. However, the regulation is such that the load current is now continuous. As in the previous subsection the analysis is restricted to one 6-pulse bridge only. The line currents and power factor expected at the primary of the furnace transformers are analyzed assuming that the load voltages from each 6-pulse rectifier are equal. All other assumptions regarding system reactance and reference voltages used in the previous subsection also apply equally to the continuous conduction case.

To accurately represent the EAF nominal operating characteristics the voltage regulation is chosen such that the combined converter operates in the 5-4 mode. This requires each bridge circuit to operate in the 3-2 mode with enough overlap to provide the desired effect. To obtain a typical operating condition the voltage regulation is set to 0.900. Assuming that the line-to-line voltages are 1 pu then the required output voltage would be 1.2728 pu. As in the previous subsection the line currents are normalized using Equation 3.10.

A sine wave is chosen as the reference as this allows the delay angle to be obtained using Equation 3.11. In the continuous case conduction begins slightly before the line-to-line voltage exceeds the capacitor voltage. The amount before will be denoted by angle ψ [40], and can be determined by solving Equation 3.28.

$$\sin\left(\psi + \frac{\pi}{6}\right) = \frac{V_c}{\sqrt{6}V_{LL}} \quad (3.28)$$

The extinction angle is no longer applicable to the continuous conduction case. Instead, the commutation overlap angle introduced in Chapter 2 is again used to represent the amount of overlap. Since the load current is no longer constant the definition of the commutation overlap angle is written in terms of two additional angles as

$$\mu = \varepsilon_1 + \varepsilon_2 \quad (3.29)$$

where ε_1 and ε_2 can be determined by solving Equations 3.30 and 3.31 [40].

$$\cos\left(\varepsilon_1 + \frac{\pi}{6}\right) = \frac{V_c}{\sqrt{6}V_{LL}} \quad (3.30)$$

$$\sin\left(\varepsilon_1 + \frac{\pi}{6}\right) + \cos(\varepsilon_2) = (\pi + \varepsilon_1 + \varepsilon_2) \cos\left(\varepsilon_1 + \frac{\pi}{6}\right) \quad (3.31)$$

For the period when two devices are conducting the line-to-neutral voltages can be determined using Equations 3.13 to 3.15. For instance, if current is being conducted through Phases A and B then Equation 3.13 must be used. For the period when three devices are conducting the line-to-neutral voltages can be determined using any one of Equations 3.13 to 3.15, which contains that Phase. For instance if all phases are conducting and Phase A line-to-neutral voltage is required then either Equation 3.13 or 3.15 would give the correct result. To obtain the correct line-to-neutral voltages in the positive and negative half-cycles the capacitor voltage will need to have the matching polarity.

Since the voltages at the primary and secondary of the rectifier transformers are now known the voltage drop in the supply reactance can be determined. This voltage drop is used to obtain the instantaneous line currents in the various conduction intervals. Simplified expressions for the line currents are provided by Rice [28], and are rewritten for the case presented in this section. The correct equations for the positive half-cycle are provided. Since the waveform is symmetric the same equations are applicable to the negative half-cycle by changing the polarity and increasing the phase shift angle, ϕ , by 180° . To simplify the equations two constants are used and can be written as

$$I_{c1} = I_d - \Delta i \left[\frac{2 \sin(\pi/6 - \mu/2) - (\pi/3 - \mu) \sin(\pi/3 - \mu/2)}{(\pi/3)(1 - \sin(\pi/3 + \mu/2))} \right] \quad (3.32)$$

$$I_{c2} = I_{c1} - \frac{\sqrt{2}V_{LL}}{2\omega L} \left[\cos(\beta) - \cos\left(\frac{\pi}{3} + \mu - \psi\right) + \left(\beta - \frac{\pi}{3} - \mu + \psi\right) \sin(\beta) \right] \quad (3.33)$$

where Δi represents the ripple component in the output current and can be determined as

$$\Delta i = \frac{\sqrt{2}V_{LL}}{2\omega L} \left[\cos(\beta) + \cos\left(\mu + \frac{\pi}{3}\right) - \left(\frac{2\pi}{3} - \beta - \mu\right) \sin(\beta) \right] \quad (3.34)$$

For the 6-pulse rectifier each half-cycle consists of six intervals. The first interval occurs between $\nu < \omega t < \mu - \nu$, and the current in this interval can be written as

$$i_{l1}^s = I_{c1} \left[\frac{1 - \cos(\omega t + \nu - \phi)}{1 - \cos(\mu)} \right] \quad (3.35)$$

This represents the first commutation interval in which the current begins to rise from zero. The second interval occurs between $\mu - \nu < \omega t < \pi/3 - \nu$, and the current in this interval can be written as

$$i_{l2}^s = \frac{\sqrt{2}V_{LL}}{2\omega L} \left[\cos(\beta) - \cos\left(\omega t + \frac{\pi}{3} - \phi\right) + \left(\beta - \omega t - \frac{\pi}{3} + \phi\right) \sin(\beta) \right] + I_{c2} \quad (3.36)$$

This represents the first conduction interval after the commutation period has ended. The third interval occurs between $\pi/3 - \nu < \omega t < \pi/3 + \mu - \nu$, and the current in this interval can be written as

$$i_{l3}^s = I_d \left\{ \frac{\sqrt{2}V_{LL}}{4\omega L} \left[2\cos(\beta) - \cos\left(\omega t + \frac{\pi}{3} - \phi\right) - \cos(\omega t - \phi) \right. \right. \quad (3.37) \\ \left. \left. + \left(2\beta - 2\omega t - \frac{\pi}{3} + 2\phi\right) \sin(\beta) \right] + I_{c2} \right\}$$

This represents the second commutation interval that occurs between the opposite two phases. The fourth interval occurs between $\pi/3 + \mu - \nu < \omega t < 2\pi/3 - \nu$, and the current in this interval can be written as

$$i_{l4}^s = \frac{\sqrt{2}V_{LL}}{2\omega L} [\cos(\beta) - \cos(\omega t - \phi) + (\beta - \omega t + \phi) \sin(\beta)] + I_{c2} \quad (3.38)$$

This represents the second conduction interval that occurs before the current goes to zero. The fifth interval occurs between $2\pi/3 - \nu < \omega t < 2\pi/3 + \mu - \nu$, and the current in this interval can be written as

$$i_{l5}^s = I_d \left\{ \frac{\sqrt{2}V_{LL}}{4\omega L} \left[2\cos(\beta) - \cos(\omega t - \phi) - \cos\left(\omega t - \frac{\pi}{3} - \phi\right) \right. \right. \quad (3.39) \\ \left. \left. + \left(2\beta - 2\omega t + \frac{\pi}{3} + 2\phi\right) \sin(\beta) \right] + I_{c2} \right\} - I_{c1} \left[\frac{1 - \cos(\omega t + \nu - 2\pi/3 - \phi)}{1 - \cos(\mu)} \right]$$

This represents the final commutation interval in which the current returns to zero. The sixth interval occurs between $2\pi/3 + \mu - \nu < \omega t < \pi - \nu$, and the current in this interval can be written as

$$i_{l6}^s = 0 \quad (3.40)$$

This represents the non-conduction interval between the positive and negative half-cycle. Equations 3.35 to 3.40 are based on knowing the average DC current, I_d . An expression for the average DC current in integral form is provided in Equation 3.41.

$$I_d = \frac{1}{\pi} \int_{-\nu}^{\mu-\nu} i_{l1}^s(\omega t) d\omega t + \frac{1}{\pi} \int_{\mu-\nu}^{\pi/3-\nu} i_{l2}^s(\omega t) d\omega t + \frac{1}{\pi} \int_{\pi/3-\nu}^{\pi/3+\mu-\nu} i_{l3}^s(\omega t) d\omega t \quad (3.41)$$

$$+ \frac{1}{\pi} \int_{\pi/3+\mu-\nu}^{2\pi/3-\nu} i_{l4}^s(\omega t) d\omega t + \frac{1}{\pi} \int_{2\pi/3-\nu}^{2\pi/3+\mu-\nu} i_{l5}^s(\omega t) d\omega t$$

where i_{l1}^s to i_{l5}^s represent the instantaneous currents in intervals one to five described in Equations 3.35 to 3.36.

To illustrate the operation of the uncontrolled rectifier with a constant voltage load and continuous current conduction, several plots for voltage regulation of 0.900, 0.850, 0.800, and 0.740 are presented in Figures 3.9 to 3.11. Figures 3.9 and 3.10 depict the AC voltages and currents expected at the secondary of the Δ/Δ transformer and Δ/Y transformer, respectively. Figure 3.11 shows the same information combined at the primary of the rectifier transformers. The first three cases show each rectifier operating in the 3-2 mode, whereas the fourth case shows each rectifier operating in the 3-3 mode. All waveforms are plotted over a 20 ms period and are intended to represent one cycle at a power system frequency of 50 Hz.

Since the line currents at the secondary of both transformers consist of only one pulse per half-cycle it can be concluded that the output current from each bridge circuit is continuous. For the case showing operation with a voltage regulation of 0.900 both 6-pulse rectifiers independently operate in the 3-2 mode. However, the combined line currents at the primary of the transformers suggest that the 12-pulse rectifier is operating in a 5-4 mode. This is possible since the combined currents

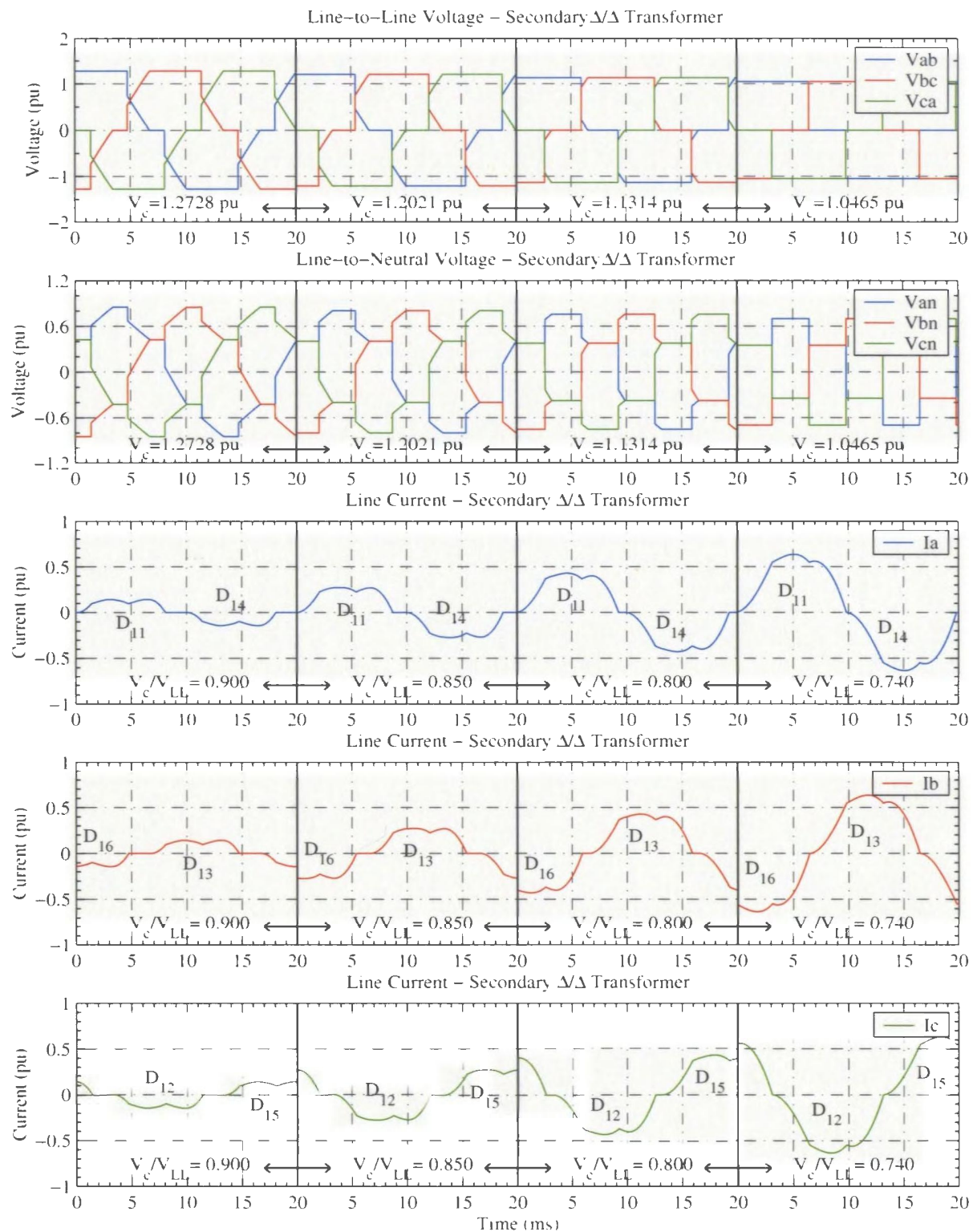


Figure 3.9: Voltage and Current Waveforms at Secondary of Δ/Δ Transformer (Continuous Conduction)

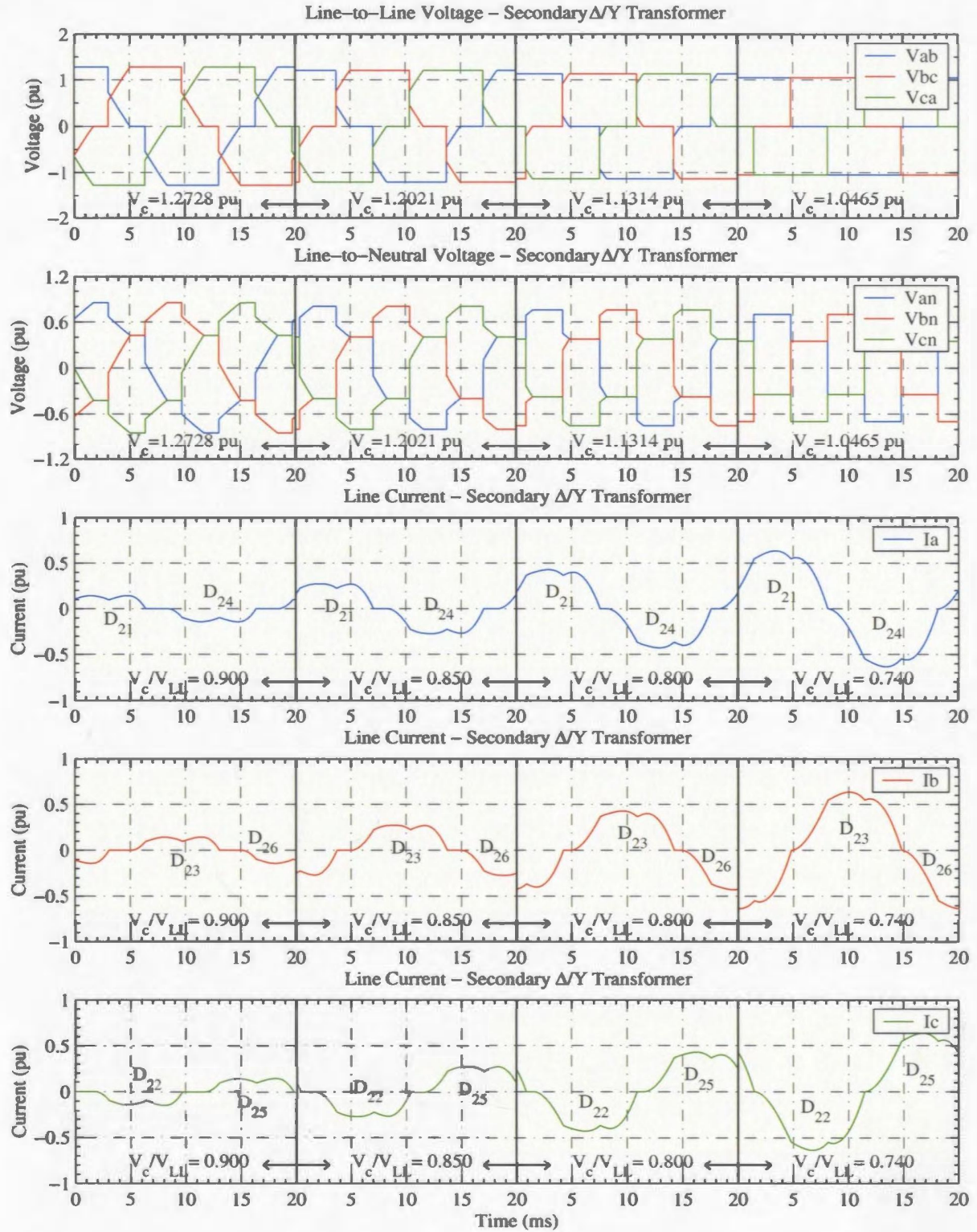


Figure 3.10: Voltage and Current Waveforms at Secondary of Δ/Y Transformer (Continuous Conduction)

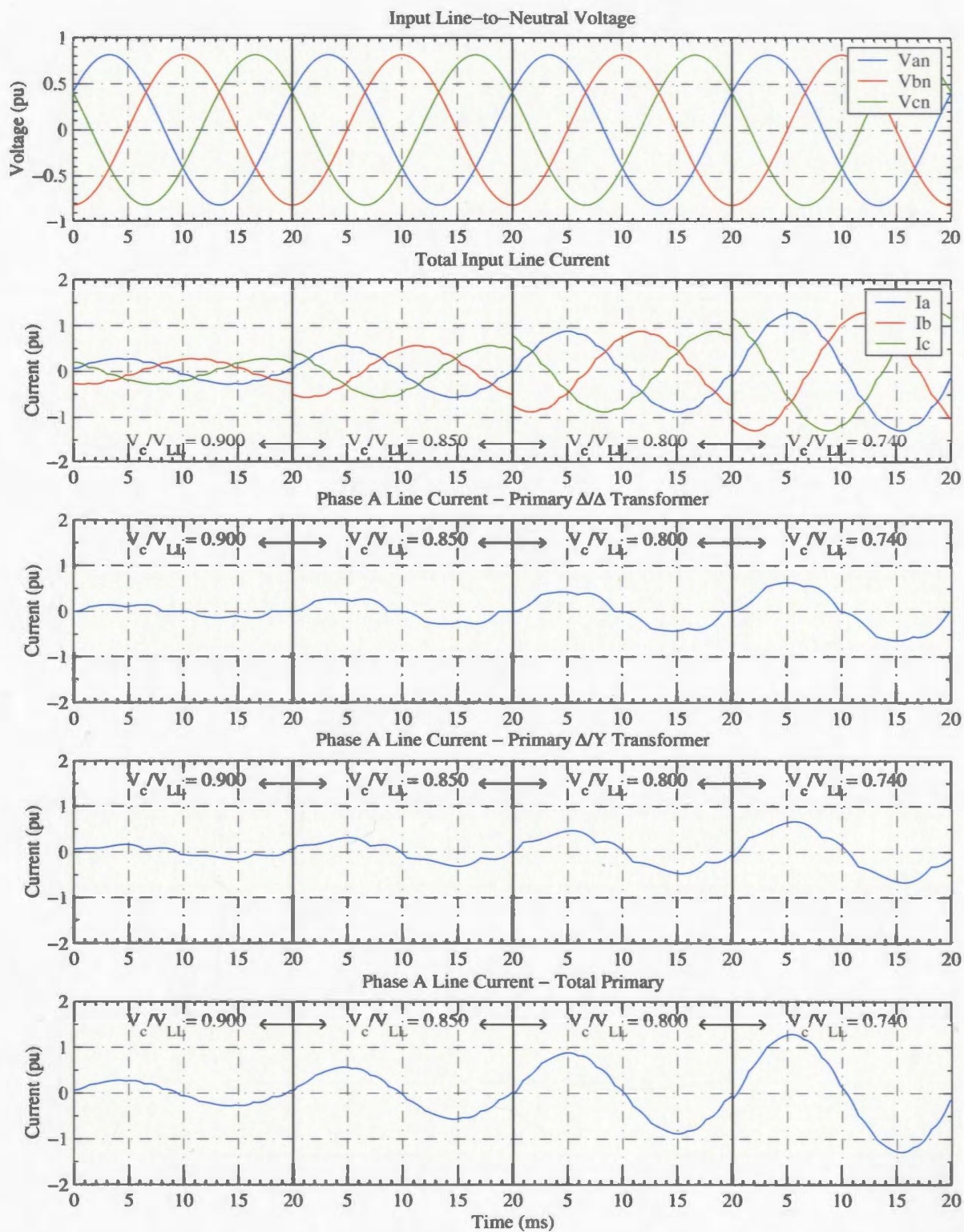


Figure 3.11: Uncontrolled Rectifier Input Voltage and Current Waveforms (Continuous Conduction)

consist of one component from the Δ/Δ transformer and the phase shifted component from the Δ/Y transformer.

The RMS line current will increase as the voltage regulation decreases. For simplicity the total RMS line current is written in integral form to keep the equations as short as possible. Based on the six intervals described above the total RMS line current including harmonics can be written as

$$I_L = \left(\frac{\sqrt{2} + \sqrt{6}}{2} \right) \left\{ \frac{1}{\pi} \int_{-\nu}^{\mu-\nu} i_{l1}^s(\omega t)^2 d\omega t + \frac{1}{\pi} \int_{\mu-\nu}^{\pi/3-\nu} i_{l2}^s(\omega t)^2 d\omega t \right. \\ \left. + \frac{1}{\pi} \int_{\pi/3-\nu}^{\pi/3+\mu-\nu} i_{l3}^s(\omega t)^2 d\omega t + \frac{1}{\pi} \int_{\pi/3+\mu-\nu}^{2\pi/3-\nu} i_{l4}^s(\omega t)^2 d\omega t + \frac{1}{\pi} \int_{2\pi/3-\nu}^{2\pi/3+\mu-\nu} i_{l5}^s(\omega t)^2 d\omega t \right\}^{1/2} \quad (3.42)$$

The integrals inside the square root represent an half-cycle of one 6-pulse bridge only, whereas the factor outside the square root provides the necessary correction to take into account the contribution from both rectifiers at the primary of the transformers. Since the waveform is symmetric an half-cycle is sufficient to give the correct result for the total RMS line current.

Assuming that the bridge currents and output voltages are balanced, harmonics in the line currents will occur at the frequencies obtained from Equation 3.21. The harmonics depend on the voltage regulation and can be obtained from Equation 3.22, using the coefficients shown in Equations 3.43 and 3.44 [14].

$$a_h = \frac{2}{\pi} \int_{-\nu}^{\mu-\nu} i_{l1}^s(\omega t) \cos(h\omega t) d\omega t + \frac{2}{\pi} \int_{\mu-\nu}^{\pi/3-\nu} i_{l2}^s(\omega t) \cos(h\omega t) d\omega t \quad (3.43) \\ + \frac{2}{\pi} \int_{\pi/3-\nu}^{\pi/3+\mu-\nu} i_{l3}^s(\omega t) \cos(h\omega t) d\omega t + \frac{2}{\pi} \int_{\pi/3+\mu-\nu}^{2\pi/3-\nu} i_{l4}^s(\omega t) \cos(h\omega t) d\omega t \\ + \frac{2}{\pi} \int_{2\pi/3-\nu}^{2\pi/3+\mu-\nu} i_{l5}^s(\omega t) \cos(h\omega t) d\omega t$$

$$b_h = \frac{2}{\pi} \int_{-\nu}^{\mu-\nu} i_{l1}^s(\omega t) \sin(h\omega t) d\omega t + \frac{2}{\pi} \int_{\mu-\nu}^{\pi/3-\nu} i_{l2}^s(\omega t) \sin(h\omega t) d\omega t \quad (3.44) \\ + \frac{2}{\pi} \int_{\pi/3-\nu}^{\pi/3+\mu-\nu} i_{l3}^s(\omega t) \sin(h\omega t) d\omega t + \frac{2}{\pi} \int_{\pi/3+\mu-\nu}^{2\pi/3-\nu} i_{l4}^s(\omega t) \sin(h\omega t) d\omega t \\ + \frac{2}{\pi} \int_{2\pi/3-\nu}^{2\pi/3+\mu-\nu} i_{l5}^s(\omega t) \sin(h\omega t) d\omega t$$

Since the parameters of interest are now represented by Fourier analysis, the equations for the fundamental component of the line current, displacement power factor, and power factor can be determined by solving Equations 3.25, 3.26, and 3.27, respectively. The only change between the discontinuous and continuous cases are the Fourier coefficients.

3.3 Chopper Operation

In this section it is assumed that the chopper is supplied from an ideal ripple free voltage source. The function of the chopper is simply to control the output voltage by switching between zero and the magnitude of the uncontrolled DC input voltage. The switching frequency for an IGBT is generally in the low kHz range, and for the purpose of writing equations, it is often expressed in terms of the switching period as

$$T_s = \frac{1}{f_s} \quad (3.45)$$

Another simplification used to describe the chopper power supply is to express the ratio of time that the switch is closed to the total period defined by the switching frequency. This is referred to as the duty ratio and is provided for reference in Equation 3.46.

$$D = \frac{t_{on}}{T_s} \quad (3.46)$$

As shown in Figure 3.1 the EAF power supply consists of multiple chopper sections connected in parallel. This has several benefits for a high current power supply since it allows the ripple to be reduced without increasing the number of power electronic components. When multiple chopper sections are connected in parallel the output frequency is increased by the number of chopper sections. Hence the ripple frequency at the converter output can be expressed as

$$f_c = n f_s \quad (3.47)$$

The number and type of devices conducting in any given period depends on the duty ratio. Each T_s/n interval can be divided into two subintervals, which will be referred to as T_x and T_y and represent periods when m and $m-1$ IGBTs are conducting, respectively. The period when m IGBTs are conducting can be determined from Equation 3.48.

$$T_x = \left(D - \frac{m-1}{n} \right) T_s \quad (3.48)$$

the period when $m-1$ IGBTs are conducting can be determined from Equation 3.49,

$$T_y = \frac{T_s}{n} - T_x \quad (3.49)$$

where n is the number of chopper sections and m is an integer determined from the inequality

$$\frac{m-1}{n} < D \leq \frac{m}{n} \quad (3.50)$$

When four chopper sections are connected in parallel this results in nine modes of operation. Mode 0-0 occurs when $D = 0$ and consists of one period in which four freewheeling diodes are always conducting. Mode 0-1 occurs in the range $0 < D < 0.25$ and contains a period when four freewheeling diodes are conducting followed by a period when one IGBT and three freewheeling diodes are conducting.

Mode 1-1 occurs when $D = 0.25$ and consists of one period in which one IGBT and three freewheeling diodes are always conducting. Mode 1-2 occurs in the range $0.25 < D < 0.50$ and contains a period when one IGBT and three freewheeling diodes are conducting followed by a period when two IGBTs and two freewheeling diodes are conducting.

Mode 2-2 occurs when $D = 0.50$ and consists of one period in which two IGBTs and two freewheeling diodes are always conducting. Mode 2-3 occurs in the range $0.50 < D < 0.75$ and contains a period when two IGBTs and two freewheeling diodes are conducting followed by a period when three IGBTs and one freewheeling diode are conducting.

Mode 3-3 occurs when $D = 0.75$ and consists of one period in which three IGBTs and one freewheeling diode are always conducting. Mode 3-4 occurs in the range $0.75 < D < 1$ and contains a period when three IGBTs and one freewheeling diode are conducting followed by a period when four IGBTs are conducting.

Mode 4-4 occurs when $D = 1$ and consists of one period in which four IGBTs are always conducting. In all of the modes listed above the actual number of devices will be greater since each chopper section consists of multiple devices connected in parallel. For simplicity the descriptions have assumed that each chopper section consists of only one IGBT and one freewheeling diode.

In order to minimize losses, the power supply is operated with a duty ratio in the range $0.60 < D < 0.80$. When process changes and load fluctuations are taken into account this will dictate that the chopper power supply will generally operate in mode 2-3, mode 3-3, or mode 3-4.

3.3.1 Constant Current Load With Output Reactance

Under ideal operation it is assumed that the chopper is feeding a constant current load and is supplied from an ideal DC voltage source. Furthermore, it is assumed that each chopper section contains enough output reactance to maintain constant current output from each individual section. Although these conditions do not occur in practice, the case is beneficial to describe the basic operation of the converter and is presented in detail. Since the output current is constant it does not require analysis and therefore only the output voltage and power are analyzed.

To illustrate the operation of the chopper power supply four cases are presented in Figures 3.12-3.14. The waveforms are for a chopper power supply of the type shown in Figure 3.1 operating with a switching frequency of 2 kHz. The cases represent $D = 0.50$, $D = 0.60$, $D = 0.70$, and $D = 0.80$ and include waveforms of the output voltage (Figure 3.12), currents associated with chopper unit 1 (Figure 3.13), and currents associated with chopper unit 2 (Figure 3.14). The waveforms are plotted

over a 2 ms period and are intended to represent 1/10 of a cycle at a power system frequency of 50 Hz. All resulting waveforms are normalized using $V_c = 1pu$ and $I_d = 1pu$.

As shown in Figures 3.12-3.14 the chopper values are affected by changing the duty ratio. Expressions for the average quantities from one chopper section feeding an RL load are provided in [8] and can easily be rewritten for an n-phase chopper. With the assumptions made in this subsection the expression for the average output voltage is the same as that provided in [8] and is provided for reference in Equation 3.51.

$$V_d = \frac{t_{on}}{T_s} V_c = DV_c \quad (3.51)$$

Assuming that the output currents from each chopper section are balanced and constant, and that the output voltages from each bridge rectifier are equal and constant, harmonics in the DC output voltage will occur at multiples of the switching frequency. If there are multiple phase shifted chopper sections connected in parallel then the harmonic frequencies at the combined output will be increased by the number of sections. For an n-phase chopper this results in harmonics at the following frequencies

$$h = nk \quad (3.52)$$

where n is the number of phase shifted chopper sections and k is an integer. The magnitude of the harmonics is inversely proportional to their harmonic number and depends on the duty ratio. An expression for the harmonic magnitudes from a single phase chopper section is provided in [30]. This equation has been rewritten for an n-phase chopper as a function of the duty ratio and is provided for reference in Equation 3.53.

$$V_h = \frac{\sqrt{2}V_c}{\pi nh} [1 - \cos(2\pi nhD)]^{1/2} \quad (3.53)$$

where V_c is the average input voltage and h is a value obtained from Equation 3.52.

Since the output current is assumed to be constant, the average power drawn by

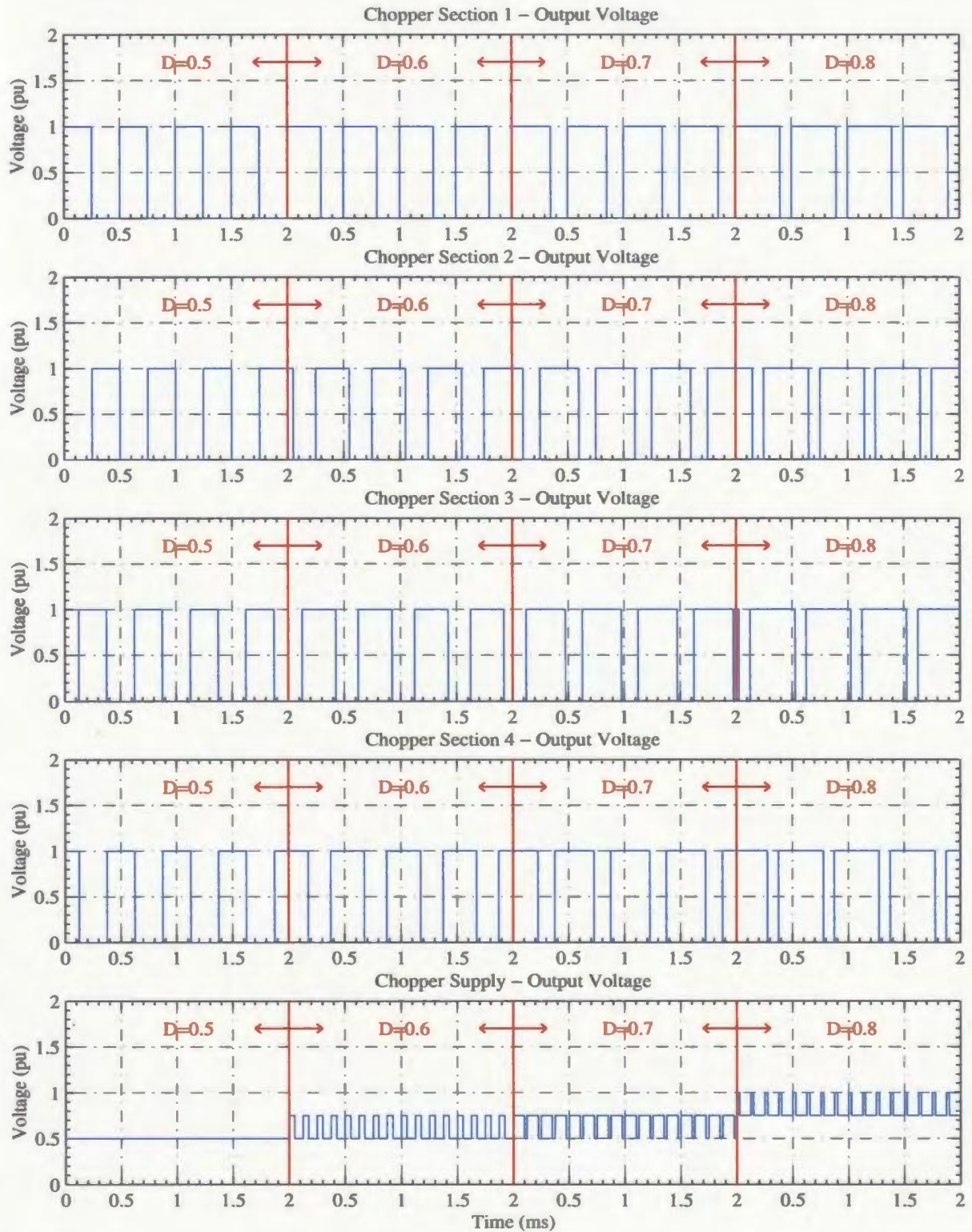


Figure 3.12: Chopper Output Voltages

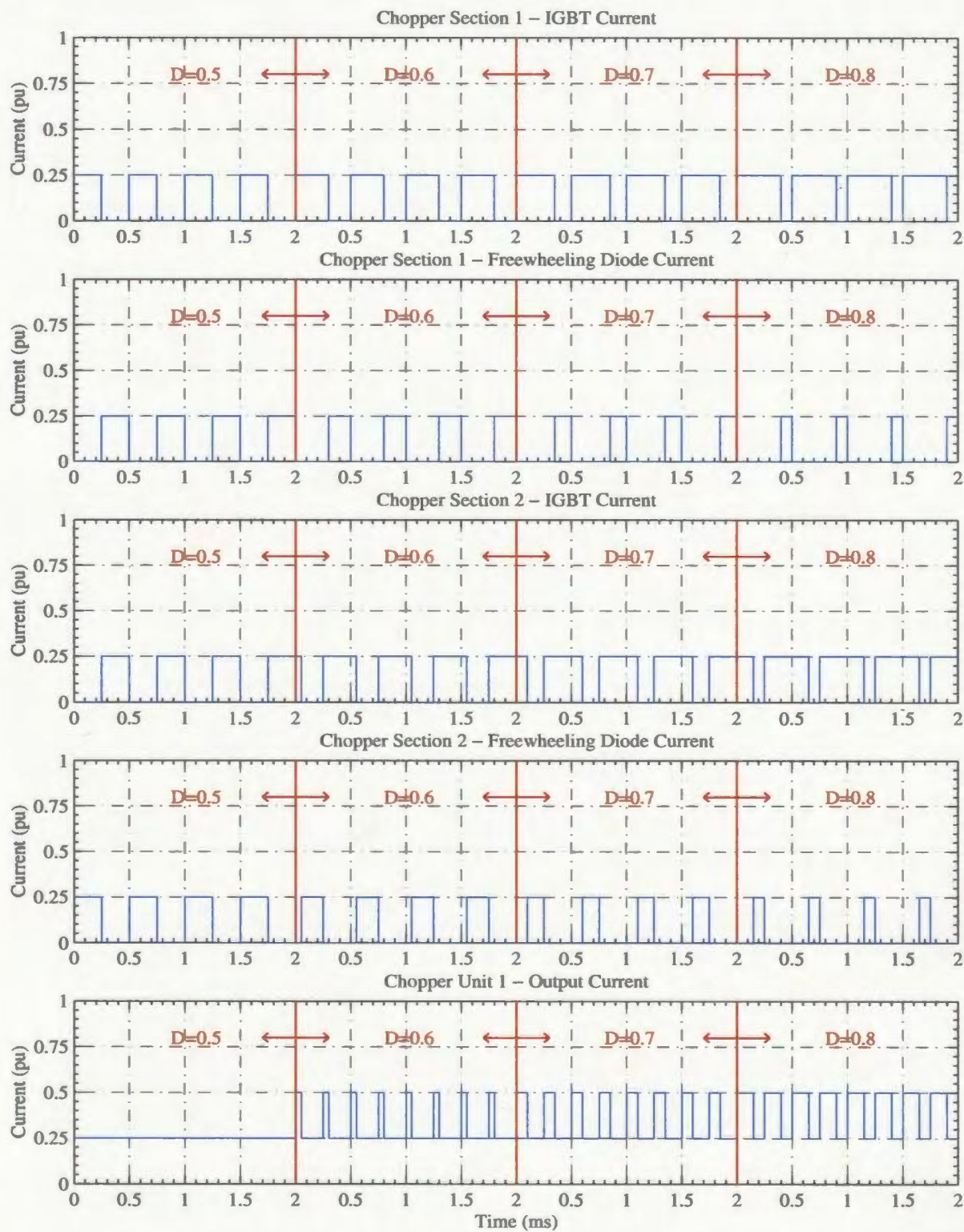


Figure 3.13: Chopper Unit 1 Currents

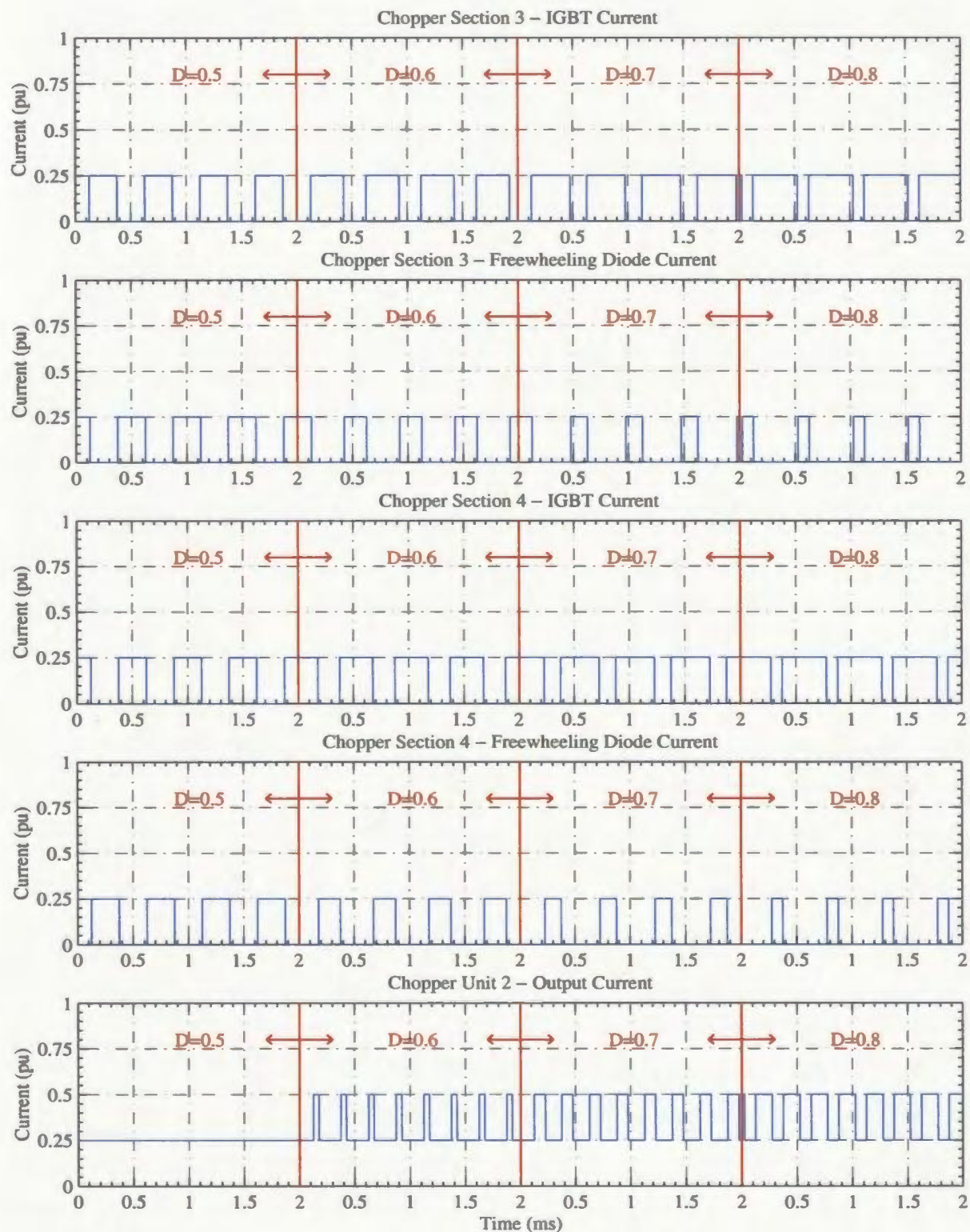


Figure 3.14: Chopper Unit 2 Currents

the converter can be expressed as

$$P = V_d I_d = D V_c I_d \quad (3.54)$$

In actual fact the output current will not be constant nor will the output voltage be a square wave. however, this approximation is valid when describing the operation of the converter.

3.3.2 Normal Operation

Under normal operation the converter will not operate with a constant current load, the DC link voltage will not be constant, the power system will not provide an ideal sinusoidal voltage waveform, balanced between the phases, nor will the components used in the power supply be perfectly matched. Each of these system parameters will cause deviations from the ideal analysis presented in this chapter. In addition, controller imperfections will also cause further deviations from the ideal case.

The arc will randomly change in length at various frequencies and cause non-characteristic voltage harmonics to be produced at the load, which cause distortion on the AC system. This distortion can be at any frequency and as such will causes interharmonic distortion, as well as harmonic distortion. If the DC link were ideal this fluctuation would not be transferred to the AC system. Since the DC link is not ideal some effects of the load fluctuation will be observed, however, not to the same degree as in the controlled rectifier case.

Any unbalance in the supply voltages will cause asymmetries that lead to an increase in the levels of triplen harmonics, particularly those of the third order [13]. Impedance imbalance between both 6-pulse groups will result in non-characteristic harmonics at orders $6k \pm 1$. If the diodes in the positive and negative valve groups begin to conduct at slightly different offsets from the intended firing angle then even order harmonics will be produced on the AC system [13]. The magnitude of these even order harmonics will be decreased as the commutation overlap angle is increased.

The deviations from the ideal case change the expected relationship between the duty ratio and the output parameters. As such the control system must be robust enough to operate under the various conditions and still effectively maintain the desired setpoint at the output. This is generally achieved by using a controller with a feedback loop.

3.4 Converter Control

As illustrated in the previous section the output from the chopper power supply is controlled by changing the duty ratio or on time. The output as a function of the duty ratio is nearly linear and as such no linearization of the controller will be required.

In order to maintain a constant setpoint the chopper power supply uses a feedback PI controller. Unlike the controlled rectifier power supply the output from each bridge circuit is independently controlled to deliver the required total current or power to the furnace. This requires one controller for each chopper unit. Since each unit contains two sections a balancing loop must also be included. Under normal operating conditions each chopper unit is set to share the load equally. In the case of power control a current limit is included to protect the equipment from additional stresses without tripping the protection relays.

Typical control block diagrams for constant current control, constant power control, and constant power control with current limit are presented in this section. Controller response to a change in setpoint is also provided for a constant resistive load scaled to provide typical current and power levels associated with the operation of a 50 MW smelting furnace. For the purpose of this chapter the load is set to $14m\Omega$ and the transformer secondary voltages are set to 1080 V.

Transient response for both current control and power control are investigated by applying a $\pm 10\%$ step change in setpoint and measuring the transient response

parameters. Parameters are recorded for both increasing setpoints and decreasing setpoints to show controller linearity. The current limiting function within the power controller is shown to function properly by applying a slowly varying power setpoint which results in currents above the set limit.

3.4.1 Constant Current Control

Constant current control is implemented using the control configuration outlined in Figure 3.15. The process variables include the output current from each chopper section, which are filtered using a first order low-pass filter with a gain of 1 and a time constant of 0.2 ms. The current regulator was tuned using the stability limit method and has a proportional gain of 10 and an integral time constant of 0.14 ms. The balance regulator was set to have the same proportional gain as the current regulator and an integral time constant of 3 ms to avoid interaction between the two control loops.

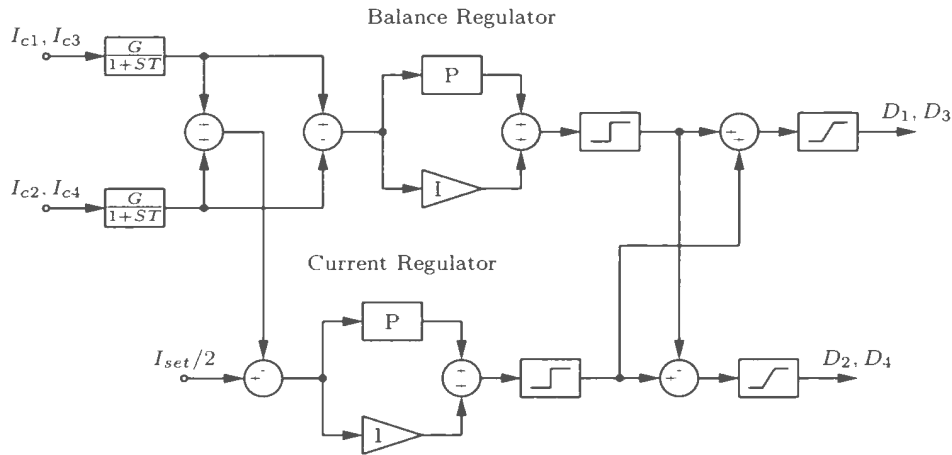


Figure 3.15: Chopper Current Control Block Diagram

Although a slew rate limit is shown on both control signals it was determined through simulation that it was not required for the current controller. Instead, only a hard limit of 0 to 1 was implemented at the output of the controller and represents the control range of the chopper. Another hard limit of 0 to 1 was also included at the output of each regulator.

The transient response for the current controller shown in Figure 3.15 is provided for reference in Figure 3.16. The nominal output current was chosen as 60 kA and the setpoints were switched between 54 kA to 66 kA then back again. For the positive step change the delay time and rise time were 0.575 ms and 1.075 ms, respectively. The maximum overshoot was 1.155 kA corresponding to 1.75% and occurred at 1.45 ms after the step change. The settling time based on a 2% tolerance band was not exceeded.

For the negative step change the delay time and rise time were 0.375 ms and 0.775 ms, respectively. The maximum overshoot was 0.733 kA corresponding to 1.36% and occurred at 1.1 ms after the step change. The settling time based on a 2% tolerance band was not exceeded. The maximum overshoots for the positive and negative step changes are slightly different which indicate that the controller is not perfectly linear, however, the difference is less than 500 A.

3.4.2 Constant Power Control

Constant power control is implemented using the control configuration outlined in Figure 3.17. The process parameters include the output current from each chopper section and the output voltage, which are filtered using a first order low-pass filter with a gain of 1 and a time constant of 0.2 ms. The power regulator was tuned using the stability limit method and has a proportional gain of 7.5 and an integral time constant of 0.3 ms. The balance regulator was set as in the previous section.

A slew rate limit is shown on both control signals and is required to prevent sudden changes in the control variable. The slew rate limit functions to stabilize the

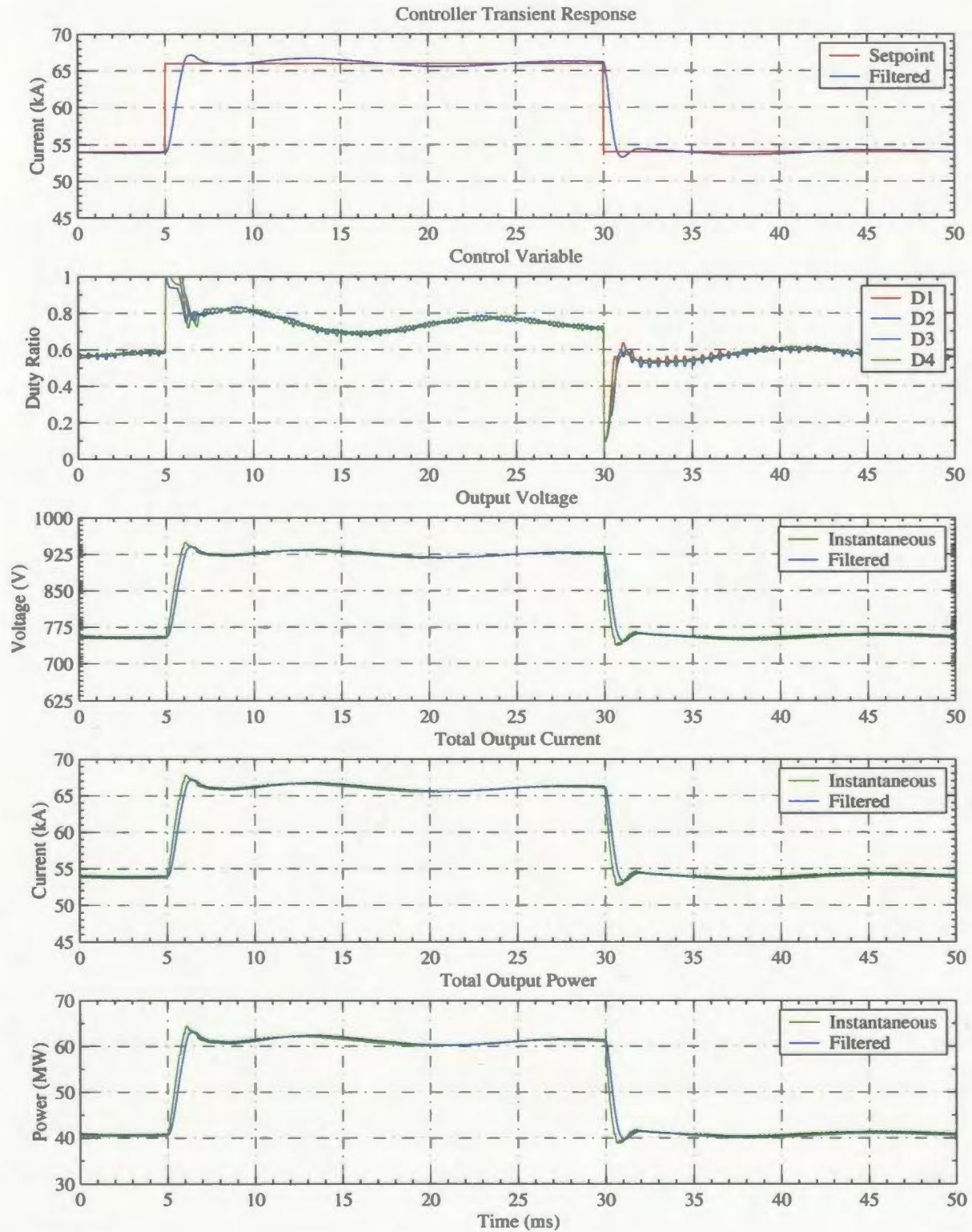


Figure 3.16: Chopper Current Control (Step Response)

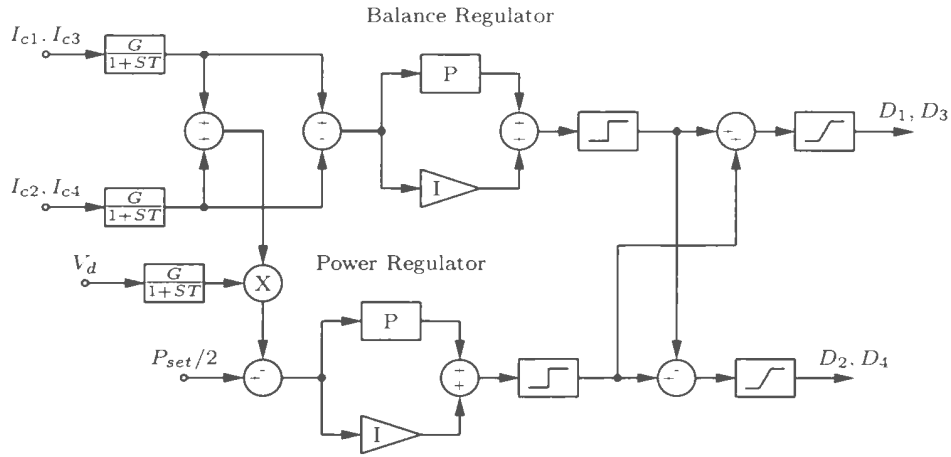


Figure 3.17: Chopper Power Control Block Diagram

controller during large disturbances and for the purpose of this study was chosen as 500/cycle. A hard limit of 0 to 1 was also implemented at the output of the controller and represents the control range of the chopper. Another hard limit of 0 to 1 was used at the output of each regulator.

The transient response for the power controller shown in Figure 3.17 is provided for reference in Figure 3.18. The nominal output power was chosen as 50 MW and the setpoints were switched between 45 MW to 55 MW then back again. For the positive step change the delay time and rise time were 0.65 ms and 1.0 ms, respectively. The maximum overshoot was 1.252 MW corresponding to 2.28% and occurred at 1.325 ms after the step change. The settling time based on a 2% tolerance band was 1.45 ms.

For the negative step change the delay time and rise time were 0.625 ms and 0.975 ms, respectively. The maximum overshoot was 1.269 MW corresponding to 2.82% and occurred at 1.25 ms after the step change. The settling time based on a 2% tolerance band was 1.5 ms. The maximum overshoots for the positive and negative step changes are slightly different which indicate that the controller is not perfectly linear, however, the difference is less than 275 kW.

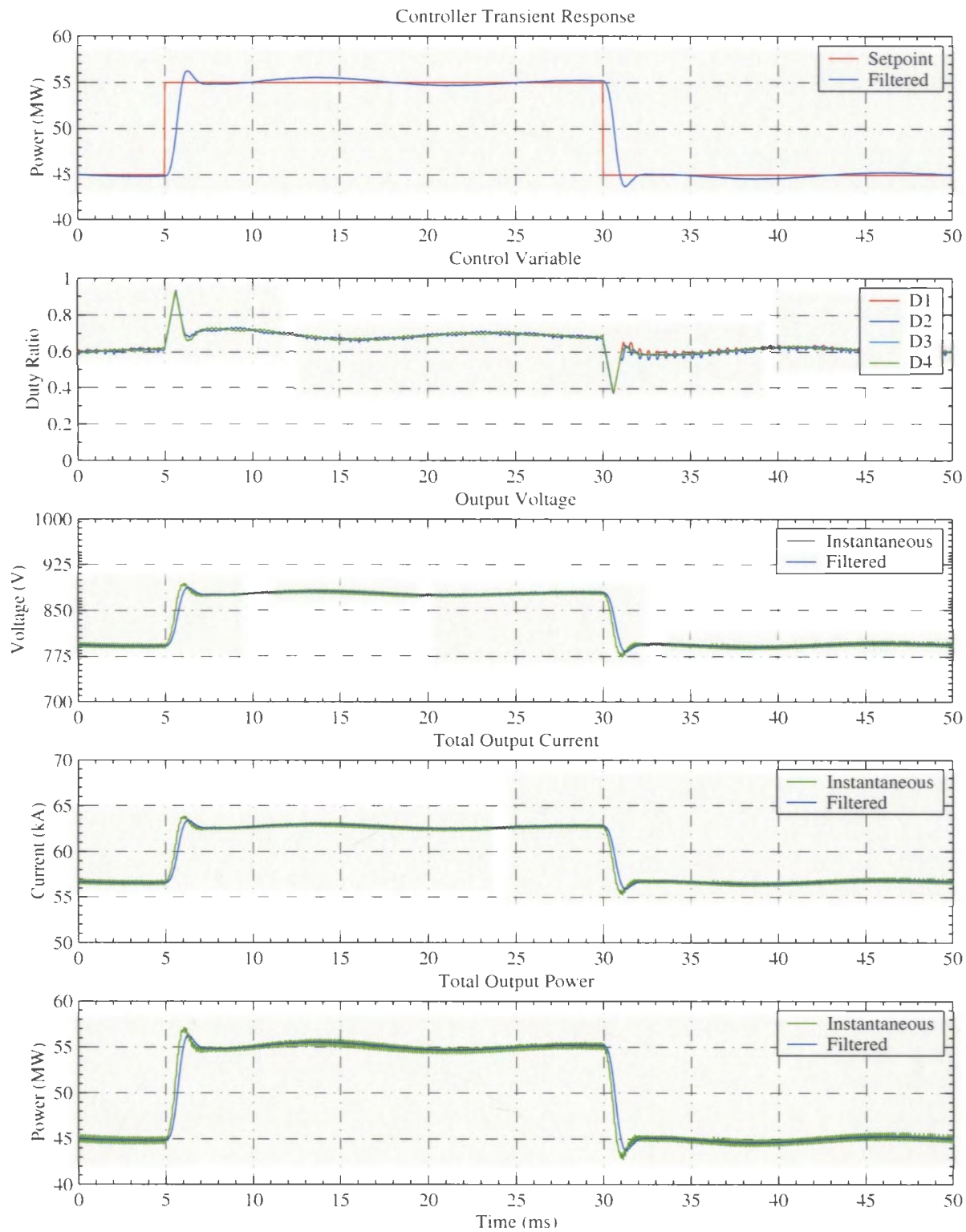


Figure 3.18: Chopper Power Control (Step Response)

3.4.3 Constant Power Control With Current Limit

Normally when constant power control is used a current limit is also imposed to keep within the equipment ratings. The control configuration chosen for power control with current limit is provided for reference in Figure 3.19 and is a combination of the first two configurations. The proportional gains and integral time constants in the power regulator, current regulator, and balance regulator are the same as those previously specified. The slew rate limit was set as in the power controller.

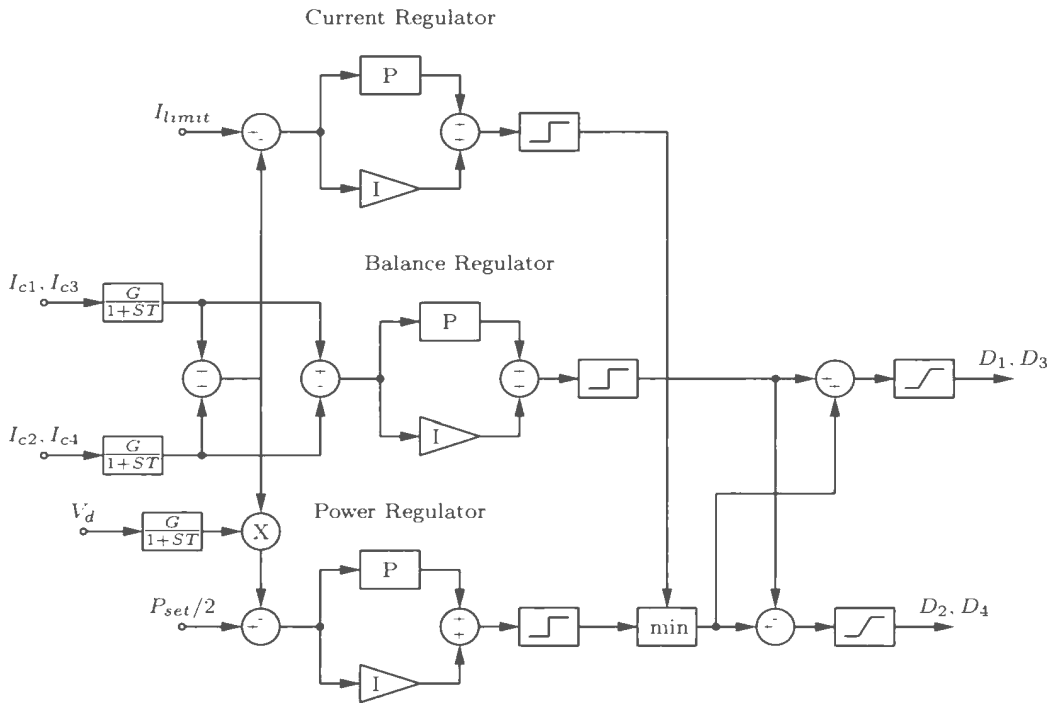


Figure 3.19: Chopper Power Control with Current Limit Block Diagram

To verify that the current limit functions correctly the power setpoint was slowly varied between 45 MW and 55 MW with a current limit of 60 kA. The results are presented in Figure 3.20 and clearly show the current being limited to 60 kA. It can also be observed that power control is lost when the converter operates in current limiting mode. As with the controlled rectifier power control is most often used during normal operation since smelting is a continuous process which relies on a constant power to feed ratio [74].

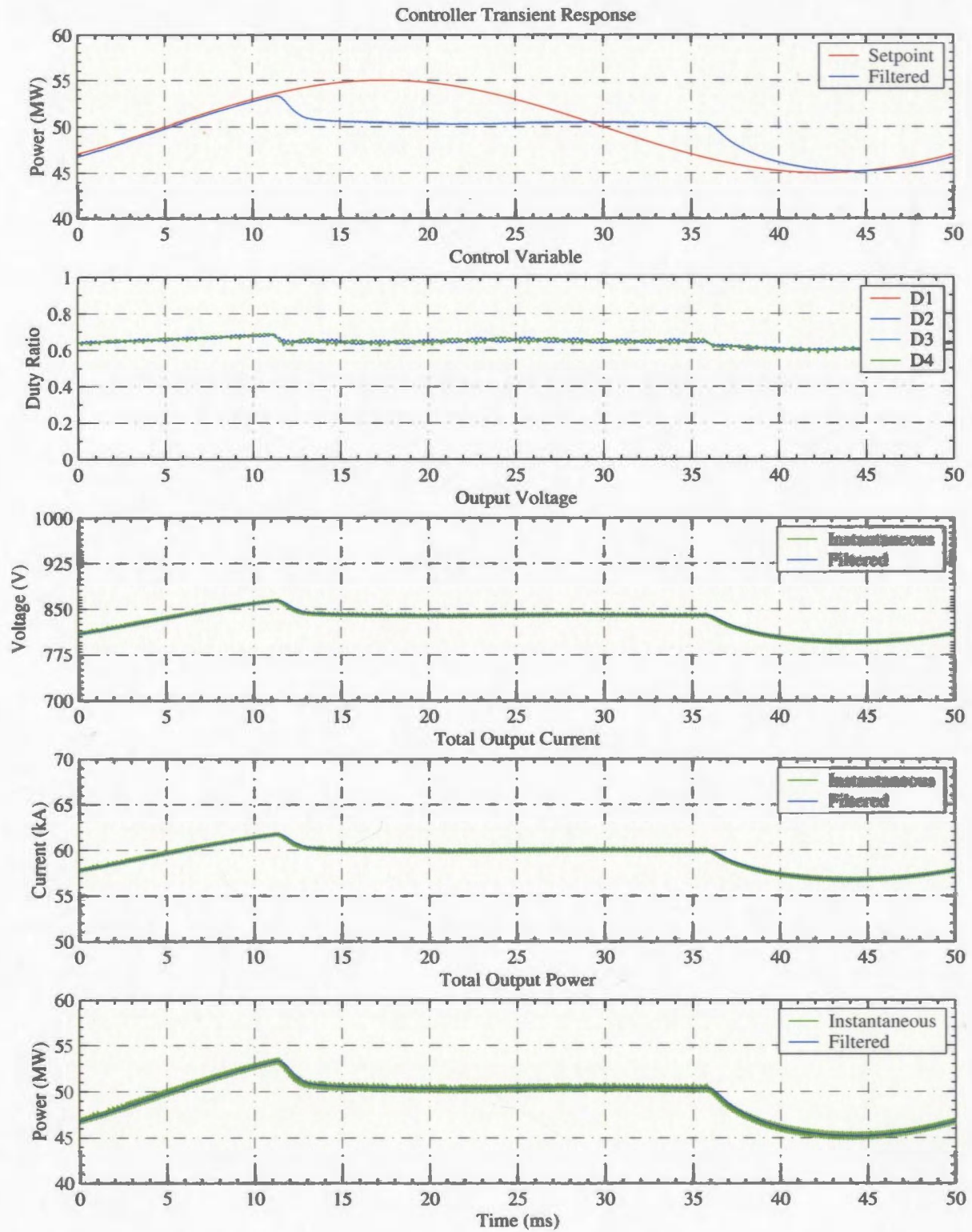


Figure 3.20: Chopper Current Limited Power Control (Setpoint Tracking)

3.5 Summary

A description of the configuration and operation of the uncontrolled rectifier chopper power supply has been presented in this chapter. The converter has been mainly implemented in low power motor drives. However, some high power applications have been constructed and include chemical refining processes, and one low power electric smelting furnace. Generally for high current operation the converter is arranged with a 12-pulse rectifier at the front end, feeding multiple chopper sections connected in parallel. Each chopper section consists of multiple chopper modules connected in parallel to meet the current requirements.

Due to the additional power conversion stage the uncontrolled rectifier chopper power supply contains more components than an equivalent controlled rectifier power supply. This represents the major drawback of the technology since more devices generally tend to increase the losses and decrease the reliability of the converter. The benefits in the technology include reduced harmonics and increased power factor at the input, and faster control and less ripple at the output. The improved input parameters allow smaller transformers to be used while the improved output parameters allow smaller reactors to be used. The control is nearly linear over a large range and eliminates the need for tap changers on the transformers.

Equations for the uncontrolled rectifiers were provided for the ideal case of constant output voltage with both discontinuous and continuous current conduction. The analysis focused on the line current magnitude and harmonics, power and power factor. The parameters were shown to be dependent on voltage regulation.

Equations for the chopper sections were provided for the ideal case of a constant voltage supply and a constant current load. The analysis focused on the output voltage magnitude and harmonics. The output parameters were shown to be dependent on the duty ratio. Unlike the controlled rectifier case the output parameters were nearly linear functions of the control variable.

Converter control for both constant current and constant power was described

and shown to function properly during transient disturbances. The responses to a positive step change and a negative step change in setpoint were slightly different indicating that a degree of nonlinearity exist. However, the differences were small and acceptable for the required application. The power controller was also shown with a current limit, which represents the actual case and was shown to function correctly. A balance regulator was included in each configuration to ensure that both chopper sections from each bridge rectifier share the output current equally.

The performance of the uncontrolled rectifier presented in this chapter can be improved by increasing the pulse number or by adding filter capacity. The pulse number can be increased by adding bridge circuits and using transformers that provide the required phase shift. This will effectively reduce the harmonics at the input, however, it is not usually employed due to additional transformer requirements. In the case of the uncontrolled rectifier filtering is normally added at the output to reduce the ripple in the output voltage. The performance of the chopper is normally improved by increasing the switching frequency. This can be achieved by actually increasing the frequency or by adding more phase shifted sections.

Chapter 4

DC Electric Arc Furnace Model

The majority of electric arc furnace models have been developed for AC furnaces to investigate the effects of various compensation schemes on voltage flicker and harmonic distortion. Since very little work has been done on DC arc furnace models the physical DC arc will be modeled first then fluctuation added to represent a typical DC smelting furnace. Although simplified DC arc models are available in the literature, most of these use approximations that are not valid for high current arcs.

The available arc models are generally of two types which include the Magneto Fluid Dynamic Model (MFD) [52–61], and the Channel Arc Model (CAM) [62–67]. The MFD model generally solves a set of coupled partial differential equations for the conservation of mass, momentum and energy. The procedure can become quite complicated, but some simplified 2D models considering arcs dominated by one heat loss mechanism are available. The MFD model uses fixed boundary conditions to solve for the spatial distribution of arc parameters and as such is not well suited for electric arc furnace simulation.

The CAM model assumes that the arc is a cylindrical homogeneous current conductor surrounded by an insulating shell. The energy balance equations are solved using thermodynamic and transport properties from a typical arc furnace plasma taking into account the heat loss mechanisms from convection, conduction, and radi-

ation. For the purpose of this report the CAM model will be used since the equations are more easily solved and the model has been proven to represent an EAF arc.

In addition to the static electric arc the smelting furnace dynamics and operating conditions must be included in the simulation. The arc dynamics are a result of process conditions such as feeding and tapping which tend to add instabilities to the arc. Unlike a melting furnace a large portion of the energy in a smelting furnace is dissipated in the slag layer. This tends to make the operation more stable and will be included in the simulation by adding a fixed resistance to the load.

The purpose of this chapter is to develop an electric arc model that can be used to represent an electric arc furnace load within a time domain simulation environment. As such the approach is simplified and does not go into great detail of the underlying arc physics. The dynamics of a typical smelting furnace are added to the arc model to ensure that the load is as realistic as possible. The model is verified using measured data from several electric arc furnace installations.

4.1 Electric Arc Properties

An electric arc consists of current flowing in an ionized gas between two electrodes at different potentials. The negative electrode is known as the cathode whereas the positive electrode is known as the anode. In general the arc is divided into three regions including the anode region, cathode region, and the arc column. A typical arc profile showing each region along with the voltage gradient characteristic is shown in Figure 4.1 [51]. The figure is a schematic only and is not drawn to scale.

In the cathode region there is a constant voltage drop of approximately 10 V ranging over a distance of approximately $1\text{ }\mu\text{m}$ [51]. The voltage drop is constant and not dependent on arc length. The voltage drop in the anode region is two to three times higher than that in the cathode region and is caused by secondary emission due to the heavy bombardment of electrons. Voltage drop in the anode region is also

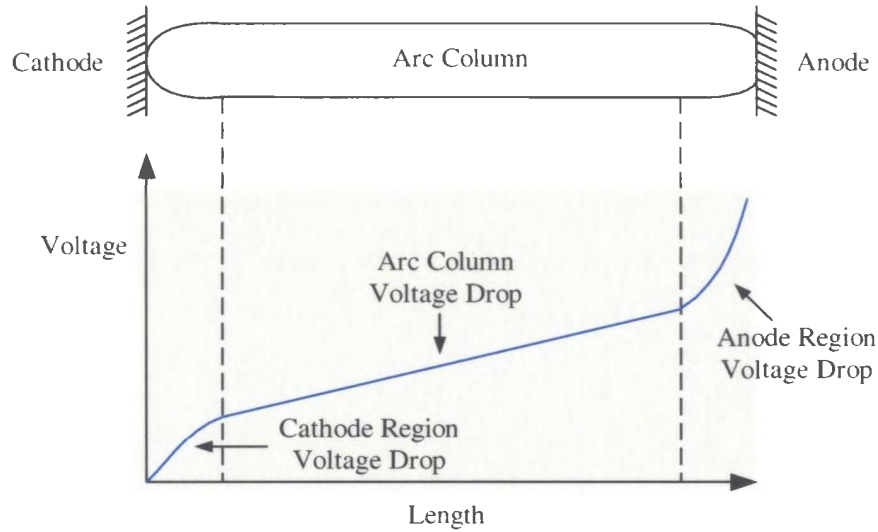


Figure 4.1: Simplified Schematic Diagram of Arc Profile

constant and not dependent on arc length.

The voltage drop in the arc column depends on several factors including the arc length and is generally in the range of 10 V/cm to 15 V/cm. This is an approximation used in industry and the actual arc length varies as a function of current, temperature, and the arc environment. Measurements from high current DC arc furnaces show that the arc voltage initially increases rapidly with length then tends toward a steady slope in the range of 7.5 V/cm. It is also observed that the whole curve moves to higher voltages at higher current levels [70].

Information relating to the arc environment is not readily available in the literature. However, two sources [67,68] of information were obtained. Both sources contain data for typical EAF gas with Fe ions and without Fe ions. The composition with Fe ions included 40% H_2 , 35% N_2 , 20% CO , and 5% Fe . The composition without Fe ions included 42% H_2 , 37% N_2 , and 21% CO . For the purpose of this section both cases are presented to show the effect of changing the arc composition on the thermodynamic and transport properties.

The Chapman and Euskog method was used in [68] to determine the electrical

conductivity, thermal conductivity, viscosity, and reduced specific heat for the two gas mixtures. The results were presented graphically for the temperature range between 1000 K to 25000 K. The same temperature range was used in [67] to show the electrical conductivity, density, enthalpy, and volumetric radiation density in tabular form. Since neither source provided equations, the parameters required for the CAM model are obtained from data fit of the given information and are presented for future reference.

The thermodynamic and transport properties of the electric arc are temperature dependent and can be represented by an exponential polynomial

$$\chi(T) = e^{(A_1 T^{10} + A_2 T^9 + A_3 T^8 + A_4 T^7 + A_5 T^6 + A_6 T^5 + A_7 T^4 + A_8 T^3 + A_9 T^2 + A_{10} T + A_{11})} \quad (4.1)$$

or a polynomial

$$\begin{aligned} \chi(T) = B_1 T^{10} + B_2 T^9 + B_3 T^8 + B_4 T^7 + B_5 T^6 + B_6 T^5 + B_7 T^4 + B_8 T^3 \\ + B_9 T^2 + B_{10} T + B_{11} \end{aligned} \quad (4.2)$$

where χ can represent the electrical conductivity, thermal conductivity, enthalpy, density or radiation density. The coefficients are presented in the following section, which describes the relevant portions of the CAM model.

4.2 Channel Arc Model

The channel arc model was developed by Steenbeck to solve the energy balance equations by introducing an extra variable, arc radius. The model assumes that the arc column consists of a central core that conducts current surrounded by an insulating shell [62]. A schematic diagram depicting the CAM model is provided for reference in Figure 4.2. The core is identified by zone I, which has a temperature dependent electrical conductivity and an infinite thermal conductivity. The shell is identified by zone II, which has a temperature dependent thermal conductivity and an electrical conductivity of zero.

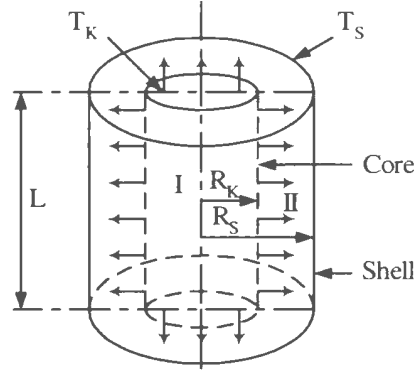


Figure 4.2: Channel Arc Model

The radial distributions of parameters within the arc are completely neglected, as are the gravity and viscous dissipation effects. The model also makes several other assumptions including the fact that the arc is in local thermodynamic equilibrium, the arc consists of an incompressible fluid, and the arc acts as a homogeneous current conductor [67]. While these approximations may appear to be significant the results are appropriate for the type of simulations performed in this study.

The CAM model is described in [62,63] and considers all heat loss mechanisms from the arc. The heat loss components are then balanced against the electrical energy input as shown

$$P_{el}(T_k, R_k) = P_{cond}(T_k, R_k) + P_{conv}(T_k, R_k) + P_{rad}(T_k, R_k) \quad (4.3)$$

where P_{el} is the electrical energy input, P_{cond} is the conduction heat transfer, P_{conv} is the convection heat transfer, and P_{rad} is the radiation heat transfer. The model parameters in Equation 4.3 are all functions of the arc core radius and temperature, which are not known and must be solved using Steenbeck's Minimum Principle.

The Minimum Principle states that the arc will always assume a radius and temperature that minimizes power loss [63]. The approach to solve for these parameters is to use Equation 4.3 to obtain an expression for the arc temperature in terms of the arc radius

$$T_k = f(R_k) \quad (4.4)$$

Equation 4.4 is then solved to determine the arc core radius and temperature that results in minimum power loss. Inputs to the model include the arc length and current, as well as several boundary conditions, which are required in the heat transfer expressions. The heat transfer equations and boundary conditions are described in the following sections and have been confirmed to accurately represent the arc in a DC EAF [64,65] and an AC EAF [66].

4.2.1 Electrical Energy Input

The electrical energy input to the arc can be expressed by summing up the various components of voltage drop and multiplying by the arc current. A simple expression for electrical energy input power is provided below in Equation 4.5.

$$P_{el} = I_{arc}(V_{arc} + V_{cathode} + V_{anode}) \quad (4.5)$$

The voltage drop in the anode and cathode regions have been given in the previous section as 30 V and 10 V, respectively. The voltage drop in the arc column will depend on the arc geometry and temperature. Since the arc geometry is known the arc resistance can be solved for using the following equation

$$R_{arc} = \frac{L}{\sigma(T_k)\pi R_k^2} \quad (4.6)$$

where $\sigma(T_k)$ is the temperature dependent electrical conductivity. With R_{arc} determined from Equation 4.6 the electrical energy input can be rewritten as

$$P_{el} = \frac{I_{arc}^2 L}{\sigma(T_k)\pi R_k^2} + I_{arc}(V_{cathode} + V_{anode}) \quad (4.7)$$

The temperature dependent electrical conductivity has been determined for various compositions of EAF gas and are provided in Figure 4.3. The curves were data fit from results presented in [68] using Equation 4.1 and the coefficients listed in Table 4.1. The iron atoms begin to ionize at about 3000 K and are shown to have a strong effect on the electrical conductivity. At temperatures above 12000 K the ionization is complete and it makes no appreciable contribution to the electrical conductivity [68].

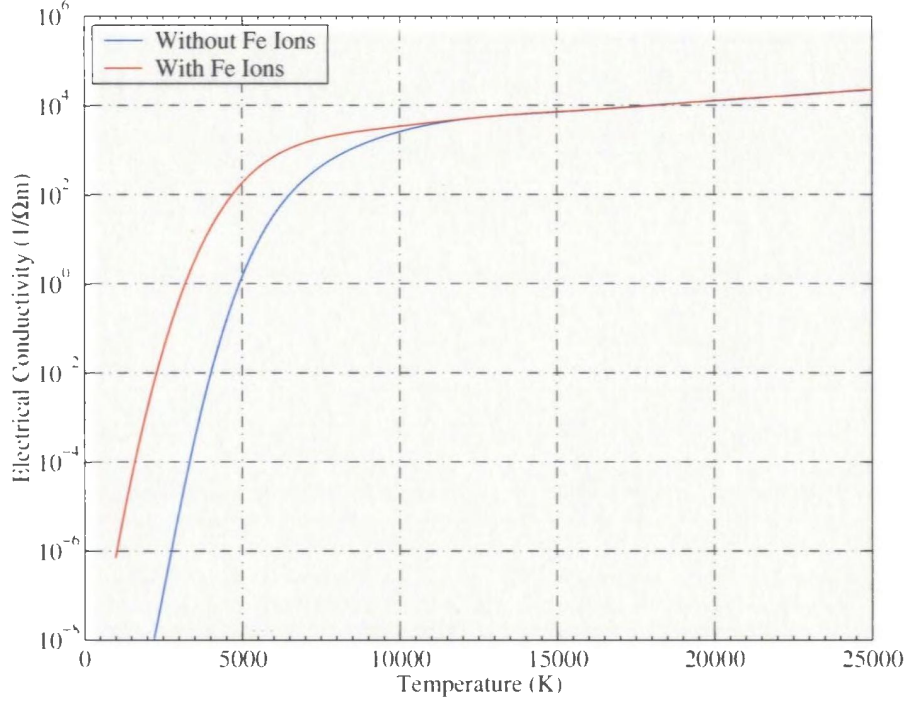


Figure 4.3: EAF Plasma Electrical Conductivity

Table 4.1: Electrical Conductivity Coefficients (1000 K - 25000 K)

Coefficient	Without Fe Ions	With Fe Ions
A_1	$6.291071095184890e^{-10}$	$-1.322903377559916e^{-10}$
A_2	$-9.379623657974799e^{-35}$	$1.573144301574714e^{-35}$
A_3	$6.102595842167776e^{-30}$	$-7.645107553502754e^{-31}$
A_4	$-2.271741090894631e^{-25}$	$1.907544342304147e^{-26}$
A_5	$5.327505931651883e^{-21}$	$-2.423359180639838e^{-22}$
A_6	$-8.156295068986779e^{-17}$	$1.044286639719308e^{-18}$
A_7	$8.145478698227270e^{-13}$	$6.838560410654266e^{-15}$
A_8	$-5.102443056421676e^{-9}$	$-2.711767421879246e^{-11}$
A_9	$1.790118197171750e^{-5}$	$-1.105743419138670e^{-6}$
A_{10}	$-2.325360164419588e^{-2}$	$1.107398973142712e^{-2}$
A_{11}	$-1.500010873131575e^1$	$-2.411856018695952e^1$

4.2.2 Conduction Heat Transfer

Conduction heat transfer has been described in the literature using three components to represent heat loss from the arc core to the furnace surroundings, at the arc cathode boundary, and at the arc anode boundary. An expression for conduction heat transfer is presented below in Equation 4.8 [62].

$$P_{cond} = \frac{2\pi L}{\ln(R_f/R_k)} k(T_k - T_s) + 2\pi R_k k(T_k - T_c) + 2\pi R_a k(T_k - T_a) \quad (4.8)$$

Where T_s is the temperature inside the furnace, T_a is the temperature at the anode, T_c is the temperature at the cathode, and $k(T)$ is the temperature dependent thermal conductivity, which has been determined for various compositions of EAF gas and is provided in Figure 4.4. The curves were data fit from results presented in [68] using Equation 4.2 and the coefficients listed in Tables 4.2-4.5. The characteristic peaks are due to the dissociation and ionization of the molecular species in the gas mixture [68].

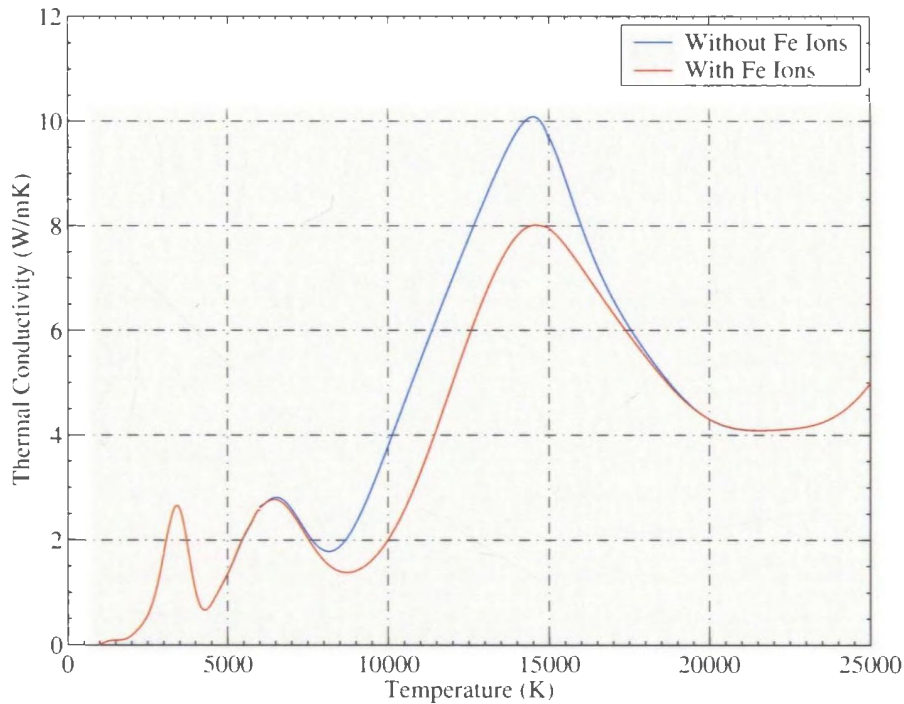


Figure 4.4: EAF Plasma Thermal Conductivity

Table 4.2: Thermal Conductivity Coefficients (1000 K - 3000 K)

Coefficient	Without Fe Ions	With Fe Ions
B_1	$-1.367775042752669e^{-31}$	$-1.367775042752669e^{-31}$
B_2	$3.229218330353735e^{-27}$	$3.229218330353735e^{-27}$
B_3	$-3.335631127656665e^{-23}$	$-3.335631127656665e^{-23}$
B_4	$1.983233989957722e^{-19}$	$1.983233989957722e^{-19}$
B_5	$-7.511006385410579e^{-16}$	$-7.511006385410579e^{-16}$
B_6	$1.892520981066090e^{-12}$	$1.892520981066090e^{-12}$
B_7	$-3.212438047397192e^{-9}$	$-3.212438047397192e^{-9}$
B_8	$3.628392737022597e^{-6}$	$3.628392737022597e^{-6}$
B_9	$-2.612189145901866e^{-3}$	$-2.612189145901866e^{-3}$
B_{10}	$1.084344584849629e^0$	$1.084344584849629e^0$
B_{11}	$-1.975881752101759e^2$	$-1.975881752101759e^2$

Table 4.3: Thermal Conductivity Coefficients (3000 K - 6000 K)

Coefficient	Without Fe Ions	With Fe Ions
B_1	$-2.933792120330923e^{-31}$	$-2.920215442927064e^{-31}$
B_2	$1.325861371117269e^{-26}$	$1.319740017313278e^{-26}$
B_3	$-2.677158475047245e^{-22}$	$-2.664829251574855e^{-22}$
B_4	$3.179627042607236e^{-18}$	$3.165021795862304e^{-18}$
B_5	$-2.459198081596151e^{-14}$	$-2.447931293873563e^{-14}$
B_6	$1.293837858040762e^{-10}$	$1.287924687469999e^{-10}$
B_7	$-4.688324711255232e^{-7}$	$-4.666944044184314e^{-7}$
B_8	$1.155086932994260e^{-3}$	$1.149828131702318e^{-3}$
B_9	$-1.851480821771029e^0$	$-1.843060230756409e^0$
B_{10}	$1.743280527363543e^3$	$1.735353782589564e^3$
B_{11}	$-7.321416032941688e^5$	$-7.288101258498075e^5$

Table 4.4: Thermal Conductivity Coefficients (6000 K - 15000 K)

Coefficient	Without Fe Ions	With Fe Ions
B_1	$2.714674342112901e^{-36}$	$2.744202929441881e^{-36}$
B_2	$-2.982909815485392e^{-31}$	$-2.924646246269500e^{-31}$
B_3	$1.460397202870464e^{-26}$	$1.388880859389802e^{-26}$
B_4	$-4.193250080634256e^{-22}$	$-3.868385466277625e^{-22}$
B_5	$7.815182175046335e^{-18}$	$6.994641310200328e^{-18}$
B_6	$-9.872010646239327e^{-14}$	$-8.574664592940041e^{-14}$
B_7	$8.552470983625764e^{-10}$	$7.213199132934136e^{-10}$
B_8	$-5.013148401720624e^{-6}$	$-4.108834531161205e^{-6}$
B_9	$1.900999519676746e^{-2}$	$1.515635333229521e^{-2}$
B_{10}	$-4.207369876250774e^1$	$-3.266662959372587e^1$
B_{11}	$4.124426686251461e^4$	$3.121885878531223e^4$

Table 4.5: Thermal Conductivity Coefficients (15000 K - 25000 K)

Coefficient	Without Fe Ions	With Fe Ions
B_1	$1.891344462833925e^{-37}$	$2.135730470225567e^{-37}$
B_2	$-3.677025423290970e^{-32}$	$-4.249746775995341e^{-32}$
B_3	$3.190908958241452e^{-27}$	$3.785560915903379e^{-27}$
B_4	$-1.626624924100612e^{-22}$	$-1.987660721473948e^{-22}$
B_5	$5.390123004312659e^{-18}$	$6.811870362957463e^{-18}$
B_6	$-1.212062877004621e^{-13}$	$-1.591966657246615e^{-13}$
B_7	$1.870995901478367e^{-9}$	$2.569209290464814e^{-9}$
B_8	$-1.954930153685145e^{-5}$	$-2.827029006814362e^{-5}$
B_9	$1.320769765169741e^{-1}$	$2.029617014896759e^{-1}$
B_{10}	$-5.197308588252898e^2$	$-8.584168797215114e^2$
B_{11}	9.015016858756094^5	$1.624050853902543e^6$

4.2.3 Convection Heat Transfer

The convection heat transfer is the dominant heat loss mechanism and can be represented by the following equation [66]

$$P_{conv} = \pi R_k^2 \rho(T_k) \overline{V}_k [h(T_k) - h(T_s)] \quad (4.9)$$

where V_k is the velocity of the arc column, $\rho(T)$ is the temperature dependent density, and $h(T)$ is the temperature dependent enthalpy. An expression for the velocity is provided in [66] and is rewritten below in Equation 4.10,

$$\overline{V}_k = \frac{I_{arc}}{2\pi R_k} \sqrt{\frac{5\mu_0}{6\rho(T_k)} \left(\frac{R_k^2}{R_c^2} - 1 \right)} \quad (4.10)$$

where R_c is the radius of the cathode spot. Since this quantity is not known it is replaced with the current density at the cathode spot, which has been observed to be nearly constant and equal to 3.5 kA/cm^2 [70].

$$\overline{V}_k = \frac{I_{arc}}{2\pi R_k} \sqrt{\frac{5\mu_0}{6\rho(T_k)} \left(\frac{\pi J_c R_k^2}{I_{arc}} - 1 \right)} \quad (4.11)$$

The increased velocity is due to the magnetic pinch force at the cathode spot. The magnetic field and hence velocity is proportional to the arc current and as the current increases so does the velocity and the proportion of heat loss due to convection [52]. At very low currents the heat transfer from the arc is dominated by conduction. However, this will not occur in an EAF arc due to the fact that the current is generally in the kA range.

The temperature dependent density and enthalpy are determined for various compositions of EAF gas and are provided in Figures 4.5 and 4.6, respectively. The curves were data fit from results presented in [67] using Equation 4.2 and the coefficients listed in Tables 4.6 and 4.7, respectively. The figures show that the iron has the effect of slightly increasing the density and decreasing the enthalpy over the entire temperature range.

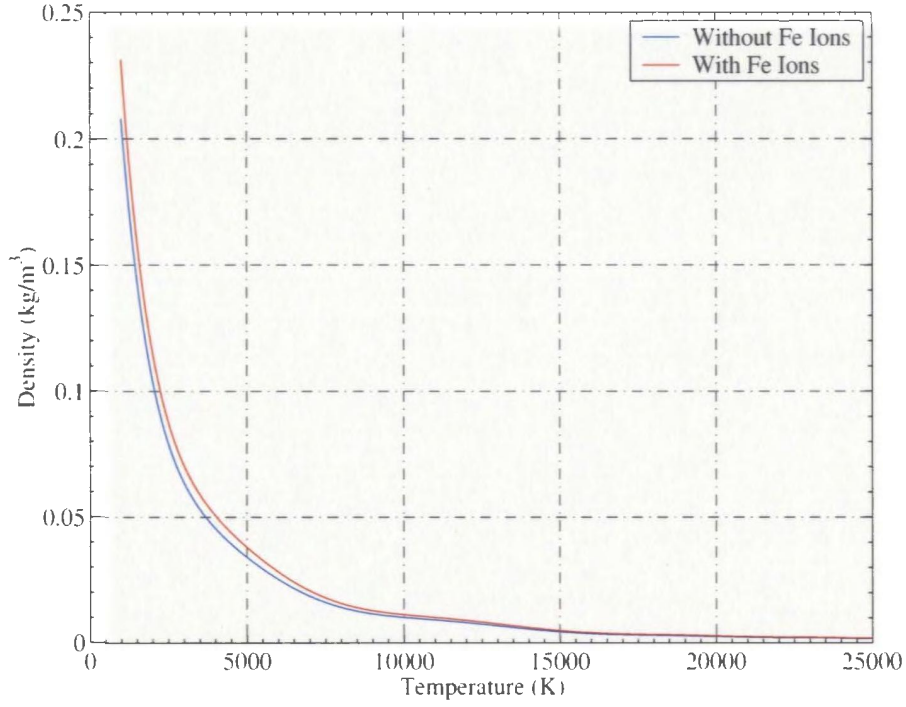


Figure 4.5: EAF Plasma Density

Table 4.6: Density Coefficients (1000 K - 25000 K)

Coefficient	Without Fe Ions	With Fe Ions
B_1	$4.985168849842867e^{-12}$	$5.615809466454545e^{-12}$
B_2	$-7.381386842696383e^{-37}$	$-8.316689303220108e^{-37}$
B_3	$4.760243660720561e^{-32}$	$5.365049238316090e^{-32}$
B_4	$-1.753230895501397e^{-27}$	$-1.976787797645853e^{-27}$
B_5	$4.063973771445272e^{-23}$	$4.584319924965862e^{-23}$
B_6	$-6.161952042225659e^{-19}$	$-6.953995626641703e^{-19}$
B_7	$6.158156498923153e^{-15}$	$6.951373924408480e^{-15}$
B_8	$-3.995882514461875e^{-11}$	$-4.509155059386358e^{-11}$
B_9	$1.622657207711049e^{-7}$	$1.828311090265503e^{-7}$
B_{10}	$-3.865684182021047e^{-4}$	$4.339866195991478e^{-4}$
B_{11}	$4.666657071126825e^{-1}$	$5.209178169547710e^{-1}$

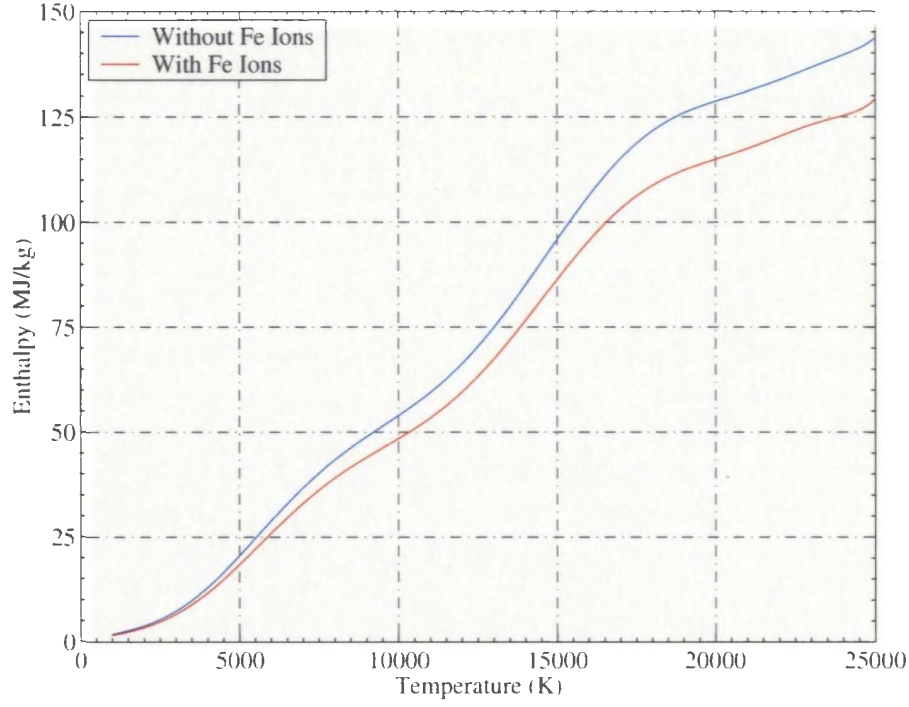


Figure 4.6: EAF Plasma Enthalpy

Table 4.7: Enthalpy Coefficients (1000 K - 25000 K)

Coefficient	Without Fe Ions	With Fe Ions
B_1	$3.569543260099615e^{-33}$	$4.353129819786811e^{-33}$
B_2	$-4.375919523653218e^{-28}$	$-5.326305839718710e^{-28}$
B_3	$2.232713234130707e^{-23}$	$2.727816774721907e^{-23}$
B_4	$-6.109197703705925e^{-19}$	$-7.564015182197551e^{-19}$
B_5	$9.607721750915982e^{-15}$	$1.226724578027962e^{-14}$
B_6	$-8.603028757273338e^{-11}$	$-1.173747557554315e^{-10}$
B_7	$4.023625969235532e^{-7}$	$6.393057158200754e^{-7}$
B_8	$7.838570615456688e^{-4}$	$1.879114480378111e^{-3}$
B_9	$7.314044447882898e^{-1}$	$3.497834114227283e^0$
B_{10}	$1.465155995502331e^3$	$2.133579002284915e^3$
B_{11}	$5.176604423660653e^4$	$1.594334422611731e^6$

4.2.4 Radiation Heat Transfer

The radiation heat transfer from the arc is not only dependent on the arc temperature but also on the arc wavelength. An expression for the radiation heat transfer including the mean absorption length is provided in [66] and is given below in Equation 4.12.

$$P_{rad} = 2\pi L_{arc} u(T_k) L_{abs}^2 \left[\frac{R_k}{L_{abs}} - 1 + e^{-R_k/L_{abs}} \right] \quad (4.12)$$

Where L_{abs} is the mean absorption length, and $u(T_k)$ is the temperature dependent radiation density. When the absorption is weak, $L_{abs} \gg R_k$, radiation occurs from the arc core volume and the heat transfer can be expressed by Equation 4.13.

$$P_{rad} = \pi L_{arc} u(T_k) R_k^2 \quad (4.13)$$

When the absorption is strong, $L_{abs} \ll R_k$, radiation occurs from the outer surface of the arc core up to a thickness of L_{abs} and the heat transfer can be expressed by Equation 4.14.

$$P_{rad} = 2\pi L_{arc} u(T_k) L_{abs} R_k \quad (4.14)$$

In general an EAF arc is dominated by optically thin radiation ($L_{abs} = \infty$), which essentially means that Equation 4.13 can be used to approximate the radiation heat transfer component [67]. With optically thin radiation the voltage-current characteristic is positive. With optically thick radiation the voltage-current characteristic is negative for currents below a few kA. The radiation loss then dominates over the convection loss, which is proportional to the current. The effect is strongest in long arcs as the radiation is proportional to the arc length [67].

The temperature dependent radiation density is determined for various compositions of EAF gas and is provided for reference in Figure 4.7. The curve was data fit from results presented in [67] using Equation 4.1 and the coefficients listed in Table 4.8. The radiation density for both gas compositions used in this study were the same, which suggest that the iron does not effect the radiation density.

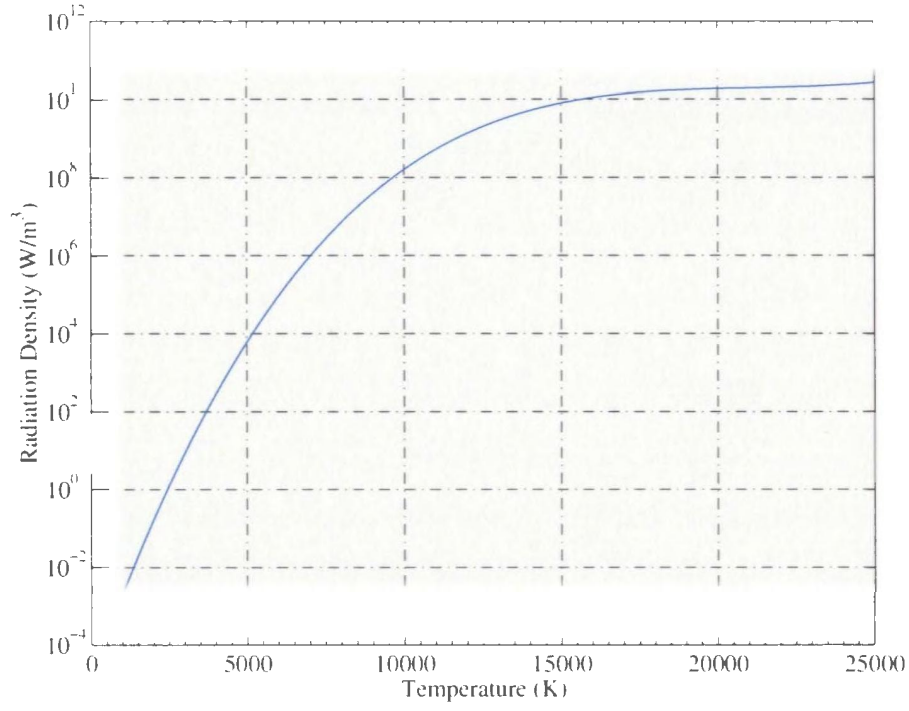


Figure 4.7: EAF Plasma Radiation Density

Table 4.8: Radiation Density Coefficients (1000 K - 25000 K)

Coefficient	Without Fe Ions	With Fe Ions
A_1	0	0
A_2	0	0
A_3	0	0
A_4	0	0
A_5	0	0
A_6	$-8.797333350086550e^{-22}$	$-8.797333350086550e^{-22}$
A_7	$2.691437460726853e^{-17}$	$2.691437460726853e^{-17}$
A_8	$4.332373460417504e^{-12}$	$4.332373460417504e^{-12}$
A_9	$-2.622004843110654e^{-7}$	$-2.622004843110654e^{-7}$
A_{10}	$5.175453216077298e^{-3}$	$5.175453216077298e^{-3}$
A_{11}	$-1.115969198439887e^1$	$-1.115969198439887e^1$

4.2.5 Model Validation

Simulations were performed using Matlab to verify that the static model yields acceptable results. The simulation results were compared with those published in the literature and were observed to be consistent with those observations. The results from the static arc model are compared using data measured from operating DC electric arc furnaces. Data from a DC electric furnace used to melt steel is used to verify that the CAM model described in [64] is accurate in [65]. Other reference sources [67,69–71] also describe steel melting furnaces, which are appropriate to verify that the arc portion of the smelting furnace model is correct.

The parameters obtained from simulation are plotted as a function of arc current and arc length for EAF gas with Fe ions in Figures 4.8 and 4.9, and without Fe ions in Figures 4.11 and 4.12. The parameters of interest include the voltage, resistance, power, velocity, core radius, and temperature. The resulting energy balance is also provided for EAF gas compositions with and without Fe ions in Figures 4.10 and 4.13, respectively. Boundary conditions for R_s , T_s , T_a , and T_c have been chosen as 1 m, 2000 K, 2500 K, and 3000 K, respectively.

The voltage profile as a function of arc length is similar to the results presented in [65,70,71] and shows a quick increase at the beginning followed by a near constant voltage gradient. The arc velocity for an experimental setup is provided in [57] and shows the correct results at lower currents. The velocity profile obtained from the CAM model is consistent with that predicted in [54]. The arc core temperature as a function of arc length is similar to those provided in [53,57]. The results obtained from the CAM model presented in this study were compared with the results from the model in [67] and were found to be close to the measured values.

To completely represent a smelting furnace dynamic conditions the static model is used in conjunction with fluctuations observed from operating DC smelting furnaces. The process resistance must also be adequately represented as explained in the following section.

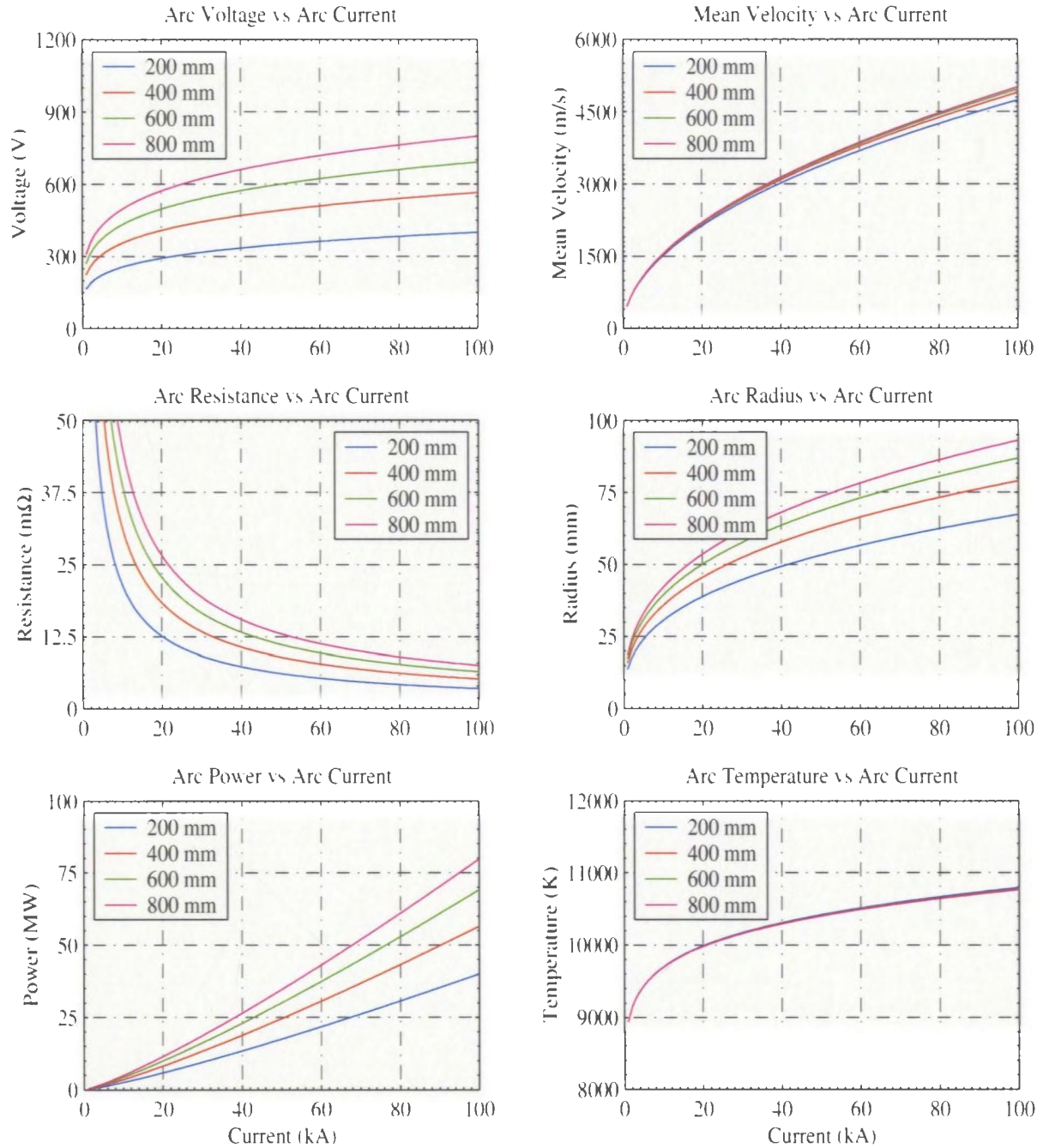


Figure 4.8: Arc Parameters as A Function of Arc Current (With Fe Ions)

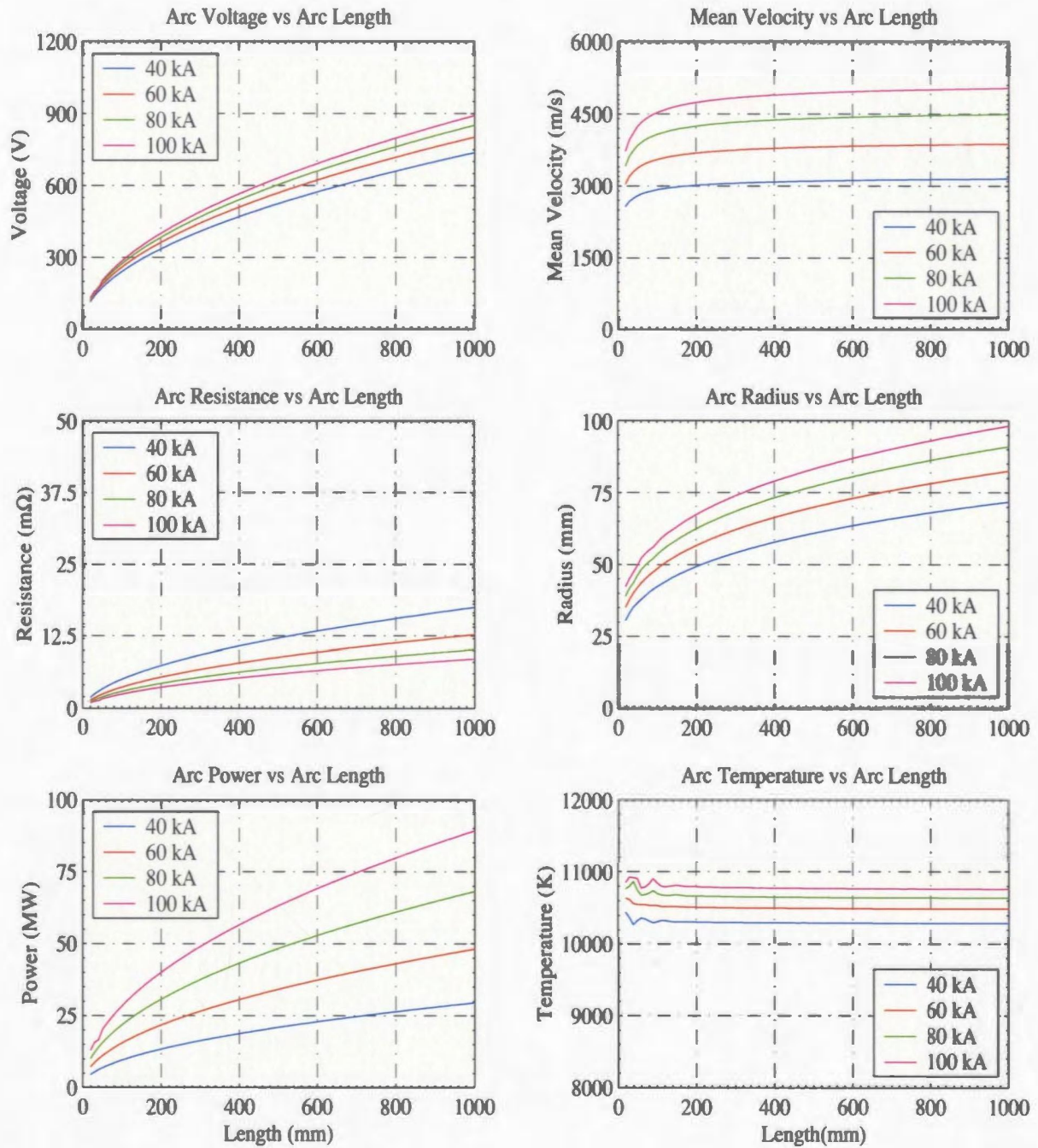


Figure 4.9: Arc Parameters as A Function of Arc Length (With Fe Ions)

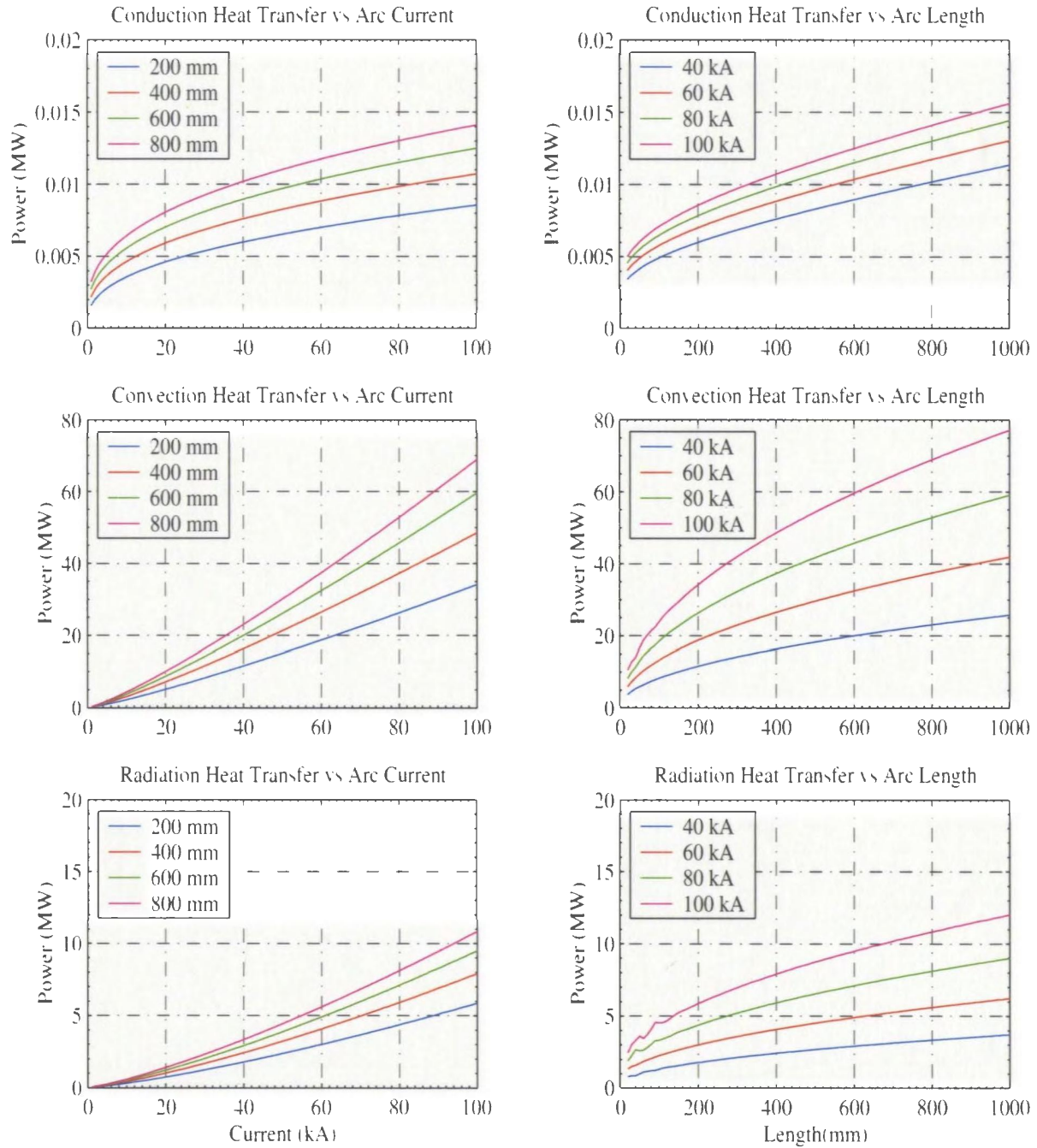


Figure 4.10: Energy Balance (With Fe Ions)

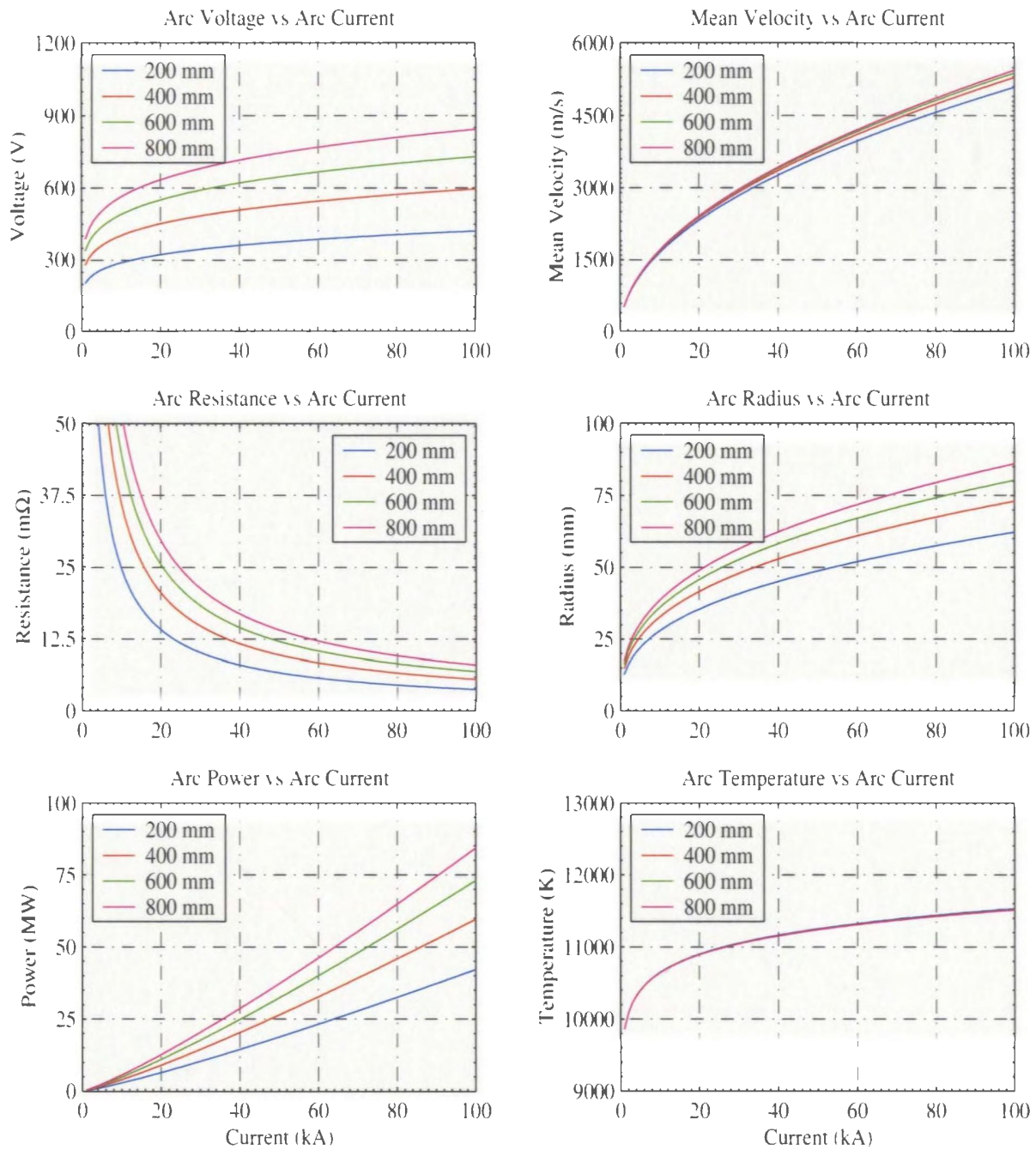


Figure 4.11: Arc Parameters as A Function of Arc Current (Without Fe Ions)

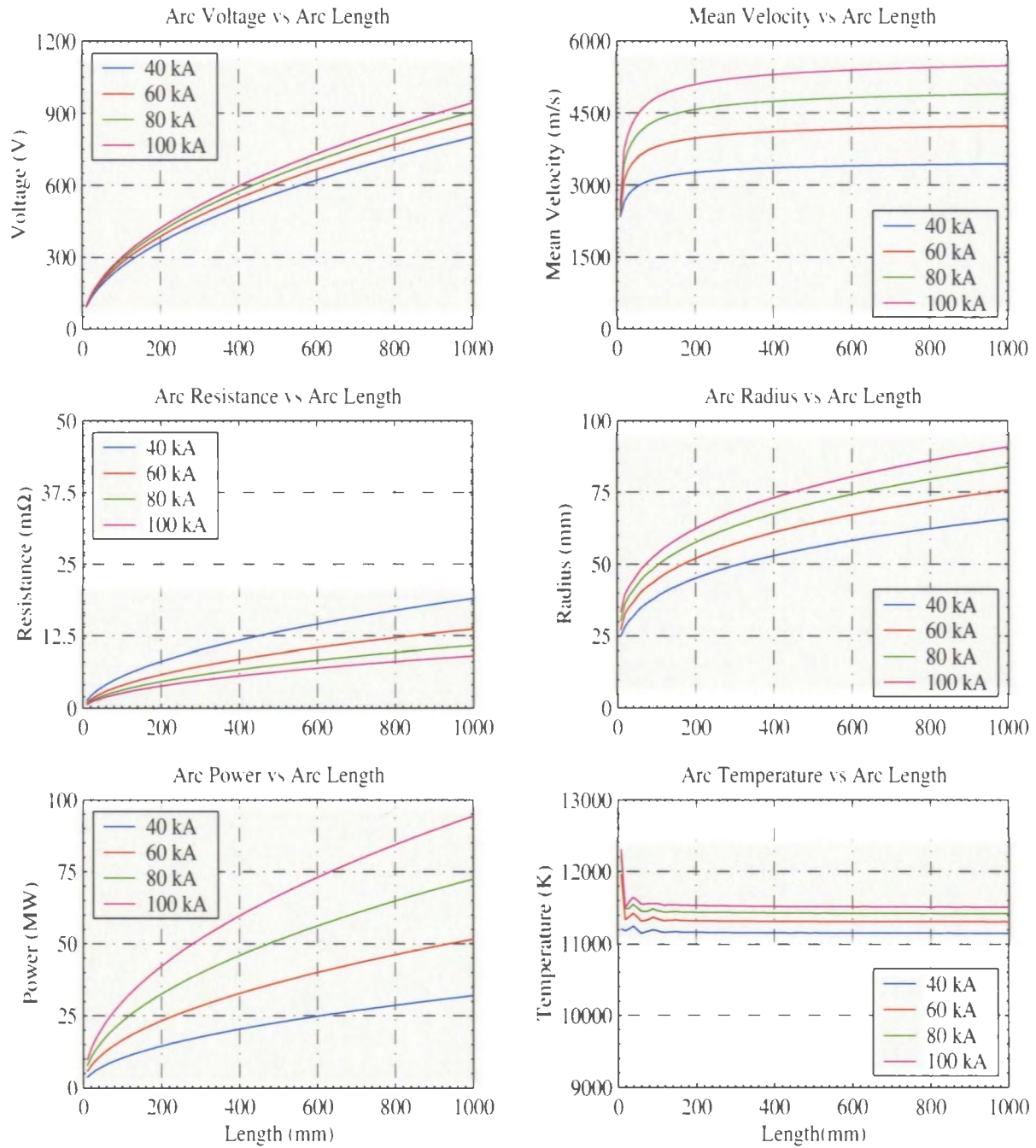


Figure 4.12: Arc Parameters as A Function of Arc Length (Without Fe Ions)

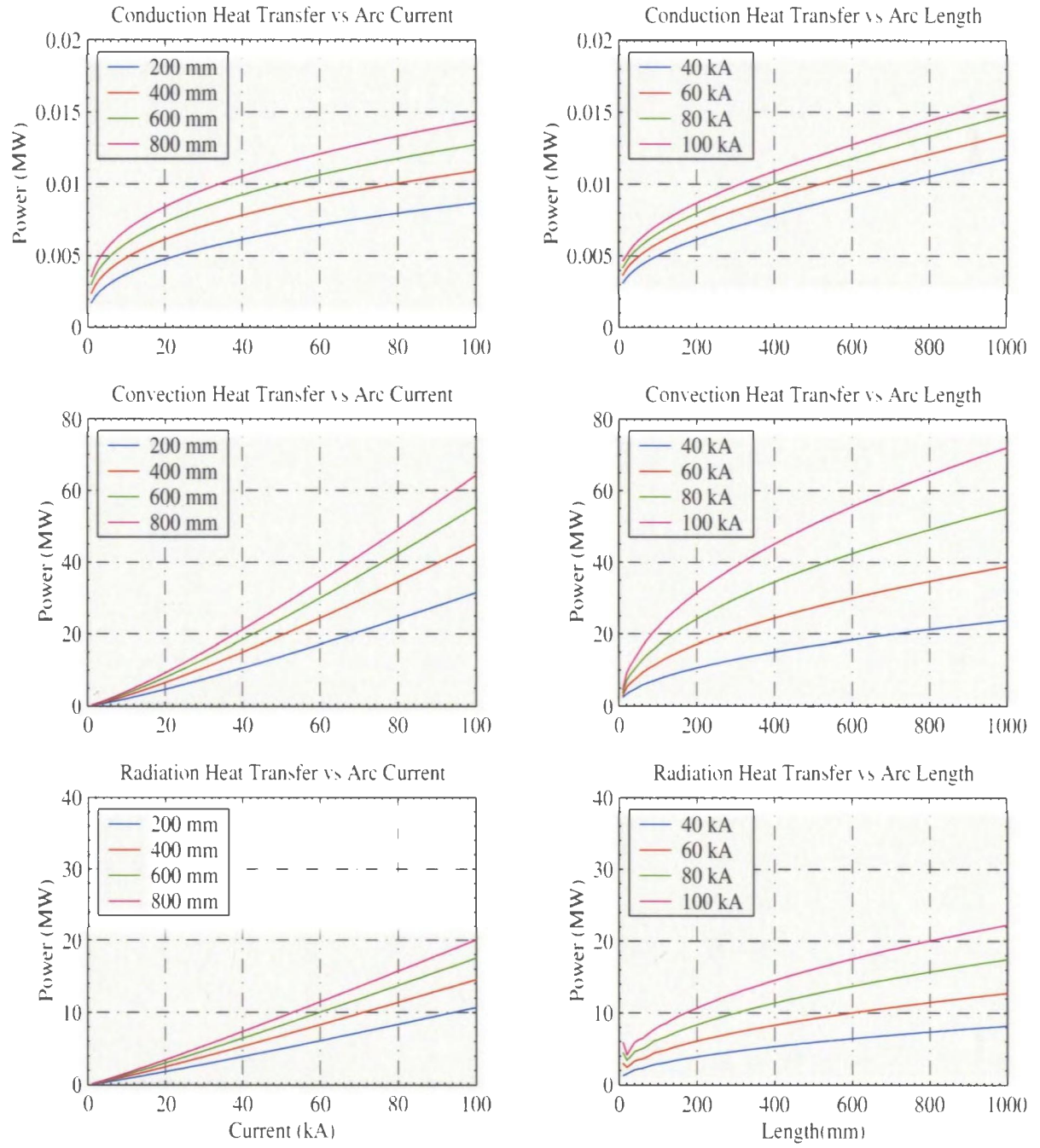


Figure 4.13: Energy Balance (Without Fe Ions)

4.3 Electric Arc Furnace Model

Electric smelting furnaces use heat to extract metals or metallic alloys from ore obtained through mining or as by-products of other industrial operations. Often fluxes are added to the reaction to assist in the separation of the liquid metals and unwanted components of the ore as fluid slags. There are two main types of smelting namely, reduction smelting and matte smelting with the type being dictated by the ore being processed [72]. In a typical matte smelting furnace there would be two to three layers of material in the furnace including a bottom metal layer (matte), a slag layer, and possibly a top layer of unmelted charge.

Smelting furnaces generally consist of a refractory shell in which the concentrate from the mining process is fed and melted using electrical energy. DC furnaces are constructed with a circular shell plate in which the sidewall refractory is installed. Thermal expansion of the brick against the shell provides the necessary compressive force to hold the brickwork in place [76]. The brick used in the hearth of a DC furnace is made of conductive refractory. Only the center of the roof is bricked the remaining outer portion consists of water cooled panels.

In a typical DC smelting furnace the electrical energy is delivered to the furnace using a single-electrode placed through the furnace roof with a return path through the bottom of the furnace hearth. This requires that the furnace bottom be conductive and contain some form of an electrode. To date several designs have been successfully used including steel pins and copper anodes placed underneath the conductive refractory. The arrangement is for the bottom electrode to be the anode since current flow in this direction is more stable and increases the convective heat transfer to the bath [69].

Traditionally all smelting furnaces were supplied at an AC mains frequency and were operated with the electrodes immersed in the slag bath. In this mode the slag becomes superheated at the electrode tips while electromagnetic and convective forces move the slag up around the electrodes and outward toward the furnace walls [75].

The hot slag flows under the charge banks, which are in turn melted by its superheat. In order to maintain high production levels sufficient contact area must be provided between the floating charge banks and superheated slag. The electrical energy is released by resistance heating of the slag layer, which can be approximated for a DC furnace as [73]

$$P_{fur} = I_{arc}^2 R_{bath} \quad (4.15)$$

where R_{bath} is the resistance in the slag layer.

Since no arcing is produced in immersed electrode smelting the power fluctuations are minimal. As the energy input is increased both the slag superheat temperature and the convective forces in the bath increase. If the furnace is not adequately sized to accommodate the input power the hot slag will impinge and erode the furnace sidewalls. Practice has repeatedly shown that there is a limiting bath power density in the range 90-150 kW/m^2 depending on the specific application, above which rapid erosion of the sidewall refractories results [75].

A significant increase in power density can be achieved by using higher voltages to create arcs above the slag bath. With this approach a portion of the electrical energy can be liberated in the arcs then transferred to the freeboard area and radiated back to melt the charge [75]. The arcs themselves represent an additional resistance in series with the bath and provide a means of increasing the overall resistance in the furnace circuit. As such open arc furnaces find their largest application in melting charges that produce insufficient slag resistance to liberate high power densities. In this mode the electrical energy can be expressed as [73]

$$P_{fur} = I_{arc}^2 (R_{bath} + R_{arc}) \quad (4.16)$$

where R_{arc} is the resistance of the arc. The ratio of bath power to arc power has an effect on the amount of fluctuation. For instance, steel melting furnaces cause large disturbances and are operated with all arc power. A figure depicting the resistance as a function of the electrode tip position for a typical AC or low power DC matte smelting furnace is provided in Figure 4.14 [73].

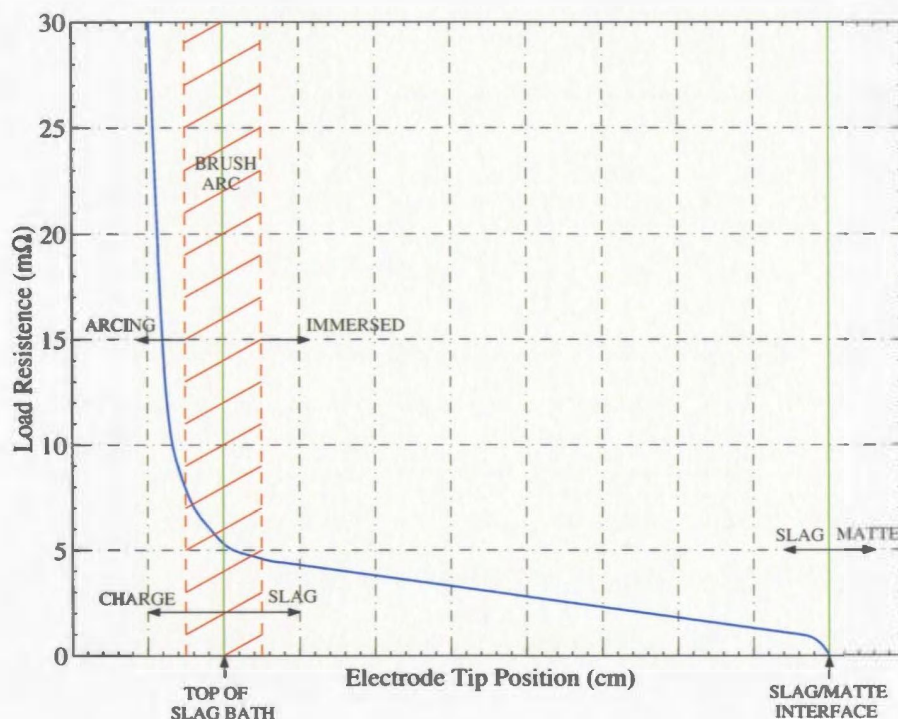


Figure 4.14: Load Resistance Versus Electrode Tip Position

As shown in the figure the process resistance goes to zero when the electrode touches the top of the conductive matte layer. When the electrode is raised into the slag layer the process resistance, which depends on the slag resistivity, begins to rise. Once the electrode begins to come out of the slag layer microarcing will begin and is identified in the figure by the brush arc region. As the electrode is raised further arcing will begin and results in a sharp increase in the process resistance.

Once arcing begins instability and fluctuation will also start. The instabilities in the arc are caused by process conditions such as feeding and tapping, as well as instabilities due to cathode spot movement, aerodynamic forces, and magnetic forces [70]. The cathode spot has been observed to move over the face of the electrode in a continuous, but random manner. Reasons for the movement are not known but are speculated to be due to the evaporation of graphite in the cathode spot area [70]. The aerodynamic instabilities are due to the velocity of the arc column, which is

often modeled as a turbulent flow. The magnetic instabilities are caused by the high currents in the arc column, any small bends in the arc column are magnetically unstable.

4.3.1 Slag Resistance

The slag layer in a smelting furnace is generally between 80 cm to 120 cm and, depending on the process, can be quite resistive. In most cases this bath resistance provides a significant contribution to the total energy liberated in the process, however, in a DC furnace the arc may have enough energy to create a large depression in the slag layer. The size of this depression is greatly reduced by instabilities in the arc including movement of the cathode spot, aerodynamic instability, and magnetic instability [70]. These factors are difficult to predict and to date have not been accurately modeled.

The depression can be observed in photographs presented in [69, 71]. However, it does not appear to be significant in relation to the slag depth. Due to the difficulty associated with predicting the size of the depression for the purpose of this study the bath resistance is assumed constant and set such that approximately 40% of the electrical energy input is liberated in the slag layer. An analysis to determine the depression caused by the DC arc is beyond the scope of this work and will not be attempted.

4.3.2 Voltage and Current Fluctuation

The process instabilities cause fluctuation in the load resistance and arc voltage, the magnitude of which depends on the circuit parameters and the ability of the power supply to minimize these disturbances. The voltage fluctuations from the arc model and power supply are provided in the following chapter and verified to be similar to those measured from an industrial DC smelting furnace. The voltages are compared using the voltage flicker values at the input, whereas the currents are compared using

the current harmonics at the input. A waveform level analysis based on measured data is also provided in this chapter to further verify that PSCAD produces the expected results for a known system.

The arc model used in the PSCAD simulation uses the parameters from the CAM model to determine the arc resistance and voltage based on the arc current and arc length. The arc current is measured while the arc length is an input chosen to give the nominal operating point for a specific application. Fluctuation is then added by randomly changing the arc length at various frequencies to reproduce the characteristics of a typical DC smelting furnace load. Both the arc voltage and resistance are nonlinear and read into PSCAD using lookup tables.

The first lookup table determines the arc resistance, which is provided as a function of arc current in Figures 4.8 and 4.11, and as a function of arc length in Figures 4.9 and 4.12. The resistance based on arc length and arc current is placed in the power circuit using the variable resistor model provided in PSCAD. The PSCAD variable resistor model also includes the option to add a branch voltage. Since the arc is nonlinear the current through the resistor will not give the correct voltage drop. This is compensated by adding the correct amount of voltage to the PSCAD variable resistor model. The arc voltage as a function of arc current and arc length are provided in Figures 4.8 and 4.11, and Figures 4.9 and 4.12, respectively.

This approach allows the nonlinear characteristics of the arc to be represented in PSCAD based on an arc length without fluctuation. The fluctuation is then added as a bandlimited white noise modulation of the arc length, around the nominal arc length for a given operating point. The same approach was developed in [90] to model flicker from an AC melting furnace and is further verified to be accurate in references [91,92]. Unlike an AC furnace the DC furnace converter and control system must also be included in the analysis to obtain the correct results [106,107]. The complete system for an uncontrolled rectifier chopper power supply is simulated in the following subsection and is shown to be comparable to data measured from the

corresponding industrial DC EAF.

4.3.3 Model Validation

The arc model is shown to give the correct results by comparing the PSCAD output to measured waveform data from an uncontrolled rectifier chopper power supply. The power supply consists of two chopper units, rated at 10.7 MW with a maximum combined current output of 48 kA. Each chopper unit consists of two sections, for a total of four sections connected in parallel with a combined ripple frequency of approximately 8 kHz. The rectifiers are arranged for 12-pulse operation and are supplied from a 12.47 kV system. The configuration is the same as that depicted in Figure 3.1. All details relating to the power system, converter configuration, and converter control system are known and included in the PSCAD simulation.

The utility supply system is operated at 69 kV, which is stepped down to 12.47 kV to supply the furnace rectifier transformers. The furnace bus is separated from the plant motive load and does not contain reactive power compensation. Above 2 MW the power supply operates under power control and automatically switches to current control for values below 2 MW. The control configuration for each chopper unit is the same as that depicted in Figure 3.19.

Measurements were taken at three locations and include the voltages from the 12.47 kV bus and the total line currents into the power supply, the line currents into the Δ/Δ transformer and Δ/Y transformer, and the output voltage. Due to the physical locations all parameters could not be recorded simultaneously. The measurements at the 12.47 kV bus were recorded for a power setpoint of 3.2 MW, the measurements at the input to the rectifier transformers were recorded at a setpoint of 3.6 MW, and the arc voltage measurement at the output was recorded at a setpoint of 5.0 MW.

The measured arc voltage waveform at 5.0 MW is compared to the simulated waveform in Figure 4.15. The average, maximum, and minimum values are similar.

which suggest that the arc length and arc current are also similar since the results are shown at the same power setpoint. The fluctuations are different, however, this can be adjusted by changing the frequency of the arc length modulation in the PSCAD model.

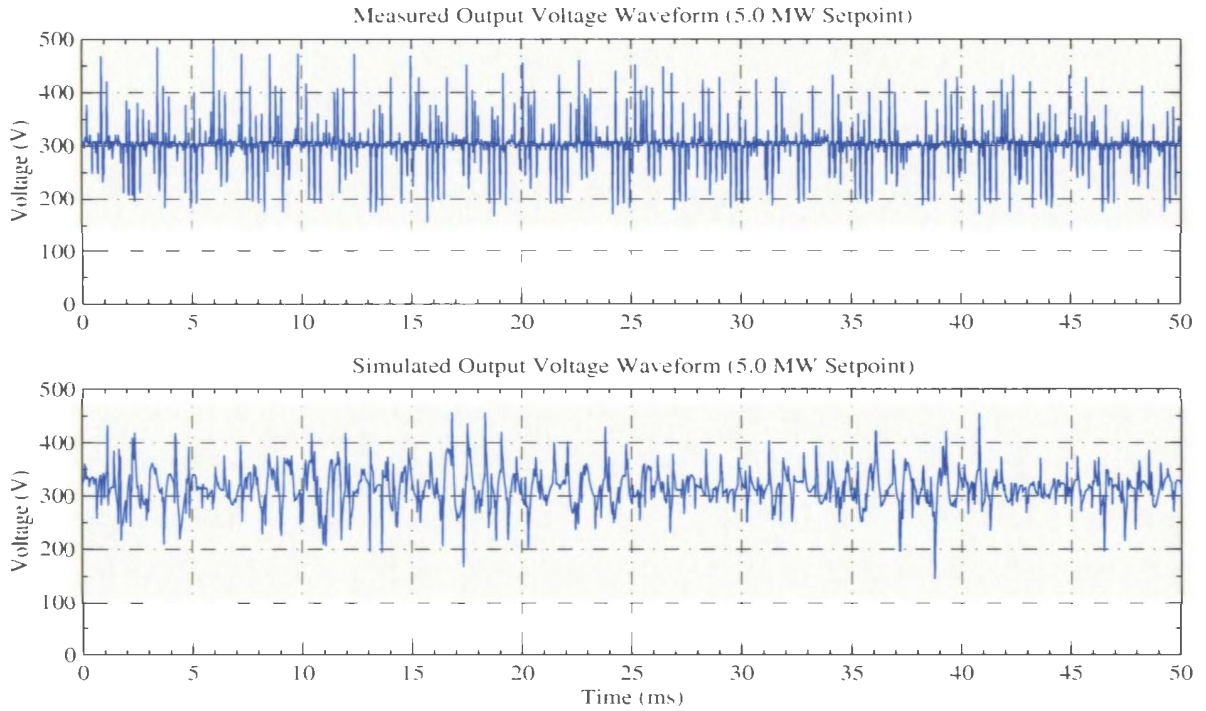


Figure 4.15: Measured and Simulated Uncontrolled Rectifier Chopper Output Voltage Waveform

The measured voltage and current waveforms at the input to the converter are shown in Figure 4.16, while the simulated waveforms under the same conditions are shown in Figure 4.17. Both the measured and simulated results are similar, which suggest that the power system, converter, and control system are accurately represented in PSCAD. This confirms that the program and models can be used to represent an actual system if all the information including system imbalances are known and included in the model.

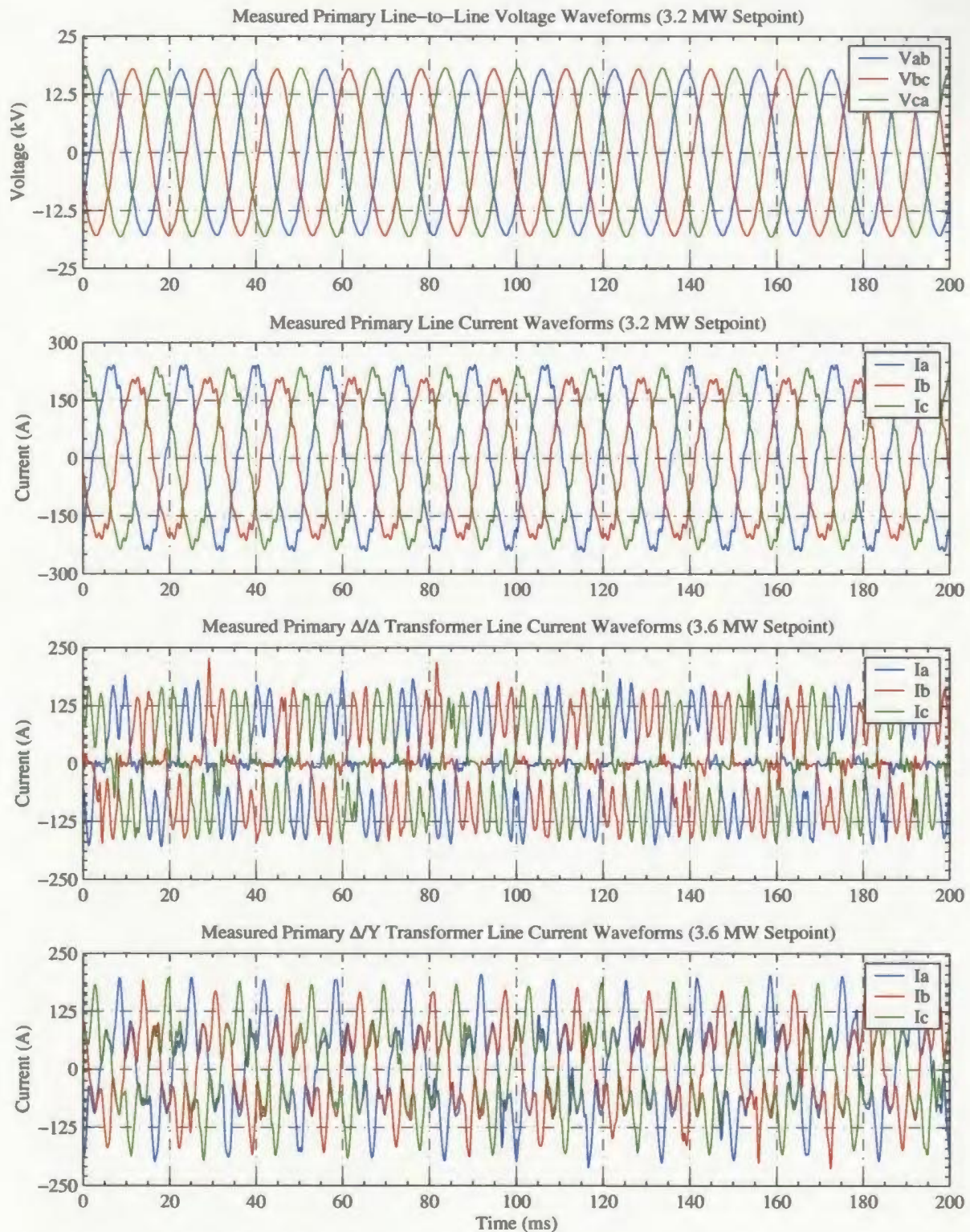


Figure 4.16: Measured Uncontrolled Rectifier Chopper Input Voltage and Current Waveforms

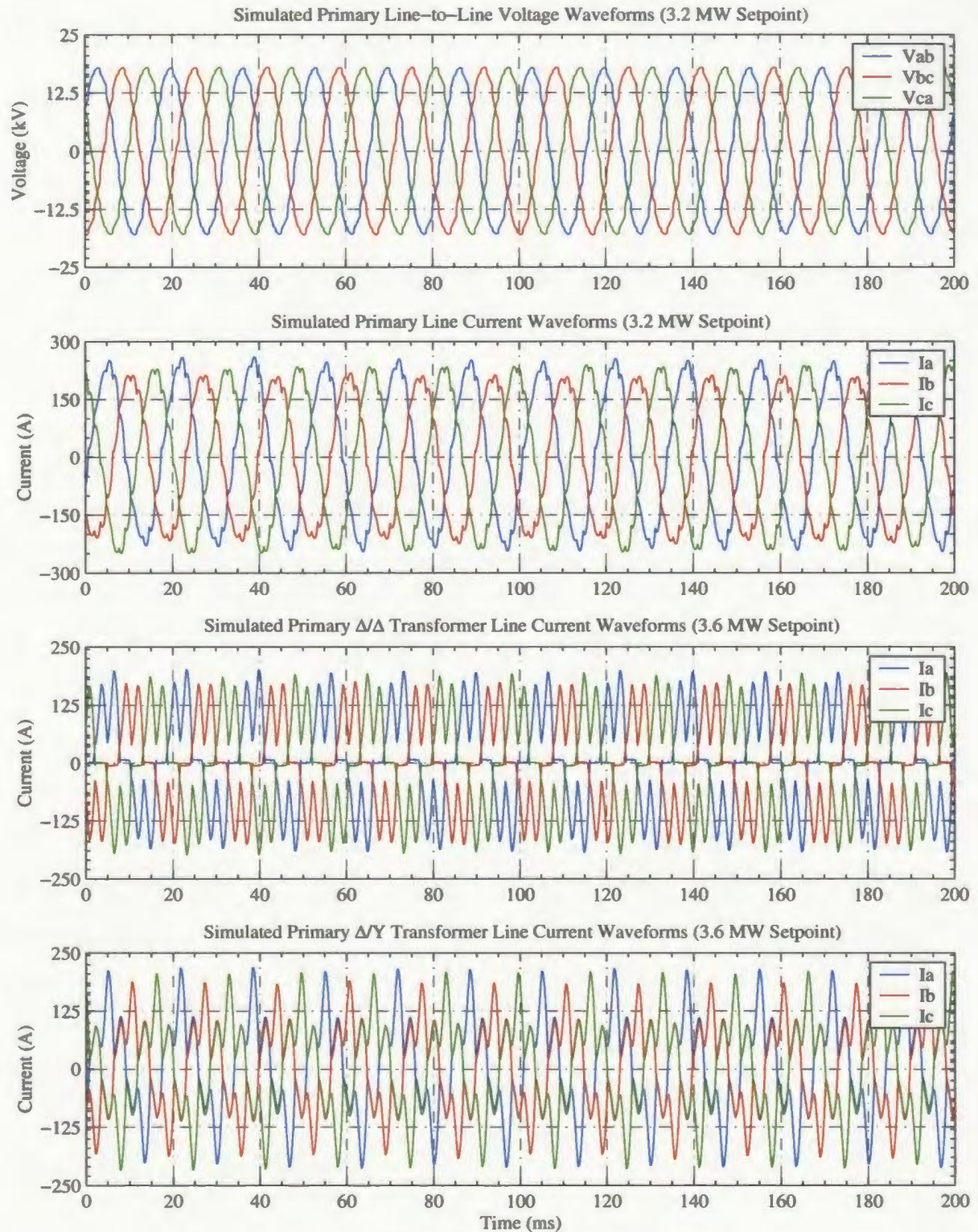


Figure 4.17: Simulated Uncontrolled Rectifier Chopper Input Voltage and Current Waveforms

4.4 Summary

Since very little work has been done on DC arc furnace models this chapter has presented an electric arc model that can be used to represent a DC smelting furnace. The CAM model was chosen primarily because the equations are easily solved and implemented in an electromagnetic transient simulation environment. The temperature dependent physical inputs to the static model were obtained from typical EAF gas compositions. This was not done in previous CAM models which used constant values as inputs.

The model is based on energy balance between the electrical input and the various components of heat loss at the output, including conduction heat transfer, convection heat transfer, and radiation heat transfer. The resulting energy balance for a high current arc was shown to be dominated by convection heat transfer, followed by radiation heat transfer, then conduction heat transfer, which is negligible. The equations are functions of the arc radius and temperature and were solved using Steenbeck's Minimum Principle, which states that the arc will always assume a radius and temperature to minimize power loss.

The CAM model was shown to represent an industrial arc by comparing the simulated values to measured data published in the literature. In the PSCAD simulation the arc current is measured and the arc length is chosen to represent the nominal operating point of the furnace under investigation. The arc length is then fluctuated to represent an actual arc furnace load. The approach also requires knowledge of the power system, converter, and control system to be accurate. The model was shown to give similar results to those measured at an industrial DC EAF using an uncontrolled rectifier chopper power supply.

Chapter 5

Power Supply Comparison

Simulation comparison enables systems to be compared on a common basis with the same load type and operating parameters. This is not always possible when comparing industrial data since it is often obtained under different process conditions at different operating points. Furthermore, the electrical systems from any two plants are not identical and will behave differently to the same disturbance. It is for these reasons that simulation based on industrial data will be used to compare both converters operating under the same conditions.

The purpose of this chapter is to compare both power supply configurations with respect to their impact on power quality, rectifier performance, and reliability. The power quality parameters of interest include the power factor, harmonic and interharmonic distortion, unbalanced voltage, and voltage flicker. The performance indices include the efficiency, rectification ratio, ripple factor, form factor, and transformer utilization factor. In addition, a simplified reliability analysis is performed using the parts count method from each power supply configuration.

The power quality parameters are generally of interest to the power provider since disturbances may impact other customers connected to the same supply. Performance parameters such as efficiency and reliability are generally of interest to the operator since these have an effect on the operating cost of the supply and any associated down

time of the process.

The equipment sizes and quantities for each power supply are provided and are similar to those used at operating smelting facilities. The power electronic switches have been chosen to minimize the parts count thereby increasing the reliability of each configuration. The load parameters and details pertaining to the AC supply are provided and set to be the same in each case to allow a meaningful comparison.

5.1 Case Study

The case study is for the design of a 50 MW DC smelting furnace. It is assumed that the process bath resistance is $6\text{ m}\Omega$ and remains constant over the entire operating range. The nominal operating point is 50 MW at an electrode current of approximately 60 kA, which requires a total process resistance of approximately $14\text{ m}\Omega$. Since the arc model requires arc length as an input parameter it has been approximated from the channel arc model without Fe Ions as 35 cm.

The power system is assumed to have a fault level of 500 MVA at the plant medium voltage bus with an X/R ratio of 15. Given the power level the voltage has been assumed to be 34.5 kV, which enables the selection of breakers and transformer tap changers. The power system frequency is assumed to be fixed at 60 Hz and does not change during the simulations. Furthermore, the incoming voltage is assumed to be free of distortion and balanced among the three phases.

5.1.1 Controlled Rectifier

The controlled rectifier power supply used for this study was described in Chapter 2 and consists of two rectifier transformers, two 6-pulse thyristor controlled rectifiers, and two output reactors. The rectifier transformers were chosen to provide a 12-pulse characteristic by using a Δ/Δ transformer and a Y/Δ transformer. Due to the possibility of low power factor and high harmonic loading, the transformers were chosen as

38.5 MVA units. Both transformers were assumed to have a leakage reactance of 0.08 pu, no load losses of 0.002 pu, and copper losses of 0.0005 pu. The nominal secondary voltage used in the simulations was set to 940 V and was chosen to operate with a firing angle of approximately 40° .

The thyristor chosen for the bridge rectifier is an EUPEC T4771N (data sheet provided in Appendix A), which can operate with a mean current of 4770 A. The rectifier was designed to have a maximum output current of 75 kA or 37.5 kA per bridge. For an N-1 reliability this required connecting 9 thyristors in parallel for a total requirement of 108 thyristors. Each thyristor also requires an RC snubber and fuse which must be added to the total parts count for the reliability analysis. The PSCAD simulation uses an equivalent model based on the data sheet parameters and snubber sizes.

The output reactors were rated at 37.5 kA with an inductance of $100\ \mu H$. In order to provide the magnetic coupling, that would be obtained with the reactor layout in the controlled rectifier power supply, a single phase transformer was added to the PSCAD simulation to parallel the output of each individual bridge circuit. The losses in the reactors and secondary bus were approximated by adding a $0.3\ m\Omega$ resistor at the output just before the smelting furnace model. Screenshots from the controlled rectifier simulation showing the major equipment parameters are provided for reference in Appendix B.

The simulated controlled rectifier power supply was controlled using a PI controller set to provide a 50 MW power output with a current limit of 75 kA. The controller also included a balancing loop with the tuning parameters set to be the same as those presented in Chapter 2.

Results from a 200 ms window of the simulation with the dynamic arc model are shown in Figures 5.1 to 5.4. Figure 5.1 shows the load parameters including the arc length and current, and process parameters including the resistance, voltage, and power. Figures 5.2 and 5.3 show the time domain waveforms at the input and output

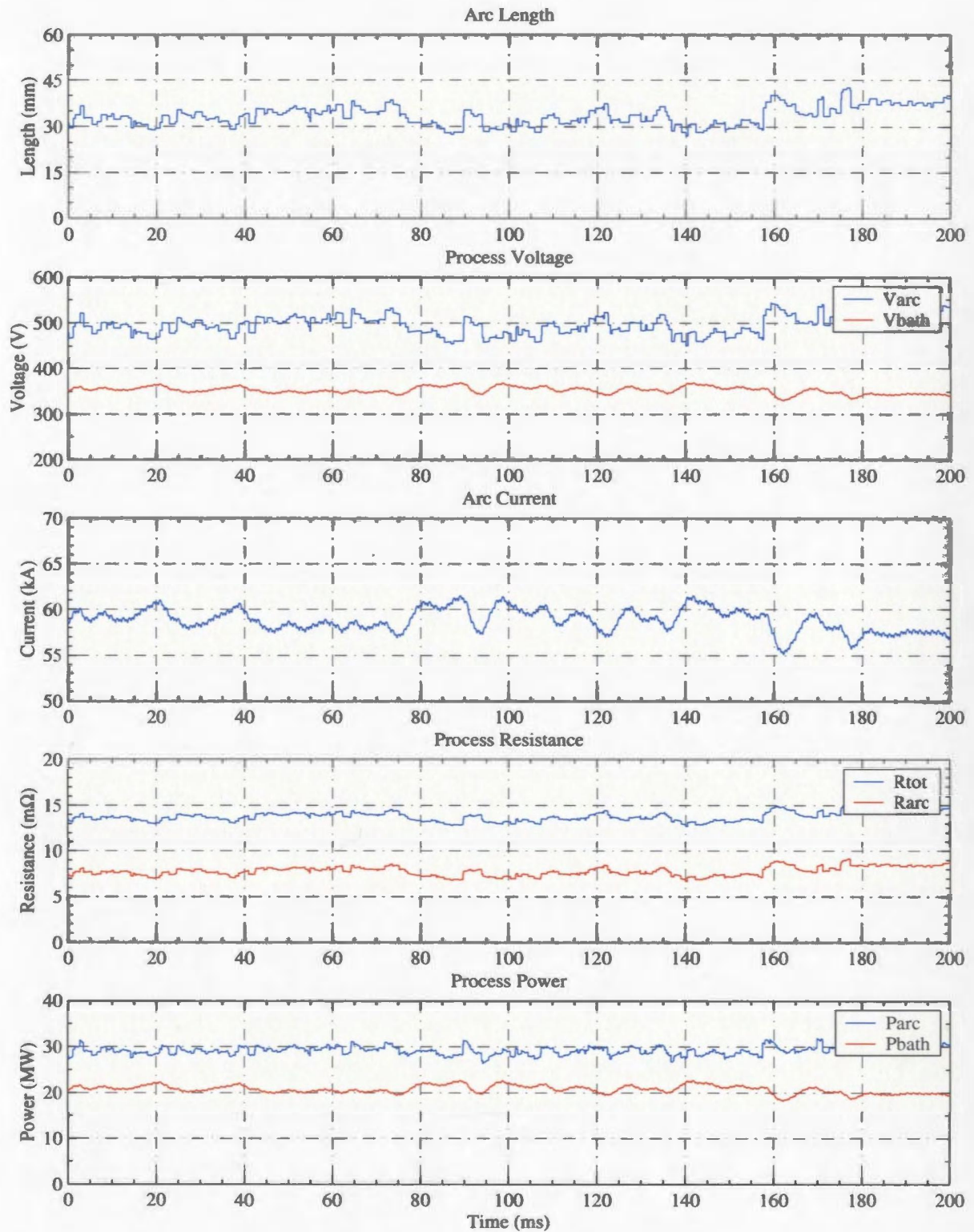


Figure 5.1: Simulated Controlled Rectifier Process Parameters

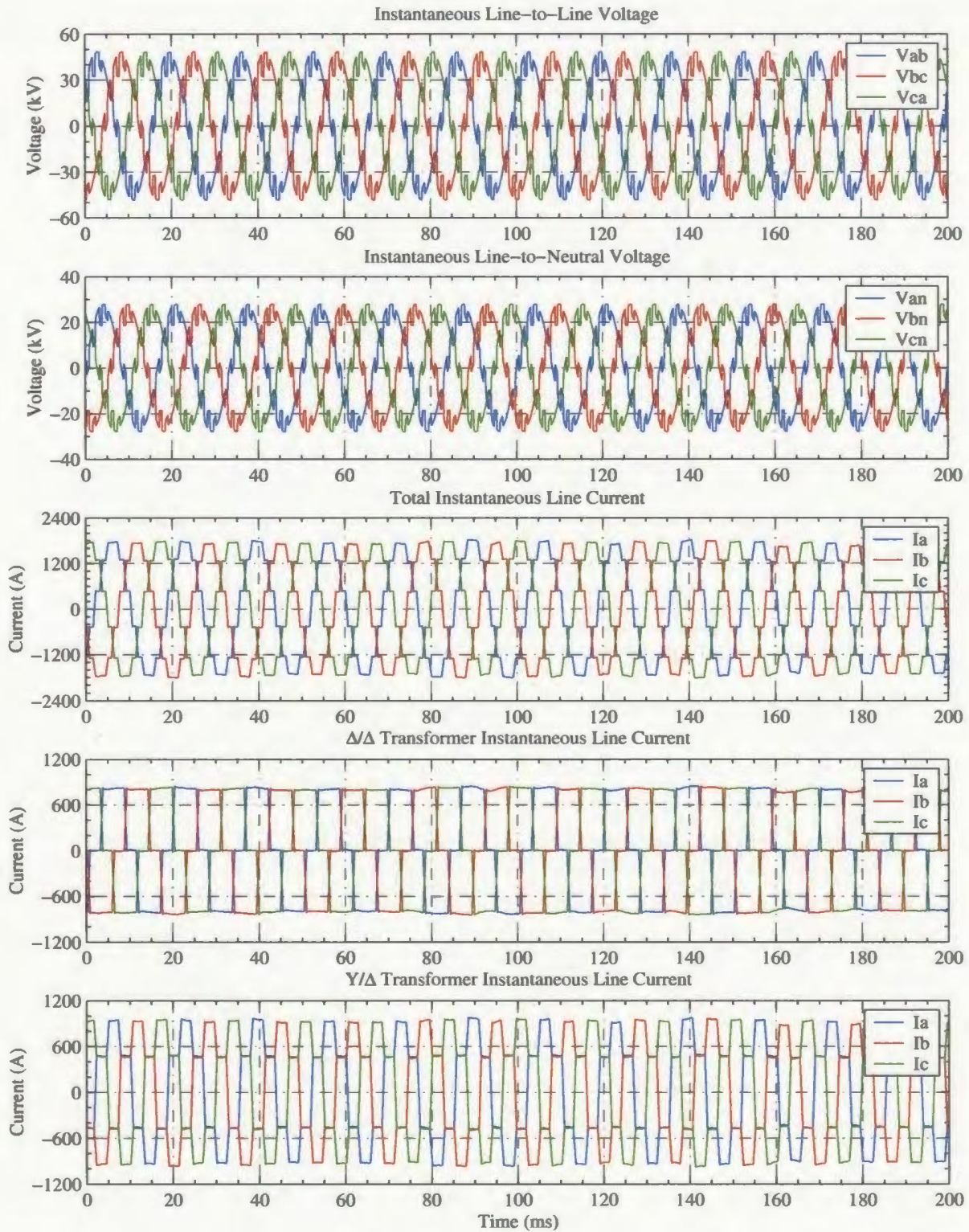


Figure 5.2: Simulated Controlled Rectifier Input Characteristics

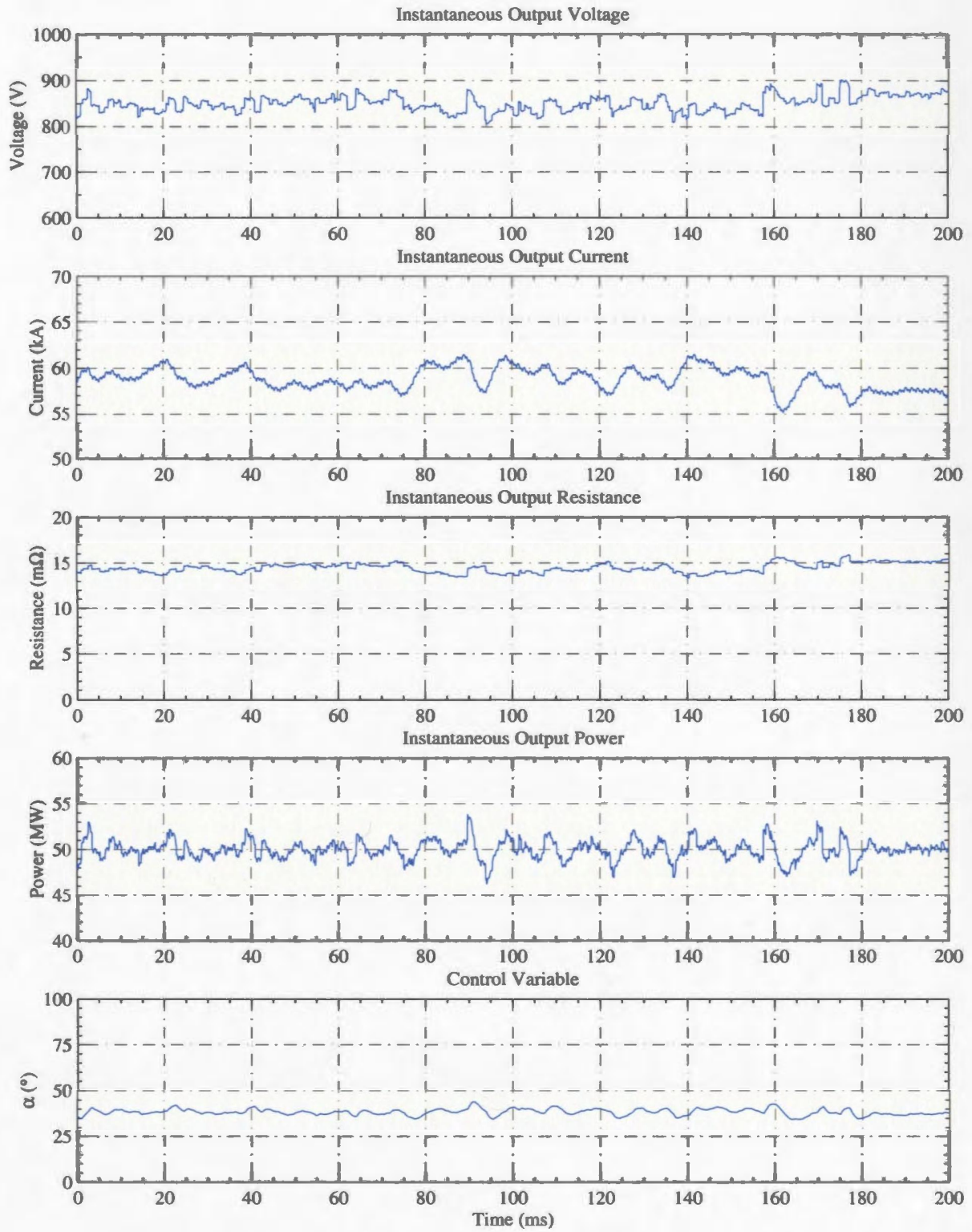


Figure 5.3: Simulated Controlled Rectifier Output Characteristics

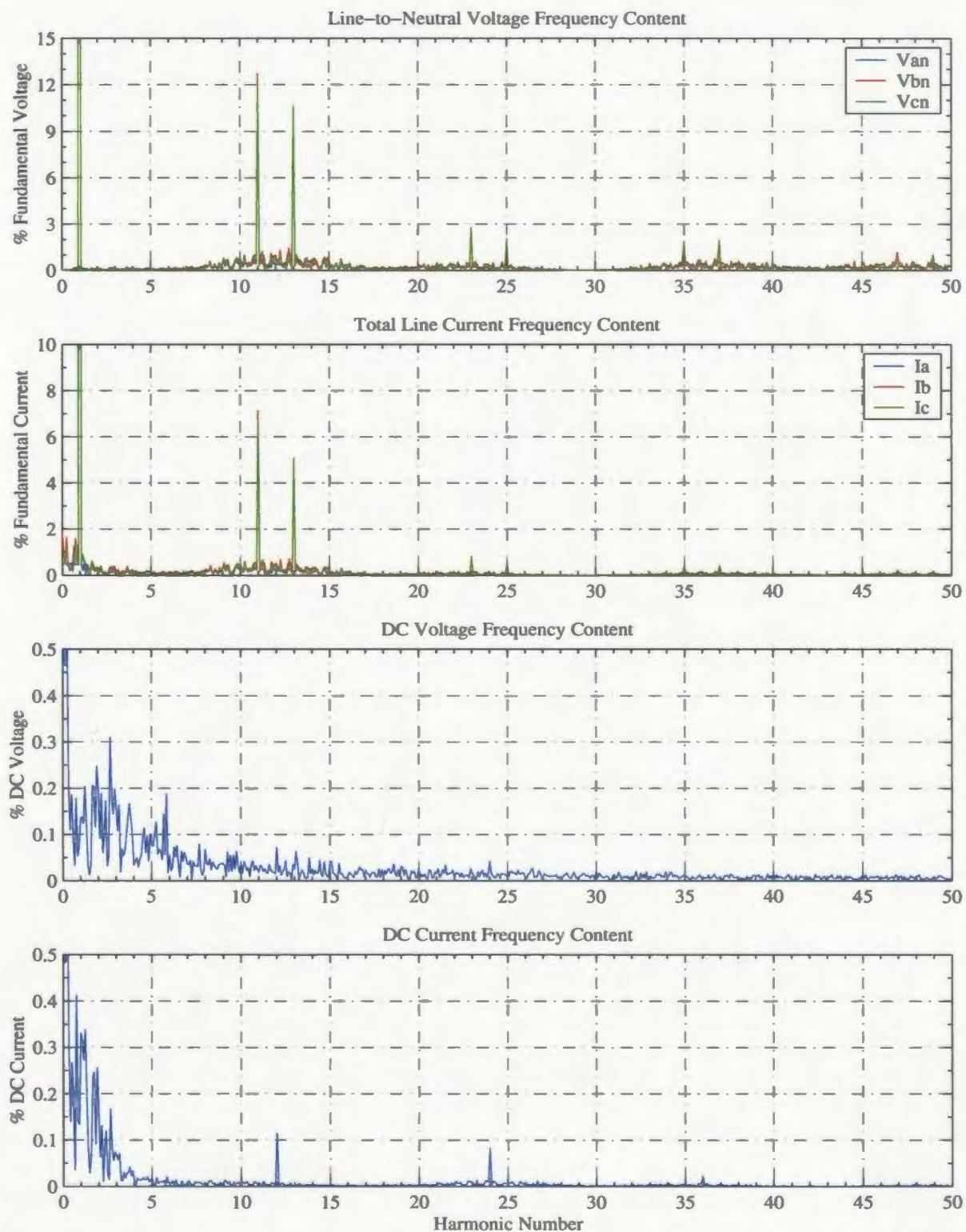


Figure 5.4: Simulated Controlled Rectifier Harmonic Content

of the power supply, respectively. Figure 5.4 shows the frequency spectrum of both the input and output voltage and current.

5.1.2 Uncontrolled Rectifier Chopper

The uncontrolled rectifier chopper power supply used for this study was described in Chapter 3 and consists of two rectifier transformers, two 6-pulse diode rectifiers, four chopper sections, and four output reactors. The rectifier transformers were chosen to provide a 12-pulse characteristic by using a Δ/Δ transformer and a Δ/Y transformer. Since the power factor is high and the harmonic loading relatively lower than that of the controller rectifier power supply the transformers were chosen as 30.0 MVA units. Both transformers were assumed to have a leakage reactance of 0.08 pu, no load losses of 0.002 pu, and copper losses of 0.0005 pu. The nominal secondary voltage used in the simulations was set to 1020 V and was chosen to operate with a duty ratio of approximately 0.70.

The diode chosen for the bridge rectifier was an EUPEC D4709N (data sheet provided in Appendix A), which can operate with a mean current of 4700 A. The rectifier was designed to have a maximum output current of 75 kA or 37.5 kA per bridge. For an N-1 reliability this required connecting 9 diodes in parallel for a total requirement of 108 diodes. Each diode also requires an RC snubber and fuse which must be added to the total parts count for the reliability analysis.

Each chopper section must be capable of carrying 18.75 kA and for the purpose of this study each section was constructed using 2400 A chopper modules. For an N-1 reliability this requires 9 chopper modules per section for a total of 36. The IGBT and diode package chosen for the modules was an EUPEC FZ1200R (data sheet provided in Appendix A), which can operate with a mean current of 1200 A. Hence each module contains two IGBT packages and one freewheeling diode, complete with the associated fuses and snubbers. The freewheeling diode chosen for this study was an EUPEC D2659N (data sheet provided in Appendix A), which can operate with a

mean current of 2650 A.

The IGBT and freewheeling diode snubbers consist of a resistor, capacitor, and a diode. The snubber diode chosen for this application was an EUPEC D1408S (data sheet provided in Appendix A), which can operate with a mean current of 1410 A. Each module required four fuses including one at the input, one at the output of each IGBT, and one to protect the freewheeling diode. The modules also required an input capacitor rated at $8400\ \mu F$ and a resistor. For the reliability analysis it is assumed that the capacitance can be obtained using four $2100\ \mu F$ capacitors. Each module also required a reactor at the input and one at the output to ensure current sharing between the modules when connected parallel.

The reactors connected at the output of each module, as well as, those connected at the output of each unit are choke reactors. The reactors at the output of each chopper unit were rated at 18.75 kA with an inductance of $100\ \mu H$. The losses in the reactors and secondary bus were approximated by adding a $0.3\ m\Omega$ resistor at the output just before the smelting furnace model. Screenshots from the uncontrolled rectifier chopper simulation showing the major equipment parameters are provided for reference in Appendix B.

The simulated uncontrolled rectifier chopper power supply was controlled using two PI controllers set to provide a total power output of 50 MW with a current limit of 75 kA. Each controller also included a balancing loop with the tuning parameters set to be the same as those presented in Chapter 3. The controllers from each chopper unit were set to provide the same power setpoint of 25 MW with a current limit of 37.5 kA.

Results from a 200 ms window of the simulation with the dynamic arc model are shown in Figures 5.5 to 5.8. Figure 5.5 shows the load parameters including the arc length and current, and process parameters including the resistance, voltage, and power. Figures 5.6 and 5.7 show the time domain waveforms at the input and output of the power supply, respectively. Figure 5.8 shows the frequency spectrum of both

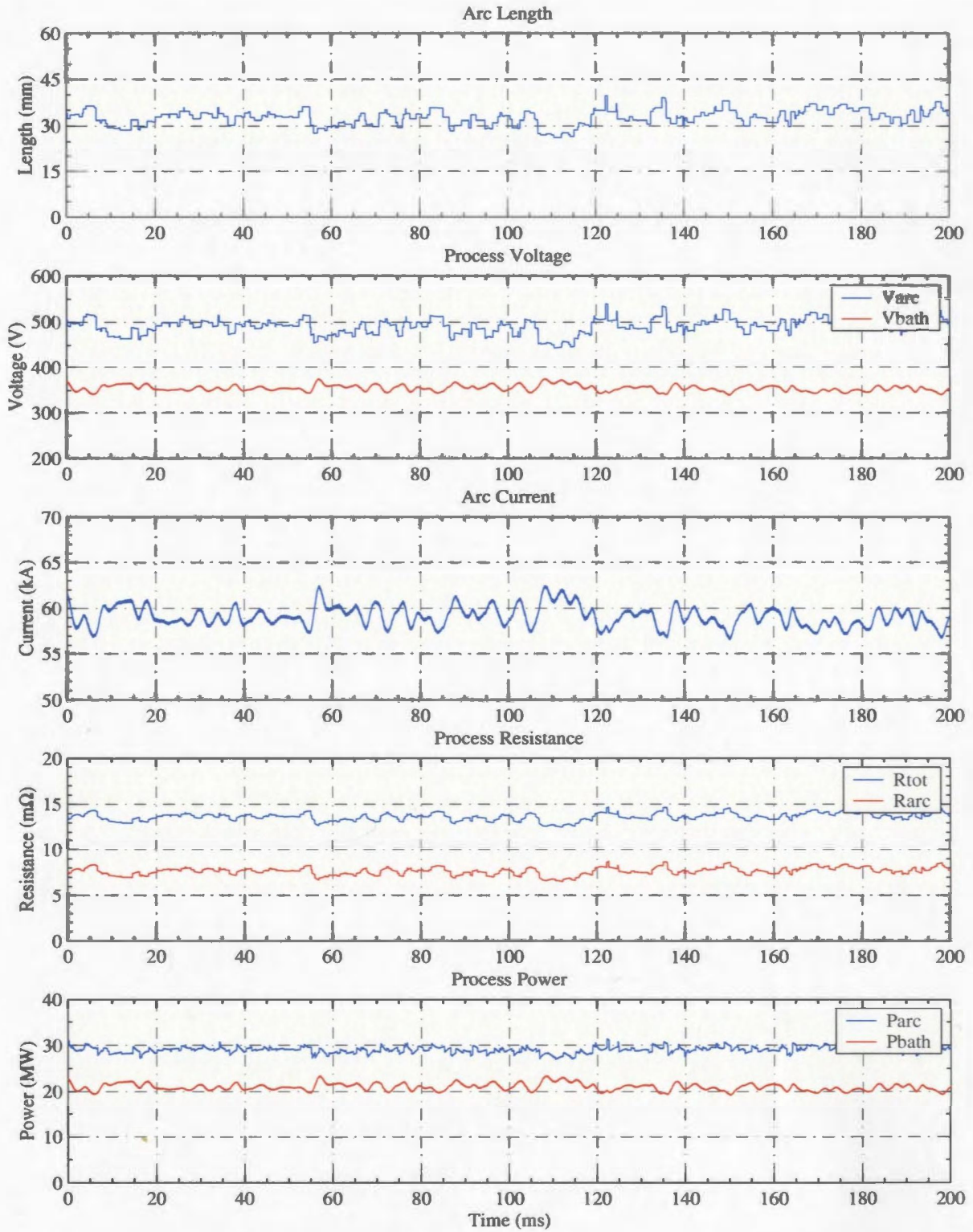


Figure 5.5: Simulated Uncontrolled Rectifier Chopper Process Parameters

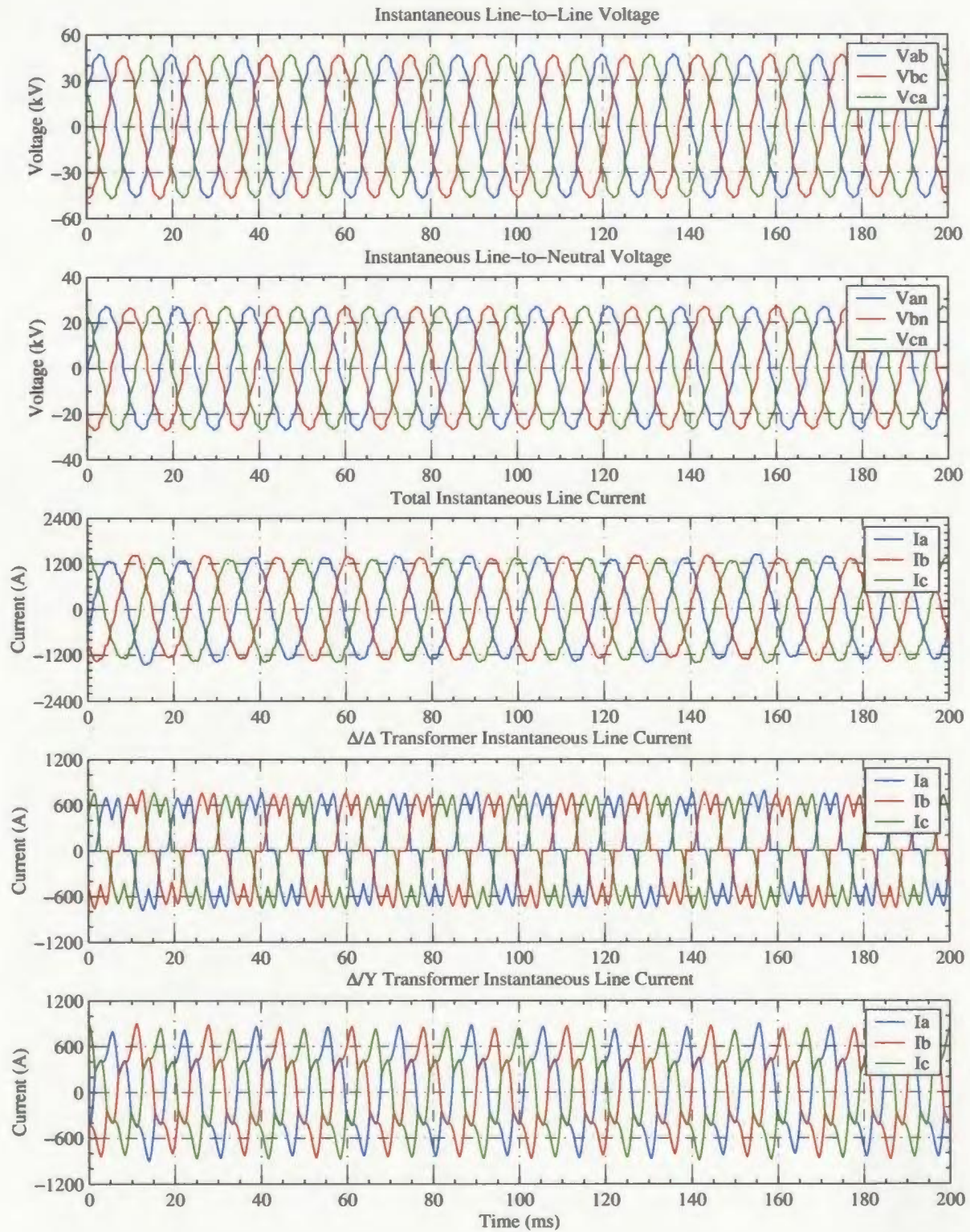


Figure 5.6: Simulated Uncontrolled Rectifier Chopper Input Characteristics

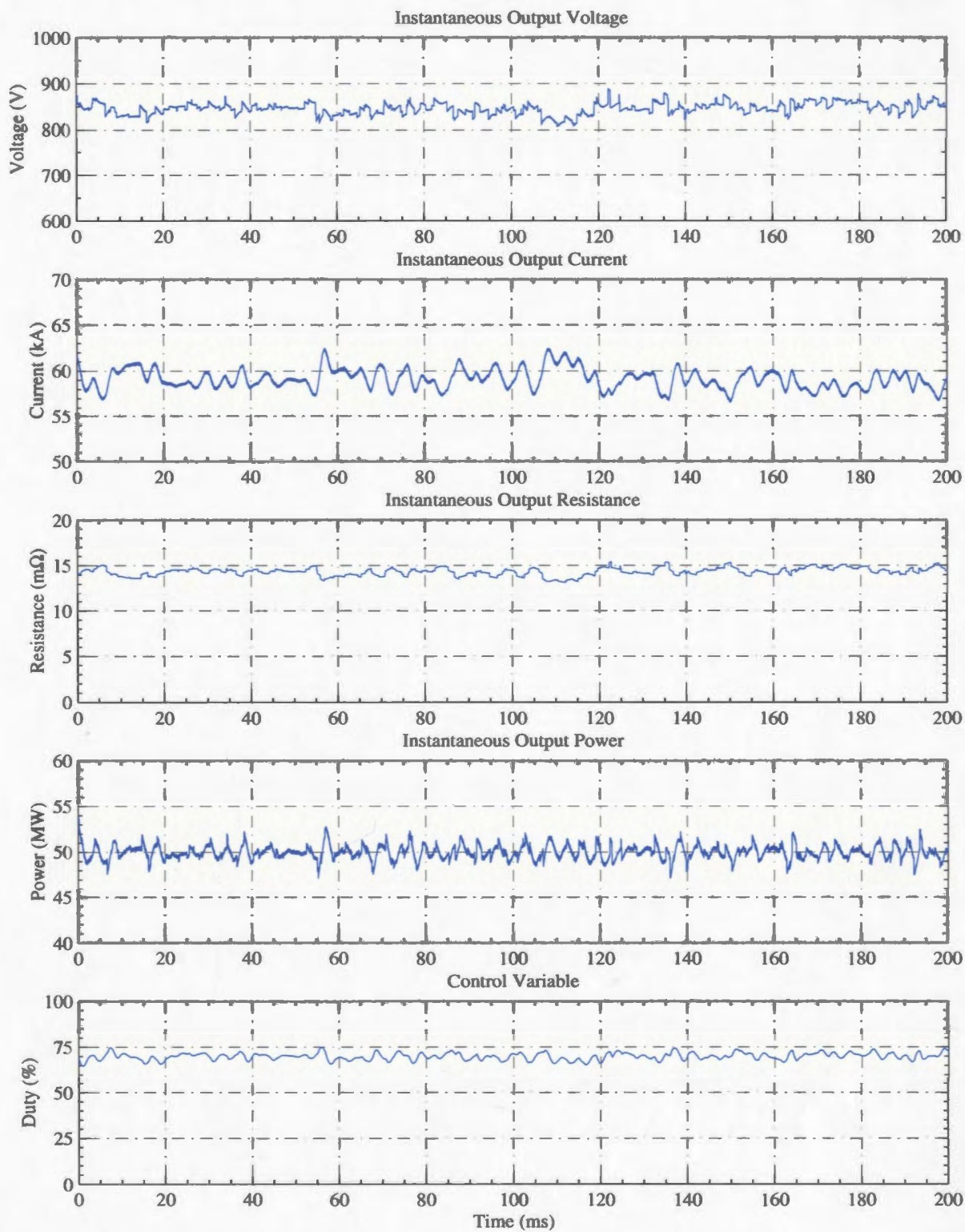


Figure 5.7: Simulated Uncontrolled Rectifier Chopper Output Characteristics

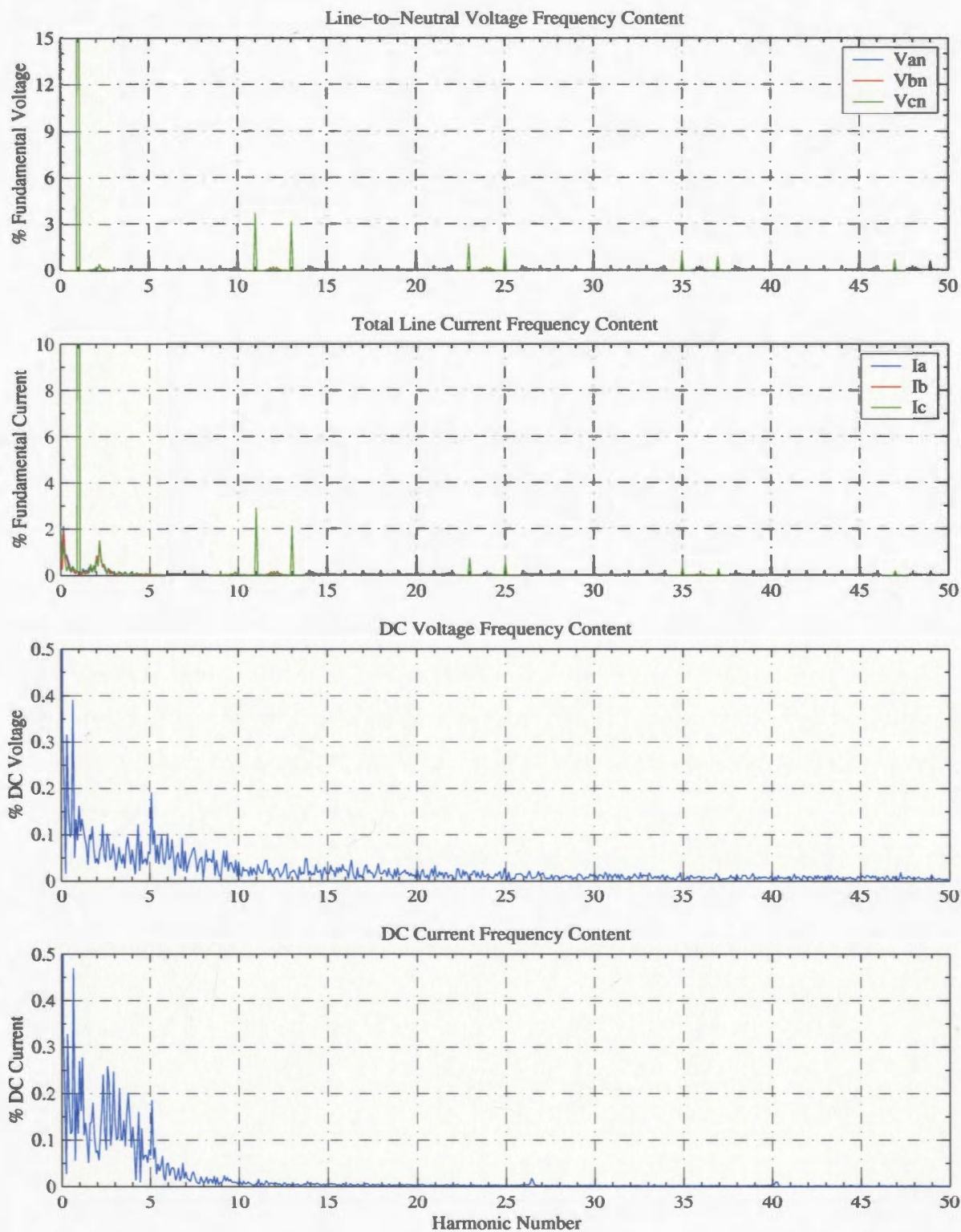


Figure 5.8: Simulated Uncontrolled Rectifier Chopper Harmonic Content

the input and output voltage and current.

5.2 Power Quality

Power quality is the degree to which both the utilization and delivery of electric power affects the performance of electrical equipment. A power quality disturbance can be manifested in voltage or current and is described as any deviation in the magnitude or frequency of the ideal sinusoidal waveform [109]. Power quality indices can be divided into two categories including those written in terms of voltage (utility responsibility) and those written in terms of current (customer responsibility).

The majority of power quality indices are defined for periodic waveforms, however, since a smelting furnace load is continually changing the waveforms are not periodic. The analysis of this type of load is generally performed using windows of data statistically compiled over a period of time to provide an overall characteristic. Power quality indices are generally imposed at the 99% CPF level, which allows the limits to be exceeded during abnormal operation. The IEC recommends a window width of 200 ms [117,119], which corresponds to 10 cycles on 50 Hz systems and 12 cycles on 60 Hz systems.

For the purpose of this study power quality parameters were calculated using 100 windows of data which represent 20 seconds of simulation time. An actual power quality study should be completed over a much longer period. However, this is not practical when performing an electromagnetic transient simulation. The main values of interest include the power factor (PF), total harmonic distortion (THD), total demand distortion (TDD), and the short term flicker severity index (P_{st}). A single P_{st} value has been calculated for the entire 20 seconds of simulated data.

5.2.1 Harmonic and Interharmonic Distortion

Harmonics are voltages or currents present on a power system at some integer multiple of the fundamental frequency. These harmonics result in distorted waveforms, which are a sum of the fundamental component and the individual harmonic components. Distortion levels are described by a complete harmonic spectrum including magnitudes and phase angles for each individual harmonic component [14]. In addition, single quantities known as the total harmonic distortion (THD) and the total demand distortion (TDD) are often used as effective values to represent harmonic distortion levels.

Process instabilities and controller response dictate that the DC smelting furnace will also cause distortion at other frequencies referred to as interharmonic and subharmonic distortion. Interharmonics and subharmonics occur at non integer multiples of the fundamental frequency and are either above or below the fundamental frequency, respectively. For the purpose of this study the interharmonics and subharmonics are grouped together into one interharmonic distortion term.

The THD is generally written for voltage and consist of two components when non integer harmonics are included [117,119]

$$THD = \sqrt{TDHD^2 + TIHD^2} \quad (5.1)$$

where TDHD is the total discrete harmonic distortion

$$TDHD = \frac{1}{V_1} \sqrt{\sum_{h=2}^{h_{\max}} V_h^2} \quad (5.2)$$

and TIHD is the total interharmonic distortion

$$TIHD = \frac{1}{V_1} \sqrt{\sum_{h=0}^{h_{\max}-1} VRSS_{h,h+1}^2} \quad (5.3)$$

The VRSS term is used to denote the root sum squared value of the voltage interharmonics between two consecutive harmonics h and $h + 1$. At a power system frequency

of 60 Hz, using a frequency resolution of 5 Hz, the VRSS is defined by

$$VRSS_{h,h+1} = \sqrt{\sum_{f=60h+5}^{60(h+1)-5} V_f^2} \quad (5.4)$$

The TDD is written for current and consists of two terms when non-integer harmonics are included [117,119]

$$TDD = \sqrt{TDDD^2 + TIDD^2} \quad (5.5)$$

where TDDD is the total discrete demand distortion

$$TDDD = \frac{1}{I_{demand}} \sqrt{\sum_{h=2}^{h_{max}} I_h^2} \quad (5.6)$$

and TIDD is the total interharmonic demand distortion

$$TIDD = \frac{1}{I_{demand}} \sqrt{\sum_{h=0}^{h_{max}-1} IRSS_{h,h+1}^2} \quad (5.7)$$

The IRSS term is used to denote the root sum square value of the current interharmonics between two consecutive harmonics h and $h+1$. At a power system frequency of 60 Hz, using a frequency resolution of 5 Hz, the IRSS is defined by

$$IRSS_{h,h+1} = \sqrt{\sum_{f=60h+5}^{60(h+1)-5} I_f^2} \quad (5.8)$$

Since the load is continually changing the TDD is normalized using the maximum demand load current instead of the fundamental component [112]. For the purpose of this study the maximum demand load current was set as 1500 A.

In this study the harmonics were calculated using an FFT on the time domain waveforms obtained from the PSCAD simulation. The FFT is described in [14] and was performed using Matlab to obtain the harmonic spectra and phase angles for the parameters of interest. The harmonic indices were then calculated with a 5 Hz frequency resolution using a Matlab program provided in Appendix C.

The harmonic distortion indices measured from the controlled rectifier power supply and the uncontrolled rectifier chopper power supply are summarized in Tables 5.1

Table 5.1: Simulated Controlled Rectifier Harmonic Distortion

Variable	Maximum	Minimum	Mean	Median	95% CPF	99% CPF
$V_{in}(kV)$	18.091	17.981	18.034	18.033	18.070	18.083
$I_l(A)$	1270.5	1230.1	1251.1	1251.6	1262.5	1267.2
TDHD(%)	17.387	15.795	16.608	16.607	17.131	17.276
TIHD(%)	8.3367	4.6070	6.6321	6.6255	7.8255	8.2917
THD(%)	18.230	17.566	17.903	17.910	18.089	18.173
TDDD(%)	10.436	9.6789	10.079	10.088	10.308	10.386
TIDD(%)	6.8797	3.2482	5.0787	5.0632	6.3186	6.8316
TDD(%)	12.004	10.795	11.311	11.289	11.671	11.944

Table 5.2: Simulated Uncontrolled Rectifier Chopper Harmonic Distortion

Variable	Maximum	Minimum	Mean	Median	95% CPF	99% CPF
$V_{in}(kV)$	18.980	18.974	18.978	18.978	18.980	18.980
$I_l(A)$	959.24	955.86	957.42	957.43	958.46	958.97
TDHD(%)	5.6828	5.6085	5.6580	5.6601	5.6771	5.6814
TIHD(%)	1.1481	0.4132	0.7187	0.7080	1.0206	1.1051
THD(%)	5.7255	5.6968	5.7058	5.7047	5.7180	5.7227
TDDD(%)	3.4913	3.3669	3.3974	3.3881	3.4511	3.4823
TIDD(%)	2.1507	0.8071	1.3491	1.3428	1.8959	2.0624
TDD(%)	4.7153	3.5746	3.9612	3.9383	4.4327	4.6086

and 5.2, respectively. The distortion values were calculated for each individual phase while the tabulated values represent the average distortion from all three phases.

The results show that both the THD and TDD are significantly lower when using the uncontrolled rectifier chopper power supply. At the 95% CPF level the THD from the controlled rectifier is 18.09% as opposed to 5.72% from the uncontrolled rectifier chopper. Similarly the TDD from the controlled rectifier is 11.67% as opposed to 4.43% from the uncontrolled rectifier chopper. It can also be observed that the interharmonic distortion from the controlled rectifier is higher, which will likely lead to higher voltage flicker.

To verify that the harmonics obtained through simulation are correct the harmonic spectra shown in Figures 5.4 and 5.8 were compared to the harmonics measured at two DC smelting furnaces. The measured results are shown in Figure 5.9 and show a similar level of characteristic distortion for both configurations. As expected the measured data shows higher levels of triplen and even order harmonics. This exist

on an actual system and is due to unbalance in the supply, impedance and firing angle mismatch between both 6-pulse converters, and controller instability [13]. The simulation can easily be adjusted, as shown in Chapter 4, to give similar results by changing the impedances such that there is some unbalance between the phases and between both 6-pulse converters.

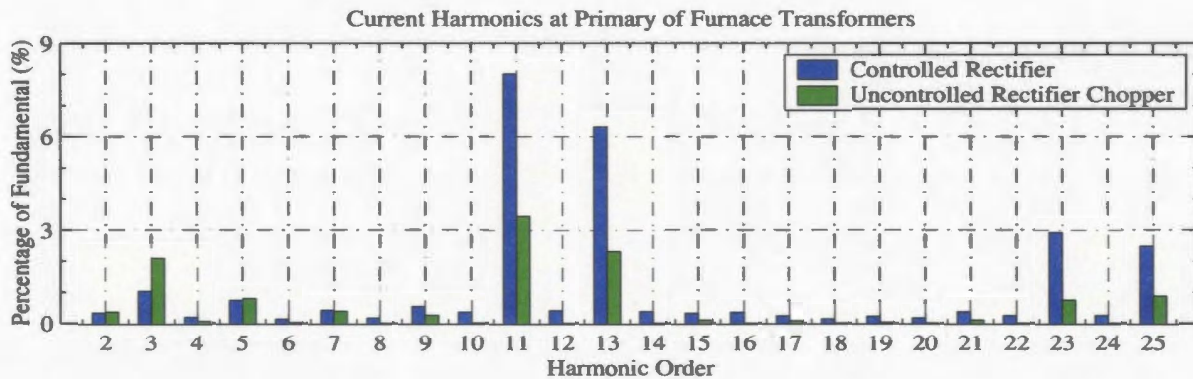


Figure 5.9: Measured DC Smelting Furnace Harmonic Distortion

The level of interharmonic distortion shown in Figures 5.4 can be compared to the harmonic spectra provided in [3], which shows measured data from a DC melting furnace. Both cases are for a 12-pulse controlled rectifier power supply and show similar levels of characteristic harmonic and interharmonic distortion.

5.2.2 Unbalanced Voltage

Voltage imbalance is calculated using symmetrical components and is defined as the ratio of the fundamental component of the negative sequence voltage to the fundamental component of the positive sequence voltage [119].

$$V_{unb} = \frac{V_{neg}}{V_{pos}} \times 100\% \quad (5.9)$$

where V_{neg} is the negative sequence voltage and V_{pos} is the positive sequence voltage. Using phasor notation the positive and negative sequence voltages can be calculated

as

$$V_{pos} = \frac{1}{3} |V_{a1} \angle \theta_{a1} + a V_{b1} \angle \theta_{b1} + a^2 V_{c1} \angle \theta_{c1}| \quad (5.10)$$

$$V_{neg} = \frac{1}{3} |V_{a1} \angle \theta_{a1} + a^2 V_{b1} \angle \theta_{b1} + a V_{c1} \angle \theta_{c1}| \quad (5.11)$$

where a is a complex number defined as

$$a = 1 \angle 120^\circ = -\frac{1}{2} + j \frac{\sqrt{3}}{2} \quad (5.12)$$

The magnitude and phase of the fundamental voltages were obtained using the FFT described in the previous subsection. The Matlab program used to calculate the unbalance values for each window of data is provided for reference in Appendix C. This results in a positive sequence, negative sequence, and unbalance value for each window of simulated data.

The voltage imbalance calculated from the controlled rectifier and uncontrolled rectifier chopper power supply simulations are summarized in Tables 5.3 and 5.4, respectively.

Table 5.3: Simulated Controlled Rectifier Voltage Unbalance

Variable	Maximum	Minimum	Mean	Median	95% CPF	99% CPF
$V_{an}(\text{kV})$	18.100	17.979	18.033	18.032	18.070	18.090
$V_{bn}(\text{kV})$	18.089	17.983	18.036	18.033	18.072	18.085
$V_{cn}(\text{kV})$	18.085	17.980	18.033	18.033	18.069	18.083
$V_{pos}(\text{kV})$	17.811	17.682	17.745	17.743	17.787	17.803
$V_{neg}(\text{V})$	33.171	1.1344	11.066	9.9960	20.316	28.545
$V_{unb}(\%)$	0.1867	0.0064	0.0624	0.0563	0.1146	0.1607

Table 5.4: Simulated Uncontrolled Rectifier Chopper Voltage Unbalance

Variable	Maximum	Minimum	Mean	Median	95% CPF	99% CPF
$V_{an}(\text{kV})$	18.984	18.973	18.978	18.978	18.982	18.984
$V_{bn}(\text{kV})$	18.983	18.971	18.978	18.977	18.982	18.983
$V_{cn}(\text{kV})$	18.984	18.972	18.978	18.978	18.981	18.983
$V_{pos}(\text{kV})$	18.948	18.942	18.946	18.946	18.948	18.948
$V_{neg}(\text{V})$	6.9327	0.6307	2.5697	2.3892	4.6635	6.4751
$V_{unb}(\%)$	0.0366	0.0033	0.0136	0.0126	0.0246	0.0342

The results show that the voltage imbalance is lower when using the uncontrolled rectifier chopper power supply. At the 95% CPF level the voltage imbalance for the controlled rectifier is 0.1146% as opposed to 0.0246% for the uncontrolled rectifier chopper. The results are very low since the supply is assumed to be balanced. In an actual industrial power system the supply voltage will have some existing unbalance which will tend to result in higher measured values.

5.2.3 Voltage Flicker

Voltage fluctuations are systematic variations of the voltage envelope, or a series of random voltage changes, the magnitude of which does not normally exceed the voltage ranges of 0.9 to 1.1 pu [125]. The term flicker is derived from the impact of the voltage fluctuations on lamps such that they are perceived to flicker by the human eye. One of the most common causes of voltage flicker on utility transmission and distribution systems are arc furnace loads.

Voltage flicker is a difficult problem to quantify and solve because a combination of factors contribute to the flicker problem. Not only is some deviation in voltage supplying lighting circuits required, but a person must be present to view the possible changes in light intensity. Flicker does not damage electrical equipment connected to the system and is mainly an annoyance, particularly if the disturbances are cyclic or occur rapidly.

The IEC defines flicker in terms of the statistical indices P_{st} and P_{lt} [116]. The P_{st} represents the short-term flicker severity index and is calculated over a 10 minute interval, while the P_{lt} represents the long-term flicker severity index and consist of 12 P_{st} values. A P_{st} value greater than unity corresponds to the level of irritability for 50% of the persons subjected to the measured flicker. The P_{st} is calculated from instantaneous P_{f5} flicker values recorded by the flickermeter described in [118]. A P_{f5} value greater than unity corresponds to the level of noticeability for 50% of the persons subjected to the measured flicker.

Since 10 minutes is too long for a PSCAD simulation a single P_{st} value is calculated for the 20 second simulation. The instantaneous flicker values were obtained by constructing a modified version of the IEC flickermeter [118] in PSCAD. The results were then subsequently analysed using Matlab to obtain the P_{st} values. The Matlab program is provided in Appendix C, while the compliance results from the PSCAD flickermeter are provided in Appendix D.

The instantaneous voltage flicker measured from the controlled rectifier power supply and the uncontrolled rectifier chopper power supply are summarized in Tables 5.5 and 5.6, respectively. The instantaneous flicker values were calculated for each individual phase, as well as for the average distortion from all three phases.

Table 5.5: Simulated Controlled Rectifier Instantaneous Voltage Flicker

Variable	Maximum	Minimum	Mean	Median	95% CPF	99% CPF
$P_{f_{a}}(\text{pu})$	6.6339	1.0967	2.5409	2.3131	4.5082	5.9110
$P_{f_{b}}(\text{pu})$	5.8278	0.7666	2.5084	2.3508	4.4023	5.5197
$P_{f_{c}}(\text{pu})$	7.2990	1.0037	2.7706	2.5649	4.8797	6.4364
$P_{f_{\text{avg}}}(\text{pu})$	6.5348	1.2097	2.6066	2.4602	4.5068	5.3238

Table 5.6: Simulated Uncontrolled Rectifier Chopper Instantaneous Voltage Flicker

Variable	Maximum	Minimum	Mean	Median	95% CPF	99% CPF
$P_{f_{a}}(\text{pu})$	0.2107	0.0317	0.0854	0.0823	0.1391	0.1816
$P_{f_{b}}(\text{pu})$	0.2660	0.0271	0.0903	0.0839	0.1566	0.2123
$P_{f_{c}}(\text{pu})$	0.1861	0.0377	0.0917	0.0912	0.1370	0.1620
$P_{f_{\text{avg}}}(\text{pu})$	0.1864	0.0491	0.0891	0.0889	0.1264	0.1639

The results clearly show that the voltage flicker is lower when using the uncontrolled rectifier chopper power supply. The P_{st} values corresponding to the tabulated instantaneous flicker for the controlled rectifier and the uncontrolled rectifier chopper power supplies are 1.4604 and 0.2663, respectively.

To verify that the flicker results are appropriate the simulation values are compared with six hours of measured data from two DC smelting furnaces. The measured flicker data is provided in Figure 5.10.

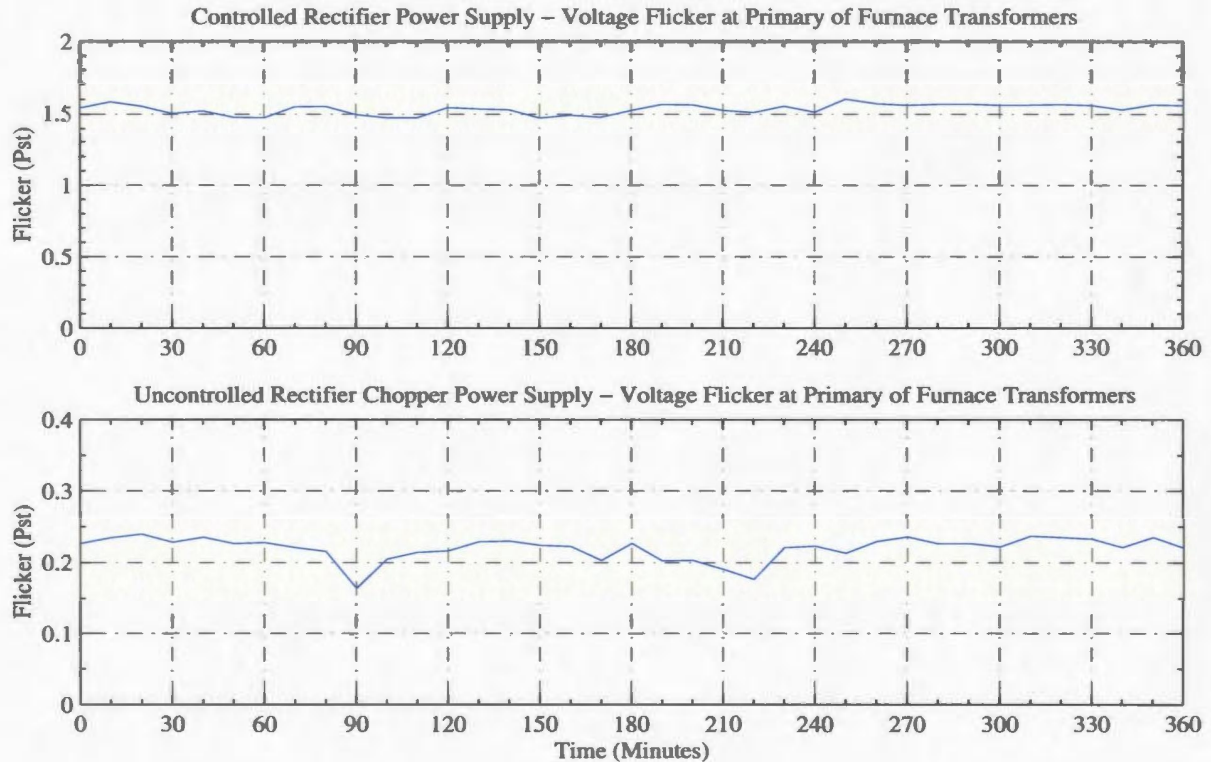


Figure 5.10: Measured DC Smelting Furnace Voltage Flicker

The simulated results are in good agreement with the measured data, which suggest that the PSCAD models are appropriate to represent a DC smelting furnace. The measured results are slightly different and this is mainly due to the fact that the DC furnaces investigated in this study are located on different power systems and running under different process conditions with different power levels.

5.2.4 Power and Power Factor

The power profile from a DC smelting furnace using a controlled rectifier power supply was compared to an AC furnace in Chapter 1 and was shown to be much more stable. A further reduction in power fluctuations are obtained when using the uncontrolled rectifier chopper power supply as shown in Figure 5.11. All data was trended at a 200 ms rate.

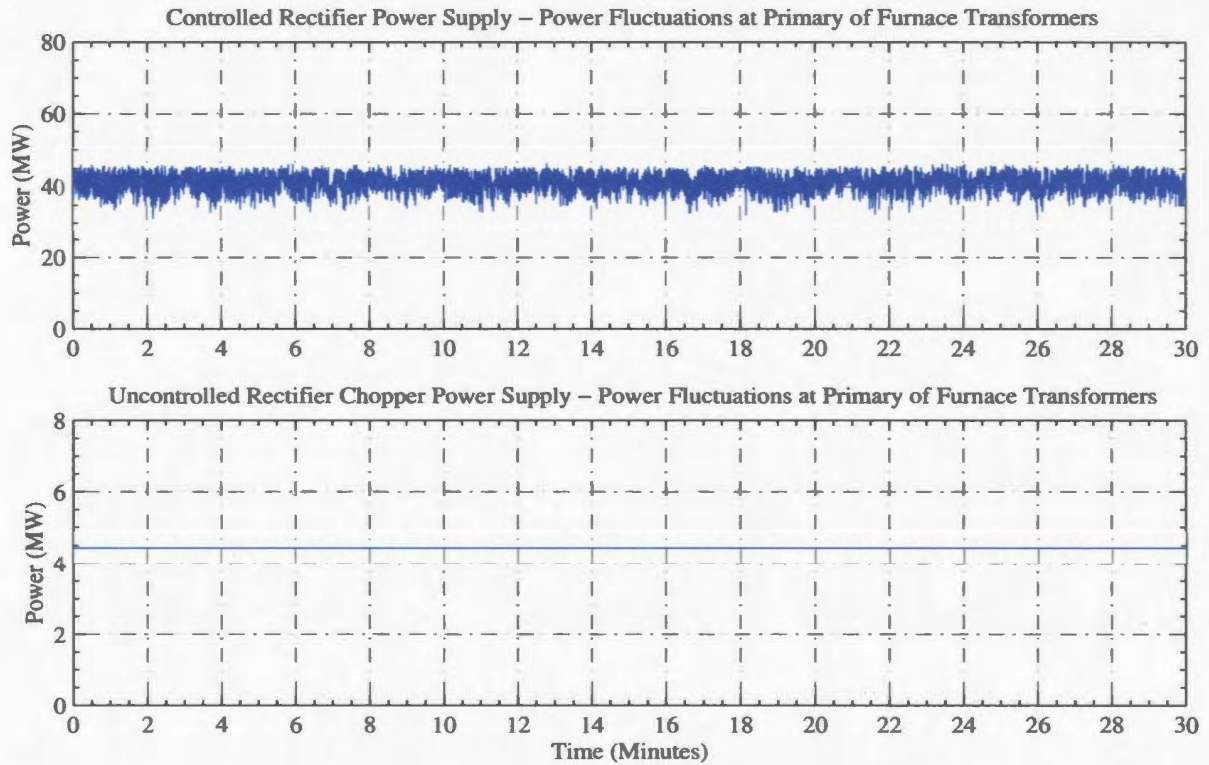


Figure 5.11: Measured DC Smelting Furnace Power

Traditionally power factor was defined as the cosine of the phase angle between the voltage and current. This definition is accurate if there are no harmonics present on the system. This, however, this will not be the case for most industrial applications, especially those operating with EAF loads. When harmonics are present the terms displacement power factor and distortion factor are often used in power factor calculations. The displacement power factor results from the lack of coincidence of the phase angles between the voltage and current at the fundamental frequency. While the distortion factor represents the effect of wave shape distortions on the power factor.

When the power and RMS values of voltage and current are known, as in this study, the per phase power factor can be calculated using [125]

$$PF = \frac{P}{S} = \frac{P}{V_{ln} I_l} \quad (5.13)$$

where P , V_{ln} , and I_l are the per phase power, RMS line-to-neutral voltage, and RMS line current including harmonics. For the purpose of this study the values were averaged from each window and used to obtain the results.

In unbalanced system with sinusoidal waveforms the definitions for apparent power and power factor in terms of sequence components are provided in [130]. When harmonics are present on unbalanced systems there are no clear definitions for power factor [125,132] and in many cases the average value is calculated.

The power factor measured from the controlled rectifier power supply and the uncontrolled rectifier chopper power supply are summarized in Tables 5.7 and 5.8, respectively. The tabulated values include the per phase power factor and displacement power factor, as well as the average power factor from all three phases.

Table 5.7: Simulated Controlled Rectifier Power Factor

Variable	Maximum	Minimum	Mean	Median	95% CPF	99% CPF
P(MW)	51.464	51.306	51.379	51.381	51.432	51.463
DPF_a(pu)	0.7879	0.7705	0.7795	0.7794	0.7862	0.7882
DPF_b(pu)	0.7907	0.7698	0.7800	0.7804	0.7864	0.7891
DPF_c(pu)	0.7907	0.7713	0.7801	0.7796	0.7868	0.7902
PF_a(pu)	0.7694	0.7495	0.7587	0.7585	0.7656	0.7677
PF_b(pu)	0.7705	0.7488	0.7592	0.7595	0.7658	0.7688
PF_c(pu)	0.7703	0.7502	0.7594	0.7589	0.7664	0.7698
PF(pu)	0.7688	0.7499	0.7591	0.7589	0.7654	0.7679

Table 5.8: Simulated Uncontrolled Rectifier Chopper Power Factor

Variable	Maximum	Minimum	Mean	Median	95% CPF	99% CPF
P(MW)	52.011	51.869	51.945	51.944	51.996	52.009
DPF_a(pu)	0.9571	0.9556	0.9562	0.9563	0.9567	0.9570
DPF_b(pu)	0.9570	0.9553	0.9562	0.9562	0.9567	0.9569
DPF_c(pu)	0.9569	0.9555	0.9562	0.9562	0.9567	0.9569
PF_a(pu)	0.9540	0.9522	0.9530	0.9530	0.9535	0.9538
PF_b(pu)	0.9538	0.9519	0.9529	0.9529	0.9535	0.9537
PF_c(pu)	0.9537	0.9521	0.9530	0.9530	0.9535	0.9537
PF(pu)	0.9532	0.9525	0.9530	0.9530	0.9531	0.9532

As expected the results show that the power factor is much lower when using the controlled rectifier power supply. At the 95% CPF level the power factor from

the controlled rectifier is 0.7654 as opposed to 0.9531 from the uncontrolled rectifier chopper. The results from the controlled rectifier can be expected to fluctuate as a function of the firing angle, while the results from the uncontrolled rectifier chopper will be more stable as the duty ratio changes.

To verify that the power factor results are appropriate the simulation values are compared with measured data from two DC smelting furnaces. The measured power factor data is provided in Figure 5.12.

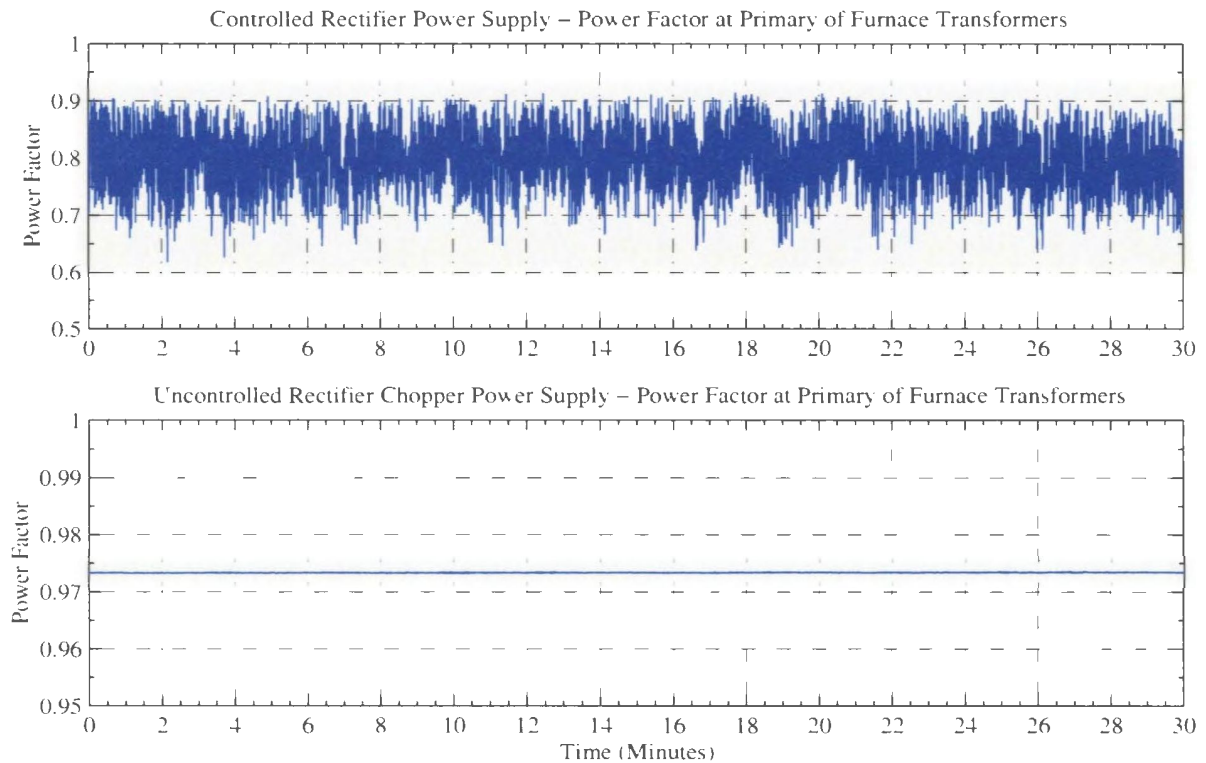


Figure 5.12: Measured DC Smelting Furnace Power Factor

The simulated results are in good agreement with the measured data, which suggest that the simulation is an appropriate means of comparing both rectification technologies. The measured data is slightly higher and this is most likely due to the fact that the actual power supply is operating with a different value for the control variable.

5.3 Rectifier Performance

Rectifier performance indices of interest include the efficiency (η_e), rectification ratio (η_r), ripple factor (RF), form factor (FF), and transformer utilization factor (TUF) [143]. Each index requires knowledge of the average output voltage (V_d), average output current (I_d), and DC output power.

$$P_{ddc} = V_d I_d \quad (5.14)$$

as well as the RMS output voltage (V_{drms}), the RMS output current (I_{drms}), and AC output power

$$P_{dac} = V_{drms} I_{drms} \quad (5.15)$$

The indices are defined using these parameters and are described in the following subsections along with the simulation results. The indices are calculated using the same windows of data presented in the previous section.

An ideal rectifier should have a purely sinusoidal input current, that is in phase with the input voltage, and a ripple free output. This condition would result in an efficiency and rectification ratio of 100%, a zero ripple factor and form factor, and a transformer utilization factor of unity.

5.3.1 Efficiency

The efficiency is a measure of the losses through the power supply and is generally defined as the ratio of the input power to output power

$$\eta_e = \frac{P}{P_d} \times 100\% \quad (5.16)$$

This is an important parameter to the furnace operator since it directly impacts on the operating cost of the furnace.

It is anticipated that the losses in the controlled rectifier transformers will be greater due to the lower power factor and higher harmonic loading. However, the

losses in the uncontrolled rectifier and chopper sections will probably be greater due to the additional components and forced commutation technique used to switch the IGBT devices.

The efficiency measured from the controlled rectifier power supply and the uncontrolled rectifier chopper power supply are summarized in Tables 5.9 and 5.10, respectively. The tabulated values include the control variable, input power, output power, and efficiency. The control variable is included to give an indication of the power supply operation under which the results were obtained.

Table 5.9: Simulated Controlled Rectifier Efficiency

Variable	Maximum	Minimum	Mean	Median	95% CPF	99% CPF
$\alpha(^{\circ})$	38.866	37.167	38.032	38.054	38.515	38.7138
P(MW)	51.464	51.306	51.379	51.381	51.432	51.463
P_d(MW)	50.041	49.964	50.000	50.001	50.024	50.037
$\eta_e(\%)$	97.434	97.165	97.316	97.316	97.393	97.432

Table 5.10: Simulated Uncontrolled Rectifier Chopper Efficiency

Variable	Maximum	Minimum	Mean	Median	95% CPF	99% CPF
Duty(%)	72.578	70.270	71.281	71.265	72.013	72.550
P(MW)	52.011	51.869	51.945	51.944	51.996	52.009
P_d(MW)	50.019	49.987	50.000	49.999	50.010	50.017
$\eta_e(\%)$	96.385	96.146	96.256	96.253	96.340	96.379

The results show that the efficiency is lower when using the uncontrolled rectifier chopper power supply. When comparing average values the efficiency from the controlled rectifier is 97.32% as opposed to 96.26% from the uncontrolled rectifier chopper. This results in approximately an additional $500kW$ loss from the uncontrolled rectifier chopper power supply when operating at the $50MW$ level.

5.3.2 Rectification Ratio

The rectification ratio is a figure of merit that allows the rectifier effectiveness to be compared. The rectification ratio is defined as [143]

$$\eta_r = \frac{P_{ddc}}{P_{dac}} \times 100\% \quad (5.17)$$

where P_{ddc} is the DC component of the output power and P_{dac} is the AC component of the output power.

The rectification ratio from the controlled rectifier power supply and the uncontrolled rectifier chopper power supply are summarized in Tables 5.11 and 5.12, respectively. The tabulated values include the DC component of the output power, the AC component of the output power, and the rectification ratio.

Table 5.11: Simulated Controlled Rectifier Rectification Ratio

Variable	Maximum	Minimum	Mean	Median	95% CPF	99% CPF
P_{ddc} (MW)	50.060	49.977	50.010	50.009	50.034	50.052
P_{dac} (MW)	50.086	49.994	50.030	50.029	50.061	50.079
η_r (%)	99.985	99.919	99.961	99.962	99.979	99.984

Table 5.12: Simulated Uncontrolled Rectifier Chopper Rectification Ratio

Variable	Maximum	Minimum	Mean	Median	95% CPF	99% CPF
P_{ddc} (MW)	50.043	49.995	50.011	50.010	50.026	50.040
P_{dac} (MW)	50.087	50.007	50.028	50.027	50.050	50.081
η_r (%)	99.984	99.913	99.966	99.968	99.978	99.983

The results do not indicate that there is a significant difference in the rectification ratio between both power supply configurations.

5.3.3 Ripple Factor

The ripple factor is a measure of the ripple content in the output voltage. The ripple factor is defined as [143]

$$RF = \sqrt{\frac{V_{drms}^2 - V_d^2}{V_d^2}} = \sqrt{\left(\frac{V_{drms}}{V_d}\right)^2 - 1} \quad (5.18)$$

where V_d is the average output voltage and V_{drms} is the RMS output voltage.

The ripple factor from the controlled rectifier power supply and the uncontrolled rectifier chopper power supply are summarized in Tables 5.13 and 5.14, respectively. The tabulated values include the average output voltage, the RMS output voltage, and the ripple factor.

Table 5.13: Simulated Controlled Rectifier Ripple Factor

Variable	Maximum	Minimum	Mean	Median	95% CPF	99% CPF
$V_d(V)$	871.43	843.34	856.89	856.63	865.93	869.46
$V_{drms}(V)$	871.35	843.20	856.74	856.40	865.76	869.35
RF(pu)	0.0268	0.0128	0.0189	0.0185	0.0236	0.0268

Table 5.14: Simulated Uncontrolled Rectifier Chopper Ripple Factor

Variable	Maximum	Minimum	Mean	Median	95% CPF	99% CPF
$V_d(V)$	874.66	845.06	858.26	858.01	867.42	874.47
$V_{drms}(V)$	874.56	844.71	858.13	857.90	867.35	874.38
RF(pu)	0.0288	0.0112	0.0168	0.0163	0.0213	0.0274

The results do not indicate that there is a significant difference in the ripple factor between both power supply configurations. The average value from the controlled rectifier is slightly higher at 0.0189 as opposed to 0.0168 from the uncontrolled rectifier chopper.

5.3.4 Form Factor

The form factor is a measure of the shape of the output current. The form factor is defined as [143]

$$FF = \frac{I_{drms}}{I_d} \quad (5.19)$$

where I_d is the average output current and I_{drms} is the RMS output current.

The form factor from the controlled rectifier power supply and the uncontrolled rectifier chopper power supply are summarized in Tables 5.15 and 5.16, respectively.

The tabulated values include the average output current, the RMS output current, and the form factor.

Table 5.15: Simulated Controlled Rectifier Form Factor

Variable	Maximum	Minimum	Mean	Median	95% CPF	99% CPF
$I_d(\text{kA})$	59.298	57.403	58.387	58.413	58.923	59.114
$I_{\text{drms}}(\text{kA})$	59.287	57.396	58.374	58.396	58.901	59.133
$\text{FF}(\text{pu})$	1.0004	1.0001	1.0002	1.0002	1.0003	1.0004

Table 5.16: Simulated Uncontrolled Rectifier Chopper Form Factor

Variable	Maximum	Minimum	Mean	Median	95% CPF	99% CPF
$I_d(\text{kA})$	59.270	57.189	58.293	58.305	59.002	59.193
$I_{\text{drms}}(\text{kA})$	59.243	57.181	58.282	58.291	58.987	59.174
$\text{FF}(\text{pu})$	1.0005	1.0001	1.0002	1.0002	1.0003	1.0004

The results do not indicate that there is a significant difference in the ripple factor between both power supply configurations.

5.3.5 Transformer Utilization Factor

The transformer utilization factor is a measure of the harmonic loading and power through the rectifier transformers. The transformer utilization factor is defined as [143]

$$TUF = \frac{P_d}{S} \quad (5.20)$$

where P_d is the output power and S is the apparent power at the input.

The transformer utilization factor from the controlled rectifier power supply and the uncontrolled rectifier chopper power supply are summarized in Tables 5.17 and 5.18, respectively. The tabulated values include the output power, apparent power at the input, and the transformer utilization factor.

As expected the transformer utilization factor from the controlled rectifier is lower than that from the uncontrolled rectifier chopper. The average value from the controlled rectifier is 0.7389 as opposed to 0.9175 from the uncontrolled rectifier chopper.

Table 5.17: Simulated Controlled Rectifier Transformer Utilization Factor

Variable	Maximum	Minimum	Mean	Median	95% CPF	99% CPF
$P_d(\text{MW})$	50.041	49.964	50.000	50.001	50.024	50.037
$S(\text{MVA})$	68.534	66.760	67.685	67.710	68.189	68.390
$\text{TUF}(\text{pu})$	0.7491	0.7294	0.7389	0.7386	0.7451	0.7477

Table 5.18: Simulated Uncontrolled Rectifier Transformer Utilization Factor

Variable	Maximum	Minimum	Mean	Median	95% CPF	99% CPF
$P_d(\text{MW})$	50.019	49.987	50.000	49.999	50.010	50.017
$S(\text{MVA})$	54.607	54.428	54.509	54.509	54.565	54.591
$\text{TUF}(\text{pu})$	0.9189	0.9160	0.9175	0.9174	0.9184	0.9188

This is a result of the phase control scheme used in the controlled rectifier power supply, which tends to lower the power factor and increase the harmonic distortion. The lower utilization factor dictates that a larger transformer must be used in the controlled rectifier case to deliver the same power to the furnace.

5.4 Reliability

Reliability is a measure of the performance of the system over a specified period of time, as opposed to quality, which is a measure of conformance to a specific standard at a given point in time [144]. A typical reliability analysis factors into account the failure rates for the components being used in the system to predict the Mean Time Between Failure (MTBF) and the Mean Time To Repair (MTTR). The failure rates for the type of components used in this study are provided in [145]. Once the MTBF and MTTR are known the system availability can be determined, and the reliability for various configurations can be compared.

A detailed reliability analysis not only uses the failure rates from the various components but the number of components and configuration are also important. For instance, if additional units are connected in parallel it is possible to increase the reliability by adding redundancy to the system. All components including connections

need to be factored into the equation to arrive at an accurate estimate. A statistical analysis of the data and the assumptions used in the calculations are then factored in to provide confidence levels for the predicted system availability. The procedure is complicated and not required to compare different configurations.

A simplified method based on parts count analysis can be performed to obtain at a quick comparison [145] between both power supply configurations. This approach is accurate since the reliability of any given technology is directly proportional to the component count and to the electrical and cooling system connections used within the system. The interest in this study is to determine which system is more reliable and not to arriving at actual numbers for the system availability, hence the parts count method will be used.

5.4.1 Controlled Rectifier

There are approximately 678 components used in the power and cooling circuits for the controlled rectifier power supply. The major components are summarized in Table 5.19.

Table 5.19: Controlled Rectifier Parts Count

Power Supply Component	Quantity
Transformers	2
Input Surge Arrestors	12
Damping Resistors	6
Damping Capacitors	6
Rectifier Thyristors	108
Rectifier Snubber Resistors	108
Rectifier Snubber Capacitors	108
Rectifier Fuses	108
Rectifier Cooling Connections	216
Output Surge Arrestors	2
Output Reactors	2
TOTAL	678

A similar analysis is performed in [7] for a 600 V controlled rectifier power supply with a 80 kA current limit. The total number of components in that example was

Table 5.20: Uncontrolled Rectifier Chopper Parts Count

Power Supply Component	Quantity
Transformers	2
Input Surge Arrestors	12
Damping Resistors	6
Damping Capacitors	6
Rectifier Diodes	108
Rectifier Snubber Resistors	108
Rectifier Snubber Capacitors	108
Rectifier Fuses	108
Rectifier Cooling Connections	216
DC Link Capacitors	144
DC Link Resistors	36
Chopper Module IGBTs	72
Chopper Module Freewheeling Diodes	36
Chopper Module Snubber Resistors	108
Chopper Module Snubber Capacitors	108
Chopper Module Snubber Diodes	216
Chopper Module Paralleling Reactors	72
Chopper Module Fuses	144
Chopper Cooling Connections	216
Output Surge Arrestors	2
Output Reactors	2
TOTAL	1830

approximately 1500, which includes 720 electronic components.

5.4.2 Uncontrolled Rectifier Chopper

There are approximately 1830 components used in the power and cooling circuits for the uncontrolled rectifier chopper power supply. The major components are summarized in Table 5.20.

A similar analysis is performed in [7] for a 600 V uncontrolled rectifier chopper power supply with a 80 kA current limit. The total number of components in that example was approximately 13500, which includes 12000 electronic components.

For the two power supplies analyzed in this chapter it can be concluded that the uncontrolled rectifier chopper system will have a failure rate that is approximately 2.5 times that of the controlled rectifier. The results in [7] are more dramatic and predict a failure rate of 4 to 8 times. In any event the MTBF of the uncontrolled

rectifier chopper power supply will be significantly greater when compared to a similar controlled rectifier power supply. It is also anticipated that the increased component count will result in longer trouble shooting periods thereby increasing the MTTR and further reducing the system availability.

The controlled rectifier has been used in numerous electric arc furnace power supplies and has field-proven reliability. The reliability of the uncontrolled rectifier chopper power supply is still not sufficiently proven to enable an actual assessment when compared with more established rectification concepts. Specifically, the performance of the DC link capacitors and their ability to withstand high ripple current over many years of operation will need to be evaluated based on actual operating data. A major contributor to the MTBF on low and medium voltage drives are the failure of similar capacitors [7].

5.5 Summary

The uncontrolled rectifier chopper power supply is less disruptive to the utility system than the controlled rectifier power supply. This is evident when comparing the power quality parameters at the input. The uncontrolled rectifier chopper combination also has a better utilization factor and thus requires a smaller transformer. The waveforms at the output are not significantly affected by either power supply configuration.

The additional energy conversion and energy storage elements in the uncontrolled rectifier chopper power supply dictate that the losses associated with this configuration are higher than those observed when using an equivalent controlled rectifier power supply. The additional components also lower the reliability and increase the cost of the uncontrolled rectifier chopper power supply.

Chapter 6

Conclusion

A description of the controlled rectifier and uncontrolled rectifier chopper power supply configurations, including the operating and control characteristics, has been presented in the thesis. The power supplies were of the type used in high current industrial applications including DC smelting furnace power supplies. Equations were provided for the ideal cases of constant current or constant voltage output, and were used to approximate the power supply characteristics without using detailed simulation.

In the event that a detailed dynamic simulation is required, an electric arc furnace model that can be used in an electromagnetic transient simulation environment was developed. The PSCAD program was chosen for this study and all model parameters including the smelting furnace model, power supply models, and control system models were included in enough detail to reproduce measured results from a known system. If necessary the models can be transferred to another similar program if PSCAD is unavailable.

In addition, a comparison of both the controlled rectifier and uncontrolled rectifier chopper power supply configurations and an assessment of their suitability for DC smelting furnace applications were presented. The comparison investigated the power quality at the input, the rectifier performance, and the reliability. It was determined

that the uncontrolled rectifier chopper power supply performed better with regard to power quality and rectifier performance while the controlled rectifier power supply had better efficiency and improved reliability.

6.1 Original Contributions

The major contribution from the thesis was to provide an unbiased opinion as to which power supply configuration is better suited for use with a DC smelting furnace load. To compare both configurations with the same load and the same power system parameters a PSCAD simulation was performed. In order to verify that the models were accurate enough to represent an actual industrial system measurements were performed at two smelting facilities operating DC smelting furnaces with each power supply configuration.

The power supply configurations and control structures shown in Chapter 2 for the controlled rectifier, and in Chapter 3 for the uncontrolled rectifier chopper power supplies are of the type used in industry. Both configurations have been described in detail and the number and type of components required to construct a 50 MW power supply have been provided in Chapter 6. This information is difficult to obtain in published literature and as such has been included in the thesis.

The electric arc model used in the PSCAD simulations was based on temperature dependent thermodynamic and transport properties from typical arc furnace plasma. The channel arc model then used these temperature dependent parameters to represent the physical electric arc portion of the smelting furnace load. The arc length was randomly fluctuated at various frequencies to represent the operating characteristics from a DC smelting furnace.

Previous arc models were used to approximate the physical characteristics of the arc or to show the steady-state electrical characteristics under various conditions. These models were often represented by a fluctuating resistor or voltage source. The

model outlined in this study consists of a fluctuating resistor along with a voltage source to represent the nonlinear arc characteristic. Unlike previous furnace models the physical characteristics from the arc can be obtained if required.

The thesis also includes a model of the IEC flickermeter adapted for use in a simulation environment where it is not possible to run cases to represent 10 minutes of operation. The model has been tested and shown to be compliant with test points provided by the IEC for both 50 Hz and 60 Hz systems. As with the electric arc furnace model the flickermeter model can easily be transferred to another program other than PSCAD provided that filter models are available or can be constructed using other components.

6.2 Future Analysis

The slag layer within the smelting furnace was approximated as a fixed resistor which does not represent the operating case. In reality the bath resistance will fluctuate as the DC arc forms a depression in the slag layer. The depression is continually changing as the arc current fluctuates and the arc position moves. The size of the depression determines the slag depth and hence the slag resistance. This requires knowledge of the slag properties and the force of the arc jet to implement and should be incorporated to more accurately represent the smelting furnace load.

The controls were modeled based on PI controller configurations as is the practice in industry. However, as new advanced controls become more widely used the simulation should be updated to investigate new controller configurations and to determine the optimum control system to effectively stabilize the arcing load. The controls for the electrode regulation should also be included in the model to fully represent the smelting furnace system.

The IEC flickermeter as it is implemented does comply with the test standard. However, it requires approximately 20 seconds to stabilize and give meaningful results.

This is often longer than the required study period and involves a long simulation time before the actual study can be started. This can be avoided by properly initializing the filters used in the model and should be completed if a number cases for a particular study dictate performing the required modifications.

References

- [1] Stenkivist S.E., Stickler H., "The DC Arc Furnace - A Low Cost Melting Unit", ABB Review, No. 10, 1992.
- [2] Carpinelli G., DiManno M., Verde P., Tironi E., Zaninelli D., "AC and DC Arc Furnaces: A Comparison on Some Power Quality Aspects", IEEE Power Engineering Society Summer Meeting, Vol. 1, Page 499-506, July 18-22, 1999.
- [3] Ashmore S., Wikston J., Ma T., "Power Compensation of AC and DC EAF's", ISS Electric Furnace Conference Proceedings, Page 225-233, November 7-10, 1993.
- [4] Robertson S., "The Debate Between AC and DC", Iron Age New Steel, Vol. 11, No. 5, Page 44-48, May 1995.
- [5] Bowman B., "A Technical Comparison Between AC and DC Furnaces", Revue de Métallurgie: Cahiers d'Informations Techniques, Vol. 90, No. 6, Page 809-816, June 1993.
- [6] Takahashi M., "Recent Trends in Technology of DC Electric Arc Furnaces", Nippon Steel Technical Report, No. 55, Page 1-10, October 1992.
- [7] Siebert T., Troedson A., Ebner S., "AC to DC Power Conversion Now and in the Future", IEEE Petroleum and Chemical Industry Conference Proceedings, Page 145-152, September 24-26, 2001.
- [8] Scaini V., Urban B.M., "High Current DC Choppers and Their Operational Benefits", IEEE Petroleum and Chemical Industry Conference Proceedings, Page 173-180, September 28-30, 1998.
- [9] Theron D., Meyer M., Kadar L., "High Current DC Chopper Versus Thyristor Rectifier Power Supplies in DC Electric Arc Furnaces", Energize, Page 60-64, July/August 2001.
- [10] Popp A.S., Tomas M., "Comparison of Thyristors Vs Chopper Rectifiers in A Common Application", IEEE Petroleum and Chemical Industry Conference Proceedings, Page 133-140, September 11-13, 2000.

- [11] Schaefer J., "Rectifier Circuits: Theory and Design", John Wiley and Sons, 1965.
- [12] Pelly B.R., "Thyristor Phase-Controlled Converters and Cycloconverters", John Wiley and Sons, 1971.
- [13] Kimbark E.W., "Direct Current Transmission: Volume 1", John Wiley and Sons, 1971.
- [14] Arrillaga J., Bradley D.A., Bodger P.S., "Power System Harmonics", John Wiley and Sons, 1985.
- [15] Mohan N., Undeland T.M., Robbins W.P., "Power Electronics: Converters, Applications, and Design, John Wiley and Sons, 1995.
- [16] Spatney W., Slatinka L., "Power Supplies for DC Arc Furnaces", ABB Review, No. 6, 1992.
- [17] Kirchenmayer E., "Electrical Engineering of Arc Furnace Transformers: Furnace Transformer Types and Design Characteristics", Siemens Energy and Automation.
- [18] Poggi L., Di Palma G., "Transformers for AC and DC Electric Arc Furnaces", MPT International, Vol. 20, No. 1, Page 66-67, February 1997.
- [19] Reinhard J., Kloss A., "Converter Systems for Industry and Chemistry Applications", IEE European Conference on Power Electronics and Applications Conference Proceedings, Vol. 3, Page 250-254, September 13-16, 1993.
- [20] McMurray W., "Optimum Snubbers for Power Semiconductors", IEEE Transactions on Industry Applications, Vol. 8, No. 5, Page 593-600, September/October 1972.
- [21] Howe A.F., Newbery G., Nurse N.P., "DC Fusing in Semiconductor Circuits", IEEE Transactions on Industry Applications, Vol. 22, No. 3, Page 483-489, May/June 1986.
- [22] Acosta O.N., "Interphase Transformer for Multiple Connected Power Rectifiers", IEEE Transactions on Industry and General Applications, Vol. 1, No. 6, Page 423-428, November/December 1965.
- [23] Tzeng Y.S., Chen N., Wu R.N., "Modes of Operation in Parallel Connected 12-Pulse Uncontrolled Bridge Rectifiers Without an Interphase Transformer", IEEE Transactions on Industrial Electronics, Vol. 44, No. 3, Page 344-355, June 1997.
- [24] Hall J.K., Kettleborough J.G., Razak A.B., "Parallel Operation of Bridge Rectifiers Without an Interbridge Reactor", IEE Proceedings B, Vol. 137, No. 2, Page 125-140, March 1990.

- [25] Bhat P.S., Dubey G.K., Ghosh R., "Modes of Operation, Analysis and Evaluation of Optimum Filter Inductance for Three-Phase Fully Controlled Converter Fed DC Motor", IEEE Transactions on Power Apparatus and Systems, Vol. 104, No. 7, Page 1783-1788, July 1985.
- [26] Dubey G.K., "Modes of Operation and Analysis of a Separately Excited Motor Fed by a Three-Phase Converter with Freewheeling Diode", IEEE Transactions on Industrial Electronics, Vol. 33, No. 3, Page 332-336, August 1986.
- [27] Tzeng Y.S., "Harmonic Analysis of Parallel Connected 12-Pulse Uncontrolled Rectifier Without an Interphase Transformer" IEE Proceedings on Electric Power Applications, Vol. 145, No. 3, Page 253-260, May 1998.
- [28] Rice D.E., "A Detailed Analysis of Six-Pulse Converter Harmonic Currents", IEEE Transactions on Industry Applications, Vol. 30, No. 2, Page 294-304, March/April 1994.
- [29] Perreault D.J., Kassakian J.G., "Effects of Firing Angle Imbalance on 12-Pulse Rectifiers With Interphase Transformers", IEEE Transactions on Power Electronics, Vol. 10, No. 3, Page 257-262, May 1995.
- [30] Dewan S.B., Straughen A., "Power Semiconductor Circuits", John Wiley and Sons, 1975.
- [31] Kassakian J.G., Schlecht M.F., Verghese G.C., "Principles of Power Electronics", Addison-Wesley, 1991.
- [32] Scaini V., Ma T., "High Current DC Choppers in the Metals Industry", IEEE Industry Applications Society Annual Meeting, Vol. 4, Page 2629-2636, October 8-12, 2000.
- [33] Ladoux P., Bas C., Foch H., Nuns J., "Structure and Design of High Power Chopper for DC Arc Furnace", EPE International Conference on Power Electronics and Motion Control, September 9-11, 2002.
- [34] Beak J., Budding P., Scaini V., "Reusing and Rerating Older Rectifiers With New DC/DC Choppers", IEEE Transactions on Industry Applications, Vol. 37, No. 4, Page 1160-1166, July/August 2001.
- [35] Linden P.W., "Transformer Design and Application Considerations for Nonsinusoidal Load Currents", IEEE Transactions on Industry Applications, Vol. 32, No. 3, Page 633-645, May/June 1996.
- [36] Rashid M.H., "Design of LC Input Filters for Multiphase DC Choppers", IEE Proceedings B, Vol. 130, No. 1, Page 39-44, January 1983.

- [37] McMurray W., "Selection of Snubbers and Clamps to Optimize the Design of Transistor Switching Converters", IEEE Transactions on Industry Applications, Vol. 16, No. 4, Page 513-523, July/August 1980.
- [38] Dawson F.P., "DC-DC Converter Interphase Transformer Design Considerations: Volt-Seconds Balancing", IEEE Transactions on Magnetics, Vol. 26, No. 5, Page 2250-2252, September 1990.
- [39] Hancock M., "Rectifier Action with Constant Load Voltage: Infinite Capacitance Condition", Proceedings of the IEE, Vol. 120, No. 12, Page 1529-1530, December 1973.
- [40] Ray W.F., "The Effect of Supply Reactance on Regulation and Power Factor for an Uncontrolled Three-Phase Bridge Rectifier with Capacitive Load", IEE International Conference on Power Electronics and Variable Speed Drives, No. 234, Page 111-114, 1984.
- [41] Ray W.F., Davis R.M., Weatherhogg I.D., "The Three-Phase Bridge Rectifier with Capacitive Load", IEE International Conference on Power Electronics and Variable Speed Drives, No. 291, Page 153-156, 1988.
- [42] Caliskan V., Perreault D.J., Jahns T.M., Kassakian J.G., "Analysis of Three-Phase Rectifiers with Constant Voltage Loads", IEEE Transactions on Circuits and Systems, Vol. 50, No. 9, Page 1220-1226, September 2003.
- [43] Sakui M., Fujita H., Shioya M., "A Method for Calculating Harmonic Currents of a Three-Phase Bridge Uncontrolled Rectifier with DC Filter", IEEE Transactions on Industry Electronics, Vol. 36, No. 3, Page 434-440, August 1999.
- [44] Barton T.H., "The Polyphase Chopper - A Symmetrical Component Analysis", IEEE Transactions on Industry Applications, Vol. 19, No. 6, Page 1070-1075, November/December 1983.
- [45] Barton T.H., "The Three-Phase Chopper - Analytic Solution", IEEE Transactions on Industry Applications, Vol. 19, No. 6, Page 1070-1075, November/December 1983.
- [46] Satpathi H., Dubey G.K., Singh L.P., "A General Method of Analysis of Chopper Fed DC Separately Excited Motor", IEEE Transactions on Power Apparatus and Systems, Vol. 102, No. 4, Page 990-997, April 1983.
- [47] Naik K.B., Dubey G.K., Jain V.K., "Steady State Response Analysis of A Chopper Controlled DC Separately Excited Motor", IEEE Transactions on Power Apparatus and Systems, Vol. 104, No. 7, Page 1775-1782, July 1985.

- [48] Bhadra S.N., Rashid M.H., Ganguly S., "Generalized Analytic Approach for Multiphase Thyristor DC Choppers Driving Separately Excited Motor", IEEE Industry Applications Society Annual Meeting, Vol. 1, Page 399-404, 1985.
- [49] Kiong T.K., Qing-Guo W., Chieh H.C., "Advances in Industrial Control", Springer-Verlag, 1999.
- [50] Ogata K., "Modern Control Engineering", Prentice-Hall, 1997.
- [51] Hoyaux M.F., "Arc Physics", Springer-Verlag, 1968.
- [52] Lowke J.J., "Simple Theory of Free-Burning Arcs", Journal of Physics D: Applied Physics, Vol. 12, No. 11, Page 1873-1886, November 1979.
- [53] Ramakrishnan S., Stokes A., Lowke J.J., "Approximate Model for High-Current Free-Burning Arcs", Journal of Physics D: Applied Physics, Vol. 11, No. 11, Page 2267-2280, November 1978.
- [54] Lowke J.J., Ludwig H.C., "A Simple Model for High-Current Arcs Stabilized by Forced Convection", Journal of Applied Physics, Vol. 46, No. 8, Page 3352-3360, August 1975.
- [55] Tuma D.T., Lowke J.J., "Prediction of Properties of Arcs Stabilized by Forced Convection", Journal of Applied Physics, Vol. 46, No. 8, Page 3361-3367, August 1975.
- [56] Lowke J.J., "Characteristics of Radiation-Dominated Electric Arcs", Journal of Applied Physics, Vol. 41, No. 6, Page 2588-2600, May 1970.
- [57] Bowman B., "Measurements of Plasma Velocity Distributions in Free-Burning DC Arcs up to 2160 A", Journal of Physics D: Applied Physics, Vol. 5, No. 8, Page 1422-1432, August 1972.
- [58] Lowke J.J., Kovitya P., Schmidt H.P., "Theory of Free-Burning Arc Columns Including the Influence of the Cathode", Journal of Physics D: Applied Physics, Vol. 25, No. 11, Page 1600-1606, November 1992.
- [59] McKelliget J.W., Szekely J., "A Mathematical Model of the Cathode Region of a High Intensity Carbon Arc", Journal of Physics D: Applied Physics, Vol. 16, No. 6, Page 1007-1022, June 1983.
- [60] Hsu K.C., Pfender E., "Analysis of the Cathode Region of a Free-Burning High Intensity Argon Arc", Journal of Applied Physics, Vol. 54, No. 7, Page 3818-3824, July 1983.

- [61] Alexis J., Ramirez M., Trapaga G., Jonsson P., "Modelling of a DC Arc Furnace - Heat Transfer from the Arc", ISIJ International, Vol. 40, No. 11, Page 1089-1097, November 2000.
- [62] Sakulin M., "Zur Berechnung von Gleichstromlichtbögen". Elektrowaerme International Edition B: Industrielle Elektrowaerme, Vol. 39, No. 2, Page 93-98, April 1981.
- [63] Sakulin M., "Rechnerische Bestimmung der Kennlinien von Gleichstromlichtbögen mit Hilfe von Kanalmodellen". Elektrowaerme International Edition B: Industrielle Elektrowaerme, Vol. 40, No. 1, Page 18-24, February 1982.
- [64] Ahlers H., Timm K., "Untersuchungen von frei brennenden Gleichstromlichtbögen bis 12 MW an Elektrostahlöfen, Teil 1: Experimentelle Ergebnisse". Elektrowaerme International Edition B: Industrielle Elektrowaerme, Vol. 45, No. 5, Page 224-235, October 1987.
- [65] Ahlers H., Timm K., "Untersuchungen von frei brennenden Gleichstromlichtbögen bis 12 MW an Elektrostahlöfen, Teil 2: Modellbildung", Elektrowaerme International Edition B: Industrielle Elektrowaerme, Vol. 45, No. 6, Page 291-302, December 1987.
- [66] Meng M.W., Irons G.A., "Comparison of Electric Arc Models with Industrial Data", ISS Electric Furnace Conference Proceedings, Page 183-193, 2000.
- [67] Meng M.W., "Modeling of Electric Arcs in Electric Arc Furnace Steelmaking and Comparisons with Industrial Measurements", M.Eng. Thesis, McMaster University, 2001.
- [68] Wilhelmi H., Lyhs W., Pfender E., "Calculation of Thermodynamic and Transport Properties of a Typical Arc Furnace Plasma", Plasma Chemistry and Plasma Processing, Vol. 4, No. 4, Page 315-323, December 1984.
- [69] Ao M., Maki T., Tanahashi A., Nakamura T., Iguchi K., "Operation Results of DC Arc Furnace and Properties of DC Arcs", ISS Electric Furnace Conference Proceedings, Page 187-194, 1989.
- [70] Bowman B., "Properties of Electric Arcs in DC Furnaces", ISS Electric Furnace Conference Proceedings, Page 111-120, 1994.
- [71] Jones R.T., Reynolds Q.G., Alport M.J., "DC Arc Photography and Modeling", Minerals Engineering, Vol. 15, No. 11, Page 985-991, November 2002.
- [72] Robiette A.G., "Electric Smelting Processes", John Wiley and Sons, 1973.

- [73] Ma T., Bendzsak G.J., Perkins M., "Power System Design for High-Power Electric Smelting and Melting Furnaces", Conference of Metallurgist of the Metallurgical Society of CIM, August 23-27, 1992.
- [74] Dosa G., Kepes A., Ma T., Fantin P., "Computer Control of High-Power Electric Furnaces", Conference of Metallurgist of the Metallurgical Society of CIM, August 24-29, 1996.
- [75] Matyas A.G., Francki R.C., Donaldson K.M., Wasmund B., "Application of New Technology in the Design of High-Power Electric Smelting Furnaces", Conference of Metallurgist of the Metallurgical Society of CIM, August 23-27, 1992.
- [76] Donaldson K.M., Ham F.E., Francki R.C., Schofield J.G., "Design of Refractories and Bindings for Modern High-Productivity Pyrometallurgical Furnaces", Conference of Metallurgist of the Metallurgical Society of CIM, August 23-27, 1992.
- [77] Persson J., "Analyzing the Electrical Characteristics of Arc Furnaces", ISS Electric Furnace Conference Proceedings, Page 31-36, 1989.
- [78] Lavers J.D., Danai B., Biringer P.P., Chee-Hing D.J., "A Method of Examining in Detail Electric Arc Furnace Performance", IEEE Transactions on Industry Applications, Vol. 21, No. 1, Page 137-146, January/February 1985.
- [79] Fu T.H., Wu C.J., "Load Characteristics Analysis of AC and DC Arc Furnaces Using Various Power Definitions and Statistic Method", IEEE Transactions on Power Delivery, Vol. 17, No. 4, Page 1099-1105, October 2002.
- [80] Wu C.J., Fu T.H., Chen Y.J., "Load Characteristics and Harmonic Analysis of DC Arc Furnaces", IEEE Power Engineering Society Summer Meeting, Vol. 2, Page 778-782, July 16-20, 2000.
- [81] Andrews D., Bishop M.T., Witte J.F., "Harmonic Measurement, Analysis, and Power Factor Correction in a Modern Steel Manufacturing Facility", IEEE Transactions on Industry Applications, Vol. 32, No. 3, Page 617-624, May/June 1996.
- [82] Robert A., Couvreur M., "Arc Furnace Flicker Assessment and Mitigation", IEE International Conference on Electricity Distribution, No. 373, Page 221-226, 1993.
- [83] Bhargava B., "Arc Furnace Flicker Measurements and Control", IEEE Transactions on Power Delivery, Vol. 8, No. 1, Page 400-410, January 1993.
- [84] Read B., "Reducing Flicker and Harmonics from EAFs", Iron Age New Steel, Vol. 12, No. 1, Page 30-34, January 1996.

- [85] Mendis S.R., Bishop M.T., Witte J.F., "Investigations of Voltage Flicker in Electric Arc Furnace Power Systems", IEEE Industry Applications Society Annual Meeting, Vol. 3, Page 2317-2325, October 2-6, 1994.
- [86] Mendis S.R., Bishop M.T., Boyd D.M., "Investigation of Transmission System Voltage Flicker Due to Multiple AC and DC Furnace Operation", Iron and Steel-maker, Vol. 22, No. 10, Page 77-83, October 1995.
- [87] Mattavelli P., Perna M., "Analysis of Flicker Generation in DC Arc Furnaces", IEEE International Conference on Electric Power Engineering, Page 170-174, August 29 - September 2, 1999.
- [88] Tang L., Mueller D., Hall D., Samotyj M., Randolph J., "Analysis of DC Arc Furnace Operation and Flicker Caused by 187 Hz Voltage Distortion", IEEE Transactions on Power Delivery, Vol. 9, No. 2, Page 1098-1107, April 1994.
- [89] Mattavelli P., Fellin L., Bordignon P., Perna M., "Analysis of Interharmonics in DC Arc Furnace Installations", IEEE International Conference on Harmonics and Quality of Power, Vol. 2, Page 1092-1099, October 14-18, 1998.
- [90] Manchur G., Erven C.C., "Development of A Model for Predicting Flicker from Electric Arc Furnaces", IEEE Transactions on Power Delivery, Vol. 7, No. 1, Page 416-426, January 1992.
- [91] Montanari G.C., Loggini M., Cavallini A., Pitti L., Zaninelli D., "Arc Furnace Model for the Study of Flicker Compensation in Electrical Networks", IEEE Transactions on Power Delivery, Vol. 9, No. 4, Page 2026-2036, October 1994.
- [92] Montanari G.C., Loggini M., Cavallini A., Pitti L., "Flicker and Distortion Compensation in Electrical Plants Supplying Arc Furnaces", IEEE Industry Applications Society Annual Meeting, Vol. 3, Page 2249-2255, October 2-5, 1994.
- [93] Petersen H.M., Koch R.G., Swart P.H., van Heerden R., "Modelling Arc Furnace Flicker and Investigating Compensation Techniques", IEEE Industry Applications Society Annual Meeting, Vol. 2, Page 1733-1740, October 8-12, 1995.
- [94] Tang L., Kolluri S., McGranaghan, M.F., "Voltage Flicker Prediction for Two Simultaneously Operated AC Arc Furnaces", IEEE Transactions on Power Delivery, Vol. 12, No. 2, Page 985-992, April 1997.
- [95] Collantes-Bellido R., Gómez T., "Identification and Modeling of a Three Phase Arc Furnace for Voltage Disturbance Simulation", IEEE Transactions on Power Delivery, Vol. 12, No. 4, Page 1812-1817, October 1997.

- [96] Ramos B.N., de Castro Parga J.L., "An EMTP Study of Flicker Generation and Transmission in Power Systems due to the Operation of an AC Electric Arc Furnace", IEEE International Conference on Harmonics and Quality of Power, Vol. 3, Page 942-947, October 1-4, 2000.
- [97] Mayordomo J.G., Beites L.F., Asensi R., Izzeddine M., Zabala L., Amantegui J., "A New Frequency Domain Arc Furnace Model for Iterative Harmonic Analysis", IEEE Transactions on Power Delivery, Vol. 12, No. 4, Page 1771-1778, October 1997.
- [98] Ting W., Wennan S., Yao Z., "A New Frequency Domain Method for the Harmonic Analysis of Power Systems with Arc Furnaces", IEE International Conference on Advances in Power System Control, Operations and Management, Vol. 2, Page 552-555, November 11-14, 1997.
- [99] Varadan S., Makram E.B., Girgis A.A., "A New Time Domain Voltage Source Model for An Arc Furnace Using EMTP", IEEE Transactions on Power Delivery, Vol. 11, No. 3, Page 1685-1691, July 1996.
- [100] Zheng T., Makram E.B., Girgis A.A., "Effect of Different Arc Furnace Models on Voltage Distortion", IEEE International Conference on Harmonics and Quality of Power, Vol. 2, Page 1079-1085, October 14-18, 1998.
- [101] O'Neill-Carrillo E., Heydt G.T., Kostelich E.J., Venkata S.S., Sundaram A., "Nonlinear Deterministic Modeling of Highly Varying Loads", IEEE Transactions on Power Delivery, Vol. 14, No. 2, Page 537-542, April 1999.
- [102] Ozgun O., Abur A., "Development of an Arc Furnace Model for Power Quality Studies", IEEE Power Engineering Society Summer Meeting, Vol. 1, Page 507-511, July 18-22, 1999.
- [103] Zheng T., Makram E.B., "An Adaptive Arc Furnace Model", IEEE Transactions on Power Delivery, Vol. 15, No. 3, Page 931-939, July 2000.
- [104] Bordignon P., Perna M., Mattavelli P., D'Amico F., "Design Tools of DC EAF Power Supply Systems for Optimum Reduction of Flicker and Interharmonic Disturbances", ISS Electric Furnace Conference Proceedings, Page 113-122, 1998.
- [105] Bekker J., Swart P.H., Landy C.F., Marshall D.A., "Modeling of a DC Arc Furnace for Optimal Integration with the Supply System", IEEE Industry Applications Society Annual Meeting, Vol. 2, Page 1741-1748, October 8-12, 1995.
- [106] Stade D., Schau H., Aprelkov I., Novitskiy A., "Mathematical Simulation of DC Arc Furnace Operation in Electric Power Systems", IEEE International Conference on Harmonics and Quality of Power, Vol. 2, Page 1086-1091, October 14-18, 1998.

- [107] Stade D., Schau H., Prinz S., "Influence of the Current Control Loops of DC Arc Furnaces on Voltage Fluctuations and Harmonics in the HV Power Supply System", IEEE International Conference on Harmonics and Quality of Power, Vol. 3, Page 821-827, October 1-4, 2000.
- [108] Kennedy B.W., "Power Quality Primer", McGraw-Hill, 2000.
- [109] Dugan R.C., McGranaghan M.F., Beaty H.W., "Electrical Power Systems Quality", McGraw-Hill, 1996.
- [110] Heydt G.T., "Electrical Power Quality", Stars in a Circle Publications, 1994.
- [111] IEEE Standard 519-1992, "IEEE Recommended Practices and Requirements for Harmonic Control in Electrical Power Systems", June 18, 1992.
- [112] IEEE Standard 141-1993, "IEEE Recommended Practices for Electric Power Distribution in Industrial Plants", December 2, 1993.
- [113] IEEE Standard 493-1997, "IEEE Recommended Practices for the Design of Reliable Industrial and Commercial Power Systems", December 16, 1997.
- [114] IEC 61000-1-1, "Electromagnetic Compatibility - Part 1: General - Section 1: Application and Interpretation of Fundamental Definitions and Terms", First Edition 1992.
- [115] IEC 61000-3-6, "Electromagnetic Compatibility - Part 3: Limits - Section 6: Assessment of Emission Limits for Distorting Loads in MV and HV Power Systems", First Edition 1996.
- [116] IEC 61000-3-7, "Electromagnetic Compatibility - Part 3: Limits - Section 7: Assessment of Emission Limits for Fluctuating Loads in MV and HV Power Systems", First Edition 1996.
- [117] IEC 61000-4-7, "Electromagnetic Compatibility - Part 4: Testing and Measurement Techniques - Section 7: General Guide on Harmonic and Interharmonic Measurements and Instrumentation for Power Supply Systems and Equipment Connected Thereto", First Edition 1991.
- [118] IEC 61000-4-15, "Electromagnetic Compatibility - Part 4: Testing and Measurement Techniques - Section 15: Flickermeter - Functional and Design Specifications", First Edition 1997, Amended 2002.
- [119] IEC 61000-4-30, "Electromagnetic Compatibility - Part 4: Testing and Measurement Techniques - Section 30: Power Quality Measurement Methods", Draft 2002.

- [120] Reid W.E., "Power Quality Issues - Standards and Guidelines". IEEE Transactions on Industry Applications", Vol. 32, No. 3. Page 625-632. May/June 1996.
- [121] Heydt G.T., Gunther E., "Post Measurement Processing of Power Quality Data". IEEE Transactions on Power Delivery. Vol. 11, No. 4, Page 1853-185, October 1996.
- [122] Heydt G.T., Jewell W.T., "Pitfalls of Electric Power Quality Indices", IEEE Transactions on Power Delivery, Vol. 13, No. 2. Page 570-578. April 1998.
- [123] Heydt G.T., Fjeld P.S., Liu C.C., Pierce D., Tu L., Hensley G., "Applications of the Windowed FFT to Electric Power Quality Assessment". IEEE Transactions on Power Delivery, Vol. 14. No. 4, Page 1411-1416, October 1999.
- [124] Jaramillo S.H., Heydt G.T., O'Niell-Carrillo E., "Power Quality Indices for Aperiodic Voltages and Currents", IEEE Transactions on Power Delivery, Vol. 15, No. 2, Page 784-790, April 2000.
- [125] IEEE Working Group on Nonsinusoidal Situations. "Practical Definitions for Powers in Systems with Nonsinusoidal Waveforms and Unbalanced Loads: A Discussion", IEEE Transactions on Power Delivery, Vol. 11, No. 1, Page 79-101, January 1996.
- [126] Slonim M.A., Van Wyk J.D., "Power Components in a System with Sinusoidal and Nonsinusoidal Voltages and/or Currents", IEE Proceedings B, Vol. 135, No. 2, Page 76-84, March 1988.
- [127] Czarnecki L.S., "Considerations on the Reactive Power in Nonsinusoidal Situations", IEEE Transactions on Instrumentation and Measurement, Vol. 34, No. 3, Page 399-404, September 1985.
- [128] Czarnecki L.S., "Distortion Power in Systems with Nonsinusoidal Voltage", IEE Proceedings B, Vol. 139, No. 3, Page 276-280, May 1992.
- [129] Czarnecki L.S., "Comments on Active Power Flow and Energy Accounts in Electrical Systems with Nonsinusoidal Waveforms and Asymmetry", IEEE Transactions on Power Delivery, Vol. 11, No. 3, Page 1244-1250. July 1996.
- [130] Emanuel A.E., "On the Definition of Power Factor and Apparent Power in Unbalanced Polyphase Circuits with Sinusoidal Voltage and Currents", IEEE Transactions on Power Delivery, Vol. 8. No. 3, Page 841-852, July 1993.
- [131] Sharon D., "Power Factor Definitions and Power Transfer Quality in Nonsinusoidal Situations", IEEE Transactions on Instrumentation and Measurement, Vol. 45. No. 3, Page 728-733, June 1996.

- [132] Manjure D.P., Makram E.B., "Effect of Nonlinearity and Unbalance on Power Factor", IEEE Power Engineering Society Summer Meeting, Vol. 2, Page 956-962, July 16-20, 2000.
- [133] Shipp D.D., "Harmonic Analysis and Suppression for Electrical Systems Supplying Static Power Converters and Other Nonlinear Loads", IEEE Transactions on Industry Applications, Vol. 15, No. 5, Page 453-458, September/October 1979.
- [134] Sutherland P.E., "Harmonic Measurements in Industrial Power Systems", IEEE Transactions on Industry Applications, Vol. 31, No. 1, Page 175-183, January/February 1995.
- [135] Cigré Working Group 36.05, "Equipment Producing Harmonics and Conditions Governing their Connection to the Mains Power Supply", Electra, No. 123, Page 20-37, March 1989.
- [136] IEEE Task Force on the Effects of Harmonics on Equipment, "Effects of Harmonics on Equipment", IEEE Transactions on Power Delivery, Vol. 8, No. 2, Page 672-680, April 1993.
- [137] IEEE Interharmonics Task Force, Cigré 36.05/CIRED 2 CCO2 Voltage Quality Working Group, "Interharmonics in Power Systems".
- [138] Wikston J.M., "The UIE/IEC Flickermeter Description".
- [139] Blooming T.M., Bishop M.T., Skendzic V., "The Measurement of Power System Voltage Flicker", ISS Electric Furnace Conference Proceedings, Page 323-332, 1996.
- [140] Key T.S., Nastasi D.J., Goodwill J.E., "Light Flicker due to Voltage Fluctuations: Changes in Lamp Technology Standards", ISS Electric Furnace Conference Proceedings, Page 285-290, 1996.
- [141] Mombauer W., "Flicker Caused by Interharmonics", etzArchiv.
- [142] Keppler T., Watson N.R., Arrillaga J., Chen S., "Theoretical Assessment of Light Flicker Caused by Sub- and Interharmonic Frequencies", IEEE Transactions on Power Delivery, Vol. 18, No. 1, Page 329-333, January 2003.
- [143] Rashid M.H., "Power Electronics: Circuits, Devices, and Applications", Prentice-Hall, 1988.
- [144] Tarter R.E., "Solid-State Power Conversion Handbook", John Wiley and Sons, 1993.
- [145] MIL-HDBK-217F, "Military Handbook - Reliability Prediction of Electronic Equipment", December 2, 1991. Notice 1. July 10, 1992. Notice 2. February 28, 1995.

Appendix A

EUPEC Device Data Sheets

This appendix contains partial data sheets for the following EUPEC power electronic devices:

1. T4771N Phase Control Thyristor
2. D4709N Rectifier Diode
3. FZ1200R IGBT Module
4. D2659N Rectifier Diode
5. D1408S Fast Diode

Technische Information / Technical Information

eupec

Netz Thyristor
Phase Control Thyristor

T 4771 N 22...29 TOF

N

Features:

Volle Sperrfähigkeit bei 125° mit 50 Hz

Full blocking capability at 125°C with 50 Hz

Hohe Stoßströme und niedriger Wärme-
widerstände durch NTV-Verbindung
zwischen Silizium und Mo-Trägerscheibe.

High surge currents and low thermal resistance
by using low temperature-connection NTV
between silicon wafer and molybdenum.

Elektroaktive Passivierung durch a - C:H

Electroactive passivation by a - C:H

Elektrische Eigenschaften / Electrical properties

Höchstzulässige Werte / Maximum rated values

Periodische Vorwärts - und Rückwärts - Spitzenspannung repetitive peak forward off-state and reverse voltage	f = 50 Hz	V_{DRM} V_{RRM}	$t_{vj\ min} = -40^{\circ}C$ $t_{vj\ min} = 0^{\circ}C$ 2200 2250 2600 2650 2800 2900 2900 3000	V V V V V
Durchlaßstrom-Grenzeffektivwert RMS forward current		I_{TRMS}	10200	A
Dauergrenzstrom mean forward current	$I_C = 85^{\circ}C, f = 50Hz$ $I_C = 60^{\circ}C, f = 50Hz$	I_{TAVM}	4770 6500	A A
Stoßstrom-Grenzwert surge forward current	$t_q = 25^{\circ}C, t_p = 10ms$ $t_q = I_{q\ max}, t_p = 10ms$	I_{TSM}	95 90	kA kA
Grenzlasiintegral I^2t -value	$t_q = 25^{\circ}C, t_p = 10ms$ $t_q = I_{q\ max}, t_p = 10ms$	I^2t	$45,1 \cdot 10^6$ $40,5 \cdot 10^6$	A ² s A ² s
Kritische Stromsteilheit critical rate of rise of on-state current	DIN IEC 747-6 f = 50Hz, $V_{D0} = 0,67 V_{DRM}$, $I_{qsm} = 3A$, $dI_{q0}/dt = 6A/\mu s$	$(di/dt)_{cr}$	300	A/ μs
Kritische Spannungssteilheit critical rate of rise of off-state voltage	$t_q = I_{q\ max}, V_{D0} = 0,67 V_{DRM}$ 5 Kennbuchstabe / 5 th letter F	$(dv/dt)_{cr}$	1000	V/ μs

BIP AM / SM PB, 2001-04-10, Przybilla J. / Keller

Release 4

Seite/page 1

Technische Information / Technical Information

eupec

Netz Thyristor
Phase Control Thyristor

T 4771 N 22...29 TOF

N



Charakteristische Werte / Characteristic values

Durchlaßspannung on-state voltage	$I_T = I_{Tmax}, I_T = 40A$	V_T	typ 1,1	max 1,14	V
Schleusenspannung / threshold voltage Ersatzwiderstand / slope resistance	$I_T = I_{Tmax}$ 30A, 80A	$V_{(TO)}$ r_T	typ 0,796 0,0760	max 0,821 0,0774	V mΩ
Durchlaßcharakteristik on - state characteristics for calculation $V_T = A + B \cdot I_T + C \cdot \ln(I_T + 1) + D \cdot \sqrt{I_T}$ 1000 A ≤ I_T ≤ 10000A	$I_T = I_{Tmax}$	A B C D	typ -0,1085 0,0000126 0,0886 0,0069	max -0,1065 0,0000273 0,0993 0,00496	
Zündstrom gate trigger current	$I_T = 25^\circ C, V_G = 6V$	I_{GT}		350	mA
Zündspannung gate trigger voltage	$I_T = 25^\circ C, V_G = 6V$	V_{GT}		2,5	V
Nicht zündender Steuerstrom gate non-trigger current	$I_T = I_{Tmax}, V_G = 6V$ $I_T = I_{Tmax}, V_G = 0,5 V_{DRM}$	I_{GD}		20 10	mA mA
nicht zündende Steuerspannung gate non-trigger voltage	$I_T = I_{Tmax}, V_G = 0,5 V_{DRM}$	V_{GD}		0,4	V
Haltestrom holding current	$I_T = 25^\circ C, V_C = 12V, R_A = 4,7\Omega$	I_H		350	mA
Einraststrom latching current	$I_T = 25^\circ C, V_C = 12V, R_{GD} \geq 10\Omega$ $I_{GD} = 3A, dv/dt = 6 A/\mu s, t_g = 20\mu s$	I_L		3	A
Vorwärts- und Rückwärts-Sperrstrom forward off-state and reverse currents	$I_T = I_{Tmax}$ $V_C = V_{DRM}, V_R = V_{RRM}$	I_O, I_R		200	mA
Zündverzugszeit gate controlled delay time	DIN IEC 747-6 $I_T = 25^\circ C,$ $I_{GD} = 3A, dv/dt = 6A/\mu s$	t_{gd}		1,5	μs
Freiwerdzeit circuit commutated turn-off time	$I_T = I_{Tmax}, I_{TR} = I_{TRmax}$ $V_{DRM} = 100V, V_{DRM} = 0,67 V_{DRM}$ $dv/dt = 20V/\mu s, -di/dt = 10A/\mu s$ 4 Kennbuchstabe 4 th letter O	t_q	typ.	250	μs
Sperrverzögerungsladung recovered charge	$I_T = I_{Tmax}$ $I_{TR} = 3500A, di/dt = 10A/\mu s$ $V_A = 0,5 V_{DRM}, V_{RRM} = 0,8 V_{DRM}$	Q_r		12	mAs
Rückstromspitze peak reverse recovery current	$I_T = I_{Tmax}$ $I_{TR} = 3500A, di/dt = 10 A/\mu s$ $V_A = 0,5 V_{DRM}, V_{RRM} = 0,8 V_{DRM}$	I_{RM}		320	A

Technische Information / Technical Information

eupec

Netz Thyristor
Phase Control Thyristor

T 4771 N 22...29 TOF

N



Thermische Eigenschaften / Thermal properties

Innerer Wärmewiderstand thermal resistance, junction to case	beidseitig / two-sided, $\Theta = 180^\circ$ an beidseitig / two-sided, DC Anode / anode DC Kathode / cathode DC	R_{thJC}	0,0048 0,0045 0,0085 5 0,0095	$^{\circ}\text{C/W}$ $^{\circ}\text{C/W}$ $^{\circ}\text{C/W}$ $^{\circ}\text{C/W}$ $^{\circ}\text{C/W}$
Übergangs-Wärmewiderstand thermal resistance, case to heatsink	beidseitig / two-sided einseitig / single-sided	R_{thCH}	0,0015 0,0030	$^{\circ}\text{C/W}$ $^{\circ}\text{C/W}$
Höchstzulässige Sperrschichttemperatur max. junction temperature		$t_{vj\text{ max}}$	125	$^{\circ}\text{C}$
Betriebstemperatur operating temperature		$t_{c\text{ op}}$	-40...+125	$^{\circ}\text{C}$
Lagertemperatur storage temperature		t_{stg}	-40...+150	$^{\circ}\text{C}$

Mechanische Eigenschaften / Mechanical properties

Gehäuse, siehe Anlage case, see appendix			Seite 4	
Si-Element mit Druckkontakt, Amplifying gate silicon pellet with pressure contact, amplifying gate	Silizium Tablette silicon wafer		100TN29	
Anpreßkraft clampig force		F	63...91	kN
Gewicht weight		G	typ. 2500	g
Kriechstrecke surface creepage distance			33	mm
Feuchtklasse humidity classification	DIN 40040		C	
Schwingfestigkeit vibration resistance	f = 50Hz		50	m/s^2

Mit dieser technischen Information werden Halbleiterbauelemente spezifiziert, jedoch keine Eigenschaften zugesichert. Sie gilt in Verbindung mit den zugehörigen technischen Erläuterungen.
This technical information specifies semiconductor devices but promises no characteristics. It is valid in combination with the belonging technical notes.

Technische Information / Technical Information

eupec

Netz Gleichrichterdioden
Rectifier Diode

D 4709 N 20...28

N 

Elektrische Eigenschaften / Electrical properties

Höchstzulässige Werte / Maximum rated values

Vorläufige Daten

Preliminary Data

Periodische Spitzenspannung repetitive peak forward reverse voltage	$T_{vj} = -40^{\circ}\text{C} \dots T_{vj\text{max}}$	V_{RRM}	2000 2400	2200 2600 2600	V V V
Stoßspitzenspannung non-repetitive peak reverse voltage	$T_{vj} = +25^{\circ}\text{C} \dots T_{vj\text{max}}$	V_{RRM}	2100 2500	2300 2700 2900	V V V
Durchlaßstrom-Grenzeffektivwert RMS forward current		I_{FRMS}	8.400		A
Deuergrenzstrom mean forward current	$T_c = 100^{\circ}\text{C}$ $T_c = 87^{\circ}\text{C}$	I_{FAVM}	4.700 5.348		A A
Stoßstrom-Grenzwert surge forward current	$T_{vj} = 25^{\circ}\text{C}, t_p = 10\text{ ms}$ $T_{vj} = T_{vj\text{max}}, t_p = 10\text{ ms}$	I_{FSM}	71.000 60.000		A A
Grenzlastintegral FI-value	$T_{vj} = 25^{\circ}\text{C}, t_p = 10\text{ms}$ $T_{vj} = T_{vj\text{max}}, t_p = 10\text{ms}$	FI	25.205 18.000		$\text{A}^2\text{s} \cdot 10^{-2}$ $\text{A}^2\text{s} \cdot 10^{-2}$

Charakteristische Werte / Characteristic values

Durchlaßspannung forward voltage	$T_{vj} = T_{vj\text{max}}, I_F = 11,0\text{ kA}$ $T_{vj} = T_{vj\text{max}}, I_F = 4,0\text{ kA}$	V_F V_F	max. max.	1,65 1,12	V V
Schleusenspannung threshold voltage	$T_{vj} = T_{vj\text{max}}$ Low-level $i_{Tmax} \leq 5000\text{ A}$	$V_{(T0)}$ $V_{(T0)2}$		0,83 0,68	V V
Ersatzwiderstand forward slope resistance	$T_{vj} = T_{vj\text{max}}$ Low-level $i_{Tmax} \leq 5000\text{ A}$	r_T r_{T2}		0,07 0,104	mΩ mΩ
Durchlaßkennlinie on-state voltage	$I_{vj} = I_{vj\text{max}}$ $v_T = A + B \cdot i_T + C \cdot \ln(i_T + 1) + D \cdot \sqrt{i_T}$	A= B= C= D=	1,403E+00 2,111E-05 -1,405E-01 1,255E-02		
Sperrstrom reverse current	$T_{vj} = T_{vj\text{max}}, V_R = V_{RRM}$	i_R	max.	200	mA

Thermische Eigenschaften / Thermal properties

Innerer Wärmewiderstand thermal resistance, junction to case	Kühlfläche / cooling surface beidseitig / two-sided, $\theta = 180^{\circ}\text{sin}$ beidseitig / two-sided, DC Anode / anode, $\theta = 180^{\circ}\text{sin}$ Anode / anode, DC Kathode / cathode, $\theta = 180^{\circ}\text{sin}$ Kathode / cathode, DC	$R_{\theta JC}$	max. max. max. max. max. max.	0,0080 0,0073 0,0147 0,0136 0,0174 0,0160	$^{\circ}\text{C/W}$ $^{\circ}\text{C/W}$ $^{\circ}\text{C/W}$ $^{\circ}\text{C/W}$ $^{\circ}\text{C/W}$ $^{\circ}\text{C/W}$
Übergangs- Wärmewiderstand thermal resistance, case to heatsink	Kühlfläche / cooling surface beidseitig / two-sided einseitig / single-sided	$R_{\theta JK}$	max. max.	0,0025 0,0050	$^{\circ}\text{C/W}$ $^{\circ}\text{C/W}$
Höchstzulässige Sperrschichttemperatur max. junction temperature		$T_{vj\text{max}}$		160	$^{\circ}\text{C}$
Betriebstemperatur operating temperature		$T_{c\text{op}}$		-40...+160	$^{\circ}\text{C}$
Lagertemperatur storage temperature		T_{stg}		-40...+150	$^{\circ}\text{C}$

prepared by: K.-A. Röhrer
approved by: J. Novotny


date of publication: 00-10-23
revision: 1


BIP AM
A26/00


Seite/page 1


Technische Information / Technical Information			eupec	
Netz Gleichrichterdiode Rectifier Diode		D 4709 N 20...28	N	
Mechanische Eigenschaften / Mechanical properties			Vorläufige Daten Preliminary Data	
Gehäuse, siehe Anlage case, see appendix			Seite 3 page 3	
Si-Element mit Druckkontakt Si-pellet with pressure contact				
Anpreßkraft clamping force		F	42...95	kN
Gewicht weight		G	typ. 1200	g
Kriechstrecke creepage distance			36	mm
Feuchteklasse humidity classification	DIN 40040		C	
Schwingfestigkeit vibration resistance	f = 50Hz		50	m/s ²
Kühlkörper/heatsinks : KE01800W				
<p>Mit dieser technischen Information werden Halbleiterbauelemente spezifiziert, jedoch keine Eigenschaften zugesichert. Sie gilt in Verbindung mit den zugehörigen Technischen Erläuterungen./ The technical information specifies semiconductor devices but promises no characteristics. It is valid in combination with the belonging technical notes.</p>				
BIP AM / 00-10-23, K.-A. Rütger		A26/00	Seite/page 2	

Technische Information / Technical Information		eupec				
IGBT-Module IGBT-Modules						
FZ 1200 R 33 KF2						
		Datenblatt data sheet				
Höchstzulässige Werte / Maximum rated values						
Elektrische Eigenschaften / Electrical properties						
Kollektor-Emitter-Spannung collector-emitter voltage	$T_J = 25^\circ\text{C}$ $T_J = -25^\circ\text{C}$	V_{CE}	3300 3300	V		
Kollektor-Dauergleichstrom DC-collector current	$T_C = 80^\circ\text{C}$ $T_C = 25^\circ\text{C}$	$I_{C, \text{nom}}$ I_C	1200 2000	A		
Periodischer Kollektor Spitzenstrom repetitive peak collector current	$t_p = 1 \text{ ms}$, $T_C = 80^\circ\text{C}$	$I_{C, \text{RM}}$	2400	A		
Gesamt-Verlustleistung total power dissipation	$T_C = 25^\circ\text{C}$, Transistor	P_{tot}	14,7	kW		
Gate-Emitter-Spitzenspannung gate-emitter peak voltage		V_{GE}	$\pm 20\text{V}$	V		
Dauergleichstrom DC forward current		I_F	1200	A		
Periodischer Spitzenstrom repetitive peak forw. current	$t_p = 1 \text{ ms}$	$I_{F, \text{RM}}$	2400	A		
Grenzlastintegral der Diode f_t - value, Diode	$V_R = 0\text{V}$, $t_p = 10\text{ms}$, $T_J = 125^\circ\text{C}$	f_t	500.000	A^2s		
Spitzenverlustleistung der Diode maximum power dissipation diode	$T_J = 125^\circ\text{C}$	P_{RDM}	1.200	kW		
Isolations-Prüfspannung insulation test voltage	RMS, $f = 50 \text{ Hz}$, $t = 1 \text{ min.}$	V_{MCI}	6.000	V		
Teilentladungs-Aussetzspannung partial discharge extinction voltage	RMS, $f = 50 \text{ Hz}$, $Q_{\text{PD}} \leq 10 \text{ pC}$ (acc. to IEC 1287)	V_{MCL}	2.600	V		
Charakteristische Werte / Characteristic values						
Transistor / Transistor			min.	typ.	max.	
Kollektor-Emitter Sättigungsspannung collector-emitter saturation voltage	$I_C = 1200\text{A}$, $V_{GE} = 15\text{V}$, $T_J = 25^\circ\text{C}$ $I_C = 1200\text{A}$, $V_{GE} = 15\text{V}$, $T_J = 125^\circ\text{C}$	$V_{CE, \text{sat}}$	- -	3,40 4,30	4,25 5,00	V
Gate-Schwellenspannung gate threshold voltage	$I_C = 120 \text{ mA}$, $V_{CE} = V_{GE}$, $T_J = 25^\circ\text{C}$	$V_{GE, \text{th}}$	4,2	5,1	6,0	V
Eingangskapazität input capacitance	$f = 1\text{MHz}$, $T_J = 25^\circ\text{C}$, $V_{CE} = 25\text{V}$, $V_{GE} = 0\text{V}$	C_{in}	-	150	-	nF
Rückwirkungskapazität reverse transfer capacitance	$f = 1\text{MHz}$, $T_J = 25^\circ\text{C}$, $V_{CE} = 25\text{V}$, $V_{GE} = 0\text{V}$	C_{res}	-	8	-	nF
Gateladung gate charge	$V_{GE} = -15\text{V} \dots +15\text{V}$, $V_{CE} = 1800\text{V}$	Q_G	-	22	-	μC
Kollektor-Emitter Reststrom collector-emitter cut-off current	$V_{CE} = 3300\text{V}$, $V_{GE} = 0\text{V}$, $T_J = 25^\circ\text{C}$ $V_{CE} = 3300\text{V}$, $V_{GE} = 0\text{V}$, $T_J = 125^\circ\text{C}$	I_{CES}	-	0,15 60	12 150	mA
Gate-Emitter Reststrom gate-emitter leakage current	$V_{CE} = 0\text{V}$, $V_{GE} = 20\text{V}$, $T_J = 25^\circ\text{C}$	I_{GES}	-	-	400	nA
prepared by: Jürgen Göttert		date of publication : 00.06.99				
approved by: Chr. Löhle; 20.07.99		revision: 3				

Technische Information / Technical Information		eupec				
IGBT-Module IGBT-Modules		FZ 1200 R 33 KF2				
						
		Datenblatt data sheet				
Charakteristische Werte / Characteristic values						
Transistor / Transistor			min.	typ.	max.	
Einschaltverzögerungszeit (ind. Last) turn on delay time (inductive load)	$I_C = 1200\text{ A}, V_{CC} = 1800\text{ V}$					
	$V_{GE} = \pm 15\text{ V}, R_G = 1,2\ \Omega, C_{DE} = 220\text{ nF}, T_J = 25^\circ\text{C}$	t_{del}	-	370	-	ns
	$V_{GE} = \pm 15\text{ V}, R_G = 1,2\ \Omega, C_{DE} = 220\text{ nF}, T_J = 125^\circ\text{C}$		-	350	-	ns
Anstiegszeit (induktive Last) rise time (inductive load)	$I_C = 1200\text{ A}, V_{CC} = 1800\text{ V}$					
	$V_{GE} = \pm 15\text{ V}, R_G = 1,2\ \Omega, C_{DE} = 220\text{ nF}, T_J = 25^\circ\text{C}$	t_r	-	250	-	ns
	$V_{GE} = \pm 15\text{ V}, R_G = 1,2\ \Omega, C_{DE} = 220\text{ nF}, T_J = 125^\circ\text{C}$		-	270	-	ns
Abschaltverzögerungszeit (ind. Last) turn off delay time (inductive load)	$I_C = 1200\text{ A}, V_{CC} = 1800\text{ V}$					
	$V_{GE} = \pm 15\text{ V}, R_G = 1,2\ \Omega, C_{DE} = 220\text{ nF}, T_J = 25^\circ\text{C}$	t_{del}	-	1550	-	ns
	$V_{GE} = \pm 15\text{ V}, R_G = 1,2\ \Omega, C_{DE} = 220\text{ nF}, T_J = 125^\circ\text{C}$		-	1700	-	ns
Fallzeit (induktive Last) fall time (inductive load)	$I_C = 1200\text{ A}, V_{CC} = 1800\text{ V}$					
	$V_{GE} = \pm 15\text{ V}, R_G = 1,2\ \Omega, C_{DE} = 220\text{ nF}, T_J = 25^\circ\text{C}$	t_f	-	200	-	ns
	$V_{GE} = \pm 15\text{ V}, R_G = 1,2\ \Omega, C_{DE} = 220\text{ nF}, T_J = 125^\circ\text{C}$		-	200	-	ns
Einschaltverlustenergie pro Puls turn-on energy loss per pulse	$I_C = 1200\text{ A}, V_{CC} = 1800\text{ V}, V_{GE} = 15\text{ V}$ $R_G = 1,2\ \Omega, C_{DE} = 220\text{ nF}, T_J = 125^\circ\text{C}, L_G = 40\text{ nH}$	E_{on}	-	2680	-	mWs
Abschaltverlustenergie pro Puls turn-off energy loss per pulse	$I_C = 1200\text{ A}, V_{CC} = 1800\text{ V}, V_{GE} = 15\text{ V}$ $R_G = 1,2\ \Omega, C_{DE} = 220\text{ nF}, T_J = 125^\circ\text{C}, L_G = 40\text{ nH}$	E_{off}	-	1530	-	mWs
Kurzschlussverhalten SC Data	$t_p \leq 10\ \mu\text{sec}, V_{GE} \leq 15\text{ V}$ $T_J \leq 125^\circ\text{C}, V_{CC} = 2500\text{ V}, V_{CE(sat)} = V_{CE} - \Delta V_{CE} < 10\text{ mV}$	I_{sc}	-	6000	-	A
Modulinduktivität stray inductance module		L_{dGE}	-	10	-	nH
Modul-Leitungswiderstand, Anschlüsse - Chip lead resistance, terminals - chip	$T = 25^\circ\text{C}$	R_{OC-GE}	-	0,12	-	m Ω
Charakteristische Werte / Characteristic values						
Diode / Diode			min.	typ.	max.	
Durchlaßspannung forward voltage	$I_F = 1200\text{ A}, V_{GE} = 0\text{ V}, T_J = 25^\circ\text{C}$	V_F	-	2,80	3,50	V
	$I_F = 1200\text{ A}, V_{GE} = 0\text{ V}, T_J = 125^\circ\text{C}$		-	2,80	3,50	V
Rückstromspitze peak reverse recovery current	$I_F = 1200\text{ A}, -dI_F/dt = 3800\text{ A}/\mu\text{sec}$					
	$V_R = 1800\text{ V}, V_{GE} = -10\text{ V}, T_J = 25^\circ\text{C}$	I_{rr}	-	1025	-	A
	$V_R = 1800\text{ V}, V_{GE} = -10\text{ V}, T_J = 125^\circ\text{C}$		-	1100	-	A
Sperverzögerungsladung recovered charge	$I_F = 1200\text{ A}, -dI_F/dt = 3800\text{ A}/\mu\text{sec}$					
	$V_R = 1800\text{ V}, V_{GE} = -10\text{ V}, T_J = 25^\circ\text{C}$	Q_r	-	710	-	μAs
	$V_R = 1800\text{ V}, V_{GE} = -10\text{ V}, T_J = 125^\circ\text{C}$		-	1320	-	μAs
Abschaltenergie pro Puls reverse recovery energy	$I_F = 1200\text{ A}, -dI_F/dt = 3800\text{ A}/\mu\text{sec}$					
	$V_R = 1800\text{ V}, V_{GE} = -10\text{ V}, T_J = 25^\circ\text{C}$	E_{rr}	-	730	-	mWs
	$V_R = 1800\text{ V}, V_{GE} = -10\text{ V}, T_J = 125^\circ\text{C}$		-	1500	-	mWs

Technische Information / Technical Information			eupec			
IGBT-Module IGBT-Modules		FZ 1200 R 33 KF2				
			Datenblatt data sheet			
Thermische Eigenschaften / Thermal properties						
			min.	typ.	max.	
Innerer Wärmewiderstand thermal resistance, junction to case	Transistor / transistor, DC Diode/Diode, DC	R_{thJC}	-	-	0,0085 0,0170	K/W K/W
Übergangs-Wärmewiderstand thermal resistance, case to heatsink	pro Modul / per module $\lambda_{Paste} = 1 \text{ W/m}^2\text{K} / \lambda_{grease} = 1 \text{ W/m}^2\text{K}$	R_{thcH}	-	0,004	-	K/W
Höchstzulässige Sperrschichttemperatur maximum junction temperature		T_{vj}	-	-	150	°C
Betriebstemperatur operation temperature		T_{op}	-40	-	125	°C
Lagertemperatur storage temperature		T_{stg}	-40	-	125	°C
Mechanische Eigenschaften / Mechanical properties						
Gehäuse, siehe Anlage case, see appendix						
Material Modulgrundplatte material of module baseplate			AlSiC			
Innere Isolation internal insulation			AlN			
Kriechstrecke creepage distance			32,2			mm
Luftstrecke clearance			19,1			mm
CTI comperative tracking index			> 400			
Anzugsdrehmoment f. mech. Befestigung mounting torque		M1	5			Nm
Anzugsdrehmoment f. elektr. Anschlüsse terminal connection torque	terminale M4	M2	2			Nm
	terminale M8		8 .. 10			Nm
Gewicht weight		G	1500			g
Mit dieser technischen Information werden Halbleiterbauelemente spezifiziert, jedoch keine Eigenschaften zugesichert. Sie gilt in Verbindung mit den zugehörigen Technischen Erläuterungen.						
This technical information specifies semiconductor devices but promises no characteristics. It is valid in combination with the belonging technical notes.						

N		Datenblatt / Data sheet		eupec	
Netz-Gleichrichterdiode Rectifier Diode		D2659N			
Elektrische Eigenschaften / Electrical properties Höchstzulässige Werte / Maximum rated values					
Periodische Spitzenspannung repetitive peak reverse voltages	$T_v = -40^{\circ}\text{C} \dots T_{v \text{ max}}$	V_{RRM}	2000 2200 2400	V V V	
Stoßspitzenspannung non-repetitive peak reverse voltage	$T_v = +25^{\circ}\text{C} \dots T_{v \text{ max}}$	V_{RSM}	2100 2300 2500	V V V	
Durchlaßstrom-Grenzeffektivwert maximum RMS on-state current		I_{FRMSM}	4710	A	
Dauergrenzstrom average on-state current	$T_c = 100^{\circ}\text{C}$ $T_c = 83^{\circ}\text{C}$	I_{FAVM}	2650 3000	A A	
Stoßstrom-Grenzwert surge current	$T_v = 25^{\circ}\text{C}, t_p = 10 \text{ ms}$ $T_v = T_{v \text{ max}}, t_p = 10 \text{ ms}$	I_{FSM}	41000 33500	A 1) A	
Grenzlastintegral I^2t -value	$T_v = 25^{\circ}\text{C}, t_p = 10 \text{ ms}$ $T_v = T_{v \text{ max}}, t_p = 10 \text{ ms}$	I^2t	8405 5611	kA ² s kA ² s	
Charakteristische Werte / Characteristic values					
Durchlaßspannung on-state voltage	$T_v = T_{v \text{ max}}, i_F = 9,0 \text{ kA}$ $T_v = T_{v \text{ max}}, i_F = 2,5 \text{ kA}$	V_F	max. max.	2,25 1,25	V V
Schleusenspannung threshold voltage	$T_v = T_{v \text{ max}}$	V_{TO1}		0,82	V
Ersatzwiderstand slope resistance	$T_v = T_{v \text{ max}}$	r_T		0,148	mΩ
Durchlaßkennlinie on-state characteristic $V_T = A + B \cdot i_T + C \cdot \ln(i_T - 1) + D \cdot \sqrt{i_T}$	$T_v = T_{v \text{ max}}$	A= B= C= D=	-4,562E-01 1,522E-04 2,069E-01 -5,183E-03		
Sperrstrom reverse current	$T_v = T_{v \text{ max}}, V_R = V_{RRM}$	i_R	max.	200	mA
Thermische Eigenschaften / Thermal properties					
Innerer Wärmewiderstand thermal resistance, junction to case	Kühlfläche / cooling surface beidseitig / two-sided, $\theta = 180^{\circ}\text{sin}$ beidseitig / two-sided, DC Anode / anode, $\theta = 180^{\circ}\text{sin}$ Anode / anode, DC Kathode / cathode, $\theta = 180^{\circ}\text{sin}$ Kathode / cathode, DC	$R_{\theta JC}$	max. max. max. max. max. max.	0,0169 0,0160 0,0329 0,0320 0,0329 0,0320	°C/W °C/W °C/W °C/W °C/W °C/W
Übergangs-Wärmewiderstand thermal resistance, case to heatsink	Kühlfläche / cooling surface beidseitig / two-sided einseitig / single-sided	$R_{\theta CH}$	max. max.	0,0025 0,0050	°C/W °C/W
Höchstzulässige Sperrschichttemperatur maximum junction temperature		$T_{v \text{ max}}$		180	°C
Betriebstemperatur operating temperature		$T_{c \text{ op}}$		-40...+150	°C
Lagertemperatur storage temperature		T_{stg}		-40...+150	°C
prepared by:	M.Droldner	date of publication:	19.08.02		
approved by:	J.Novotny	revision:	2		
1) Gehäusegrenzstrom 32 kA (50 Hz Sinushalbwellen). / peak case non-rupture current 32 kA (50 Hz sinusoidal half-wave).					
MA2-BE / 9 Sep 1994, R.Jörke		A43/94	Seite/page		1/10

N		Datenblatt / Data sheet	eupec																															
Netz-Gleichrichterdiode Rectifier Diode		D2659N																																
Mechanische Eigenschaften / Mechanical properties <table border="1"> <tr> <td>Gehäuse, siehe Anlage case, see annex</td> <td></td> <td></td> <td>Seite 3 page 3</td> <td></td> </tr> <tr> <td>Si-Element mit Druckkontakt Si-pellet with pressure contact</td> <td></td> <td></td> <td></td> <td></td> </tr> <tr> <td>Anpreßkraft clamping force</td> <td></td> <td>F</td> <td>24...60</td> <td>Nm</td> </tr> <tr> <td>Gewicht weight</td> <td></td> <td>G</td> <td>typ. 540</td> <td>g</td> </tr> <tr> <td>Kriechstrecke creepage distance</td> <td></td> <td></td> <td>40</td> <td>mm</td> </tr> <tr> <td>Schwingfestigkeit vibration resistance</td> <td>f = 50 Hz</td> <td></td> <td>50</td> <td>m/s²</td> </tr> </table>					Gehäuse, siehe Anlage case, see annex			Seite 3 page 3		Si-Element mit Druckkontakt Si-pellet with pressure contact					Anpreßkraft clamping force		F	24...60	Nm	Gewicht weight		G	typ. 540	g	Kriechstrecke creepage distance			40	mm	Schwingfestigkeit vibration resistance	f = 50 Hz		50	m/s²
Gehäuse, siehe Anlage case, see annex			Seite 3 page 3																															
Si-Element mit Druckkontakt Si-pellet with pressure contact																																		
Anpreßkraft clamping force		F	24...60	Nm																														
Gewicht weight		G	typ. 540	g																														
Kriechstrecke creepage distance			40	mm																														
Schwingfestigkeit vibration resistance	f = 50 Hz		50	m/s²																														
<p>Mit diesem Datenblatt werden Halbleiterbauelemente spezifiziert, jedoch keine Eigenschaften zugesichert. Sie gilt in Verbindung mit den zugehörigen technischen Erläuterungen.</p> <p>This data sheet specifies semiconductor devices, but promises no characteristics. It is valid in combination with the belonging technical notes</p>																																		
MA2-BE / 9 Sep 1994 , R.Jörke		A43/94	Seite/page	2/10																														

Technische Information / Technical Information

eupec

Schnelle Gleichrichterdioden
Fast Diode

D 1408 S 20...25

s 

Elektrische Eigenschaften / Electrical properties

Höchstzulässige Werte / Maximum rated values

Periodische Spitzenspannung repetitive peak forward reverse voltage	$T_q = -25^\circ\text{C} \dots T_{q\text{max}}$	V_{RRM}	2000 2500	V
Stoßspitzenspannung non-repetitive peak reverse voltage	$T_q = +25^\circ\text{C} \dots T_{q\text{max}}$	V_{RSM}	2100 2600	V
Durchlaßstrom-Grenzeffektivwert RMS forward current		I_{FRM}	3360	A
Deuergrenzstrom mean forward current	$T_c = 85^\circ\text{C}$ $T_c = 52^\circ\text{C}$	I_{FAVM}	1410 2140	A
Stoßstrom-Grenzwert surge forward current	$T_q = 25^\circ\text{C}, t_p = 10\text{ ms}$ $T_q = T_{q\text{max}}, t_p = 10\text{ ms}$	I_{FSM}	27500 24000	A
Grenzlastintegral P-t-value	$T_q = 25^\circ\text{C}, t_p = 10\text{ ms}$ $T_q = T_{q\text{max}}, t_p = 10\text{ ms}$	PR	3780000 2880000	A*s A*s

Charakteristische Werte / Characteristic values

Durchlaßspannung forward voltage	$T_q = T_{q\text{max}}, I_F = 6400\text{ A}$	V_F	max.	2,62	V
Schleusenspannung threshold voltage	$T_q = T_{q\text{max}}$	$V_{(TO)}$		1,16	V
Ersatzwiderstand forward slope resistance	$T_q = T_{q\text{max}}$	r_T		0,21	mΩ
Typischer Wert der Durchlaßverzögerungsspannung typical value of forward recovery voltage	IEC 747-2 $T_q = T_{q\text{max}}$ $dI_F/dt = A/\mu\text{s}, V_R = 0\text{ V}$	V_{FRM}	typ.		V ¹⁾
Durchlaßverzögerungszeit forward recovery time	IEC 747-2, Methode / method II $T_q = T_{q\text{max}}, I_{FM} = A$ $dI_F/dt = A/\mu\text{s}, V_R = 0\text{ V}$	t_{fr}	typ.		μs ¹⁾
Spernstrom reverse current	$T_q = 25^\circ\text{C}, V_R = V_{RRM}$ $T_q = T_{q\text{max}}, V_R = V_{RRM}$	I_R	max. max.	25 250	mA mA
Rückstromspitze peak reverse recovery current	DIN IEC 747-2, $T_q = T_{q\text{max}}$ $I_{RM} = 1000\text{ A}, dI_F/dt = 250\text{ A}/\mu\text{s}$ $V_R < 0,5 V_{RRM}, V_{RM} = 0,8 V_{RRM}$	I_{RRM}		580	A ¹⁾
Spernverzögerungsladung recovered charge	DIN IEC 747-2, $T_q = T_{q\text{max}}$ $I_{RM} = 1000\text{ A}, dI_F/dt = 250\text{ A}/\mu\text{s}$ $V_R < 0,5 V_{RRM}, V_{RM} = 0,8 V_{RRM}$	Q_r		1700	μAs ¹⁾
Spernverzögerungszeit reverse recovered time	DIN IEC 747-2, $T_q = T_{q\text{max}}$ $I_{RM} = 1000\text{ A}, dI_F/dt = 250\text{ A}/\mu\text{s}$ $V_R < 0,5 V_{RRM}, V_{RM} = 0,8 V_{RRM}$	t_{rr}		5	μs ¹⁾
Sanfttheit Softness	$T_q = T_{q\text{max}}$ $I_{RM} = 1000\text{ A}, dI_F/dt = 250\text{ A}/\mu\text{s}$ $V_R < 0,5 V_{RRM}, V_{RM} = 0,8 V_{RRM}$	SR			μs/A ²⁾

1) Richtwert für obere Streubereichsgrenze / Upper limit of scatter range (standard value)

2) Richtwert für untere Streubereichsgrenze / Lower limit of scatter range (standard value)

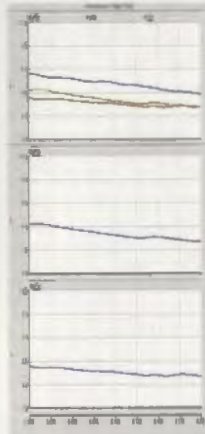
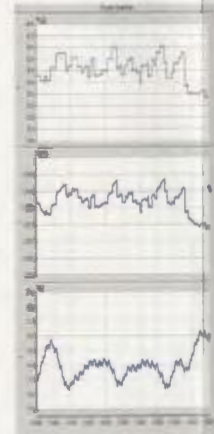
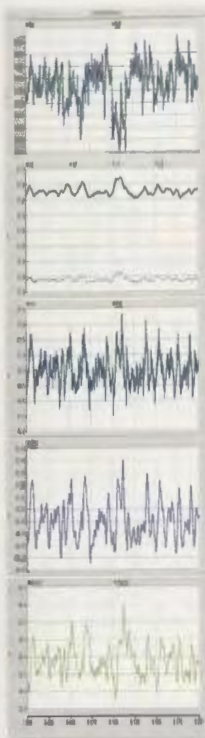
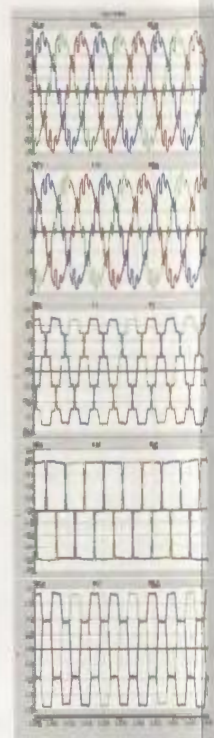
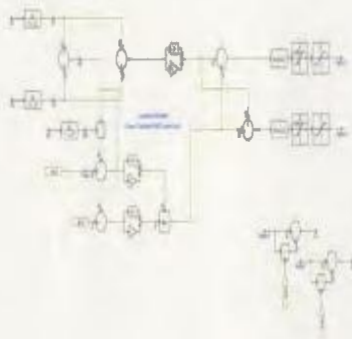
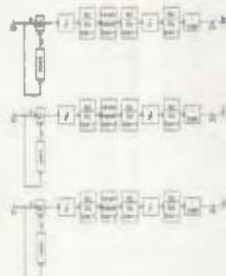
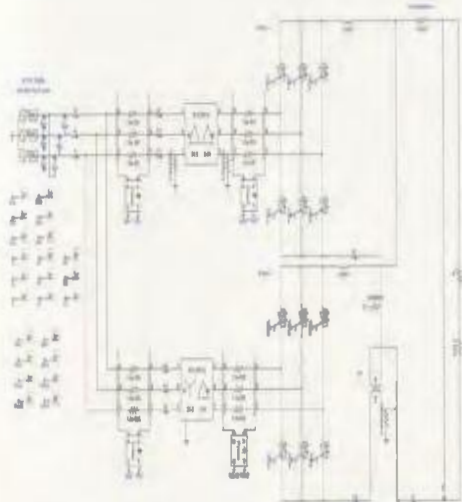
Technische Information / Technical Information			eupec	
Schnelle Gleichrichterdioden Fast Diode		D 1408 S 20...25		s 
Thermische Eigenschaften / Thermal properties				
Innerer Wärmewiderstand thermal resistance, junction to case	Kühlfläche / cooling surface beidseitig / two-sided, $\Theta = 180^\circ \text{sin}$ beidseitig / two-sided, DC Anode / anode, $\Theta = 180^\circ \text{sin}$ Anode / anode, DC Kathode / cathode, $\Theta = 180^\circ \text{sin}$ Kathode / cathode, DC	R_{thJC}	max. 0,0150 max. 0,0140 max. 0,0250 max. 0,0240 max. 0,0350 max. 0,0340	$^\circ\text{C/W}$ $^\circ\text{C/W}$ $^\circ\text{C/W}$ $^\circ\text{C/W}$ $^\circ\text{C/W}$ $^\circ\text{C/W}$
Übergangs- Wärmewiderstand thermal resistance, case to heatsink	Kühlfläche / cooling surface beidseitig / two-sided einseitig / single-sided	R_{thCK}	max. 0,0035 max. 0,007	$^\circ\text{C/W}$ $^\circ\text{C/W}$
Höchstzulässige Sperrschichttemperatur max. junction temperature		$T_{\text{vj max}}$	125	$^\circ\text{C}$
Betriebstemperatur operating temperature		$T_{\text{c op}}$	-40...+125	$^\circ\text{C}$
Lagertemperatur storage temperature		T_{stg}	-40...+150	$^\circ\text{C}$
Mechanische Eigenschaften / Mechanical properties				
Gehäuse, siehe Anlage case, see appendix			Seite 3 page 3	
Si-Element mit Druckkontakt Si-pellet with pressure contact	Durchmesser/diameter 51mm			
Anpresskraft clamping force		F	18...50	kN
Gewicht weight		G	typ. 300	g
Kriechstrecke creepage distance			26	mm
Feuchteklasse humidity classification	DIN 40040		C	
Schwingfestigkeit vibration resistance	f = 50Hz		50	m/s ²
Kühlkörper / heatsinks: K0,05F ; K0,08F ; 2K0,024W				
Mit dieser technischen Information werden Halbleiterbauelemente spezifiziert, jedoch keine Eigenschaften zugesichert. Sie gilt in Verbindung mit den zugehörigen Technischen Erläuterungen./ The technical information specifies semiconductor devices but promises no characteristics. It is valid in combination with the belonging technical notes.				
SZ-M / 29.04.93 , R.Jörke		A 12 / 93		Seite/page 2

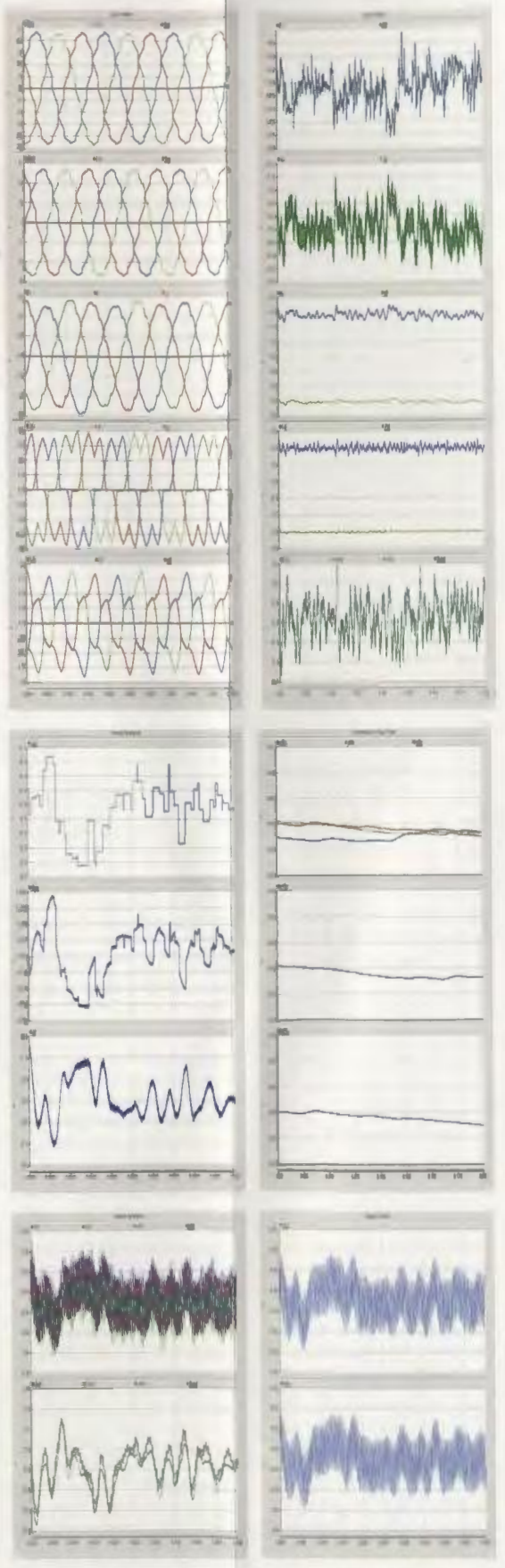
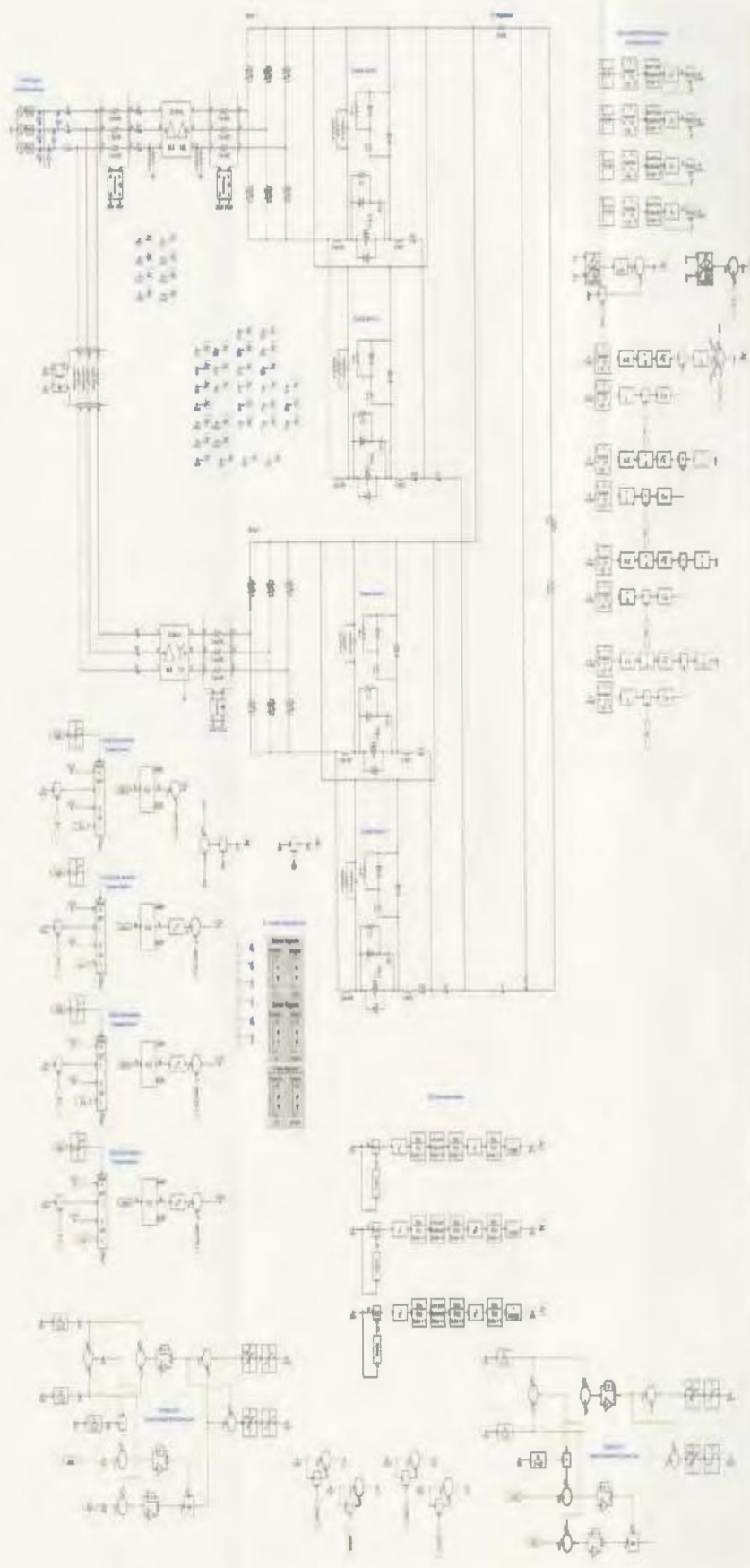
Appendix B

PSCAD Screenshots

This appendix contains screenshots from the PSCAD simulations. Screenshots are provided for:

1. Controlled Rectifier Power Supply
2. Uncontrolled Rectifier Chopper Power Supply





Appendix C

Matlab Programs

This appendix contains Matlab programs used to analyze the outputs from the PSCAD simulations. The programs assume that the PSCAD output file has already been loaded and parameters named accordingly, programs include:

1. Fast Fourier Transform Program (Rectangular Window)
2. Voltage Imbalance
3. Voltage Flicker


```

% Line-to-Neutral Voltage FFT
Vanf=fft(Van,length(Van));
Vanf1=(2*abs(Vanf)/length(Van));
Vanf2=(Vanf1./max(Vanf1))*100;
Vanp=phase(Vanf(13));
Vanf=Vanf1(13)/sqrt(2);
Vbnf=fft(Vbn,length(Vbn));
Vbnf1=(2*abs(Vbnf)/length(Vbn));
Vbnf2=(Vbnf1./max(Vbnf1))*100;
Vbnp=phase(Vbnf(13));
Vbnf=Vbnf1(13)/sqrt(2);
Vcnf=fft(Vcn,length(Vcn));
Vcnf1=(2*abs(Vcnf)/length(Vcn));
Vcnf2=(Vcnf1./max(Vcnf1))*100;
Vcnp=phase(Vcnf(13));
Vcnf=Vcnf1(13)/sqrt(2);

```

```

% Primary Line Current FFT
Iaf=fft(Ia,length(Ia));
Iaf1=(2*abs(Iaf)/length(Ia));
Iaf2=(Iaf1./max(Iaf1))*100;
Iap=phase(Iaf(13));
Iaf=Iaf1(13);
Ibf=fft(Ib,length(Ib));
Ibf1=(2*abs(Ibf)/length(Ib));
Ibf2=(Ibf1./max(Ibf1))*100;
Ibp=phase(Ibf(13));
Ibf=Ibf1(13);
Icf=fft(Ic,length(Ic));
Icf1=(2*abs(Icf)/length(Ic));
Icf2=(Icf1./max(Icf1))*100;
Icp=phase(Icf(13));
Icf=Icf1(13);

```

```

% Output Voltage FFT
Vdf=fft(Vd,length(Vd));
Vdf1=(2*abs(Vdf)/length(Vd));
Vdf2=(Vdf1./max(Vdf1))*100;

```

```

% Output Current FFT
Idf=fft(Id,length(Id));
Idf1=(2*abs(Idf)/length(Id));

```

```
Idf2=(Idf1./max(Idf1))*100;
```

```
% Voltage Unbalance
```

```
Vancx=Vanf*cos(Vanp)+i*Vanf*sin(Vanp);
```

```
Vbncx=Vbnf*cos(Vbnp)+i*Vbnf*sin(Vbnp);
```

```
Vcncx=Vcnf*cos(Vcnp)+i*Vcnf*sin(Vcnp);
```

```
a1=-0.5+i*(sqrt(3)/2);
```

```
a2=-0.5-i*(sqrt(3)/2);
```

```
Vpos=(1/3)*abs(Vancx+a1*Vbncx+a2*Vcncx);
```

```
Vneg=(1/3)*abs(Vancx+a2*Vbncx+a1*Vcncx);
```

```
Vunb=(Vneg/Vpos)*100;
```

```
% Calculates Voltage Flicker
```

```
Pa=prctile(Pf5a,[99.9 99 97 90 50]);
```

```
Psta=sqrt(0.0314*Pa(1)+0.0525*Pa(2)+0.0657*Pa(3)+0.28*Pa(4)+0.08*Pa(5));
```

```
Pb=prctile(Pf5b,[99.9 99 97 90 50]);
```

```
Pstb=sqrt(0.0314*Pb(1)+0.0525*Pb(2)+0.0657*Pb(3)+0.28*Pb(4)+0.08*Pb(5));
```

```
Pc=prctile(Pf5c,[99.9 99 97 90 50]);
```

```
Pstc=sqrt(0.0314*Pc(1)+0.0525*Pc(2)+0.0657*Pc(3)+0.28*Pc(4)+0.08*Pc(5));
```

Appendix D

PSCAD Flickermeter Test Results

This appendix contains the test results from the simulated IEC flickermeter. The test are taken from IEC 61000-4-15 and are as follows:

1. P_{st} Calibration for 230 V and 120 V Systems
2. P_{f5} Calibration for 230 V 50 Hz System
3. P_{f5} Calibration for 120 V 60 Hz System

Table D.1: P_{st} Calibration for 230 V and 120 V Systems

Changes Per Minute	Rectangular ($\Delta V/V$)	230 V 50 Hz System (P_{st})	Error (Percentage)	Rectangular ($\Delta V/V$)	120 V 60 Hz System (P_{st})	Error (Percentage)
39*	0.906	1.0202	2.02	1.044	1.0073	0.73
48	0.870	1.0138	1.38	1.000	0.9979	-0.21
68	0.810	1.0056	0.56	0.939	0.9991	-0.09
110*	0.725	1.0107	1.07	0.841	1.0073	0.73
176	0.640	1.0135	1.35	0.739	1.0042	0.42
273	0.560	1.0173	1.73	0.650	1.0061	0.61
375	0.500	1.0112	1.12	0.594	1.0069	0.69
480	0.480	1.0222	2.22	0.559	1.0092	0.92
585	0.420	1.0026	0.26	0.501	1.0056	0.56
682	0.370	1.0054	0.54	0.445	1.0043	0.43
796	0.320	1.0023	0.23	0.393	1.0047	0.47
1020	0.280	1.0177	1.77	0.350	0.9986	-0.14
1055	0.280	1.0193	1.93	0.351	0.9981	-0.19
1200	0.290	1.0209	2.09	0.371	1.0006	0.06
1390	0.340	1.0304	3.04	0.438	1.0085	0.85
1620*	0.402	0.9886	-1.14	0.547	1.0043	0.43
2400	0.770	0.9951	-0.49	1.051	1.0096	0.96
2875	1.040	1.0022	0.22	1.498	1.0104	1.04
4000*	2.400	1.0261	2.61	NA	NA	NA
4800*	NA	NA	NA	4.834	1.0047	0.47

Table D.2: P_{f5} Calibration for 230 V 50 Hz System

Frequency (Hz)	Sinusoidal ($\Delta V/V$)	P_{f5}	Error (Percentage)	Rectangular ($\Delta V/V$)	P_{f5}	Error (Percentage)
0.5	2.340	0.9758	-2.42	0.514	1.0204	2.04
1.0	1.432	1.0442	4.42	0.471	1.0226	2.26
1.5	1.080	1.0234	2.34	0.432	1.0200	2.00
2.0	0.882	1.0084	0.84	0.401	1.0195	1.95
2.5	0.754	1.0219	2.19	0.374	1.0239	2.39
3.0	0.654	1.0307	3.07	0.355	1.0207	2.07
3.5	0.568	1.0186	1.86	0.345	1.0189	1.89
4.0	0.500	1.0153	1.53	0.333	1.0097	0.97
4.5	0.446	1.0233	2.33	0.316	1.0268	2.68
5.0	0.398	1.0159	1.59	0.293	1.0176	1.76
5.5	0.360	1.0197	1.97	0.269	1.0113	1.13
6.0	0.328	1.0192	1.92	0.249	1.0102	1.02
6.5	0.300	1.0045	0.45	0.231	1.0053	0.53
7.0	0.280	1.0044	0.44	0.217	1.0104	1.04
7.5	0.266	1.0094	0.94	0.207	1.0074	0.74
8.0	0.256	1.0065	0.65	0.201	1.0196	1.96
8.8	0.250	1.0037	0.37	0.199	1.0353	3.53
9.5	0.254	1.0053	0.53	0.200	1.0144	1.44
10.0	0.260	0.9979	-0.21	0.205	1.0262	2.62
10.5	0.270	0.9986	-0.14	0.213	1.0159	1.59
11.0	0.282	0.9955	-0.45	0.223	1.0133	1.33
11.5	0.296	0.9920	-0.80	0.234	1.0109	1.09
12.0	0.312	0.9902	-0.98	0.246	1.0129	1.29
13.0	0.348	0.9858	-1.42	0.275	1.0271	2.71
14.0	0.388	0.9799	-2.01	0.308	1.0071	0.71
15.0	0.432	0.9774	-2.26	0.344	1.0218	2.18
16.0	0.480	0.9797	-2.03	0.376	1.0021	0.21
17.0	0.530	0.9792	-2.08	0.413	1.0126	1.26
18.0	0.584	0.9839	-1.61	0.452	1.0309	3.09
19.0	0.640	0.9865	-1.35	0.498	1.0066	0.66
20.0	0.700	0.9929	-0.71	0.546	0.9796	-2.04
21.0	0.760	0.9922	-0.78	0.586	1.0053	0.53
22.0	0.824	0.9946	-0.54	0.604	0.9784	-2.16
23.0	0.890	0.9946	-0.54	0.680	1.0029	0.29
24.0	0.962	1.0002	0.02	0.743	1.0041	0.41
25.0	1.042	1.0126	1.26	NA	NA	NA
33.33	2.130	1.0038	0.38	1.670	0.9968	-0.32

Table D.3: P_{f5} Calibration for 120 V 60 Hz System

Frequency (Hz)	Sinusoidal ($\Delta V/V$)	P_{f5}	Error (Percentage)	Rectangular ($\Delta V/V$)	P_{f5}	Error (Percentage)
0.5	2.457	0.9708	-2.92	0.600	1.0147	1.47
1.0	1.463	0.9969	-0.31	0.547	1.0101	1.01
1.5	1.124	1.0016	0.16	0.504	1.0178	1.78
2.0	0.940	1.0036	0.36	0.471	1.0212	2.12
2.5	0.814	1.0057	0.57	0.439	1.0105	1.05
3.0	0.716	1.0057	0.57	0.421	1.0191	1.91
3.5	0.636	1.0055	0.55	0.407	1.0047	0.47
4.0	0.569	1.0046	0.46	0.394	1.0125	1.25
4.5	0.514	1.0099	0.99	0.371	1.0018	0.18
5.0	0.465	1.0045	0.45	0.349	1.0148	1.48
5.5	0.426	1.0091	0.91	0.323	1.0031	0.31
6.0	0.393	1.0096	0.96	0.302	1.0097	0.97
6.5	0.366	1.0075	0.75	0.282	1.0006	0.06
7.0	0.346	1.0096	0.96	0.269	1.0070	0.70
7.5	0.332	1.0117	1.17	0.258	1.0066	0.66
8.0	0.323	1.0087	0.87	0.255	1.0235	2.35
8.8	0.321	1.0106	1.06	0.253	1.0217	2.17
9.5	0.330	1.0145	1.45	0.257	1.0000	0.00
10.0	0.339	1.0019	0.19	0.264	0.9992	-0.08
10.5	0.355	1.0092	0.92	0.280	1.0240	2.40
11.0	0.374	1.0150	1.50	0.297	1.0424	4.24
11.5	0.394	1.0112	1.12	0.309	1.0198	1.98
12.0	0.420	1.0255	2.55	0.323	1.0052	0.52
13.0	0.470	1.0151	1.51	0.369	1.0218	2.18
14.0	0.530	1.0201	2.01	0.411	1.0111	1.11
15.0	0.593	1.0157	1.57	0.459	1.0193	1.93
16.0	0.662	1.0160	1.60	0.513	1.0261	2.61
17.0	0.737	1.0207	2.07	0.580	1.0307	3.07
18.0	0.815	1.0215	2.15	0.632	1.0313	3.13
19.0	0.897	1.0221	2.21	0.692	1.0227	2.27
20.0	0.981	1.0184	1.84	0.752	1.0266	2.66
21.0	1.071	1.0191	1.91	0.818	1.0187	1.87
22.0	1.164	1.0180	1.80	0.853	1.0144	1.44
23.0	1.262	1.0185	1.85	0.946	1.0102	1.02
24.0	1.365	1.0206	2.06	1.072	1.0210	2.10
25.0	1.472	1.0216	2.16	NA	NA	NA
40.0	4.424	1.0243	2.43	3.460	1.0164	1.64

